# A DEVELOPMENTAL FRAMEWORK FOR COUPLING NEUROGENESIS TO CIRCUIT FORMATION IN *DROSOPHILA*

by

BRANDON MARK

A DISSERTATION

Presented to the Department of Biology
and the Graduate School of the University of Oregon
in partial fulfillment of the requirements
for the degree of
Doctor of Philosophy

December 2019

## DISSERTATION APPROVAL PAGE

Student: Brandon Mark

Title: A Developmental Framework for Coupling Neurogenesis to Circuit Formation in *Drosophila*

This dissertation has been accepted and approved in fulfillment of the requirements for the Doctor of Philosophy degree in the Department of Biology by:

| | |
|---|---|
| Tory Herman | Chairperson |
| Chris Doe | Advisor |
| Judith Eisen | Core Member |
| Shawn Lockery | Core Member |
| Matt Smear | Institutional Representative |

and

| | |
|---|---|
| Kate Mondloch | Interim Vice Provost and Dean of the Graduate School |

Original approval signatures are on file with the University of Oregon Graduate School.

Degree awarded December 2019

## DISSERTATION ABSTRACT

Brandon Mark

Doctor of Philosophy

Department of Biology

December 2019

Title: A Developmental Framework for Coupling Neurogenesis to Circuit Formation in *Drosophila*

Two central questions in neuroscience are how the brain is capable of both generating the diversity of neurons necessary for generating appropriate behaviors and how developmental programs are capable of then wiring these diverse populations of neurons together into functional circuits. While a great deal of progress has been made towards understanding the mechanisms that specify neuronal diversity, it is less clear how these mechanisms might also regulate neuronal morphology and connectivity. In this dissertation, we identified a novel mechanism for diversity generation in the *Drosophila* central brain. Next, we mapped the developmental origins of seven lineages in the *Drosophila* ventral nerve cord into a serial-section electron microscopy (SSEM) volume and used this connectome to examine how lineage, hemilineage, and birth order correlate with synaptic targeting and connectivity. Finally, we combined the same SSEM volume with single-muscle calcium imaging to explore how these functional circuits are capable of generating distinct locomotor behaviors.

In chapter two, we show that the hormone ecdysone is required to down-regulate early neuroblast temporal identity factors as well as activate later temporal identity factors. This is the first example of hormonal regulation of temporal factor expression in *Drosophila* embryonic or larval neural progenitors.

In chapter three, we map the developmental origin of neurons from seven neuroblasts and identify each neuron within a complete EM reconstruction of the *Drosophila* larval CNS. We find that lineages generate a sensory and motor processing hemilineage in a notch-dependent manner. Within each hemilineage, we observe a birth order dependent "tiling" of the neuropil, and neurons with similar temporal identity are enriched for shared connectivity. Thus, diversity generating mechanisms progressively restrict neuropil targeting, synapse localization, and connectivity.

In chapter four, we characterize neural circuits generating *Drosophila* forward and backward locomotion. We show that a subset of MNs change recruitment timing for each behavior. Next, we used a SSEM volume to reconstruct a comprehensive larval PMN-MN connectome. We conclude that different locomotor behaviors are generated by multiple mechanisms: muscle recruitment differences, dedicated PMN/MN connectivity; asymmetric PMN/MN morphology, and behavior-specific PMN activity.

This dissertation contains unpublished co-authored material.

## CURRICULUM VITAE

Name of Author: Brandon Mark

Graduate and undergraduate schools attended:

University of Oregon, Eugene, OR

Pennsylvania State University, University Park, PA

Degrees Awarded:

Doctor of Philosophy, Biology, 2019, University of Oregon

Bachelor of Science, Biology, 2012, Pennsylvania State University

Professional Experience:

Undergradute Research Assistant, Lab of Dr. Yingwei Mao - February 2010 - May 2012
Pennsylvania State University, State College, PA

Research Assistant & Lab Manager, Lab of Dr. John Ewer - January 2013 - July 2014
University of Valpariaiso, Valparaiso, Chile

Publications:

Syed, M. H., **Mark, B.**, & Doe, C. Q. 2017. *Playing Well with Others: Extrinsic Cues Regulate Neural Progenitor Temporal Identity to Generate Neuronal Diversity*. Trends in Genetics, 33(12). https://doi.org/10.1016/j.tig.2017.08.005

Syed, M. H., **Mark, B.**, & Doe, C. Q. 2017. *Steroid hormone induction of temporal gene expression in Drosophila brain neuroblasts generates neuronal and glial diversity*. ELife, 6. https://doi.org/10.7554/eLife.26287

**Mark, B.**, Lai, S.-L., Zarin, A. A., Manning, L., Cardona, A., Truman, J. W., & Doe, C. Q. (2019). *The role of lineage, hemilineage and temporal identity in establishing neuronal targeting and connectivity in the Drosophila embryo. BioRxiv*, 617936. https://doi.org/10.1101/617936

Zarin, A. A.*, **Mark, B***., Cardona, A., Litwin-Kumar, A., & Doe, C. Q. (2019). *A Drosophila larval premotor/motor neuron connectome generating two behaviors via distinct spatio-temporal muscle activity. BioRxiv*, 617977. https://doi.org/10.1101/617977 *Both authors contributed equally.

# TABLE OF CONTENTS

# LIST OF FIGURES

Figure Page

Figure Page

# CHAPTER I
# INTRODUCTION

Mubarak Hussain Syed, Brandon Mark, and Chris Q. Doe

Institute of Neuroscience, Institute of Molecular Biology, Howard Hughes Medical Institute, University of Oregon, Eugene, OR 97403

## Mechanisms for the generation of neuronal diversity

Neural diversity is essential for proper brain function including sensory perception, motor control and consciousness. Neural diversity is generated by both spatial and temporal cues acting combinatorially on neural progenitors. Spatial cues assign progenitor regional identity, whereas temporal cues or temporal patterning mechanisms allow single progenitors to make a sequence of different neurons and glia over time. Vertebrate neural progenitors have long been known to respond to changing environmental cues to undergo temporal patterning (McConnell & Kaznowski, 1991), although the molecular identity of these extrinsic cues are often still unknown. In contrast, *Drosophila* neural progenitors (neuroblasts) undergo a well-characterized, neuroblast-intrinsic transcription factor cascade that generates temporal identity (reviewed in Cepko, 2014; Doe, 2017; Franco & Muller, 2013; Kohwi & Doe, 2013; Lodato & Arlotta, 2015). In addition to spatial and temporal patterning mechanisms, *Drosophila* neuroblasts also utilize a third mechanism to increase neuronal diversity. When a neuroblast divides, it produces a Ganglion Mother Cell (GMC), which divides once more to generate a pair of neurons or glia. During this terminal GMC division, the repressor of notch, Numb, is assymetrically segregated into one of the daughter cells giving rise to two unique cells for each GMC division. These two populations of cells are known as hemilineages, and it has been shown that hemilineages can be both morphologically and functionally distinct hemilineages (Harris, Pfeiffer, Rubin, & Truman, 2015; Lacin & Truman, 2016a; Skeath & Doe, 1998; Truman, Moats, Altman, Marin, & Williams, 2010). Importantly, recent work has identified extrinsic cues that regulate *Drosophila* neuroblast temporal patterning, raising the possibility of conserved mechanisms used by vertebrate and *Drosophila* progenitors for the generation of neural diversity. Here we briefly summarize what is known about temporal patterning in *Drosophila* and vertebrates, and then discuss newly discovered extrinsic signaling pathways that generate temporal patterning and increase neural diversity in *Drosophila* central brain neuroblasts.

## Temporal patterning in mammalian and *Drosophila* neural progenitors

In mammals, most neural progenitors throughout the CNS (cortex, retina, spinal cord) can generate multiple neuronal subtypes over time, followed by a later phase of gliogenesis (Agathocleous & Harris, 2009; K. N. Brown et al., 2011; Cepko, 2014; Gao et al., 2014; Kessaris, Pringle, & Richardson, 2001; Seto et al., 2014; Xu et al., 2014). Unlike early findings in *Drosophila*, temporal patterning mechanisms characterized in mammals primarily involve extrinsic signals -- either feedback cues from previously generated neurons or cues from unknown sources -- although some evidence from in vitro culture suggests the presence of intrinsic cues (Okano & Temple, 2009; reviewed in Shen et al., 2006). Nevertheless, the best characterized temporal patterning mechanisms involve extrinsic cues, as briefly summarized in the following four examples (Figure 1). First, early cortical progenitors transplanted into older hosts switch to making late-born neurons (Desai & McConnell, 2000). Second, ablation of early-born deep layer neurons leads to prolonged early-born neuron production and a delay in generating late-born upper layer neurons, suggesting a negative feedback signal from early-born neurons to ventricular zone progenitors (Toma, Kumamoto, & Hanashima, 2014). Third, TGFβ signaling is required in three different brain regions to trigger a switch from early-born to late-born neural subtypes (Dias, Alekseenko, Applequist, & Ericson, 2014). Fourth, the Wnt7 ligand provides a feedback signal from newly-born neurons to cortical progenitors to trigger a switch from neurogenesis to gliogenesis (W. Wang et al., 2016). Additional examples are reviewed elsewhere (Bandler, Mayer, & Fishell, 2017; Bielen, Pal, Tole, & Houart, 2017; Llorens-Bobadilla & Martin-Villalba, 2017; Rossi, Fernandes, & Desplan, 2016). Thus, many aspects of vertebrate neural temporal patterning are regulated by extrinsic signals.

In *Drosophila*, most neuroblasts in the ventral nerve cord (VNC) and brain produce a type I lineage (see glossary) and undergo several important temporal transitions: they switch from proliferation to quiescence at the embryo/larval transition, resume proliferation in early larvae, and terminate their lineage soon after pupariation (Figure 2). They also make a stereotyped sequence of neural subtypes during each phase of proliferation (reviewed in Doe, 2017). Temporal patterning has been best characterized in the embryonic VNC neuroblasts. Embryonic neuroblasts sequentially express a series of five "temporal transcription factors" (TTFs) -- Hunchback, Krüppel, Pdm (the redundant Nubbin and Pdm2 proteins), Castor, and Grainy head -- that are each necessary and sufficient to specify the unique temporal identity of neurons born during each expression window (Isshiki, Pearson, Holbrook, & Doe, 2001; Novotny, Eiselt, & Urban, 2002; Tran & Doe, 2008)(Figure 2A). The TTF cascade can occur in single cultured neuroblasts and thus is regulated by

a lineage-intrinsic mechanism (Brody & Odenwald, 2000; Grosskortenhaus, Pearson, Marusich, & Doe, 2005). Interestingly, the early TTF Hunchback and the late TTF Castor have mammalian orthologs (Ikaros and CasZ1, respectively); Ikaros specifies early-born neuronal identity in the cortex and retina, while Casz1 specifies late born neuronal identity in the retina (Elliott, Jolicoeur, Ramamurthy, & Cayouette, 2008; Mattar, Ericson, Blackshaw, & Cayouette, 2015). Recent work has uncovered similar TTF cascades in optic lobe neuroblasts and the Intermediate Neural Progenitors (INPs) within larval type II neuroblast lineages; all of these TTF cascades are characterized by feed-forward transcriptional activation and feedback repression (Bayraktar & Doe, 2013; Bertet et al., 2014; Li et al., 2013a), conceptually similar to extrinsic feedback repression that triggers early-late cortical neuron switching and neuron-glial switching (Toma et al., 2014; W. Wang et al., 2016). Thus, the initial characterization of *Drosophila* temporal patterning revealed primarily lineage-intrinsic mechanisms. Below we review recent work showing that extrinsic cues are used to generate temporal patterning throughout the prolonged stages of post-embryonic neurogenesis.

## Glial-derived cues regulate the timing of neuroblast quiescence

All *Drosophila* neuroblasts undergo quiescence in the late embryo/early larva, with the exception of five central brain neuroblasts (four mushroom body neuroblasts and one ventrolateral neuroblast) (Britton & Edgar, 1998). Entry and exit from quiescence occurs in a stereotyped sequence: embryonic neuroblast proliferation, neuroblast size reduction, neuroblast quiescence, neuroblast enlargement and proliferation in the young larva, and finally neuroblast size reduction and terminal differentiation in the early pupa (Chell & Brand, 2010; Homem et al., 2014; Sousa-Nunes, Yee, & Gould, 2011). Here we discuss new findings showing that these temporal transitions are regulated, in part, by extrinsic signals that reflect organismal nutritional status (Figure 2).

Neuroblast entry into quiescence involves cell size reduction and an internal timer (completion of the TTF cascade) followed by nuclear import of the Prospero transcription factor which represses cell cycle gene expression and initiates quiescence (Lai & Doe, 2014; Tsuji, Hasegawa, & Isshiki, 2008). In contrast, neuroblast enlargement and exit from quiescence requires multiple extrinsic signals, at least one activated by larval feeding. As the newly-hatched larvae begins feeding on protein-rich food, amino acids are detected by the liver-like fat body via the amino acid transporter Slimfast (Slif), which in turn leads to a currently unknown fat-body derived signal to the subperineurial glia that contact each neuroblast (Chell & Brand, 2010; Koyama & Mirth, 2016; Sousa-

Nunes et al., 2011). Consequently, glia secrete insulin/IGF like peptides (ILPs) that activate the neuroblast insulin receptor (InR), driving them out of quiescence (Chell & Brand, 2010; Sousa-Nunes et al., 2011). More recently it has been shown that the subperineurial glial require calcium waves and the gap junction proteins Innexin 1 and 2 to trigger neuroblast reactivation (Otsuki & Brand, 2017; Speder & Brand, 2014), although the mechanism remains undefined.

In addition, nutritional cues and glia promote neuroblast enlargement and re-entry into the cell cycle by suppressing the Hippo pathway, a conserved pathway for inhibiting cell growth (Richardson & Portela, 2017). Both glia and neuroblasts express the cell surface proteins Crumbs and Echinoid, which are required to activate the Hippo pathway thereby keeping the Yorkie effector in the neuroblast cytoplasm and preventing neuroblast enlargement. Loss of Crumbs, Echinoid, or Hippo results in premature translocation of Yorkie into the neuroblast nucleus where it stimulates neuroblast growth and proliferation (Ding, Weynans, Bossing, Barros, & Berger, 2016; Poon, Mitchell, Kondo, Cheng, & Harvey, 2016). Finally, glia also secrete the Anachronism (Ana) protein, which is required to maintain neuroblast quiescence by an unknown mechanism (Ebens, Garren, Cheyette, & Zipursky, 1993). Thus, multiple extrinsic cues converge on neuroblasts to regulate the precise timing of enlargement and exit from quiescence; it will be interesting to see if these pathways also regulate exit from quiescence of mammalian neural stem cells. In the future, it will be important to identify the fat body-derived signal, and understand how glial calcium dynamics, gap junctions, and IGF, Hippo, Ana signaling pathways are all integrated to regulate neuroblast quiescence.

Mushroom body neuroblasts generate three major classes of neurons: early-born γ neurons, middle-born α'/β' neurons, and late-born α/β neurons (Lin et al., 2013). Larvae fed a sucrose diet (no amino acids) show severe growth deficits, and as described above, most neuroblasts fail to exit quiescence. Yet the four mushroom body neuroblasts will continue dividing under these conditions, perhaps because they never entered quiescence in the embryo. Interestingly, under these conditions, the mushroom body neuroblasts continue making first-born γ neurons, make fewer later-born α'/β' neurons, and fail to make the last-born α/β neurons (Lin et al., 2013). Thus, nutritional cues are required for temporal patterning in larval mushroom body neuroblast lineages. It remains unknown how amino acid uptake is communicated to the mushroom body neuroblasts to trigger the early-late switch in neuronal identity.

## Hormonal cues regulate larval neuroblast temporal identity

Embryonic neuroblasts use an intrinsic TTF cascade to generate neuronal diversity -- this mechanism is ideally suited for rapid, invariant, short cell lineages of just 3-10 progenitor divisions (Doe, 2017). In contrast, larval neuroblasts can divide >50 times over 120h to generate hundreds of neurons and glia (Truman & Bate, 1988) -- this likely requires a completely different temporal patterning mechanism, particularly to coordinate the timing of neuron production between different lineages, which might be important for neural circuit assembly. Indeed, work over the past decade has identified several genes with broad expression domains in early-born or late-born neurons (Liu et al., 2015; Maurange, Cheng, & Gould, 2008; Narbonne-Reveau et al., 2016), but few candidate TTFs expressed for just one or two cell divisions (Kao, Yu, He, Kao, & Lee, 2012), as in the embryonic TTF cascade. For example, the Chinmo transcription factor, Lin-28 transcription factor, and Imp RNA-binding protein are expressed in all early-born neurons (0-60h after larval hatching, ALH), whereas the Broad transcription factor and Syncrip RNA-binding protein are expressed in all late-born neurons (60-120h ALH) (Liu et al., 2015; Maurange et al., 2008; Narbonne-Reveau et al., 2016). Two temporal windows are not sufficient to generate the known diversity of neurons made by each larval neuroblast (K. Ito & Awasaki, 2008; H. H. Yu, Chen, Shi, Huang, & Lee, 2009; H. H. Yu et al., 2010). To identify additional, novel candidate temporal factors expressed by larval neuroblasts, unbiased transcriptomic screens were performed (Ren et al., 2017; Syed, Mark, & Doe, 2017). Our screen identified the above-mentioned factors, plus additional factors including the ecdysone receptor, raising the possibility that the steroid hormone ecdysone may be used to generate temporal identity within larval neuroblasts (Figure 3).

The steroid hormone ecdysone governs many developmental transitions in the *Drosophila* life cycle: three small pulses of ecdysone direct each of the larval molts (L1, L2, L3) and a large pulse during the pupal stage is required for metamorphosis (reviewed in Yamanaka, Rewitz, & O'Connor, 2013). Ecdysone is produced by the prothoracic gland (outside the CNS) and acts systemically throughout the animal, via binding cell type specific Ecdysone receptor (EcR) isoforms. We found that the EcR-B1 isoform was temporally expressed in most or all larval central brain neuroblasts from ~60h ALH onwards (Syed et al., 2017). Interestingly, most other temporal factors were expressed fully before or after this mid-larval timepoint: young neuroblasts expressed Castor, Seven-up , Chinmo, Imp, and Lin-28 whereas old neuroblasts expressed EcRB1, Broad, E93 and Syncrip; this raises the hypothesis that ecdysone signaling could induce a major temporal gene expression transition in larval neuroblasts. To test this hypothesis, we took three different approaches. First, we found that *ecd*$^{1}$ mutant larvae, lacking the ability to synthesize ecdysone, had neuroblasts with defects

in the early-late gene expression switch: they maintained early factors Chinmo and Imp and showed a delay or absence of late factors Broad, Syp, and E93. Second, we cultured larval brains from 48-72h ALH with or without exogenously added ecdysone: brains cultured without ecdysone failed to make the early-late temporal factor switch, but adding ecdysone allowed normal switching to occur in these cultures. Importantly, EcR-B1 was expressed normally at 60h ALH, ruling out a general developmental delay. Third, we expressed an EcR dominant negative protein specifically in larval neuroblasts, which delayed the early-late gene expression switch. This experiment also shows that failure to make the neuroblast gene expression switch is not due to an indirect effect on organismal growth or development, but rather a neuroblast-autonomous effect of ecdysone signaling (Syed et al., 2017). As expected, loss of ecdysone signaling had no effect on the timing of EcR expression. Rather, EcR expression was fully dependent on the prior expression of the early temporal factor, Seven-up, an orphan nuclear hormone receptor (Syed et al., 2017). Loss of Seven-up not only completely prevented EcR expression, but all late temporal factor expression, with continued expression of early genes such as Imp, Lin-28, and Chinmo (Maurange et al., 2008; Ren et al., 2017; Syed et al., 2017). It is likely that the difference in phenotypes between loss of Seven-up and manipulations of ecdysone are due to the fact that we were unable to remove all ecdysone signaling. Even in the case of the dominant-negative EcR, if enough ecdysone was present, it is possible that the early to late switch could eventually occur. Because Seven-up is required for EcR expression, the only manipulation that definitively removes all ecdysone signaling from neuroblasts is loss of Seven-up. It is also possible, however, that redundant pathways exist that induce the early to late gene switch, and these pathways are both Seven-up dependent and ecdysone independent. Cell type specific removal of EcR would be a good way to distinguish between these possibilities.

Ecdysone is required for a distinct late temporal step: the termination of larval neuroblast lineages in early pupal stages. Ecdysone acts together with the Mediator complex and Syncrip to promote neuroblast size reduction, nuclear Prospero localization, and terminal differentiation (Homem et al., 2014; L. Yang et al., 2017). This late event also requires Hedgehog signaling (Chai, Liu, Chia, & Cai, 2013), and down-regulation of Imp (C.-P. Yang et al., 2017). The detailed mechanism of ecdysone, Mediator, and Hedgehog signaling remains to be determined.

## Hormonal cues regulate neuronal temporal identity

*Drosophila* mushroom body neuroblasts display the longest phase of neurogenesis, beginning their lineage during embryogenesis and continuing until late pupal stages. They sequentially produce three

types of neurons; γ, α'/β', and α/β neurons, each with a unique projection pattern (K. Ito, Awano, Suzuki, Hiromi, & Yamamoto, 1997; T. Lee, Lee, & Luo, 1999). Early studies showed that the transcription factor Chinmo is detected in a high to low gradient in early-born to late-born neurons, and is required for specification of early-born γ and α'/β' neuron identity (Zhu et al., 2006). Thus, establishing the gradient of Chinmo is essential to generate neuronal diversity in mushroom body neurons -- how is the Chinmo gradient established? Recent studies from the Lee lab have shown that mushroom body neuroblasts generate opposing temporal gradients of Imp and Syncrip RNA-binding proteins -- Imp highest early and Syncrip highest late, and Syncrip is required to repress Chinmo expression at the post-transcriptional level in late-born neurons (Liu et al., 2015; Ren et al., 2017). In addition, the microRNA let-7 is also expressed in a temporal gradient, with the highest levels in late-born neurons, where it represses Chinmo expression (Y. C. Wu, Chen, Mercer, & Sokol, 2012); thus both let-7 and Syncrip are required to keep Chinmo levels low in late-born neurons. Pushing back the question, what creates the late temporally restricted let-7 expression? Recent work has shown that it is the steroid hormone ecdysone: reduced ecdysone levels eliminate let-7 expression in late-born mushroom body neurons, and the α'/β' to α/β fate transition is abrogated (Chawla & Sokol, 2012; Kucherenko, Barth, Fiala, & Shcherbata, 2012; Y. C. Wu et al., 2012). Ecdysone regulates α/β identity cell autonomously, as blocking of ecdysone signaling by expressing an EcR dominant negative transgene or an EcR RNAi transgene in these neurons generated a similar failure in α'/β' to α/β fate transition (Kucherenko et al., 2012). Thus, ecdysone can act to regulate neuroblast temporal patterning (see above) as well as directly regulating post-mitotic neuronal temporal identity.

## From neurogenesis to circuits

While a great deal is known about how developmental patterning mechanisms can generate the diversity of neurons required to populate the brain, much less is known about how these mechanisms play a role in the formation of functional circuits. In mammals, excitatory sister neurons from the same progenitor have been shown to make preferential connections to one another over other neighboring cells, and even have similar tuning properties (Yoon, Ming, & Song, 2018) (X. J. Zhang et al., 2017). While the relationship between lineage and connectivity or function has been established for excitatory neurons in both cortex and hippocampus, the relationship between lineage and targeting and connectivity of GABAergic interneurons remains unclear (Turrero García, Mazzola, & Harwell, 2016) {Sultan, 2016 #273}. In *Drosophila,* both spatial factors that contribute to lineage identity and temporal identity factors have been shown to contribute to the targeting and function of neurons.

**Figure 1. Temporal Patterning by Extrinsic Cues in Mammalian Neural Progenitors.** Grey box represents the progenitor population at the ventricular zone. Time flows from left to right. Young progenitors, white circles; old progenitors, black circles. DL, deep layer earlyborn neurons (white ovals); UL, upper layer late-born neurons (black ovals). Dashed red arrows or T-bars represent the extrinsic cues that regulate temporal patterning. (A) Wild-type cortical development. (B) Transplantation of young cortical progenitors into an older VZ shows that environmental cues can transform progenitor temporal identity to an older state. (C) Ablation of early-born neurons reduces the number of deep-layer early-born neurons and delays production of late-born upper layer neurons. (D) Cortical Wnt7 induces a switch from DL to UL neurogenesis, as well as a switch from neurogenesis to gliogenesis. (E) Transforming growth factor-b signaling terminates production of earlyborn fates and induces production of late born fates in three brain regions. Abbreviations: 5HTN, serotonergic neuron; MN, motor neuron; OLP, oligodendrocyte precursor cell; OMN, oculomotor neuron; RNN, red nucleus neurons; SMN, somatic motor neuron.

**Figure 2. Temporal Patterning by Nutrition Cues in *Drosophila*.** (A) Summary of neuroblast temporal patterning events from embryogenesis through the end of the neuroblast lineage in the early pupal stage. In the embryo, a neuroblast-intrinsic TTF cascade generates temporal patterning. In the early larvae, extrinsic nutritional cues generate the properly timed exit from quiescence. In the late larvae, extrinsic hormonal cues generate a switch from early candidate TTFs to late candidate TTFs). (B) The nutritional extrinsic signaling pathway that triggers neuroblast exit from quiescence. (C) Comparison of MB NB temporal pattering in the presence of dietary amino acids (top) or in the absence of dietary amino acids (bottom). Note the failure to undergo proper temporal patterning in the absence of extrinsic nutritional cues. Abbreviations: Crb, ; DILP6, *Drosophila* insulin-like peptide 6; Ed, Echinoid; FDS, Fat body Derived Signal; InR, insulin receptor; MB NB, mushroom body neuroblast; SLIF, Slimfast; SPG, Sub-perineurial glia; TOR, Target of Rapamycin; TTF, temporal transcription factor; Yki, Yorkie.

**Figure 3. Temporal Patterning of Larval Neuroblasts by Hormonal Cues in *Drosophila*. Larval stages from 0 to 120 h ALH shown from left to right.** (A) The non-neuronal ring gland releases the hormone ecdysone at all stages of larval life, but neuroblasts only respond to ecdysone after they express EcR-B1 at ~60 h ALH. (B) Simplified diagram of candidate TTFs expressed by larval central brain neuroblasts. Grey and red, TTFs not requiring ecdysone for their expression. Black, TTFs requiring ecdysone for their expression. (C) Type II neuroblasts at the beginning of their larval lineages make INPs that produce both neurons and glia and express Chinmo and Imp; type II neuroblasts later in their lineage produce INPs that generate neurons only and express Broad and

Syncrip – this transition illustrates how the type II neuroblasts change over time to generate neural diversity. INPs undergo temporal patterning over time (color coded). Abbreviations: ALH, after larval hatching; EcR-B1, ecdysone receptor B1; GMC, ganglion mother cell; INP, intermediate neural progenitor; TTF, temporal transcription factor.

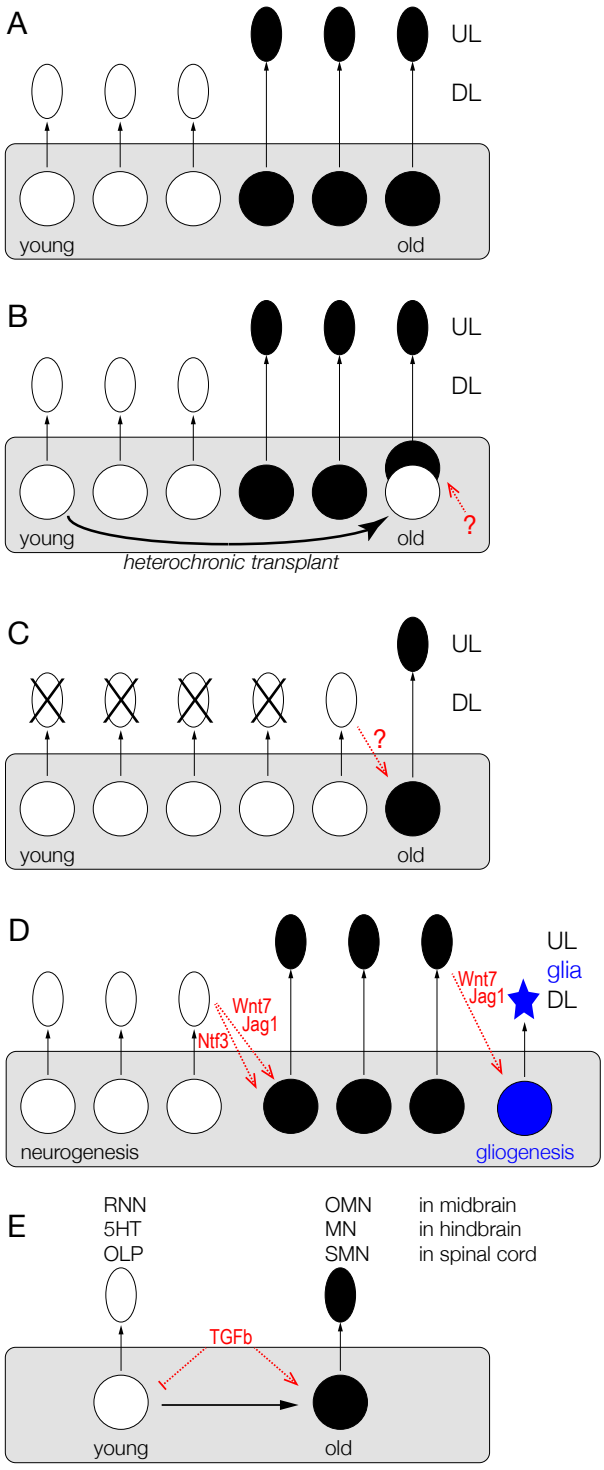
A
UL
DL
young
old
B
UL
DL
young
old
?
heterochronic transplant
C
UL
DL
?
young
old
D
UL
glia
DL
Wnt7
Jag1
Ntf3
Wnt7
Jag1
neurogenesis
gliogenesis
E
RNN
5HT
OLP
OMN
MN
SMN
in midbrain
in hindbrain
in spinal cord
TGFb
young
old

***Figure 1***

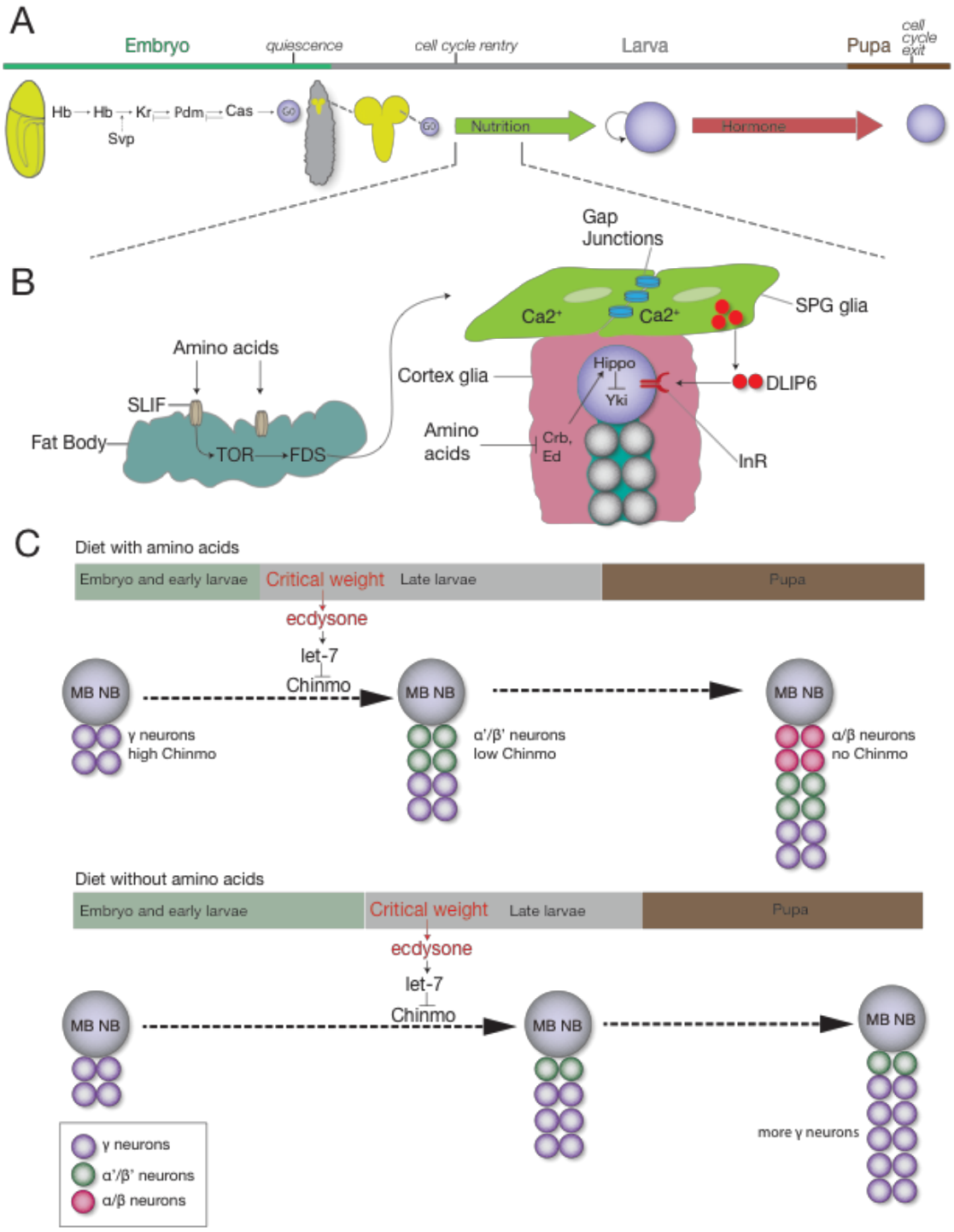
A
Embryo
quiescence
cell cycle rentry
Larva
Pupa
cell cycle exit
Hb
Hb
Kr
Pdm
Cas
Svp
Nutrition
Hormone
B
Gap Junctions
Ca2+
Ca2+
SPG glia
Amino acids
SLIF
Fat Body
TOR
FDS
Cortex glia
Hippo
Yki
DLIP6
Amino acids
Crb, Ed
InR
C
Diet with amino acids
Embryo and early larvae
Critical weight
Late larvae
Pupa
ecdysone
let-7
Chinmo
MB NB
γ neurons
high Chinmo
α'/β' neurons
low Chinmo
α/β neurons
no Chinmo
Diet without amino acids
Embryo and early larvae
Critical weight
Late larvae
Pupa
ecdysone
let-7
Chinmo
more γ neurons
γ neurons
α'/β' neurons
α/β neurons

***Figure 2***

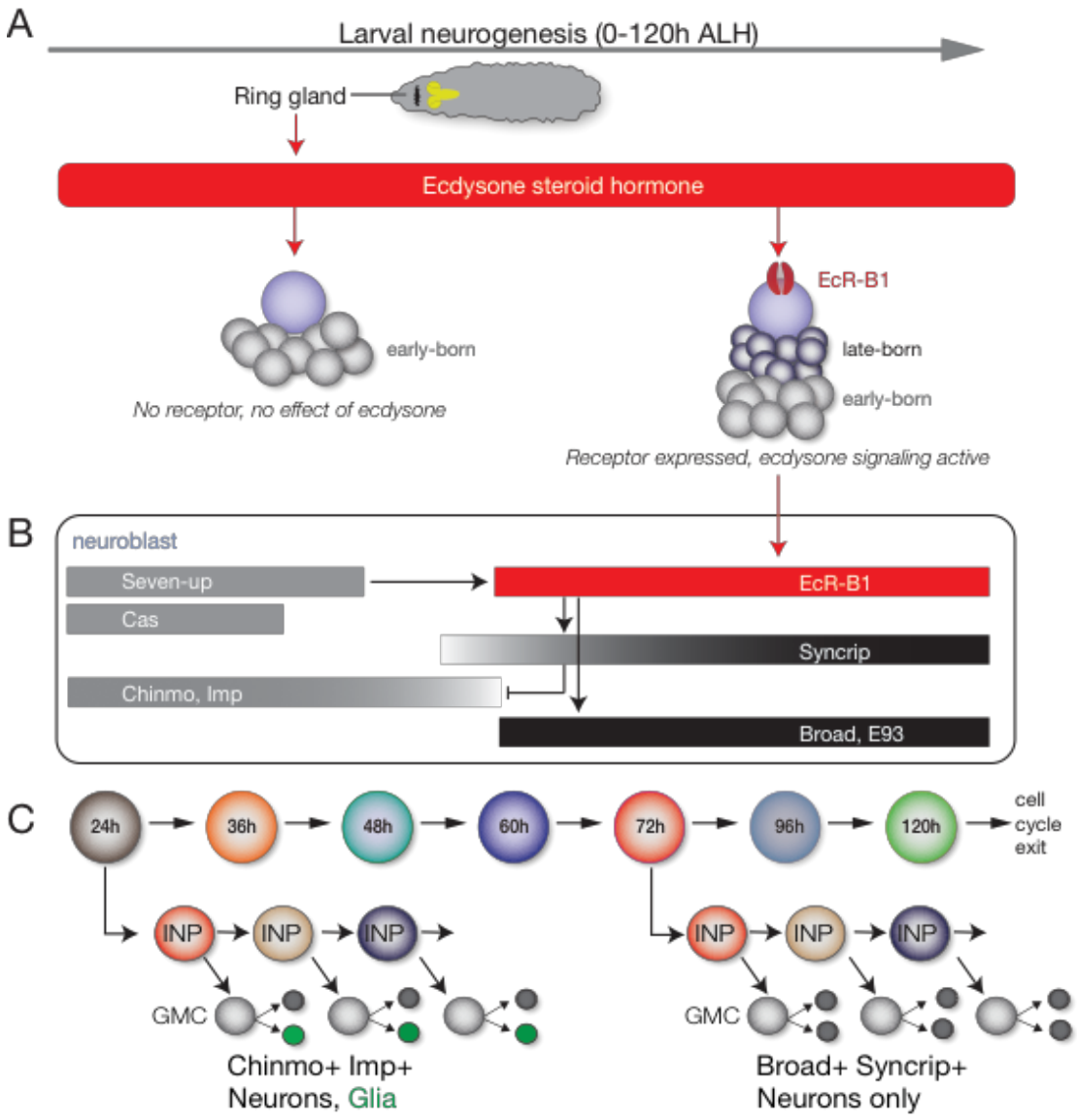
A
Larval neurogenesis (0-120h ALH)
Ring gland
Ecdysone steroid hormone
EcR-B1
early-born
late-born
early-born
No receptor, no effect of ecdysone
Receptor expressed, ecdysone signaling active
B
neuroblast
Seven-up
Cas
Chinmo, Imp
EcR-B1
Syncrip
Broad, E93
C
24h
36h
48h
60h
72h
96h
120h
cell cycle exit
INP
INP
INP
GMC
Chinmo+ Imp+ Neurons, Glia
INP
INP
INP
GMC
Broad+ Syncrip+ Neurons only

***Figure 3***

# CHAPTER II

# STEROID HORMONE INDUCTION OF TEMPORAL GENE EXPRESSION IN *DROSOPHILA* BRAIN NEUROBLASTS GENERATES NEURONAL AND GLIAL DIVERSITY

Mubarak Hussain Syed, Brandon Mark, and Chris Q. Doe

Institute of Neuroscience, Institute of Molecular Biology, Howard Hughes Medical Institute, University of Oregon, Eugene, OR 97403

Author Contributions : M.H Syed contributed to Conceptualization, Formal analysis, Investigation, Visualization, Methodology, Writing—original draft, Writing—review and editing. B. Mark contributed to Formal analysis, Investigation, Visualization, Methodology, Writing—original draft, Writing—review and editing. C.Q. Doe contributed to Conceptualization, Formal analysis, Investigation, Methodology, Writing—original draft.

## Introduction

From *Drosophila* to humans, the brain contains a vast array of morphologically and functionally distinct neurons and glia that arise from a much smaller pool of neural progenitors. How neural stem cells generate neural diversity is a fundamental question that is relevant to many areas of biology. For example, understanding normal neurodevelopmental programs may help design reprogramming protocols to replace specific neurons in clinical trials; may help elucidate principles of connectivity based on shared developmental features; and may help reveal how proliferative neural progenitors avoid tumor formation without differentiating. *Drosophila* has been a pioneering model system for the study of neural progenitor specification by spatial cues (Skeath & Thor, 2003), neural progenitor self-

renewal versus differentiation (Doe, 2008), stem cell derived tumor formation (Caussinus & Hirth, 2007; Homem, Repic, & Knoblich, 2015; Jiang & Reichert, 2014; Maurange & Gould, 2005), and more recently the identification of temporal factors that are sequentially expressed during neural progenitor lineages to increase neural diversity (reviewed in Kohwi & Doe, 2013; Maurange & Gould, 2005; Rossi et al., 2016). In most of the examples cited above, *Drosophila* studies have revealed conserved mechanisms and/or molecules used in mammals. Here we use *Drosophila* larval neural progenitors (neuroblasts) to investigate temporal patterning mechanisms that generate neuronal diversity.

There are three types of neuroblasts based on division mode: type 0 neuroblasts make a single neuron with each division; type I neuroblasts make a ganglion mother cell (GMC) with each division, and the GMC typically makes two neurons; and type II neuroblasts make an intermediate neural progenitor (INP) with each division, and each INP undergoes a short lineage to produce ~6 GMCs and thus ~12 neurons (Bello, Izergina, Caussinus, & Reichert, 2008; Boone & Doe, 2008; Bowman et al., 2008; Gunnar, Bivik, Starkenberg, & Thor, 2016; Y. C. Wang et al., 2014). Embryonic type I neuroblasts have short lineages averaging five neuroblast divisions, and they sequentially express five temporal transcription factors: Hunchback, Krüppel, Pdm (the co-expressed Nubbin and Pdm2 proteins), Castor (Cas), and Grainy head (reviewed in Kohwi & Doe, 2013; Maurange & Gould, 2005; Rossi et al., 2016). In addition, the orphan nuclear hormone receptor Seven-up (Svp) acts as a 'switching factor' required for a timely Hunchback-Krüppel transition (Kanai, Okabe, & Hiromi, 2005; Mettler, Vogler, & Urban, 2006). Most of these temporal transcription factors are necessary and sufficient to specify the identity of neurons born during their neuroblast expression window, although the Cas window can be subdivided further by expression of sub-temporal factors (Stratmann, Gabilondo, Benito-Sipos, & Thor, 2016). Similarly, larval optic lobe neuroblasts sequentially express six temporal transcription factors that are necessary to generate neuronal diversity in the adult visual system (Bertet et al., 2014; Li et al., 2013b; Suzuki, Kaido, Takayama, & Sato, 2013). Lastly, INPs sequentially express three temporal transcription factors, two of which are known to specify neural identity (Bayraktar & Doe, 2013). Thus, neuroblasts and INPs with short lineages have well-characterized temporal transcription factor cascades that change approximately every cell division, and act to increase neuronal diversity.

In contrast, the central brain type I or II neuroblasts undergo longer lineages of ~50 divisions to generate hundreds of neural progeny (M. Ito, Masuda, Shinomiya, Endo, & Ito, 2013; H. H. Yu et al., 2013). Clonal analysis reveals different levels of morphological diversity among neurons within a single neuroblast lineage (M. Ito et al., 2013; H. H. Yu et al., 2013) with some neuroblasts making

only four cell types (mushroom body neuroblasts) and other neuroblasts making over 40 different cell types (AD or ALad1 neuroblast) (Kao et al., 2012). Recent work has provided evidence that central brain neuroblasts change their gene expression profile over time. Our lab and others have shown that larvae express Cas and Svp in type I or type II neuroblasts prior to 48h (timing is relative to larval hatching at 0 hr) (Bayraktar & Doe, 2013; Chai et al., 2013; Homem et al., 2014; Maurange et al., 2008). In addition, the transcription factor Chinmo and RNA-binding proteins Imp and Lin-28 are detected in young type I neuroblasts prior to 60h (Liu et al., 2015; Narbonne-Reveau et al., 2016). Moving even later, the RNA-binding protein Syncrip and transcription factor Broad have been reported to be expressed in old type I neuroblasts or neurons, respectively from ~60-120h (Liu et al., 2015; Maurange et al., 2008; Zhou, Williams, Altman, Riddiford, & Truman, 2009). Lastly, the steroid hormone ecdysone and the secreted protein Hedgehog are required to terminate neuroblast proliferation after pupariation (Chai et al., 2013; Homem et al., 2014). Regulation of these temporal gene expression transitions has remained mostly mysterious, but the early factor Svp is required to induce down-regulation of the early Chinmo/Imp/Lin-28 factors at mid-larval stages (Narbonne-Reveau et al., 2016).

Despite the recent progress, many important questions remain. First, do larval neuroblasts express additional factors that may be used to generate neuronal diversity? Identifying additional candidate temporal transcription factors would be a major step forward in understanding how neuronal diversity in the adult brain is generated. Second, the role of Svp in regulating larval neuroblast gene expression transitions is poorly understood. Does Svp down-regulate early factors only, or does it activate late factor expression as well, and what are its effector genes? Determining how Chinmo/Imp/Lin-28 are down-regulated is likely to provide insight into how neuronal diversity is generated.

Here we answer each of these questions. We identify candidate temporal transcription factors expressed in neuroblasts that increase the number of molecularly distinct neuroblast temporal profiles; we show that the steroid hormone ecdysone, made outside the CNS, is required for the down-regulation of Chinmo/Imp and activation of Syncrip/Broad/E93 in mid-larval neuroblasts; we show that Svp activates expression of the Ecdysone receptor isoform B1 at mid-larval stages, rendering the neuroblasts competent to respond to the hormone ecdysone; and we show that EcR is required for proper neuronal and glial cell fate specification. Our results are the first example of hormonal regulation of temporal gene expression in neural progenitors, and the first to show that the conserved switching factor Svp can induce neural progenitor competence to respond to an extrinsic hormonal cue.

## Results

### Larval brain neuroblasts undergo an early Chinmo/Imp/Lin-28 to late Broad/Syncrip/E93 transition in gene expression

To determine if larval neuroblasts change their gene expression profile over time, we focused initially on the eight individually identifiable type II neuroblasts (subsequently analyzing all central brain neuroblasts, see below). We took two approaches: we assayed genes known to be expressed in early larval or late larval stages for temporal expression in neuroblasts, and we performed an unbiased transcriptional profiling using the TU-tagging method (Miller, Robinson, Cleary, & Doe, 2009). The TU-tagging method confirmed our findings on the known genes, and identified additional temporally-regulated genes not previously known to be expressed in neuroblasts (Figure 1 – figure supplement 1). Here we focus on expression of Cas, Svp, Chinmo, Imp, Lin-28, and Syncrip, which are all known to be temporally expressed in larval neuroblasts (Bayraktar & Doe, 2013; Liu et al., 2015; Maurange et al., 2008). In addition we show that the Ecdysone receptor (EcR), Broad and E93 (Flybase: Eip93F) are also temporally expressed in late larval type II neuroblasts.

The Cas and Svp temporal factors are restricted to the earliest stages of larval type II neuroblast lineages (Figure 1A-E). Interestingly, we detected Svp in variable subsets of type II neuroblasts in each brain lobe, consistent with transient, asynchronous expression in all type II neuroblasts. We confirmed that Svp was transiently expressed in all type II neuroblasts by visualizing the more stable *svp-lacZ* reporter in nearly all type II neuroblasts (Figure 1E). Three other early factors (Chinmo, Imp, and Lin-28) are expressed in all type II neuroblasts from larval hatching to ~48h , becoming undetectable by 72h (Figure 1F-K). Conversely, the Broad/Syncrip/E93 factors are detected in older type II neuroblasts (Figure 1L-Q). There are four known isoforms of Broad (Zhou et al., 2009), and we found that Broad-Z1 but not Broad-Z3 was expressed in type II neuroblasts (Figure 1 – figure supplement 2). Each late factor showed slightly different kinetics of expression: Syncrip was detectable earliest, in all type II neuroblasts by 60h, co-expressed with Imp at this stage. Broad was detected in most type II neuroblasts at 60h and staying at high levels before declining at 120h, and E93 showed gradually increasing expression beginning at 72h and remaining at high levels at 120h. Thus, these temporal factors can generate seven different molecular profiles during type II neuroblast lineages (summarized in Figure 1R); whether all of these molecular differences are functionally important remains to be determined (see Discussion). We conclude that type II

neuroblasts change molecular profile over the course of their 120h long larval cell lineage, with a striking early-to-late transition from Chinmo/Imp/Lin-28 to Broad/Syncrip/E93 at ~60h, midway through their lineage.

## The steroid hormone ecdysone is required for the early-to-late gene expression transition in larval brain neuroblasts

Here we test whether the steroid hormone ecdysone, known to regulate many larval gene expression transitions in multiple tissues (Faunes & Larrain, 2016), plays a role in the Chinmo/Imp to Broad/Syncrip/E93 neuroblast gene expression transition. We used three different experiments to test the role of ecdysone: global reduction in ecdysone levels using the *ecdysoneless*$^{1}$ (subsequently *ecd*$^{ts}$) temperature-sensitive mutation (Figure 2); in vitro brain explant culture with or without exogenous ecdysone (Figure 3); and type II neuroblast-specific expression of a dominant-negative Ecdysone receptor (Figure 4). To reduce global levels of ecdysone we raised *ecd*$^{ts}$ homozygous larvae at the 29$^{o}$C restrictive temperature (all larval ages adjusted to match normal 25$^{o}$C staging, see methods) and for controls we either assayed the same *ecd*$^{ts}$ homozygous larvae at the permissive temperature of 18$^{o}$C or age-matched wild type larvae (controls). As expected, control larvae at 72h or 96h had type II neuroblasts that expressed the late factors Syncrip, Broad and E93, but not the early factors Chinmo and Imp (Figure 2A-E; quantified in K). In contrast, *ecd*$^{ts}$ homozygous larvae at 29$^{o}$C had type II neuroblasts that persistently expressed the early factors Chinmo/Imp and lacked the late factors Syncrip/Broad/E93 (Figure 2F-J; quantified in K). We conclude that systemic reduction of ecdysone levels blocks the Chinmo/Imp to Broad/Syncrip/E93 gene expression transition in type II neuroblasts.

Loss of ecdysone signaling could block cell cycle progression of type II neuroblasts, which could prevent the early-to-late gene expression transition. To test this hypothesis, we isolated larval brains and cultured them in vitro from 48-72h (across the early-to-late transition) with or without the bioactive form of ecdysone (20-hydroxy-ecdysone; 20HE). We used live imaging to measure cell cycle times, as well as assayed for expression of representative early or late factors. Larval brains cultured with added ecdysone are similar to wild type in down-regulating the early factor Chinmo and expressing the late factor Broad by the end of the culture period at 72h (Figure 3A-B; quantified in H; Video 1). In contrast, larval brains cultured without ecdysone showed persistent Chinmo expression and failed to express Broad (Figure 3C-D; quantified in H; Video 2). Importantly, the cell cycle times of type II neuroblasts are indistinguishable with or without ecdysone (Figure 3E-F,

quantified in G; Videos 1,2), and similar to published type II neuroblast cell cycle times (Homem, Reichardt, Berger, Lendl, & Knoblich, 2013). Taking these results together with our in vivo ecdysone experiments, we conclude that the steroid hormone ecdysone induces the early-to-late Chinmo/Imp to Broad/Syncrip/E93 gene expression transition in type II neuroblasts.

## The Ecdysone receptor EcR-B1 is expressed concurrent with, and required for, the early-to-late gene expression transition in larval brain neuroblasts

The ability of ecdysone signaling to trigger a major gene expression transition at ~60h could be due to a peak of ecdysone signaling at that time, or the lack of a signaling pathway component prior to that time. Ecdysone is present at all larval stages (Kozlova & Thummel, 2000), suggesting the latter mechanism. Ecdysone signaling is quite direct, requiring the Ecdysone receptor (EcR-A, -B1, or -B2 isoforms) and the ubiquitous co-receptor Ultraspiracle (T. Lee, Marticke, Sung, Robinow, & Luo, 2000). We found that EcR-B1 was strongly detected in the nuclei of type II neuroblasts from 56h to at least 120h; prior to 56h neuroblasts did not express any EcR isoform (Figure 4B; Figure 4-figure supplement 1). To determine if EcR-B1 expression was induced by ecdysone signaling (e.g. via a different EcR receptor isoform) we assayed *ecd*$^{ts}$ mutants at non-permissive temperature and assayed for EcR-B1 expression; we also assayed for EcR-B1 expression in brain explants cultured with or without exogenous ecdysone. In both experiments, we found that expression of EcR-B1 was not dependent on ecdysone signaling (Figure 4C-F). Note that normal EcR expression during the culture window provides evidence that there is no general developmental delay in brains lacking ecdysone signaling, despite failure to undergo the Chinmo/Imp to Broad/Syncrip/E93 transition. We conclude that an ecdysone-independent pathway activates EcR-B1 expression at 56h, the time of the Chinmo/Imp to Broad/Syncrip/E93 gene expression transition (summarized in Figure 4M).

To determine if EcR was required for the Chinmo/Imp to Broad/Syncrip/E93 gene expression transition, we used *wor-gal4 ase-gal80* to drive expression of a dominant-negative Ecdysone receptor (*EcR-B1*$^{W650A}$; subsequently *EcR*$^{DN}$) specifically in type II neuroblasts, and assayed representative early and late factors. We found that neuroblasts expressing *EcR*$^{DN}$ showed completely penetrant persistent expression of the early factors Chinmo and Imp, and reduced or no expression of the late factors Syncrip (reduced) and E93 (absent) (Figure 4G-I,K; quantified 4L). Surprisingly, the late factor Broad was normally expressed (Figure 4H; quantified in 4L; see Discussion), again suggesting no general developmental delay. We conclude that ecdysone signaling acts via EcR-B1 within type II neuroblasts to promote the Chinmo/Imp/Lin-28 to Broad/Syncrip/E93 gene expression transition.

## The Seven-up nuclear hormone receptor activates EcR in larval brain neuroblasts

Previous work has shown that *svp* mutant clones fail to down-regulate Chinmo/Imp in late-born neurons (Narbonne-Reveau et al., 2016). Svp could promote EcR expression, or act in parallel to EcR to down-regulate Chinmo/Imp. To distinguish between these alternatives, we examined *svp* mutant clones for EcR expression. We induced *svp* mutant clones at 0-4h and assayed them at 96h. As expected, we observed a highly penetrant failure to down-regulate expression of the early factors Chinmo/Imp (Figure 5A-B; quantified in G). More importantly, we found a complete loss of EcR-B1 and the late factors Broad/Syncrip/E93 (Figure 5C-F; quantified in G). We conclude that Svp is required to induce EcR expression, and that EcR expression renders neuroblasts competent to respond to ecdysone signaling.

Svp could directly activate EcR expression, or alternatively Svp could terminate Cas expression and Cas could repress EcR (double repression motif). We assayed *svp* mutant clones for Cas expression, and did not observe prolonged Cas expression (Figure 5-figure supplement 1). In addition, *cas* mutant clones showed no change in early or late temporal factor expression (data not shown; T. Lee, personal communication). We conclude that Svp uses a Cas-independent mechanism to activate EcR expression in type II neuroblasts.

## Syncrip represses Imp expression to allow down-regulation of Chinmo in larval neuroblasts

We wanted to characterize the genetic interactions occurring downstream of the Ecdysone receptor, to better understand the mechanism of the early-to-late gene expression transition. Does each affected gene respond independently to EcR, or is there a cascade of interactions occurring downstream of a single primary EcR target gene?

First, we tested whether the Imp and Syncrip proteins are downstream of EcR-B1. We observed normal EcR-B1 timing and levels in both *Imp* and *Syncrip* mutants (Figure 6A-C), confirming that they act in parallel or downstream of EcR-B1. Second, we tested whether Imp and Syncrip cross-repress each other, as has been shown for mushroom body neuroblasts (Liu et al., 2015). We found that *Syncrip* mutants had prolonged Imp expression in type II neuroblasts, but that *Imp* mutants did not show precocious Syncrip expression in the six DM1-DM6 type II neuroblasts (Figure 6D-E);

there was variable precocious expression in one of the DL1/2 type II neuroblasts at 48h (data not shown). We conclude that the regulatory interactions between Imp and Syncrip are neuroblast-specific. Third, we assayed *Imp* and *Syncrip* mutants for changes in early and late factor expression. Whereas *Imp* mutants had no change in expression of the early factor Chinmo or late factors Broad and E93 (Figure 6F-H), *Syncrip* mutants showed prolonged expression of early factor Chinmo but normal expression of the late factors Broad and E93 (Figure 6I-K), leading to a novel Chinmo+ Broad+ co-expression molecular profile (Figure 6N). Lastly, we tested for cross-repression between the early factor Chinmo and the late factor Broad, as these proteins are typically mutually exclusive in both neuroblasts and their neuronal progeny (Maurange et al., 2008; Narbonne-Reveau et al., 2016; Zhu et al., 2006)(Figure 6-figure supplement 1). We found that Broad was expressed normally in *chinmo$^{1}$* mutant clones and Chinmo was expressed normally in *broad$^{npr3}$* mutants (Figure 6L, M). Taken together, our results support a model in which EcR independently activates all known late factors, with the late factor Syncrip required to repress early factor expression.

## Late temporal transcription factors are required to specify adult neuronal identity

The functional analysis of all eight candidate temporal transcription factors is beyond the scope of this study, in part due to the absence of markers for neurons or glia produced during each specific window of gene expression. Nevertheless, two markers label progeny born either early or late in type II neuroblast lineages: the glial marker Repo stains a pool of early-born glia whereas the neuronal marker Brain-specific homeobox (Bsh) stains late-born neurons within type II neuroblast lineages (Bayraktar & Doe, 2013). To determine if the late temporal factors play a role in repressing early-born Repo+ glial identity or inducing late-born Bsh+ neuronal identity, we expressed the EcR dominant negative transgene specifically and permanently in type II neuroblast lineages (see "lineage tracing" Methods). We found that reducing EcR caused an increase in the early marker Repo (Figure 7A,B; quantified in C) and a decrease in the late marker Bsh (Figure 7D,E; quantified in F), consistent with a role for EcR or a downstream late temporal factor in suppressing early-born glial identity and promoting late-born neuronal identity.

### The ecdysone-dependent Chinmo/Imp to Broad/Syncrip/E93 gene expression transition is widely used by central brain type I neuroblasts

We have focused on a small pool of type II neuroblasts because they are individually identifiable and tools to mark and manipulate them are available. Yet the majority of central brain neuroblasts are type I neuroblasts (~95 per lobe). Here we test whether the early-to-late Chinmo/Imp to Syncrip/Broad/E93 gene expression transition occurs in this populations of neuroblasts, by assaying representative early or late factors in larvae with reduced ecdysone signaling (*ecd$^{ts}$* mutants). In *ecd$^{ts}$* mutants raised at the permissive temperature to allow ecdysone signaling, we observe normal down-regulation of the early factor Chinmo and activation of the late factors Broad and E93 at 96h in type I central brain neuroblasts (Figure 8A-C; quantified in G). In contrast, *ecd$^{ts}$* mutant larvae placed at restrictive temperature to block ecdysone signaling showed persistent expression of the early factor Chinmo and failure to activate the late factors Broad and E93 at 96h (Figure 8D-F; quantified in G). Notably, we find that Syncrip is expressed in a small number of type I neuroblasts (~10) prior to widespread EcR expression at 56h (Figure 8 - figure supplement 1). It is likely that these neuroblasts use an EcR-B1-independent mechanism for activating Syncrip expression. We conclude that most central brain neuroblasts undergo an ecdysone-dependent early-to-late Chinmo/Imp to Syncrip/Broad/E93 gene expression transition.

## Discussion

Here we show that the steroid hormone ecdysone is required to trigger a major gene expression transition at mid-larval stages: central brain neuroblasts transition from Chinmo/Imp to Broad/Syncrip/E93. Furthermore, we show that Svp activates expression of EcR-B1 in larval neuroblasts, which gives them competence to respond to ecdysone signaling, thereby triggering this gene expression transition. Although a global reduction of ecdysone levels is likely to have pleiotropic effects on larval development, we have performed multiple experiments to show that the absence or delay in late temporal factor expression following reduced ecdysone signaling is not due to general developmental delay. First, the EcR gene itself is expressed at the normal time (~56h) in the whole organism *ecdysoneless$^{1}$* mutant, arguing strongly against a general developmental delay. Second, a type II neuroblast *seven-up* mutant clone shows a complete failure to express EcR and other late factors, in the background of an entirely wild type larvae; this is perhaps the strongest evidence that the phenotypes we describe are not due to a general developmental delay. Third, lineage-specific expression of EcR dominant negative leads to loss of Syncrip and E93 expression without affecting

Broad expression; the normal Broad expression argues against a general developmental delay. Fourth, we used live imaging to directly measure cell cycle times and found that lack of ecdysone did not slow neuroblast cell cycle times. Taken together, these data support our conclusion that ecdysone signaling acts directly on larval neuroblasts to promote an early-to-late gene expression transition.

## Ecdysone is the first neuroblast-extrinsic cue known to regulate temporal gene expression

The role of ecdysone in regulating developmental transitions during larval stages has been well studied; it can induce activation or repression of suites of genes in a concentration dependent manner (reviewed in Thummel, 2001; Yamanaka et al., 2013). Ecdysone induces these changes through a heteromeric complex of EcR and the retinoid X receptor homolog Ultraspiracle (King-Jones & Thummel, 2005; Yamanaka et al., 2013). Ecdysone is required for termination of neuroblast proliferation at the larval/pupal transition (Homem et al., 2014), and is known to play a significant role in remodeling of mushroom body neurons and at neuromuscular junctions (Awasaki & Lee, 2011; Kucherenko & Shcherbata, 2013; T. Lee et al., 2000; Schubiger, Wade, Carney, Truman, & Bender, 1998; F. Yu & Schuldiner, 2014). Here we add to this list another function: to trigger a major gene expression transition in mid-larval brain neuroblasts.

Does ecdysone signaling provide an extrinsic cue that synchronizes larval neuroblast gene expression? We do not see good coordination of late gene expression, arguing against synchronization. For example, Syncrip can be detected in many neuroblasts by 60h, whereas Broad appears slightly later at ~72h, and E93 is only detected much later at ~96h, by which time Broad is low. This staggered expression of ecdysone target genes is reminiscent of early and late ecdysone-inducible genes in other tissues (Baehrecke, 1996). In addition, for any particular temporal factor there are always some neuroblasts expressing it prior to others, but not in an obvious pattern. It seems the exact time of expression can vary between neuroblasts. Whether the pattern of response due to different neuroblast identities, or a stochastic process, remains to be determined.

We have previously shown that the Hunchback-Krüppel-Pdm-Castor temporal gene transitions within embryonic neuroblasts are regulated by neuroblast-intrinsic mechanisms: they can occur normally in neuroblasts isolated in culture, and the last three factors are sequentially expressed in $G_2$-arrested neuroblasts (Grosskortenhaus et al., 2005). Similarly, optic lobe neuroblasts are likely to undergo neuroblast-intrinsic temporal transcription factor transitions, based on the observation

that these neuroblasts form over many hours of development and undergo their temporal transitions asynchronously (Bertet et al., 2014; Hasegawa et al., 2011; Li et al., 2013b; Suzuki et al., 2013). In contrast, we show here that ecdysone signaling triggers a mid-larval transition in gene expression in all central brain neuroblasts (both type I and type II). Although ecdysone is present at all larval stages, it triggers central brain gene expression changes only following Svp-dependent expression of EcR-B1 in neuroblasts. Interestingly, precocious expression of EcR-B1 (*worniu-gal4 UAS-EcR-B1*) did not result in premature activation of the late factor Broad, despite the forced expression of high EcR-B1 levels in young neuroblasts (data not shown). Perhaps there is another required factor that is also temporally expressed at 56h. We also note that reduced ecdysone signaling in $ecd^{ts}$ mutants or following $EcR^{DN}$ expression does not permanently block the Chinmo/Imp to Broad/Syncrip/E93 transition; it occurs with variable expressivity at 120-160h animals (pupariation is significantly delayed in these $ecd^{ts}$ mutants), either due to a failure to completely eliminate ecdysone signaling or the presence of an ecdysone-independent mechanism.

We find a small but reproducible difference in the effect of reducing ecdysone levels using the biosynthetic pathway mutant $ecd^{ts}$ versus expressing a dominant negative EcR in type II neuroblasts. The former genotype shows a highly penetrant failure to activate Broad in old neuroblasts, whereas the latter genotype has normal expression of Broad (despite failure to down-regulate Chinmo/Imp or activate E93). This may be due to failure of the dominant negative protein to properly repress the *Broad* gene. Differences between $EcR^{DN}$ and other methods of reducing ecdysone signaling have been noted before (H. L. Brown, Cherbas, Cherbas, & Truman, 2006; Homem et al., 2014).

## Seven-up, but not Castor, is required to activate EcR receptor expression

*Drosophila* Svp is an orphan nuclear hormone receptor (Mlodzik, Hiromi, Weber, Goodman, & Rubin, 1990) with an evolutionarily conserved role in promoting a switch between temporal identity factors (Kohwi & Doe, 2013). In *Drosophila*, Svp it is required to switch off *hunchback* expression in embryonic neuroblasts (Benito-Sipos et al., 2011; Kanai et al., 2005; Mettler et al., 2006), and in mammals the related COUP-TF1/2 factors are required to terminate early-born cortical neuron production (Naka, Nakamura, Shimazaki, & Okano, 2008), as well as for the neurogenic to gliogenic switch (Barnabe-Heider et al., 2005; reviewed in Kohwi & Doe, 2013). Here we show that Svp is required for activating expression of EcR, which drives the mid-larval switch in gene expression from Chinmo/Imp to Syncrip/Broad/E93 in central brain neuroblasts. Our results are supported by

independent findings that svp mutant clones lack expression of Syncrip and Broad in old type II neuroblasts (T. Lee, personal communication). Interestingly, Svp is required for neuroblast cell cycle exit at pupal stages (Maurange et al., 2008), but how the early larval expression of Svp leads to pupal cell cycle exit was a mystery. Our results provide a satisfying link between these findings: we show that Svp activates expression of EcR-B1, which is required for the expression of multiple late temporal factors in larval neuroblasts. Any one of these factors could terminate neuroblast proliferation at pupal stages, thereby explaining how an early larval factor (Svp) can induce cell cycle exit five days later in pupae. It is interesting that one orphan nuclear hormone receptor (Svp) activates expression of a second nuclear hormone receptor (EcR) in neuroblasts. This motif of nuclear hormone receptors regulating each other is widely used in *Drosophila*, C. elegans, and vertebrates (Boulanger et al., 2011; Faunes & Larrain, 2016; Gissendanner, Crossgrove, Kraus, Maina, & Sluder, 2004; Lam, Hall, Bender, & Thummel, 1999; Thummel, 2001; Yamanaka et al., 2013; Zelhof, Yao, Chen, Evans, & McKeown, 1995).

The position of the Svp+ neuroblasts varied among the type II neuroblast population from brain-to-brain, suggesting that Svp may be expressed in all type II neuroblasts but in a transient, asynchronous manner. This conclusion is supported by two findings: the *svp-lacZ* transgene, which encodes a long-lived β-galactosidase protein, can be detected in nearly all type II neuroblasts; and our finding that Svp is required for EcR expression in all type II neuroblasts, consistent with transient Svp expression in all type II neuroblasts. It is unknown what activates Svp in type II neuroblasts; its asynchronous expression is more consistent with a neuroblast-intrinsic cue, perhaps linked to the time of quiescent neuroblast re-activation, than with a lineage-extrinsic cue. It would be interesting to test whether Svp expression in type II neuroblasts can occur normally in isolated neuroblasts cultured in vitro, similar to the embryonic temporal transcription factor cascade (Grosskortenhaus et al., 2005).

Castor and its vertebrate homolog Cas-Z1 specify temporal identity in *Drosophila* embryonic neuroblast lineages and vertebrate retinal progenitor lineages, respectively (Grosskortenhaus, Robinson, & Doe, 2006; Mattar et al., 2015). Although we show here that Cas is not required for the Chinmo/Imp to Syncrip/Broad/E93 transition, it has other functions. Cas expression in larval neuroblasts is required to establish a temporal Hedgehog gradient that ultimately triggers neuroblast cell cycle exit at pupal stages (Chai et al., 2013).

## How many distinct gene expression windows are present in larval neuroblasts?

*Drosophila* embryonic neuroblasts change gene expression rapidly, often producing just one progeny in each temporal transcription factor window (Baumgardt, Karlsson, Terriente, Diaz-Benjumea, & Thor, 2009; Isshiki et al., 2001; Moris-Sanz, Estacio-Gomez, Alvarez-Rivero, & Diaz-Benjumea, 2014; Novotny et al., 2002; B. J. Pearson & Doe, 2003; Tran & Doe, 2008). In contrast, larval neuroblasts divide ~50 times over their 120h lineage (Truman & Bate, 1988; H. H. Yu & Lee, 2007). Mushroom body neuroblasts make just four different neuronal classes over time (K. Ito & Awasaki, 2008; Liu et al., 2015; Zhu et al., 2006), whereas the AD (ALad1) neuroblast makes ~40 distinct projection neuron subtypes (Kao et al., 2012; Lai, Awasaki, Ito, & Lee, 2008; H. H. Yu et al., 2010). These neuroblasts probably represent the extremes (one low diversity, suitable for producing Kenyon cells; one high diversity, suitable for generating distinct olfactory projection neurons). Here we find that larval type II neuroblasts undergo at least seven molecularly distinct temporal windows (Figure 9). If we assume that the graded expression of Imp (high early) and Syncrip (high late) can specify fates in a concentration-dependent manner, many more temporal windows could exist.

## An ecdysone-independent activator of Syncrip?

All of the factors characterized here respond to ecdysone signaling in an all-or-none manner, with the exception of Syncrip. For example, loss of ecdysone signaling in the *ecd*$^{ts}$ mutant results in persistent expression of the early factors Chinmo and Imp, and loss of expression of the late factors Broad and E93, in all central brain neuroblasts. In contrast, Syncrip is only partially reduced by loss of ecdysone signaling, suggesting that there is at least one additional input that drives Syncrip expression. This is supported by our finding that ~10 central brain neuroblasts express Syncrip at 36h and 48h (Figure 8-figure supplement 1), prior to widespread EcR-B1 neuroblast expression. *Imp* RNAi has been shown to modestly increase *syncrip* levels in the MB neuroblasts (Liu et al., 2015), but does not de-repress Syncrip in 24h type II neuroblasts (T. Lee, personal communication). We find that *Imp* mutants do not show an increase in the number of Syncrip+ type II neuroblasts at 48h, although the level of Syncrip protein following *imp* RNAi is elevated at 48h (T. Lee, personal communication). Although Imp repression of Syncrip may vary in penetrance and among different types of neuroblasts, Syncrip repression of Imp seems to be robust and conserved among all neuroblast populations tested to date (Liu et al., 2015; this work).

### Future directions

Our study illuminates how the major mid-larval gene expression transition from Chinmo/Imp to Broad/Syncrip/E93 is regulated; yet many new questions have been generated. What activates Svp expression in early larval neuroblasts – intrinsic or extrinsic factors? How do type II neuroblast temporal factors act together with Dichaete, Grainy head, and Eyeless INP temporal factors (Bayraktar & Doe, 2013) to specify neuronal identity? Do neuroblast or INP temporal factors activate the expression of a tier of "morphogenesis transcription factors" (Enriquez et al., 2015) similar to leg motor neuron lineages? What are the targets of each temporal factor described here? What types of neurons (or glia) are made during each of the seven distinct temporal factor windows, and are these neurons specified by the factors present at their birth? The identification of new candidate temporal factors in central brain neuroblasts opens up the door for addressing these and other open questions.

## Materials and Methods

### Fly Strains

All stock numbers refer to the Bloomington stock center unless noted.

*ecd*$^{1}$ (#218) (Garen, Kauvar, & Lepesant, 1977); called *ecd*$^{ts}$ here.

*svp*$^{e22}$ (Mlodzik et al., 1990)

*cas*$^{24}$ (Cui & Doe, 1992)

*Br*$^{npr3}$ *FRT19A* (Kiss et al., 1976)

*chinmo*$^{1}$ *FRT40* (Zhu et al., 2006)

*chinmo*$^{1}$ *FRT40; pointed-gal4* (this study)

*Imp*$^{7}$ (Florence Besse, CNRS, France)

*Syncrip*$^{f03775}$ (Exelixis collection Harvard)

*Df(3L)R-G7* (# 2400)

*Df(3R) BSC124* (#9289)

*Df(2R) Exel6058* (#7540)

*UAS-Ecr-B1*$^{W650A}$ (#6872); called *Ec*R$^{DN}$ here.

*UAS-cas* (Ward Odenwald, NIH)

*UAS-svp* (Yash Hiromi, NIG, Japan)

*svp-lacZ* (#26669) (Mlodzik et al., 1990)

*cas-lacZ* (also called *1532-lacZ* or *ming-lacZ*) (Cui & Doe, 1992)

*EcR:GFP* [MI05320] (#59823)

*hs-flp UAS-mcd8: GFP*; *FRT40, tubulin-gal80*

*hs-flp UAS-mcd8: GFP; ; FRT82B,tubulin-gal80* (Bassem Hassan, ICM, France)

*UAS-FLP actin-FRT-stop-FRT-gal4*; *wor-gal4 ase-gal80 ; UAS-mCD8: GFP* (this study)

*wor-gal4 ase-gal80; svp*$^{e22}$*, FRT82B/TM6btb* (this study)

*wor-gal4 ase-gal80; cas*$^{24}$*, FRT82B/TM6btb* (this study)

## Fly Genetics

To generate svp or cas mutant type II NB MARCM clones, hs-flp UAS-mcd8: GFP; , ; FRT82B,tubulin-gal80 /TM6tb flies were crossed to wor-gal4 ase-gal80; Svp$^{e22}$, FRT82B/TM6, Tb

or wor-gal4 ase-gal80; $Cas^{29}$, FRT82B/TM6, Tb flies, respectively. $Chinmo^{1}$ clones were induced by crossing hs-flp, UAS-mcd8: GFP; FRT40, tubulin-gal80 flies to $chinmo^{1}$, FRT40; pointed-gal4 flies. chinmo and castor MARCM clones were induced during embryogenesis and analyzed at the indicated larval time point. Briefly, embryos were collected over a period of 6h and heat shocked in 37°C water bath for 30-40 minutes. After hatching, larvae were collected for 3-6h and reared at 25°C until the desired time point. To induce svp MARCM clones, 0-4h larvae were heat shocked in water bath for 1h and reared at 25°C until the desired time point.

## TU-tagging, RNA isolation, and RNA-seq

We used *wor-Gal4,ase-Gal80; UAS-UPRT / 9D11-Gal80* larvae to obtain type II neuroblast and progeny expression of uracil phosphoribosyltransferase (UPRT) at 48h, 72h and 96h. Larvae of appropriate age were fed on food containing 0.5mM 4-thiouracil (Sigma, St. Louis, MO) for 5 hours, dissected larval brains were pooled and stored in RNAlater (ThermoFisher). RNA purification and RNA-seq was done as described previously (Gay, Karfilis, Miller, Doe, & Stankunas, 2014; Gay et al., 2013). Briefly, larval brains were homogenized in Trizol (ThermoFisher) followed by RNA isolation and construction of cDNA libraries followed by 100 bp single end read sequencing on Illumina HiSeq 2000. For each time point three biological replicates were sequenced, which resulted in 30-40 million single end 100 bp reads for each barcoded library. Sample reads were trimmed to remove adaptor sequences using FASTX-Toolkit (Hannon lab) and then aligned to the *Drosophila* genome using GSNAP aligner (T. D. Wu & Nacu, 2010). Only uniquely aligned reads were considered for downstream differential gene expression analysis. We used HTSeq with union mode to generate gene counts from the BAM alignment files for each sample. Gene counts table were analyzed for differential gene expression by DeSeq2 method (Love, Huber, & Anders, 2014). We narrowed down our candidate gene list by selecting genes which were more than two fold either enriched or depleted across the two samples, and we focused mainly on transcription factors and RNA-binding proteins having available reagents.

## Standardizing larval development at different temperatures

All larvae were grown at 25°C unless noted, and all hours after larval hatching are standardized to growth at 25°C based on published conversions: 18°C is 2.25x slower than 25°C, and 29°C is 1.03x faster than 25°C (Powsner, 1935).

## In vitro culturing of larval brains

In vitro cultures were set up in 24 well plates in Schneider's insect medium (Gibco) supplemented with 10% (vol/vol) heat inactivated FBS (Sigma), 0.01% (vol/vol) Insulin solution (Sigma, I0516-5ML), and 1% (vol/vol) Pen/Strep (Sigma). 1 ug/ml of 20-hydroxy-ecdysone (Sigma) was added for control conditions. Dissections were performed at 48h and the prothoracic glands were removed prior to culture. Brains were cultured for 24 hours and the media was changed every 12 hours.

## Immunohistochemistry

Primary antibodies were Chicken anti-GFP (1:1000, Aves), Rat anti-Dpn (1:500 Abcam, Eugene, OR), Rabbit anti-Asense (1:2000 Cheng-Yu Lee, Univ Michigan), Mouse anti-Svp (1:50 Developmental Studies Hybridoma Bank, Iowa), Guinea pig anti-Castor (1:1000 Stefan Thor, Sweden), Rabbit anti-Castor (1:1000 Ward Odenwald, NIH; subsequently distributed by Doe lab), Rat anti-Chinmo (1:500 Nick Sokol), Rabbit anti-Imp (1:500, Paul MacDonald), Mouse anti-EcR common (1:500 Carl Thummel; detects all isoforms), Mouse anti-EcR-B1 (1:2000 Carl Thummel), Mouse anti-BrC (1:100 Gregory M. Guild ), Mouse anti-BrZ1 (1:100 Gregory M. Guild), Guinea pig anti-Syncrip (1:2000 Ilan Davis, UK), or Guinea pig anti-E93 (1:500 this work). Dissection and immunostaining were performed using a standard larval immune staining protocol (C. Y. Lee et al., 2006). Larval brains were dissected in insect media (Sigma), fixed in 4% formaldehyde in PBST (PBS with 0.3% Triton X-100) for 20 min. After fixing, brains were washed in PBST for 40 min and blocked in PBST with 5% normal goat and donkey serum mix (Vector Laboratories) for 40 min. Fixed brains were transferred to the primary antibody solutions of the appropriate dilutions and incubated overnight at 4C. The next day, brains were rinsed and washed for 40 min and then incubated in secondary antibody for 2h at room temperature. After secondary antibody incubation, a 40 min wash was performed and brains were stored and mounted in Vectashield (Vector Laboratories).

## Confocal imaging, data acquisition, and image analysis

Fluorescent images were acquired on a Zeiss LSM 710. Larval brain cell counting was performed using the FIJI cell counter plug in, and statistical analysis (Student's T test) was done in Graph Pad Prism software. 0h pupal brain glia and neuron counting were by immortalizing GFP expression in type II neuroblast progeny using *UAS-FLP actin-FRT-stop-FRT-gal4; wor-gal4 ase-gal80 UAS-mCD8:GFP*, and then counting the Repo+ or Bsh+ nuclei within the GFP+ volume; nuclei were rendered using Imaris (Bitplane) and only those within the GFP+ volume were shown to eliminate expression from outside type II lineages. Figures were assembled in Illustrator (Adobe).


## Acknowledgements

We thank Sen-Lin Lai, Minoree Kohwi, Qingzhong Ren and Tzumin Lee for comments on the manuscript; Claude Desplan, Hugo Bellen, Ward Odenwald, Tzumin Lee, Carl Thummel, Stefan Thor, Nick Sokol, Paul MacDonald, Gregory Guild, Ilan Davis, Florence Besse, and Cheng-Yu Lee for reagents. We thank Qingzhong Ren and Tzumin Lee for sharing data prior to publication and comments on the manuscript. We acknowledge the Bloomington *Drosophila* Stock Center (NIH P40OD018537), the Vienna *Drosophila* RNAi Center (VDRC), TRiP at Harvard Medical School (NIH/ NIGMS R01-GM084947), and the Developmental Studies Hybridoma Bank (DSHB). This work was funded by NIH HD27056 (CQD), a Developmental Biology Training grant T32HD007348-26 (BM), and the Howard Hughes Medical Institute.


## Competing interests

All authors have no competing financial or non-financial competing interests.

## Figure 1. Identification of temporally expressed proteins in larval type II neuroblasts

(A-E) Cas and Svp are expressed from 24-36h (A,C,E) but not at 48h (B, D, E). Neuroblasts, outlined.

(F-K) Early factors. Chinmo, Imp, and Lin-28:GFP (Lin-28) are detected in neuroblasts at 48h but not at 72h.

(L-Q) Late factors. Syncrip, Broad, and E93 are not detected in neuroblasts at 48h but are present at 72h or 96h.

(R) Summary of temporal factor expression. Dashed bars indicate asynchronous expression during the indicated temporal window. Gradients indicate graded change in expression levels.

In all panels, temporal factors are in magenta, and type II neuroblasts are identified by *wor-gal4 ase-gal80 UAS-mcd8:GFP* transgene expression (GFP, green, outlined) or as Dpn+ Ase- (green/red, respectively). Arrowhead, neuroblasts. For each panel n > 10 neuroblasts scored. Scale bar, 10μm.

**Figure 2. Ecdysone hormone is required for the early-to-late temporal factor transition.**

(A-E) Control *ecd$^{ts}$/deficiency* larvae at 18$^{o}$C show normal temporal factor expression in type II neuroblasts (circled): the early factors Chinmo and Imp are off at 72h (A-B) and the late factors Syncrip, Broad, and E93 are on at 72h and 96h (C-E).

(F-J) Loss of ecdysone in *ecd$^{ts}$ /deficiency* larvae at 29$^{o}$C shows failure to down-regulate the early factors Chinmo and Imp (F-G) and failure to activate the late factors Syncrip, Broad and E93 (H-J) in type II neuroblasts (circled).

(K) Quantification. n >10 for each bar. Asterisk, $p < 0.003$.

In all panels, times are adjusted to the equivalent larval stage at 25$^{o}$C, type II neuroblasts are identified as Dpn+ Ase- or large cells expressing *wor-gal4 ase-gal80 UAS-mcd8:GFP* (green in insets). Scale bar, 10μm.

**Figure 3. Ecdysone hormone activates neuroblast expression of Chinmo and Broad in isolated brain cultures.**

(A-B) Isolated larval brains cultured with added 20-hydroxy-ecdysone (+20HE) from 48-72h show normal down-regulation of the early factor Chinmo (A) and activation of the late factor Broad (B).

(C-D) Isolated larval brains cultured without added 20-hydroxy-ecdysone (-20HE) from 48-72h fail to down-regulate Chinmo (C) or activate Broad (D).

(E-F) Live imaging of isolated larval brains from 48-72h cultured with ecdysone (+20HE) or without ecdysone (-20HE). In each case two neuroblasts and their progeny were imaged; successive telophase stages are shown for one neuroblast (yellow outline); note that for both +20HE and -20HE the cell cycle time is ~100 minutes (see timestamps). See Supplemental Movies 1 & 2.

(G) Quantification of the experiment shown in E-F.

(H) Quantification of the experiment shown in A-D.

In all panels, type II neuroblasts are identified as large cells expressing *wor-gal4 ase-gal80 UAS-mcd8:GFP* (green in insets, A-F; white in G-H), $n \geq 10$ per experiment. Asterisk, $p < 0.003$. Scale bar, 10$\mu$m.

**Figure 4. Ecdysone receptor expression and function.**

(A-B) EcR-B1 is first detected at ~56h in most type II neuroblasts.

(C-F) EcR-B1 expression is ecdysone-independent. (C-D) EcR-B1 is activated normally in *ecd$^{ts}$* mutants at both permissive (18$^{o}$C) and restrictive (29$^{o}$C) temperatures by 72h. (E-F) EcR-B1 expression is activated normally in isolated brains cultured from 48-72h with (E) or without (F) added 20-hydroxy-ecdysone (20HE).

(G-K) Expression of an EcR dominant negative transgene in type II neuroblasts (*wor-gal4 ase-gal80 UAS-mcd8:GFP UAS-EcR$^{DN}$*) results in persistent expression of the early factors Chinmo and Imp

(G,H) and failure to express the late factors Syncrip and E93 (I,K). Surprisingly, the late factor Broad is still expressed (J).

(L) Quantification. Percent of type II neuroblasts expressing the indicated factors at the indicated levels (dark red, strong expression; light red, weak expression; dark green, strong expression). All data are from 72h larvae except E93 is from 96h larvae.

(M) Summary: ecdysone signaling via EcR-B1 terminates expression of early factors and activates expression of late factors.

In all panels, type II neuroblasts are identified by expression of *wor-gal4 ase-gal80 UAS-mcd8:GFP* (left panels or insets), developmental times are adjusted to the equivalent time at 25°C. n > 10 for each experiment. Scale bar 10 μm.

## Figure 5. Seven-up activates expression of the Ecdysone receptor in type II neuroblasts.

(A-F) *svp* mutant MARCM clones (GFP+, green and outlined) induced at 0-4h and assayed at 96h for the indicated factors.

(G) Quantification (red, *svp* mutant clone; black, wild type *UAS-FLP actin-FRT-stop-FRT-gal4*; *wor-gal4 ase-gal80 ; UAS-mCD8: GFP*). 100% of mutant type II neuroblasts fail down-regulate the early factors Imp and Chinmo, and fail to activate the late factors Syncrip, EcR-B1, E93 and Broad. Number of *svp* mutant clones scored: Imp n=11, Chinmo n=4, Syncrip n=19, EcR-B1 n=11, E93 n=2, Broad n=4. Number of wild type neuroblasts scored n>10 for each marker. In all panels, type II neuroblasts are identified by expression of *wor-gal4 ase-gal80 UAS-mcd8:GFP* (outlined). Scale bar 10 μm.

## Figure 6. Syncrip and Imp function downstream of the Ecdysone receptor in type II neuroblasts

(A-C) *Imp* mutants *($imp^{G0072}$ / $imp^{G0072}$)* and *Syncrip* mutants (*$Syncrip^{f03775}$/ deficiency*) show normal expression of EcR in type II neuroblasts: off at 48h and on at 72h.

(D) *Imp* mutants *($Imp^{G0072}$ / $Imp^{G0072}$)* do not precociously upregulate Syncrip in type II neuroblasts at 48h.

(E) *Syncrip* mutants (*$Syncrip^{f03775}$/ deficiency*) show prolonged expression of Imp in type II neuroblasts at 72h.

(F-H) *Imp* mutants *($Imp^{G0072}$ / $Imp^{G0072}$)* show normal temporal expression of Chinmo, Broad, or E93 in type II neuroblasts.

(I-K) *Syncrip* mutants (*$Syncrip^{f03775}$/ deficiency*) show prolonged expression of Chinmo but normal expression of the late factors Broad and E93 in type II neuroblasts.

(L) *broad* mutants (*$broad^{npr3}$/ $broad^{npr3}$*) have normal Chinmo expression: absent from 72h type II neuroblasts.

(M) *chinmo* mutants (*$chinmo^{1}$* mutant clones) have normal Broad expression: absent from 48h type II neuroblasts.

(N) *Syncrip* mutants (*$Syncrip^{f03775}$/ deficiency*) have type II neuroblasts that abnormally co-express Chinmo and Broad at 72h.

(O) Quantification. Percent of type II neuroblasts expressing the indicated factors at the indicated timepoints.

Insets identify the pictured type II neuroblast (green) based on its expression of Dpn (green) not Ase (red) or by expression of *wor-gal4 ase-gal80 UAS-mcd8:GFP* (green). n > 5 for all panels. Scale bar, 10 μm.

## Figure 7. Late temporal transcription factors specify neuronal and glial identity.

(A,B) Wild type or (C,D) *$EcR^{DN}$* brains at 0h after puparium formation. The inset shows GFP+ cells permanently marking the type II neuroblast lineage (*wor-gal4 ase-gal80 UAS-FLP actin-FRT-stop-FRT-gal4 UAS-mCD8:GFP*; green) which is circled with dashed lines in the main figure. Repo+ or Bsh+ nuclei located within the volume of the type II progeny were identified using Imaris and represented

as magenta spheres. This provides the optimal way to visualize cell numbers within the three dimensional GFP+ volume.

(E,F) Quantification. ** $p<0.01$, **** $p<0.0001$.

**Figure 8. Ecdysone is required for early to late temporal factor transition in type I neuroblasts.**

(A-C) Control brains (*ecd-ts/deficiency* at 18°C) at the indicated timepoint. (A-C) Normal down-regulation of the early factor Chinmo and activation of the late factors Broad and E93.

(E-G) Experimental brains with reduced ecdysone (*ecd-ts/deficiency* at 29°C) at the indicated timepoint. (E-G) Abnormal prolonged expression of the early factor Chinmo and failure to activation of the late factors Broad and E93.

(D, H) Quantification. n=6 brain lobes; *, $p<0.03$, **, $p<0.03$; ****, $p<0.0001$

In all panels, central brain type I neuroblasts are identified as Dpn+Ase+ (subset outlined), and times are adjusted to the equivalent larval stage at 25°C as described in the methods. Note that *ecd$^{ts}$/deficiency* brains are smaller than control brains primarily due to severe loss of the optic lobe. Scale bar, 50 μm.

**Figure 9. Model showing hormonal regulation of early to late temporal transitions in central brain larval neuroblasts**

Summary of regulatory interactions driving larval neuroblast early-to-late temporal factor expression. Arrows indicate positive regulation; "T" indicates negative regulation; dashed bars indicate asynchronous expression during the indicated temporal window; gradients indicate graded change in expression levels.

Video 1. Explanted larval brain cultured in vitro from 48-72h with added 20-hydroxy-ecdysone.

Two type II neuroblasts are shown expressing *wor-gal4 ase-gal80 UAS-myr:GFP* (see methods). Still panels from video shown in Figure 3E, and cell cycle times quantified in Figure 3G.

Video 2. Explanted larval brain cultured in vitro from 48-72h without 20-hydroxy-ecdysone.

Two type II neuroblasts are shown expressing *wor-gal4 ase-gal80 UAS-myr:GFP* (see methods). Still panels from video shown in Figure 3F, and cell cycle times quantified in Figure 3G.

**Figure 1-figure supplement 1. TU-tagging to identify temporally expressed genes in type II neuroblasts and their progeny.**

(A) Type II neuroblast lineage schematic, showing young or old neuroblast progeny markers.

(B) Expression of HA:UPRT specifically in type II neuroblasts and their progeny. Scale bar, 50μm.

(C) Heat map of showing genes differentially expressed at least one developmental stage. Each column is an independent biological replicate; three per timepoint. Red, high expression; blue low expression. Note that elevated levels of Cas and Chinmo at 72h are likely due to the large number of neuroblast progeny expressing each gene; by 72h Cas and Chinmo proteins are undetectable in type II neuroblasts (Figure 1).

**Figure 1-figure supplement 2. Broad-Z1 but not Broad-Z3 is expressed in type II neuroblasts**

(A) Broad-Z1 (magenta) is detected in type II neuroblasts (dashed circle) at 96h.

(B) Broad-Z3 (magenta) is not detected in type II neuroblasts (dashed circle) at 96h.

In all panels, type II neuroblast lineages are marked by *wor-gal4 ase-gal80 UAS-cd8:GFP* expression (green).

**Figure 4-figure supplement 1. Ecdysone receptor isoform expression in type II neuroblasts**

(A) EcR-B1 (magenta) is detected in type II neuroblasts (dashed circle) at 96h; n>10. See also Figure 4A,B.

(B) EcR-A (magenta) is not detected in type II neuroblasts (dashed circle) at 96h; n>10.

(C) EcR-common (magenta) is not detected in type II neuroblasts (dashed circle) at 48h; n>10.

(D) EcR-common (magenta) is detected in type II neuroblasts (dashed circle) at 72h; n>10.

EcR-common detects all EcR isoforms. In all panels, type II neuroblast lineages are marked by *wor-gal4 ase-gal80 UAS-cd8:GFP* expression (green). Scale bar, 10 μm.

**Figure 5-figure supplement 1. Cas is not required to activate Svp expression, and Svp is not required to terminate Cas expression.**

*cas* mutant clones induced during embryogenesis show normal Seven-up expression at 36h. *svp* mutant clones induced during 0-4h show normal loss of Cas expression at 72h. In all panels, type II neuroblast lineages are marked by *wor-gal4 ase-gal80 UAS-cd8:GFP* expression (green). Scale bar, 10 μm.

**Figure 6-figure supplement 1. Chinmo and Broad have mutually exclusive expression in neuroblasts and neurons.**

(A) Chinmo is expressed in type II neuroblasts (dashed circle) and adjacent neuronal progeny at 48h, whereas Broad is not detected.

(B) Broad is expressed in type II neuroblasts (dashed circle) and adjacent neuronal progeny at 120h, whereas Chinmo is not detected in the neuroblast but only in the earlier-born neurons furthest away from the parental neuroblast.

In all panels, type II neuroblast lineages are marked by *wor-gal4 ase-gal80 UAS-cd8:GFP* expression (green). Scale bar, 10 μm.

**Figure 8-figure supplement 1. Syncrip is expressed in a subset of central brain neuroblasts at 36h and 48h.**

(A,B) Syncrip is detected in ~10 central brain neuroblasts at 36h and 48h. Maximum intensity projection of entire brain lobes. Anterior up. (C) Quantification.

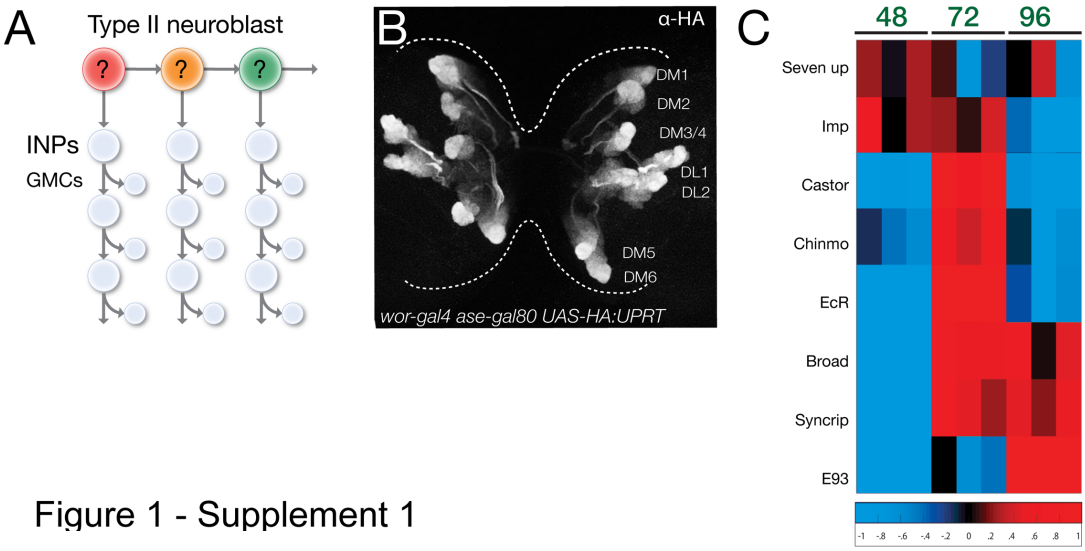


Figure 1 - Supplement 1

*Figu*

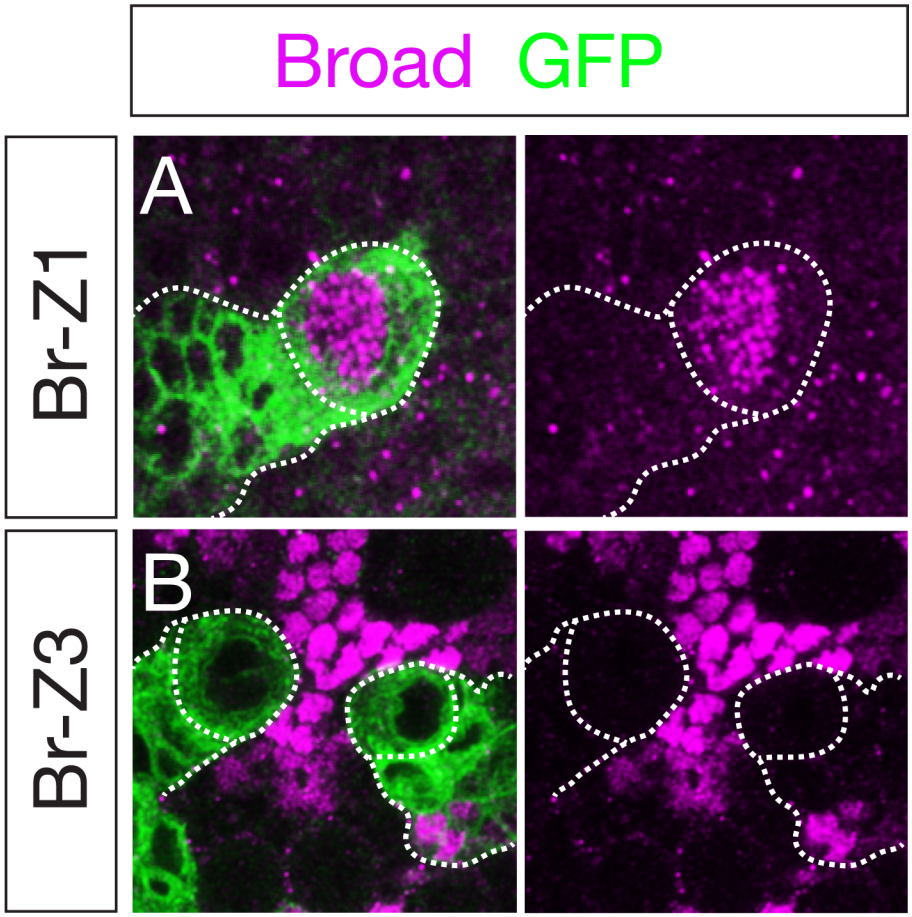


Figure 1-figure supplement 2

***Figure 1- supplement 2***

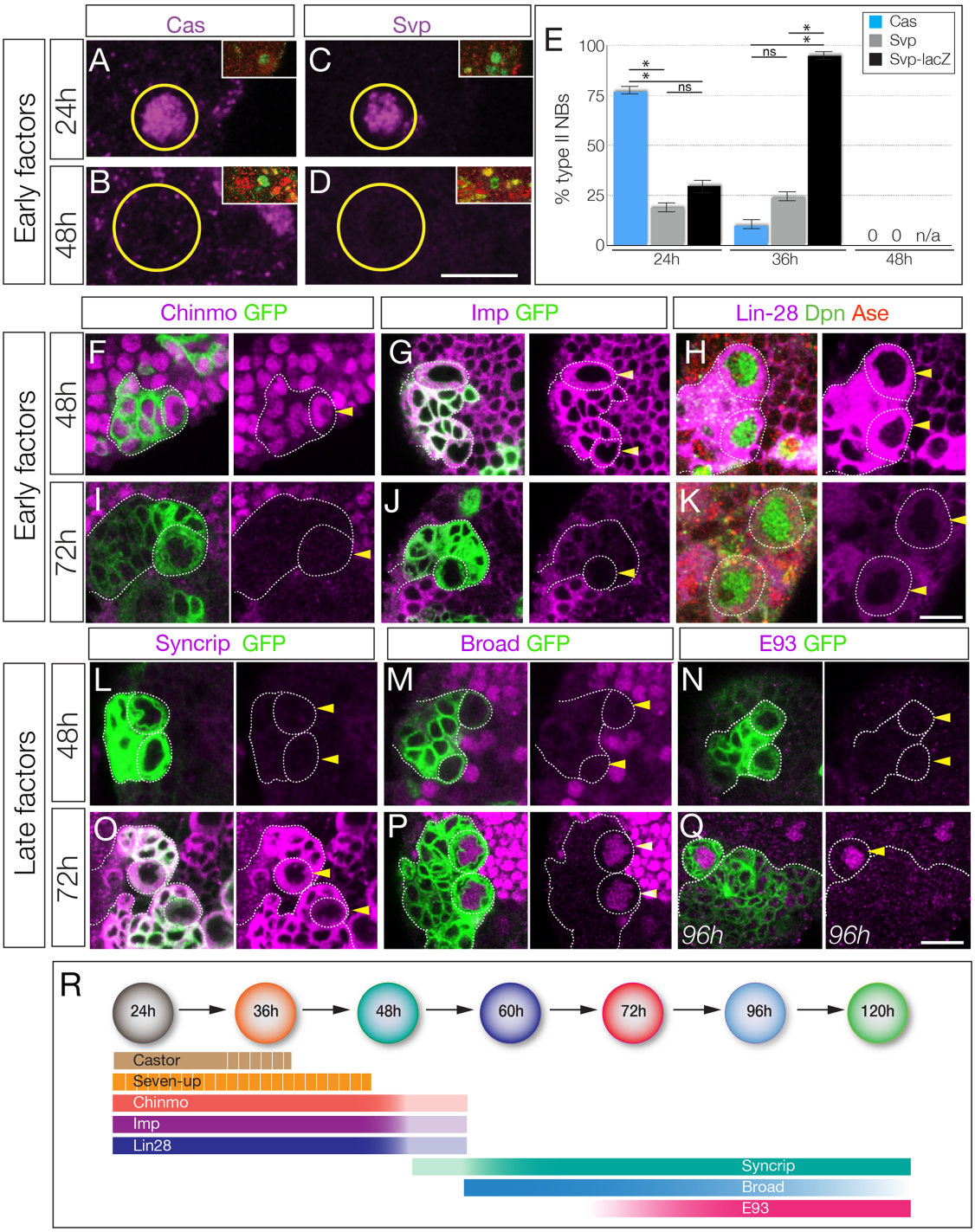


Figure 1

***Figure 1***

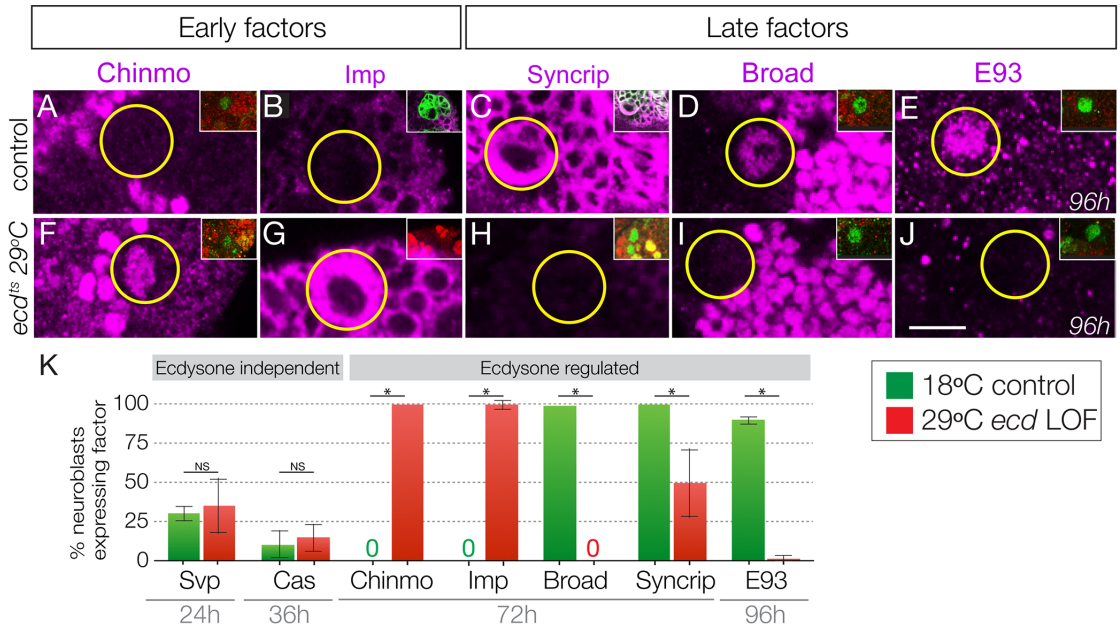


Figure 2

***Figure 2***

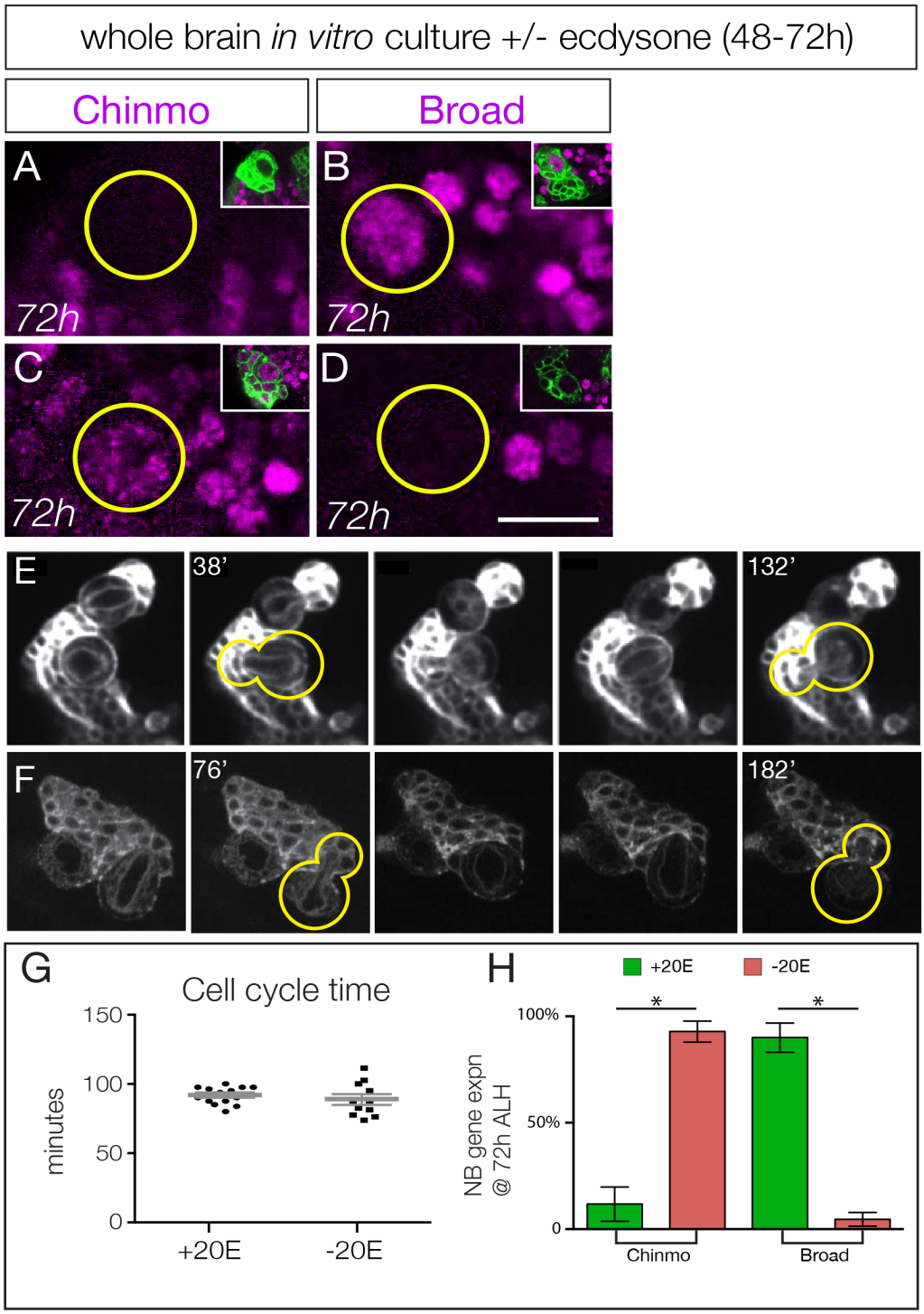


Figure 3

***Figure 3***

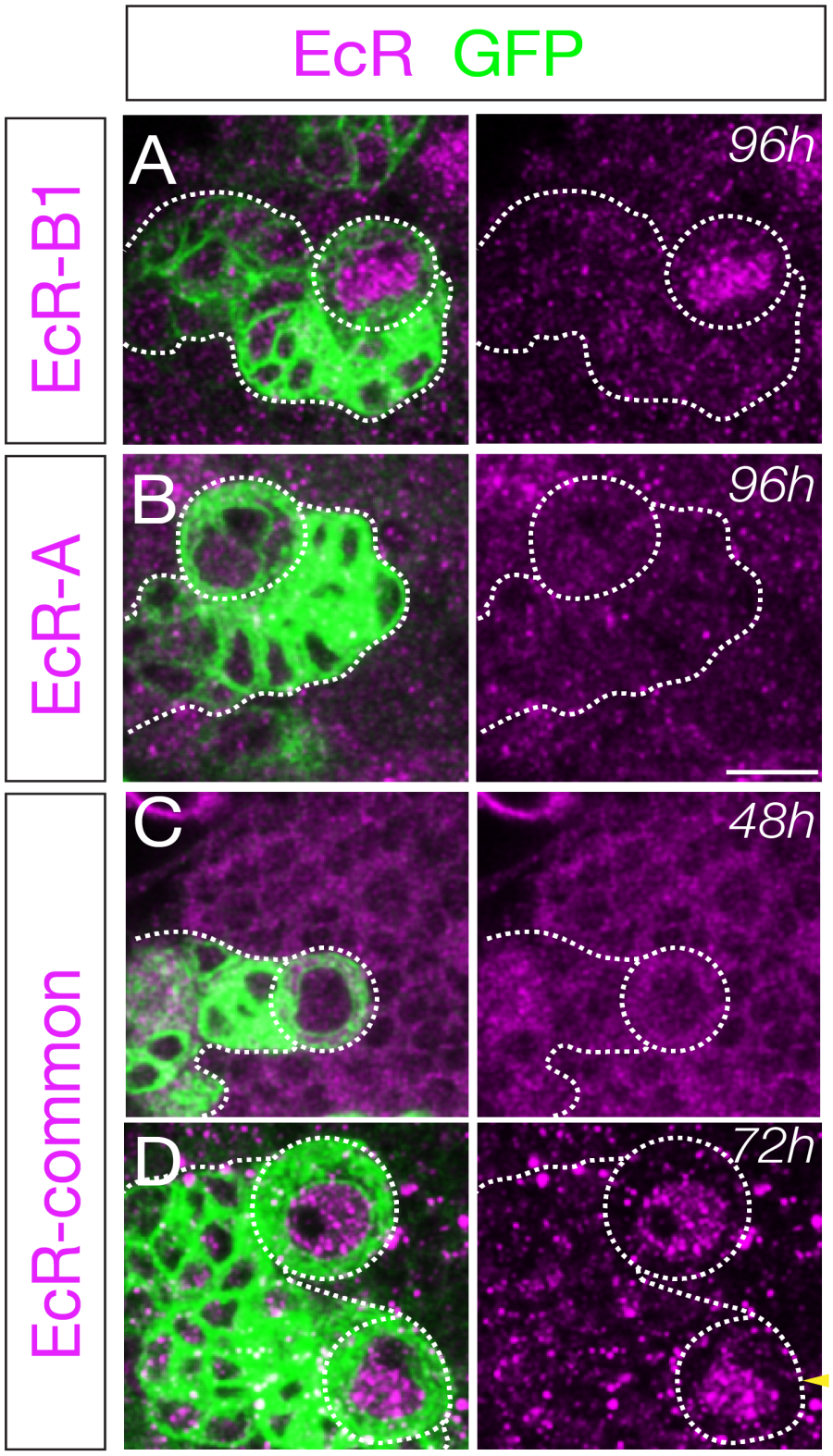


Figure 4-figure supplement 1

***Figure 4 – supplement 1***

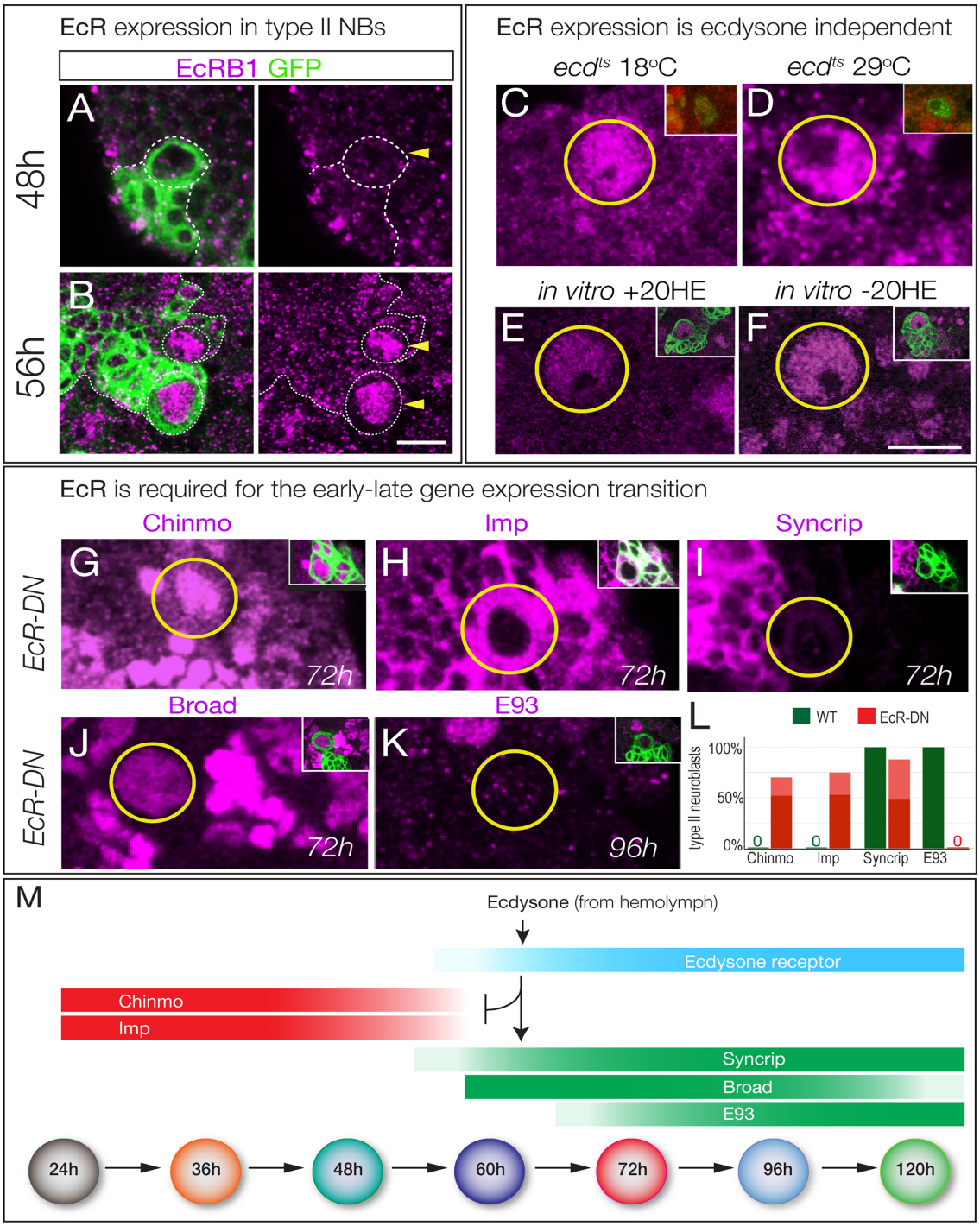


Figure 4

***Figure 4***

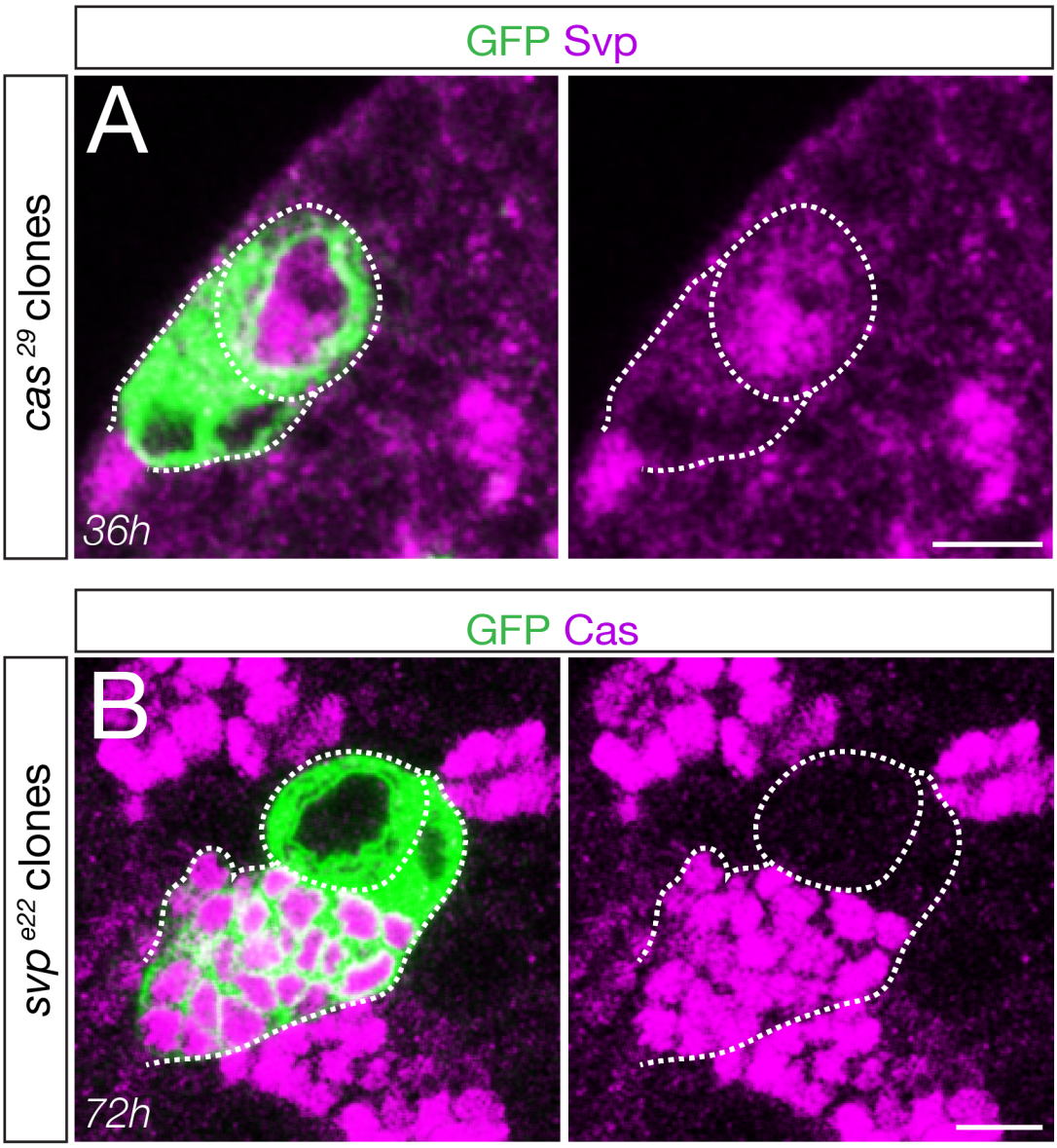


Figure 5-figure supplement 1

***Figure 5 – supplement 1***

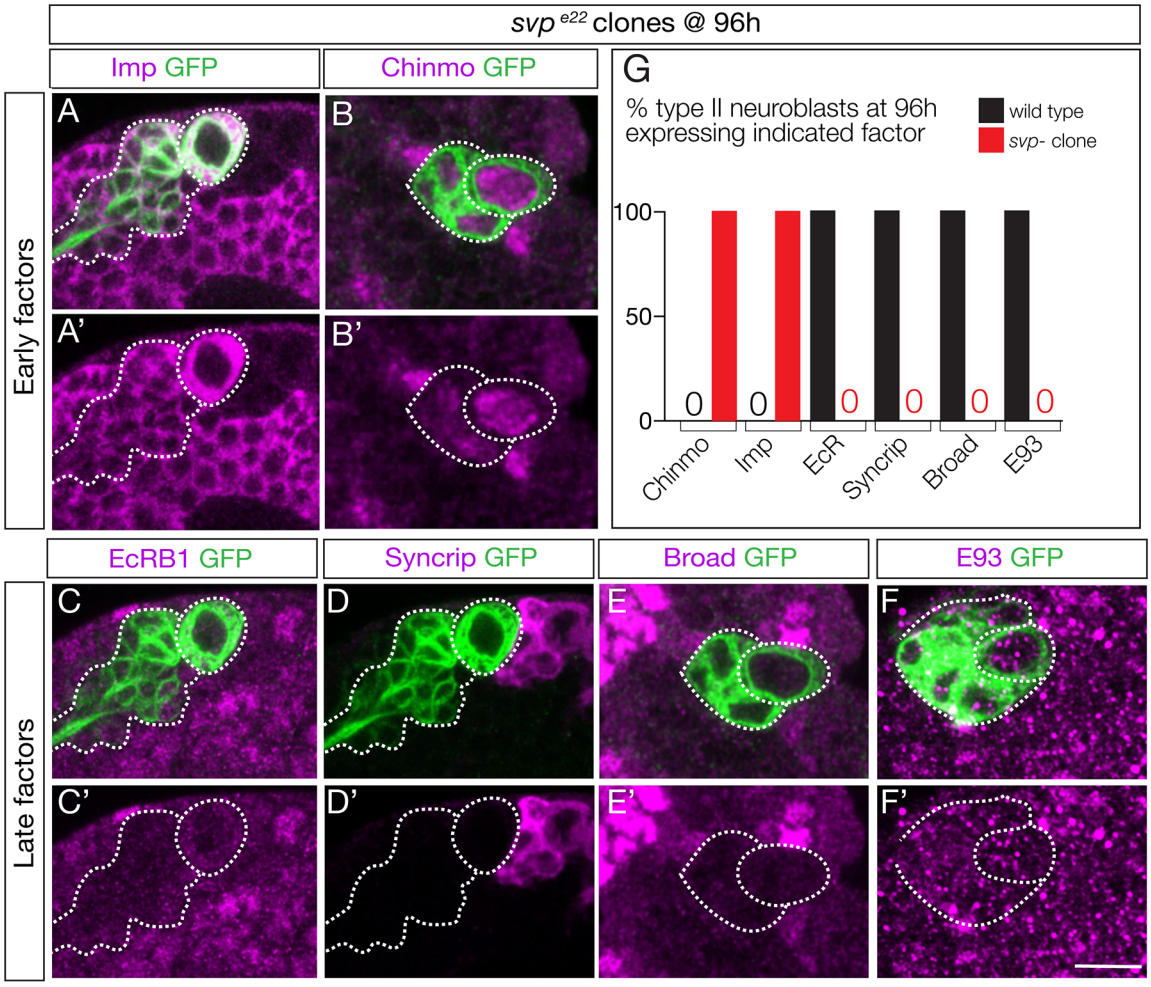


Figure 5

***Figure 5***

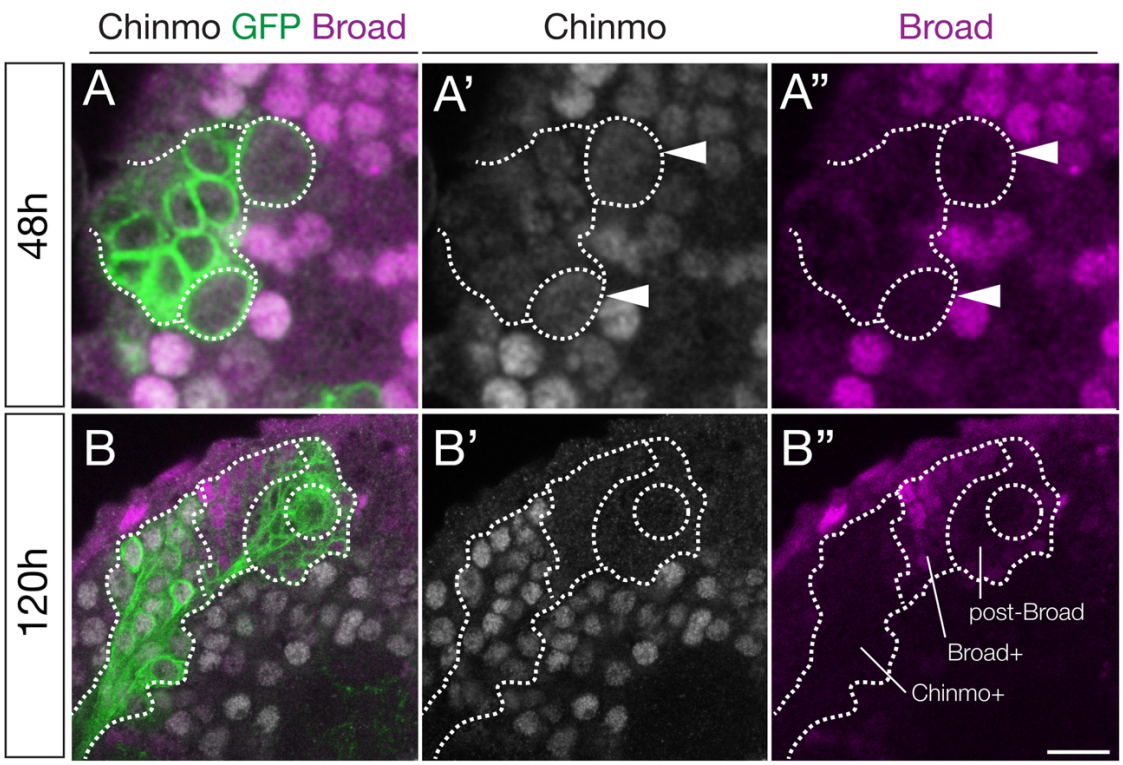


Figure 6-figure supplement 1

***Figure 6 – Supplement 1***

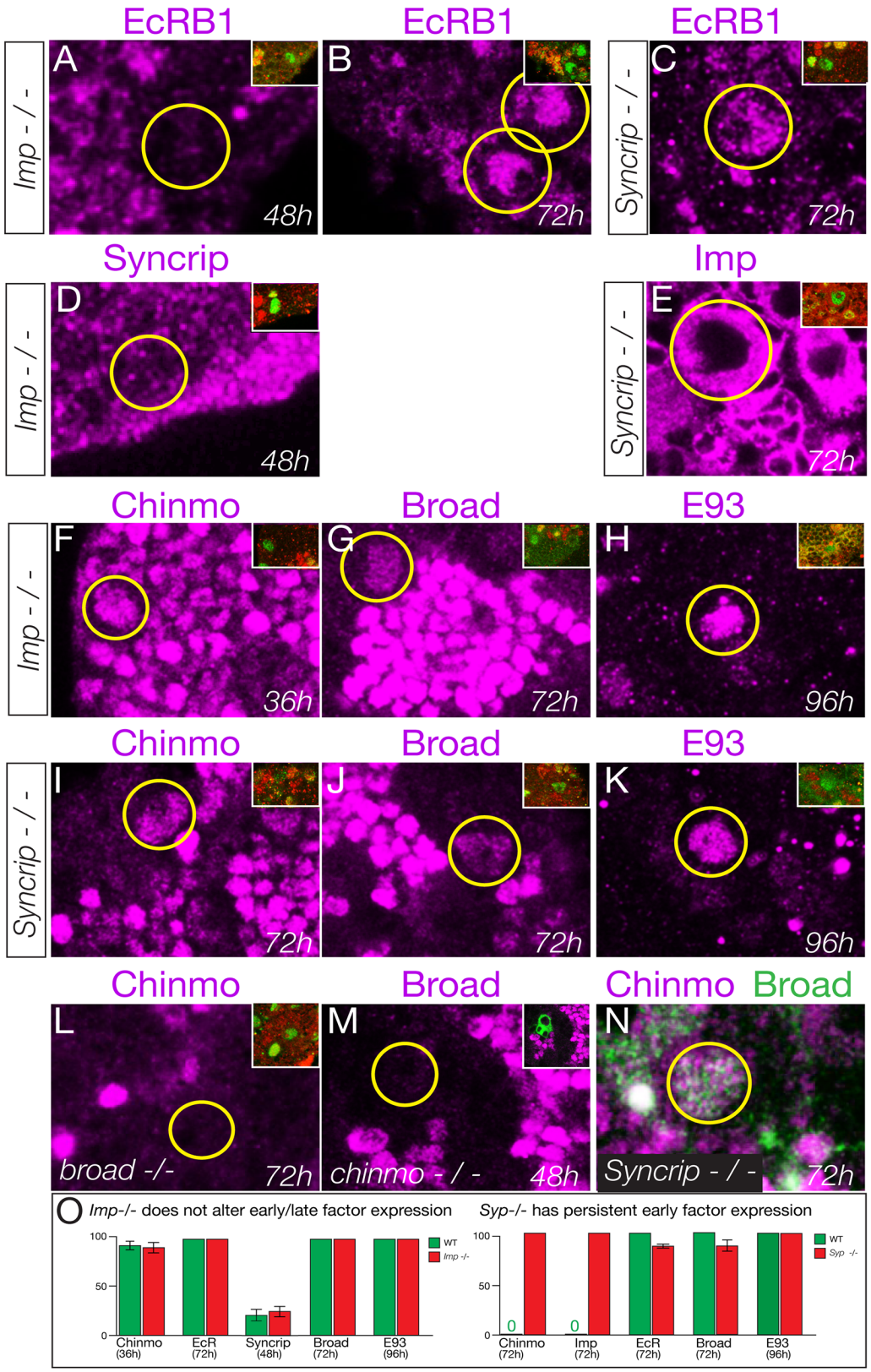


Figure 6

*Figure 6*

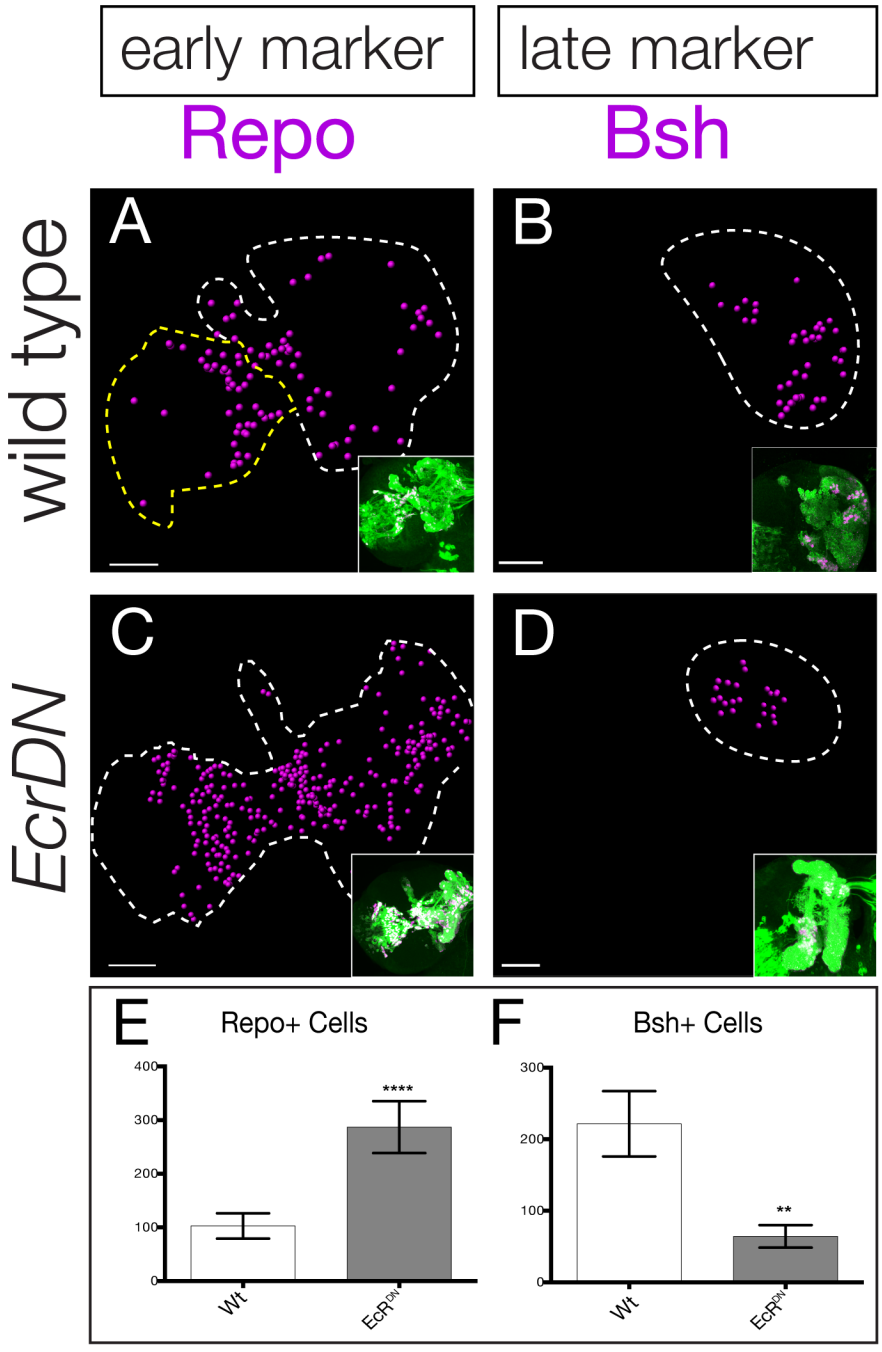


Figure 7

***Figure 7***

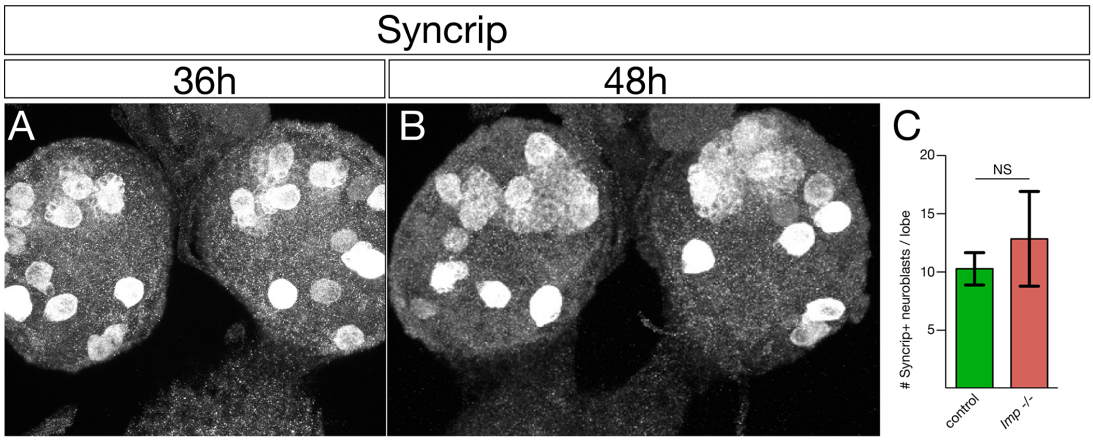


Figure 8-figure supplement 1

***Figure 8 – Supplement 1***

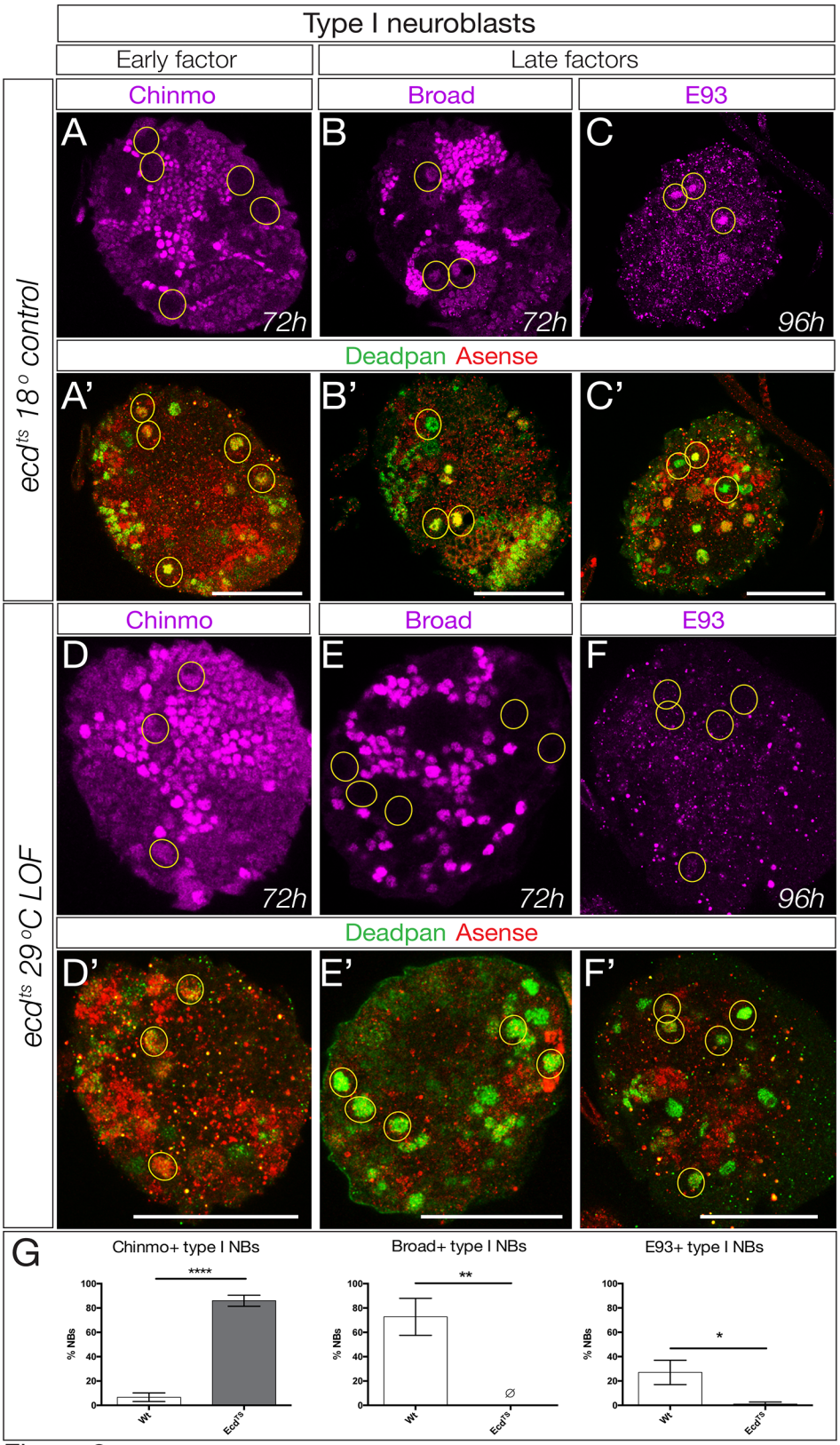


Figure 8

***Figure 8***

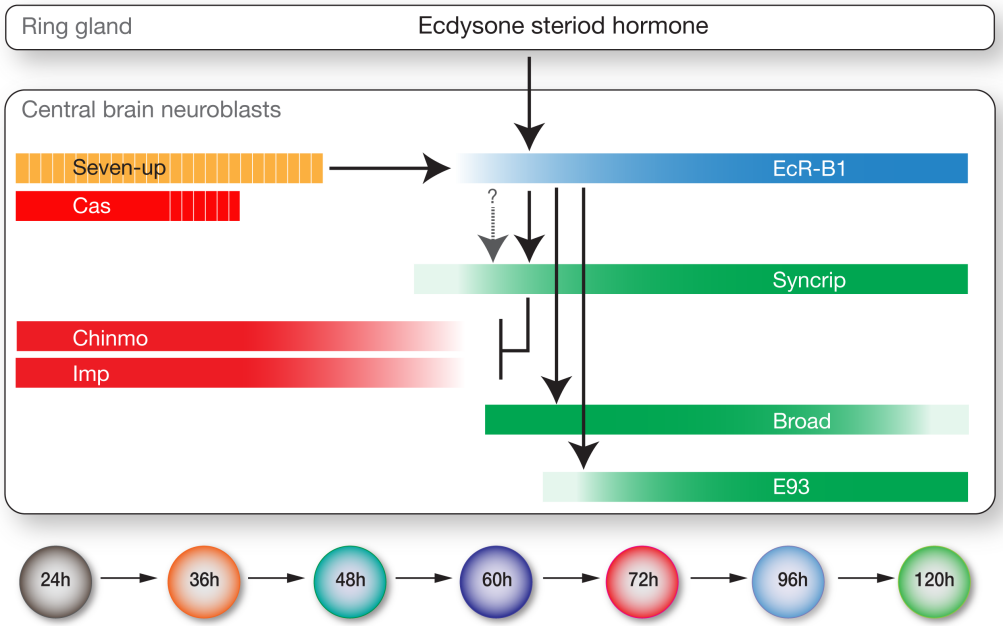


Figure 9

*Figure 9*

# CHAPTER III

# THE ROLE OF LINEAGE, HEMILINEAGE, AND TEMPORAL IDENTITY IN ESTABLISHING NEURONAL CONNECTIVITY IN THE *DROSOPHILA* LARVAL CNS

Brandon Mark1, Sen-Lin Lai1, Aref Arzan Zarin1, Laurina Manning1, Albert Cardona2, James W. Truman2,3, and Chris Q. Doe1*

1Institute of Neuroscience, Institute of Molecular Biology, Howard Hughes Medical Institute, University of Oregon, Eugene, OR 97403

2Janelia Research Campus, Howard Hughes Medical Institute, Ashburn, VA 20147

3Friday Harbor Laboratories, University of Washington. Friday Harbor, WA 98250

* Author for correspondence at cdoe@uoregon.edu

Author Contributions : B. Mark contributed to conceptualization, formal analysis, investigation, visualization, methodology, writing—original draft, writing—review and editing. S.L Lai and L. Manning contributed to formal analysis, investigation, visualization, methodology. A. Cardona and J.W. Truman contributed to methodology. C.Q. Doe contributed to conceptualization, formal analysis, investigation, methodology, writing—original draft.

## Introduction

Tremendous progress has been made in understanding the molecular mechanisms generating neuronal diversity in both vertebrate and invertebrate model systems. In mammals, spatial cues

generate distinct pools of progenitors which generate a diversity of neurons and glia appropriate for each spatial domain (Jessell, 2000). The same process occurs in invertebrates like *Drosophila*, but with a smaller number of cells, and this process is particularly well-understood. Spatial patterning genes act combinatorially to establish single, unique progenitor (neuroblast) identity; these patterning genes include the dorsoventral columnar genes *vnd*, *ind*, *msh* (Isshiki, Takeichi, & Nose, 1997; McDonald et al., 1998; Weiss et al., 1998) and the orthogonally expressed *wingless*, *hedgehog*, *gooseberry*, and *engrailed* genes (Chu-LaGraff & Doe, 1993; McDonald & Doe, 1997; Skeath, Zhang, Holmgren, Carroll, & Doe, 1995; Y. Zhang, Ungar, Fresquez, & Holmgren, 1994). These factors endow each neuroblast with a unique spatial identity, the first step in generating neuronal diversity (Figure 1A, left). Here we focus on the left and right sides of abdominal segment 1 (A1L, A1R) and so segment-specific patterning due to Hox gene expression is not relevant. The second step occurs as each neuroblast "buds off" a series of ganglion mother cells (GMCs) which acquire a unique identity based on their birth-order, due to inheritance from the neuroblast of a "temporal transcription factor"– Hunchback (Hb), Krüppel (Kr), Pdm, and Castor (Cas) – which are sequentially expressed by nearly all embryonic neuroblasts (Isshiki et al., 2001). The combination of spatial and temporal factors leads to the production of a unique GMC with each neuroblast division (Figure 1A, middle). The third and final step in generating neuronal diversity is the asymmetric division of each GMC into a pair of post-mitotic neurons; during this division, the Notch inhibitor Numb (Nb) is partitioned into one neuron ($Notch^{OFF}$ neuron) whereas the other sibling neuron receives active Notch signaling ($Notch^{ON}$ neuron), thereby establishing two distinct hemilineages (Harris et al., 2015; Lacin & Truman, 2016a; Skeath & Doe, 1998; Truman et al., 2010)(Figure 1A, right). In summary, three developmental mechanisms generate neuronal diversity within the embryonic CNS: neuroblast spatial identity, GMC temporal identity, and neuronal hemilineage identity.

A great deal of progress has also been made in understanding neural circuit formation in both vertebrates and invertebrate model systems, revealing a multi-step mechanism. Mammalian neurons initially target their axons to broad regions (e.g. thalamus/cortex), followed by targeting to a neuropil domain (glomeruli/layer), and finally forming highly specific synapses within the targeted domain (reviewed in Kolodkin & Tessier-Lavigne, 2011).

Despite the progress in understanding the generation of neuronal diversity and the mechanisms governing axon guidance and neuropil targeting, how these two developmental processes are related remains unknown. While it is accepted that the identity of a neuron is tightly linked to its connectivity, the developmental mechanisms involved remain unclear. For example, do clonally-related neurons target similar regions of the neuropil due to the expression of similar

guidance cues? Do temporal cohorts born at similar times show preferential connectivity? Are neurons expressing the same transcription factor preferentially interconnected? It may be that lineage, hemilineage, and temporal factors have independent roles in circuit formation; or that some mechanisms are used at different steps in circuit assembly; or that mechanisms used to generate neural diversity could be independent of those regulating circuit formation. Here we map neuronal developmental origin, neuropil targeting, and neuronal connectivity within a whole CNS TEM reconstruction (Ohyama et al., 2015). This provides us the unprecedented ability to identify correlations between development and circuit formation – at the level of single neurons/single synapses – and test those relationships to gain insight into how mechanisms known to generate diversity might be coupled to mechanisms of neural circuit formation. We find that lineage, hemilineage, and temporal identity are all strongly correlated with features of neuronal targeting that directly relate to establishing neural circuits.

## Results

### Clonally related neurons project widely within the neuropil

It is not possible to determine the clonal relationship of neurons in the TEM volume based on anatomical features alone; for example, clonally-related neurons are not ensheathed by glia as they are in grasshopper embryos or the *Drosophila* larval brain (Doe & Goodman, 1985; Dumstrei, Wang, & Hartenstein, 2003). We took a multi-step approach to identify clonally-related neurons in the TEM reconstruction. First, we generated sparse neuroblast clones and imaged them by light microscopy. All neuroblasts assayed had a distinctive clonal morphology including the number of fascicles entering the neuropil, cell body position, and morphology of axon/dendrite projections (Figure 1B-G; and data not shown). The tendency for neuroblast clones to project one or two fascicles into the neuropil has also been noted for larval neuroblast clones (Harris et al., 2015; Lacin & Truman, 2016a; Truman et al., 2010). We assigned each clone to its parental neuroblast by comparing our clonal morphology to that seen following single neuroblast DiI labeling (Bossing, Udolph, Doe, & Technau, 1996; Schmid, Chiba, & Doe, 1999; Schmidt et al., 1997), and what has been reported previously for larval lineages (Birkholz, Rickert, Nowak, Coban, & Technau, 2015; Lacin & Truman, 2016b), as well as the position of the clone in the segment, and in some cases the presence of well-characterized individual neurons (e.g. the "looper" neurons in the NB2-1 clone). Note that we purposefully generated clones after the first-born Hb+ neurons, because the Hb+ neurons have cell bodies contacting the neuropil and do not fasciculate with later-born neurons in the clone, making it

difficult to assign them to a specific neuroblast clone. We found that neurons in a single neuroblast clone, even without the Hb+ first-born neurons included, project widely throughout the neuropil, often targeting both dorsal motor neuropil and ventral sensory neuropil, as well as widely along the mediolateral axis of the neuropil (Figure 1B).

Next, we used these neuroblast lineage-specific features to identify the same clonally-related neurons in the TEM reconstruction in A1L. We identified neurons that had clustered cell bodies, clone morphology matching that seen by light microscopy (Figure 1C), and one or two fascicles entering the neuropil (Figure 1D,E). The similarity in overall clone morphology between genetically marked clones and TEM reconstructed clones was striking (compare Figure 1B and 1C). We used two methods to validate the clonal relationship observed in the TEM reconstruction. We used neuroblast-specific Gal4 lines (Kohwi, Lupton, Lai, Miller, & Doe, 2013; Lacin & Truman, 2016a) to generate MCFO labeling of single neurons, and found that in each case we could match the morphology of an MCFO-labeled single neuron from a known neuroblast to an identical single neuron in the same neuroblast clone within the TEM reconstruction (data not shown). We also validated the reliability of clone morphology and neuron numbers by tracing the same seven lineages in A1R, where we observed similar neuron numbers and fascicles per clone (Figure 1D, E), and similar clonal morphology (data not shown). Overall, we mapped seven bilateral neuroblast clones into the TEM reconstruction (Figure 1F,G; Supp. Table 1). Note that we chose these seven neuroblasts based on successful clone generation and availability of single neuroblast Gal4 lines, and thus there should be no bias towards a particular connectivity or circuit. We conclude that each neuroblast clone has stereotyped cell body positions, 1-2 fascicles entering the neuropil, and widely projecting axons and dendrites.

## Lineages generate two morphologically distinct classes of neurons, which project to motor or sensory neuropil domains.

After mapping seven lineages into the EM volume, we observed that most lineages seemed to contain two broad classes of neurons with very different projection patterns. Recent work has shown that within a larval neuroblast lineage all Notch$^{ON}$ neurons have a similar clonal morphology (called the Notch$^{ON}$ hemilineage), whereas the Notch$^{OFF}$ hemilineage shares a different morphology (Harris et al., 2015; Lacin & Truman, 2016a; Truman et al., 2010). We hypothesized that the observed morphological differences may be due to hemilineage identity (Figure 2). First, we used NBLAST (Costa, Manton, Ostrovsky, Prohaska, & Jefferis, 2016) to compare the morphology of clonally

related neurons. We observed that five of the seven neuroblast lineages generated two highly distinct candidate hemilineages that each projected to a focused domain in the dorsal or ventral neuropil (Figure 2A-D). A sixth neuroblast lineage, NB7-4, generated neurons projecting to the ventral neuropil, and a pool of glia (Figure 2E). The seventh neuroblast lineage, NB3-3 (Figure 2F), has previously been shown to directly generate a single Notch$^{OFF}$ hemilineage due to direct differentiation of the neuroblast progeny as neurons, bypassing the terminal asymmetric cell division (Baumgardt et al., 2014; Wreden et al., 2017). We conclude that NBLAST can identify candidate hemilineages, with one projecting to the ventral neuropil, and one projecting to the dorsal neuropil (Figure 2G). This is a remarkable subdivision within each lineage, because the dorsal neuropil is the site of motor neuron dendrites and premotor neurons while the ventral neuropil is the site of sensory neuron presynapses and post-sensory neurons (Landgraf, Sanchez-Soriano, Technau, Urban, & Prokop, 2003; Mauss, Tripodi, Evers, & Landgraf, 2009) (Fig. S1). Additionally, neurons from the same candidate hemilineage are morphologically related, but different from the neurons in the other candidate hemilineage from the same parental neuroblast (Figure 2H). Thus, each neuroblast lineage generates two totally different classes of neurons, doubling the neuronal diversity generated in a single lineage. We conclude that neuroblasts produce two types of neuronal progeny: one targeting motor neuropil and one targeting ventral neuropil.

## Hemilineage identity determines axon projection targeting

We next wanted to (a) validate the NBLAST hemilineage assignments, (b) determine whether Notch$^{ON}$ hemilineages always project to dorsal/motor neuropil domains (ventral/sensory neuropil for Notch$^{OFF}$ hemilineages), and (c) to experimentally test whether hemilineage identity determines neuropil targeting. We can achieve all three goals by using neuroblast-specific Gal4 lines to drive expression of constitutively active Notch (Notch$^{intra}$) to transform Notch$^{OFF}$ hemilineages into Notch$^{ON}$ hemilineages.

There are Gal4 lines specifically expressed in NB1-2, NB7-1, and MB7-4 (Lacin & Truman, 2016a; Seroka & Doe, 2019) which we used to drive Notch$^{intra}$ expression. Notch$^{intra}$ expression in NB1-2 or NB7-1 led to a loss of ventral projections and a concomitant increase in dorsal neuropil projections (compare Figure 3A,B to Figure 3D,E). Similarly, Notch$^{intra}$ expression in the NB7-4 lineage led to a loss of ventral projections and an increase in the number of glia (Figure 3C). For all lineages, the loss of ventral neurons is also visible in dorsal views (Figure 3A-F insets). In addition,

we generated a Notch reporter by Crispr engineering the Notch target gene *hey*, placing a T2A:FLP exon in frame with the *hey* exon, resulting in Notch$^{ON}$ neurons expressing FLP. When we use NB7-1-Gal4 to drive expression of UAS-GFP we see the full NB7-1 clone (Figure 3G), whereas a FLP-dependent reporter (*UAS-FRT-stop-FRT-RFP*) will only be expressed in Notch$^{ON}$ neurons innervating the dorsal neuropil (Figure 3G'). Taken together, our Notch experiments strongly support the NBLAST assignments of neurons into two distinct hemilineages, and show that all tested neuroblast lineages make a Notch$^{ON}$ hemilineage that projects to dorsal/motor neuropil (or makes glia), and a Notch$^{OFF}$ hemilineage that projects to ventral/sensory neuropil. In conclusion, we show that NBLAST can be used to accurately identify neuroblast hemilineages; that Notch$^{ON}$/Notch$^{OFF}$ hemilineages project to motor/sensory neuropil domains, respectively; and most importantly, that hemilineage identity determines neuronal targeting to the motor or sensory neuropil.

## Hemilineage identity determines synapse targeting

Here we use motor and sensory domains (Fig. S1) as landmarks to map synapse localization for different hemilineages. We observed that dorsal hemilineages localize both pre- and post-synaptic sites to the motor neuropil, whereas ventral hemilineages localize both pre- and post-synaptic sites to the sensory neuropil (Figure 4A-D; Fig. S3), but see Discussion for caveats. Consistent with these observations, the vast majority of sensory output is onto ventral hemilineages, and the vast majority of motor neuron input is from dorsal hemilineages (Figure 4E). We conclude that within the seven assayed neuroblast lineages, Notch$^{ON}$ hemilineages target synapses to the motor neuropil, whereas Notch$^{OFF}$ hemilineages target synapses to the sensory neuropil (Figure 4F).

After showing that hemilineages target synapses to restricted domains of dorsal or ventral neuropil, we asked if individual hemilineages tile the neuropil or have overlapping domains. We mapped the pre- and post-synaptic position for six ventral hemilineages and four dorsal hemilineages. Each of the dorsal hemilineages targeted pre-synapses and post-synapses to distinct but overlapping regions of the neuropil (Figure 5A,C). Similarly, each of the ventral hemilineages targeted pre-synapses and post-synapses to distinct but overlapping regions of the neuropil (Figure 5B,D). Clustering neurons by synapse similarity (a measure of similar position in the neuropil volume) confirms that most neurons in a hemilineage cluster their pre- and post-synapses (Figure 5E). We conclude that neuroblast hemilineages contain neurons that project to distinct but overlapping neuropil regions, strongly suggesting that the developmental information needed for neuropil targeting is shared by neurons in a hemilineage (see Discussion).

## Mapping temporal identity in the TEM reconstruction: radial position is a proxy for neuronal birth-order

Most embryonic neuroblasts sequentially express the temporal transcription factors Hb, Kr, Pdm, and Cas with each factor inherited by the GMCs and young neurons born during each window of expression (reviewed in Doe, 2017). Previous work has shown that early-born Hb+ neurons are positioned in a deep layer of the cellular cortex adjacent to the developing neuropil, whereas late-born Cas+ neurons are at the most superficial position, with Kr+ and Pdm+ neurons positioned in between (Figure 6A)(Isshiki et al., 2001; Kambadur et al., 1998). Thus, in the late embryo, radial position can be used as a proxy for temporal identity (Figure 6B). To determine if this relationship is maintained in newly hatched larvae, we could not simply stain for temporal transcription factors, as their expression is not reliably maintained in newly hatched larvae. Instead, we used more stable reporters for Hb (a recombineered Hb:GFP transgene) and Cas (*cas-gal4* line driving *UAS-histone:RFP*). We confirm the radial position of Hb:GFP and Cas>RFP in the late embryonic CNS, and importantly, show that the same deep/superficial layering is maintained in newly hatched larvae (Figure 6C,D). Note that although we are not attempting to map Hb+ neurons to specific lineages (see above), here we use Hb+ neurons in a lineage-independent way to help validate the use of radial position as a proxy for temporal identity.

Additionally, we generated a new Hb-LexA construct in order to identify additional Hb+ neurons, which we then traced in the EM volume (Figure 6E,F, cyan neurons). We also used *cas-gal4* to drive MCFO in order to identify new late-born neurons (Figure 6E,F magenta neurons). In total, we identified 18 neurons in the EM volume with known birthdates (Figure 6E,F; Fig.S4). In order to quantify distance from the neuropil, we measured the neurite length between the cell body and the neuropil entry point. We found that all confirmed Hb+ neurons were located close to the neuropil, whereas late-born neurons were located more distantly (Figure 6G,H). We also confirmed that left/right neuronal homologs had extremely similar cortex neurite lengths (Figure 6I). Thus, we confirm that neuronal cortex neurite length is consistent across two hemisegments, and can be used to approximate the temporal identity of any neuron in the TEM reconstruction.

## Temporal cohorts "tile" hemilineage neuropil domains

In order to determine the role of temporal identity in neuronal targeting and connectivity we first used cortex neurite length to map the birthdates of all neurons in 10 hemilineages (Fig. S5). Unlike the striking dorsal-ventral division observed from mapping hemilineages, the synaptic distributions of individual temporal cohorts appeared far more overlapping (Fig. S5). To quantify this, we compared the synapse similarity of hemilineage-related neurons and temporal-related neurons and found that neurons related by hemilineage were more similar than those related by birthdate (Fig. S6). We conclude that hemilineages, not temporal cohorts, are more important determinants of neuropil targeting.

We next asked whether temporal identity is linked to more precise sub-regional targeting or "tiling" of neuronal projections and synapses within a hemilineage. Here we focus on NB3-3. Previous work has shown that temporal identity in NB3-3 plays a role in segregating neurons into distinct circuits: early-born neurons (A08x/m) are involved in escape behaviors while late-born neurons (A08e1/2/3) are involved in proprioception (Wreden et al., 2017). We confirmed the identity of early- and late-born neurons in this lineage using radial position (Figure 7A), and found that these five previously characterized neurons projected to different regions of the neuropil, and different regions of the central brain (Figure 7B,C). We grouped the remaining neurons in this lineage into temporal cohorts based on their radial position, and found a striking correlation between birth-order and synapse similarity (Figure 7E,F). We conclude that neurons in the proprioceptive or nociceptive circuits target their synapses to different regions of the neuropil.

We next tested whether other lineages contained hemilineage/temporal cohorts that "tile" neuronal projections and synapse localization. Indeed, examination of the NB5-2 ventral hemilineage showed that early- and late-born neurons targeted their projections to "sub-regional" domains of the full hemilineage (Figure 8A,B). Additionally, both pre- and post-synaptic distributions were strongly correlated with birth-order (Figure 8C-H). Similar results were observed for pre-synaptic targeting (but not post-synaptic targeting) in the NB5-2 dorsal hemilineage (Figure 8I-P). Examination of the remaining hemilineages found that only one did not have a significant correlation between birth-order and presynaptic targeting (NB1-2 dorsal) and only one hemilineage did not show a significant relationship between birth-order and post-synaptic targeting (NB5-2 dorsal). Pooling data from all hemilineages reveals a positive correlation between synapse location and temporal identity (Figure 8Q). We conclude that temporal identity subdivides hemilineages into smaller populations of neurons that target both projections and synapses to different sub-domains within the larger hemilineage

targeting domain (Figure 8R). Thus, hemilineage identity provides coarse targeting within neuropil, and temporal identity refines targeting to several smaller sub-domains.

### Temporal cohorts share common connectivity

Temporal cohorts share restricted neuronal projections and synapse targeting within each hemilineage, raising the possibility that temporal cohorts may also share connectivity. To test this idea, we analyzed the connectome of 12 hemilineages as well as the motor and sensory neurons in segment A1 left and right (Figure 9A-C). In total, we analyzed 160 interneurons, 56 motor neurons, and 86 sensory neurons, which corresponded to approximately 25% of all inputs and 14% of all outputs for the 12 hemilineages. We found that hemilineage connectivity is highly structured, with a higher degree of interconnectivity within dorsal and ventral hemilineages (Figure 9A), consistent with the idea that dorsal and ventral hemilineages are functionally distinct (SFig. 1). Next, we generated force directed network graphs, in which neurons with greater shared connectivity are positioned closer together in network space (Figure 9D-H). Examination of the network as a whole revealed an obvious division between both A1L and A1R as well as the sensory and motor portions of the network (Figure 9D). Neurons in a hemilineage showed increased shared connectivity (i.e. they are clustered in the network). Importantly, temporal cohorts within a hemilineage also showed increased shared connectivity, even compared to other temporal cohorts in the same hemilineage (Figure 9E-J). To quantify shared connectivity using a different method, we determined the minimum number of synapses linking neuronal pairs (a) picked at random, (b) picked from a hemilineage, or (c) picked from a temporal cohort within a hemilineage (Figure 9I,J). Neuron pairs that are directly connected have a value of 1 synapse apart; neurons that share a common input or output have a value of 2 synapses apart, with a maximum of seven synapses apart. We found that neurons in a hemilineage had a much lower minimum synapse distance than random, indicating shared connectivity; similarly, neurons in a temporal cohort within a hemilineage also have significantly lower minimum synapse distances, with over 60% of all neurons in the same temporal cohort being separated by two synapses or less (Figure 9I,J). We conclude that temporal cohorts share common connectivity.

## Discussion

Our results show that individual neuroblast lineages have unique but broad axon and dendrite projections to both motor and sensory neuropil; thus, each neuroblast contributes neurons to both

sensory and motor processing circuits. In contrast, the two hemilineages within a neuroblast clone have highly focused projections into either the sensory or motor neuropil, with all Notch$^{ON}$ hemilineages assayed projecting to the motor neuropil and all Notch$^{OFF}$ hemilineages assayed projecting to sensory neuropil. Conversion of Notch$^{OFF}$ to Notch$^{ON}$ identity by lineage-specific misexpression of constitutively active Notch redirects sensory hemilineages into the motor neuropil, showing that Notch signaling regulates dorsal/ventral choice in axon projections; it is unknown whether connectivity is also changed from sensory to motor circuits. Most importantly, we show that temporal cohorts within each hemilineage "tile" their projections and synapses to neuropil subdomains, and each temporal cohort has shared connectivity. Our results strongly support the hypothesis that the developmental mechanisms driving the generation of neural diversity are directly coupled to the mechanisms governing circuit organization

Previous work on *Drosophila* larval neuroblasts show that the pair of hemilineages have different projection patterns and neurotransmitter expression (Harris et al., 2015; Lacin & Truman, 2016a; Truman et al., 2010). We extend these pioneering studies to embryonic neuroblasts, and show that pairs of hemilineages not only have different projection patterns, but also target pre- and post-synapses to distinct regions. Surprisingly, in all lineages where we performed Notch mis-expression experiments, neurons in the Notch$^{ON}$ hemilineage projected to the dorsal neuropil, whereas Notch$^{OFF}$ neurons projected to the ventral neuropil. It is unlikely that all Notch$^{ON}$ hemilineages target the dorsal neuropil, however, as the NB1-1 interneuron pCC is from a Notch$^{ON}$ hemilineage (Skeath & Doe, 1998) yet projects ventrally and receives strong sensory input, and its sibling aCC motor neuron is from the Notch$^{OFF}$ hemilineage (Skeath & Doe, 1998) and projects dendrites in the dorsal motor neuropil. We think it is more likely that the Notch$^{ON}$/Notch$^{OFF}$ provides a switch to allow each hemilineage to respond differently to dorsoventral guidance cues: in some cases the Notch$^{ON}$ hemilineage projects dorsally, and in some cases it projects ventrally. Nevertheless, our finding that neuroblasts invariably produce both sensory and motor hemilineages reveals the striking finding that the sensory and motor processing components of the neuropil are essentially being built in parallel, with one half of every GMC division contributing to either sensory or motor networks. This has not been observed in larval hemilineages, and may be the result of an evolutionary strategy to efficiently build the larval brain as fast as possible.

While we do observe some differences between embryonic and larval hemilineages, the similarities are far more striking. Previous work has shown that larval and embryonic hemilineages have similar morphological features (13), suggesting the possibility that these neurons could be performing analogous functions. Here we show that two components of a proprioceptor circuit, the

Jaam and Saaghi neurons (Heckscher et al., 2015), are derived from two hemilineages of NB5-2 (also called lineage 6 (Lacin & Truman, 2016b)). Activation of either of these hemilineages in adults results in uncoordinated leg movement, consistent with the idea that these hemilineages could be involved in movement control. Similarly, adult activation of the NB3-3 lineage (also called lineage 8 (Lacin & Truman, 2016b)) caused postural effects, again consistent our previous findings that activation of this lineage in larvae cause postural defects (Heckscher et al., 2015). In the future, it will be interesting to further explore the functional and organizational similarities of the embryonic and larval nervous systems.

Our results suggest that all neurons in a hemilineage respond similarly to the global pathfinding cues that exist within the embryonic CNS. Elegant previous work showed that there are gradients of Slit and Netrin along the mediolateral axis (Zlatic, Landgraf, & Bate, 2003), gradients of Semaphorin 1/2a along the dorsoventral axis (Zlatic, Li, Strigini, Grueber, & Bate, 2009), and gradients of Wnt5 along the anteroposterior axis (Yoshikawa, McKinnon, Kokel, & Thomas, 2003). We would predict that the palette of receptors for these patterning cues would be shared by all neurons in a hemilineage, to allow them to target a specific neuropil domain; and different in each of the many hemilineages, to allow them to target different regions of the neuropil. Expression of constitutively-active Notch in single neuroblast lineages will make two Notch$^{ON}$ hemilineages (see Figure 3), or expression of Numb will make two Notch$^{OFF}$ hemilineages. In this way it will be possible to obtain RNAseq data on neurons with a common neuropil targeting program.

Many studies in *Drosophila* and mammals are based on the identification and characterization of clonally-related neurons, looking for common location (Fekete, Perez-Miguelsanz, Ryder, & Cepko, 1994; Mihalas & Hevner, 2018), identity (Mihalas & Hevner, 2018; Wong & Rapaport, 2009), or connectivity (Y. C. Yu, Bultje, Wang, & Shi, 2009). Our results suggest that analyzing neuronal clones may be misleading due to the clone comprising two quite different hemilineages. For example, performing RNAseq on individual neuroblast lineages is unlikely to reveal key regulators of pathfinding or synaptic connectivity, due to the mixture of disparate neurons from two hemilineages.

We used the cortex neurite length of neurons as a proxy for birth-order and shared temporal identity. We feel this is a good approximation (see Figure 5 for validation), but it clearly does not precisely identify neurons born during each of the Hb, Kr, Pdm, Cas temporal transcription factor windows. In the future, using genetic immortalization methods may allow long-term tracking of neurons that only transiently express each of these factors. Nevertheless, we had sufficient resolution to show that neurons within a temporal cohort could target their pre- or post-synapses to distinct

sub-domains of each hemilineage targeting domain. Temporal cohort tiling could arise stochastically due to self-avoidance mechanism (Zipursky & Grueber, 2013), by using spacing cues (Kulkarni, Ertekin, Lee, & Hummel, 2016; Petrovic & Hummel, 2008), or by precise responses to global patterning cues. Previous work in the mushroom body has shown how changes in temporal transcription factor expression can affect neuronal targeting, and in the optic lobe it known that altering temporal identity changes expression of axon pathfinding genes (Kulkarni et al., 2016; Zhu et al., 2006). Our data suggest a similar mechanism could be functioning in the ventral nerve cord. We find that temporal cohorts within a hemilineage share common neuropil targeting, synapse localization, and connectivity. It will be important to test whether altering neuronal temporal identity predictably alters its neuronal targeting and connectivity. We have recently shown that manipulation of temporal identity factors in larval motor neurons can retarget motor neuron axon and dendrite projections to match their new temporal identity rather than their actual time of birth (Seroka & Doe, 2019). For example, mis-expression the early temporal factor Hb can collapse all five sequentially-born U motor neuron axons to the U1 early temporal identity, with axon and dendrite projections matching the endogenous U1 motor neuron (Seroka & Doe, 2019); whether they change connectivity remains to be determined.

Our results strongly suggest that hemilineage identity and temporal identity act combinatorially to allow small pools of 2-6 neurons to target pre- and post-synapses to highly precise regions of the neuropil, thereby restricting synaptic partner choice. Hemilineage information provides coarse targeting, whereas temporal identity refines targeting within the parameters allowed by hemilineage targeting. Thus, the same temporal cue (e.g. Hb) could promote targeting of one pool of neurons in one hemilineage, and another pool of neurons in an adjacent hemilineage. This limits the number of regulatory mechanisms needed to generate precise neuropil targeting for all ~600 neurons in a segment of the CNS.

In this study we demonstrate how developmental information can be mapped into large scale connectomic datasets. We show that lineage information, hemilineage identity, and temporal identity can all be accurately predicted using morphological features (e.g. number of fascicles entering the neuropil for neuroblast clones, and radial position for temporal cohorts). This both greatly accelerates the ability to identify neurons in a large EM volume as well as sets up a framework in which to study development using datasets typically intended for studying connectivity and function. We have used this framework to relate developmental mechanism to neuronal projections, synapse localization, and connectivity; in the future we plan on identifying the developmental origins of neurons within larval locomotor circuits. It is likely that temporally distinct neurons have different

connectivity due to their sub-regionalization of inputs and outputs, however testing how temporal cohorts are organized into circuits remains an interesting open question.

## Methods summary

For detailed methods see Supplemental File 1. Fly stocks are mentioned in the text and described in more detail in the Supplemental Methods. We used standard confocal microscopy, immunocytochemistry and MCFO methods (Clark, McCumsey, Lopez-Darwin, Heckscher, & Doe, 2016; Heckscher et al., 2015; Syed et al., 2017). When adjustments to brightness and contrast were needed, they were applied to the entire image uniformly. Mosaic images to show different focal planes were assembled in Fiji or Photoshop. Neurons were reconstructed in CATMAID as previously described (Carreira-Rosario et al., 2018; Heckscher et al., 2015; Ohyama et al., 2015). Analysis was done using MATLAB. Statistical significance is denoted by asterisks: ****$p<0.0001$; ***$p<0.001$; **$p<0.01$; *$p<0.05$; n.s., not significant.

Acknowledgements

We thank Haluk Lacin for unpublished fly lines. We thank Todd Laverty, Gerry Rubin, and Gerd Technau for fly stocks; Luis Sullivan, Emily Sales and Tim Warren for comments on the manuscript; Avinash Khandelwal and Laura Herren for annotating neurons; Keiko Hirono for generating transgenic constructs; and Keiko Hirono, Rita Yazejian, and Casey Doe for confocal imaging. Stocks obtained from the Bloomington *Drosophila* Stock Center (NIH P40OD018537) were used in this study. Funding was provided by HHMI (CQD, BM, LM, AAZ), NIH HD27056 (CQD), and NIH T32HD007348-24 (BM).

**Figure 1. Individual neuroblast progeny project widely within the neuropil**

(A) Three mechanisms specifying neuronal diversity.

(B) Single neuroblast clones generated with *dpn(FRT.stop)LexA.p65* in newly-hatched larvae. We recovered n>2 clones for each lineage except NB4-1 whose lineage morphology is well characterized in (13); posterior view; scale bar, 20 um.

(C) The corresponding neurons traced in the TEM reconstruction. Dashed lines, neuropil border.

(D) Each clone has one or two fascicles at the site of neuropil entry (blue). Number of neurons per clone show below for A1L and A1R.

(E) Quantification of fascicle number at neuropil entry by light and EM microscopy.

(F,G) Seven neuroblast lineages traced in the TEM reconstruction; posterior view (F), lateral view (G).

**Figure 2. Lineages generate two morphological distinct classes of neurons which project to dorsal and ventral regions of the neuropil.**

(A-F) NBLAST clustering for the indicated neuroblast progeny typically reveals two morphological groups (red/cyan) that project to dorsal or ventral neuropil; these are candidate hemilineages. Cluster cutoffs were set at 3.0 for all lineages.

(G) Superimposition of all dorsal candidate hemilineages (red) and all ventral candidate hemilineages (cyan).

(H) Dendrogram showing NBLAST results clustering neurons based on similar morphology. Clustered neurons were all from hemisegment A1L. Colored bars denote lineage identity.

**Figure 3. Hemilineage identity determines axon projection targeting to dorsal or ventral neuropil**

(A-C) Wild type. Posterior view of three neuroblast lineages expressing GFP using single NB-Gal4 divers (see methods for genetics). Note the projections to dorsal neuropil (red arrowhead) and ventral neuropil (cyan arrowhead). Insets, anterior view of A1-A8 segments. Note: NB7-4 makes neurons (cyan arrowhead) and glia (red arrowhead). Below: summaries. Blue channel is either FasII or phalloidin.

(D-F) Notch$^{intra}$ mis-expression. Posterior view of three neuroblast lineages expressing GFP and constitutively active Notch$^{intra}$. Note loss of the ventral projections and expansion of dorsal projections (red arrowhead). Insets, anterior view of A1-A8 segments. n>3 for all experiments. Below: summaries.

(G,G') Crispr genomic engineering of the *hey* locus to create a Notch reporter. The *hey* locus was engineered to express Hey:T2A:FLP, crossed to *NB7-1-Gal4 UAS-GFP UAS-FRT-stop-FRT-myr:RFP*, and stained for GFP (G, whole lineage) and RFP (G', Notch$^{ON}$ hemilineage) in a newly hatched larva. Dorsal up, midline, dashed; arrows indicate neuronal processes in the dorsal or ventral neuropil.

## Figure 4. Hemilineage identity determines synapse targeting to motor or sensory neuropil domains

(A,B) Each lineage generates a sensory targeting hemilineage and a motor targeting hemilineage, represented here by NB1-2 and NB5-2 (other neuroblasts shown in SFig. 3). Pre- and post-synaptic sites displayed as 2D kernel density. Note the restricted domains, and how both pre- and post-synaptic sites remain in the same functional neuropil domain. Purple and green regions are the contour line denoting the greatest 40% of all pre-motor (purple) or post-sensory (green) synaptic densities.

(C) Pre-synaptic density maps for all hemilineages tile the neuropil.

(D) Post-synaptic maps for all hemilineages tile the neuropil.

(E) Connectivity diagram showing sensory neurons preferentially connect to neurons in ventral hemilineages, while motor neurons preferentially connect to neurons in dorsal hemilineages. Edges represent fractions of outputs for sensory neurons, and fraction of inputs for motor neurons.

(F) Summary showing that lineages generate a sensory and a motor processing hemilineage in a Notch-dependent manner.

**Figure 5. Hemilineages target synapses to distinct but overlapping motor or sensory neuropil domains**

(A,B) Presynaptic distributions of four hemilineages (A) or five ventral hemilineages (B) shown in posterior view. Dots represent single pre-synaptic sites with their size scaled by the number of outputs from a given pre-synaptic site.

(C,D) Postsynaptic distributions of four dorsal hemilineages (C) or five ventral hemilineages (D) shown in posterior view. Dots represent single postsynaptic sites.

(E) Neurons with similar synapse positions tend to be in the same hemilineage. Dendrogram clustering neurons based on combined synapse similarity. Combined synapse similarity was determined by calculating a similarity matrix for pre-synapses and post-synapses separately and then averaging similarity matrices.

**Figure 6. Mapping temporal identity in the TEM reconstruction: radial position is a proxy for neuronal birth-order**

(A) Schematic showing correlation between temporal identity and radial position. Posterior view.

(B-D) Immunostaining to show the radial position of Hb+ and Cas+ neurons at embryonic stage 16 (B), recombineered *Hb:GFP* (C), or *cas-gal4 UAS-RFP* (D) newly-hatched larvae (L0).

(E) Single cell clones of either Hb or late-born neurons. Hb neurons were labeled using *hb-T2A-LexA* (see methods). Late-born neurons were labeled using *cas-Gal4; MCFO*. We use the term late-born as we can not rule Gal4 perdurance into neuroblast progeny born after Cas expression ends.

(F) Neurons identified in the TEM reconstruction that match those shown in E.

(G) All Hb+ and late-born neurons identified in the TEM reconstruction.

(H) Distribution of cortex neurite lengths for known Hb+ and late-born neurons shows that late-born neurons are further from the neuropil than Hb+ neurons.

(I) Left/right homologous pairs of neurons with verified birthdates show highly stereotyped cortex neurite lengths across two hemisegments. Solid red line represents a linear fit, with dotted red lines representing 95% CIs. $R^2 = .87$, p = 1.4e-8.

## Figure 7. Temporal cohorts in the NB3-3 lineage have distinct synapse targeting domains.

(A) Plot of mean cortex neurite lengths across bilateral pairs of NB3-3 neurons. Colors are assigned by dividing the lineage into two temporal cohorts. Mean cortex neurite length for the lineage was 18μm, with four neurons having less than the mean (cyan cells). A08m has a mean length greater than 18μm, but has been shown previously to be early-born. Asterisks denote neurons with confirmed birthdates matching their color assignment. 6/7 previously birthdated neurons had cortex neurite lengths consistent with their birthdate.

(B-D) Full 11 cell clone of NB3-3 in hemisegments A1L and A1R. Colors were assigned by dividing the lineage into two temporal cohorts on the basis of cortex neurite length with the exception of A08m, which has been shown previously to be born early.

(E) Presynaptic similarity clustering of NB3-3 neurons again shows a clustering of early and late-born neurons with the exception of A08m. Presynaptic distributions of these two populations of cells show both a dorsoventral split in the VNC as well as differential target regions for the projection neurons in the brain.

(F) Postsynaptic similarity clustering of NB3-3 neurons shows two groups divided by temporal cohort. Postsynaptic distributions of these two populations of cells show a dorsoventral division consistent with their differential input from chordotonal neurons (early-born NB3-3 neurons) or proprioceptive sensory inputs (late-born NB3-3 neurons).

## Figure 8. Temporal cohorts in multiple neuroblast lineages have distinct synapse targeting domains

(A-H) NB5-2 ventral hemilineage. (A) NB5-2 ventral hemilineage (cyan, early-born; magenta, late-born).

(B) Cortex neurite lengths of neurons in the hemilineage. (C-D) Presynaptic distributions of neurons in NB5-2V colored by birth-order. Little separation in the dorsoventral or mediolateral axes in the VNC was observed, but early-born neurons project axons to the brain while late-born neurons do not. (E-F) Presynaptic (E) and postsynaptic (F) similarity clustering of NB5-2V neurons shows neurons of a similar birth-order have similar synaptic positions. (G-H) Presynaptic (G) and postsynaptic (H) similarity plotted against birth order similarity. Birth-order similarity was defined as the pairwise Euclidean distance between cell bodies divided by the greatest pairwise distance between two cell bodies in the same hemilineage. Solid lines represent linear fits while dotted lines represent 95% CIs.

(I-L) NB5-2 dorsal hemilineage. (I) NB5-2 dorsal hemilineage (cyan, early-born; magenta, late-born). (J) Cortex neurite lengths of neurons in NB5-2D. (K-L) Presynaptic distributions of neurons in NB5-2D colored by birth-order. Little separation in A/P axis in the VNC was observed, early-born and late-born neurons segregate in the D/V and M/L axes. (M-N) Presynaptic (M) and postsynaptic (N) similarity clustering of NB5-2D neurons shows neurons of a similar birth-order have similar synaptic positions. (O-P) Presynaptic (O) and postsynaptic (P) similarity plotted against birth order similarity. Birth-order similarity was defined as the pairwise Euclidean distance between cell bodies divided by the greatest pairwise distance between two cell bodies in the same hemilineage. Solid lines represent linear fits while dotted lines represent 95% confidence interval. For NB5-2D, a significant relationship between postsynaptic targeting and birth-order was not observed.

(Q) Presynaptic (blue) and postsynaptic (red) similarity plotted against birth order similarity across nine hemilineages. NB1-2V was excluded as it only contained two neurons. When examined separately, only one hemilineage (NB1-2D) did not show a significant relationship between presynaptic similarity and birth-order similarity, and only one hemilineage (NB5-2D) did not show a significant relationship between postsynaptic similarity and birth-order similarity. Solid lines represent linear fits, and dashed lines represent 95% confidence interval.

(R) Summary showing hemilineage targeting setting up broad neuropil targeting and temporal information sub-regionalizing hemilineage targeting.

**Figure 9. Temporal cohorts within hemilineages have shared connectivity**

(A) Heatmap of connectivity between hemilineages and A1 sensory and motor neurons shows structure in hemilineage interconnectivity. Entries indicate the degree of connectivity (not the number of synapses) between each hemilineage. Edges with a strength of less of less than 1% of the input for a given neuron were discarded.

(B,C) Fraction of inputs/outputs for each hemilineage. Adjacent bars of the same color represent the homologous hemilineage in the left and right hemisegments.

(D) Force directed network graph of all neurons in the dataset highlighting the sensory and motor subdivision. Neurons with similar connectivity appear closer in network space. Purple edges represent all incoming connections to motor neurons, while green edges represent all outgoing connections from sensory neurons.

(E-H) Force directed network graphs of all neurons highlighting specific lineages (E,F) or temporal cohorts (G,H). Edge colors represent outputs from given nodes.

(I) Cumulative distribution of the number of synapses between temporal cohorts of hemilineage related neurons, hemilineage related neurons, or random neurons. Neurons that belonged to a temporal cohort with only one neuron were not analyzed (16 neurons). Random neurons were selected from the same hemisegment.

(J) Quantification of the number of directly connected pairs of neurons, neurons separated by 2 synapses, and neurons separated by more than two synapses. Black circles represent pairs of neurons connected by 1 synapse (top) or two synapses (bottom).

(K) Summary.

## Fig. S1. The dorsal neuropil contains motor neuron post-synapses and premotor neurons pre- and post-synapses, whereas the ventral neuropil contains sensory neuron pre-synapses and post-sensory neuron pre- and post-synapses

(A) Motor neuron post-synapses (purple) and sensory neuron pre-synapses (green) showing dorsoventral segregation. Plots are 1D kernel density estimates for dorsoventral or mediolateral axes.

Purple dots represent a single post-synaptic site. Green dots represent a single pre-synaptic site scaled by the number of outputs from that presynaptic site.

(B) Premotor neuron post-synaptic sites (>3 synapses onto a motor neuron in segment A1), or post-sensory neuron pre-synaptic sites (pre >3 synapses with an A1 sensory neuron) show that connecting neurons are still restricted to dorsal or ventral neuropil domains.

(C) 2D kernel density estimates of all pre/post synaptic sites for pre-motor and post-sensory neurons outlines the regions of sensory (green) and motor (magenta) processing in the VNC.

## Fig. S2. Ventral hemilineages have projection neurons

The indicated neuroblast lineages traced in catmaid showing the dorsal (red) and ventral (cyan) predicted hemilineages. Note that the ventral (cyan) hemilineages contains significantly longer axons (ascending and descending projection neurons) compared to dorsal (red) hemilineage neurons consistent with what has been observed in larva (Truman, 2010). P = .0034, via 2-sided Wilcoxon rank sum test.

## Fig. S3. Hemilineage identity determines synapse targeting to motor or sensory neuropil domains

2D kernel density estimates for all hemilineages not shown in Figure 4. Density maps are of post-synaptic and pre-synaptic densities for four neuroblast lineages. Note the restricted domains, and how both pre- and post-synaptic sites remain in the same functional neuropil domain. Green and magenta regions represent density estimates for the pre-motor and post-sensory neurons for segment A1. Posterior view, dorsal up, midline dashed line.

## Fig. S4. Known Hb+ or Cas+ neurons identified in the TEM reconstruction

Cyan: neurons known to be Hb+. Magenta, neurons known to be Cas+. Posterior view, midline, dashed line; inset, dorsal view, anterior up.

**Fig. S5. Neurons with a common temporal identity project widely within the neuropil**

(A-F) Skeletons of 6 lineages colored by inferred birth order (cyan, early-born) to (magenta, late-born). Posterior view, dorsal up.

(G) Quantification of cortex neurite length in each neuroblast lineage.

(H) Overlay of all six lineages; note the intermingling of early- and late-born neuronal projections.

(I,J) Pre- or post-synapse distributions of neurons position labeled by neuronal temporal identity; note the intermingling of synapses from early- and late-born neurons.

**Fig. S6. Neurons in a hemilineage have more similar synaptic targeting than neurons in a temporal cohort**

(A) Combined synapse similarity clustering similar to Figure 5E. Neuron names are colored either by hemilineage or by temporal cohort. Note the lack of coherent clusters of temporally-related neurons from different hemilineages.

(B) Mean combined synapse similarity of neurons from hemilineages or temporal cohorts. Mean similarity was calculated by randomly selecting pairs of neurons in the same hemilineage or the same temporal cohort 100 times. $p<.0001$ via 2-sided Wilcoxon rank sum test.

## Supplemental Methods

We used the following fly stocks: R15A05$^{AD}$R28H10$^{DBD}$ (NB1-2), R70D06$^{AD}$R28H10$^{DBD}$ (NB2-1), Ac$^{AD}$ Gsb$^{DBD}$, 25A05$^{kz}$ (NB7-1), *R19B03$^{AD}$ R18F07$^{DBD}$ (NB7-4)*, *castor-gal4* (Technau lab), *hs-Flp.G5.PEST.Opt*(FBti0161061), *13xlexAop2(FRT.stop)myr:smGfP-Flag*(FBti0169275), *13xlexAop2(FRT.stop)myr:smGfP-V5(*FBti0169272), *13xlexAop2(FRT.stop)myr:smGfP-*

*HA*(FBti0169269), and *hb-T2A-LexA.GADfl*. Transgenic lines were made by BestGene (Chino Hills, CA) or Genetivision (Houston, TX).

## Immunostaining and imaging

Standard confocal microscopy, immunocytochemistry and MCFO methods were performed as previously described for larvae (Clark et al., 2016; Heckscher et al., 2014; Syed et al., 2017) or adults (Nern, Pfeiffer, & Rubin, 2015; Pfeiffer et al., 2008). Primary antibodies used recognize: GFP or Venus (rabbit, 1:500, ThermoFisher, Waltham, MA; chicken 1:1000, Abcam13970, Eugene, OR), GFP or Citrine (Camelid sdAB direct labeled with AbberiorStar635P, 1:1000, NanoTab Biotech., Gottingen, Germany), GABA (rabbit, 1:1000, Sigma, St. Louis, MO), mCherry (rabbit, 1:1000, Novus, Littleton, CO), Corazonin (rabbit, 1:2000, J. Veenstra, Univ Bordeaux), FasII (mouse, 1:100, Developmental Studies Hybridoma Bank, Iowa City, IA), HA (mouse, 1:200, Cell signaling, Danvers, MA), or V5 (rabbit, 1:400, Rockland, Atlanta, GA), Flag (rabbit, 1:200, Rockland, Atlanta, GA). Secondary antibodies were from Jackson Immunoresearch (West Grove, PA) and used according to manufacturer's instructions. Confocal image stacks were acquired on Zeiss 700, 710, or 800 microscopes. Images were processed in Fiji (https://imagej.net/Fiji), Adobe Photoshop (Adobe, San Jose, CA), and Adobe Illustrator (Adobe, San Jose, CA). When adjustments to brightness and contrast were needed, they were applied to the entire image uniformly. Mosaic images to show different focal planes were assembled in Fiji or Photoshop.

## Clone generation and lineage identification

The clones were generated with the following flies: hs-Flp.G5.PEST.Opt(FBti0161061), 13xlexAop2(FRT.stop)myr:smGfP-Flag (FBti0169275), 13xlexAop2(FRT.stop)myr:smGfP-V5(FBti0169272), 13xlexAop2(FRT.stop)myr:smGfP-HA(FBti0169269), and hb-T2A-LexA.GADfl (see below). The embryos were collected for 7 hours in 25 ˚C, submerged in 32 ˚C water bath for 15-min heat shock, and then incubated at 25 ˚C until larvae hatched. The CNS of newly hatched larvae was dissected, stained and mounted as previously described (Clark et al., 2016; Heckscher et al., 2014; Syed et al., 2017). Antibodies used were: Dylight™405-conjugated rabbit anti-HA (Rockland), Dylight™488-conjugated rabbit anti-Flag (Rockland), and Dylight™549-conjugated rabbit anti-V5 (Rockland), and the neuropil was stained with Alexa Fluor™ 647 Phalloidin (ThermoFisher) by

following manufacturer's protocol. The images were collected with Zeiss710 and processed with Imaris.

hb-T2A-LexA.GADfl was generated by in-frame fusion of T2A-LexA.GADfl to the C-terminus of the hb open reading frame with CRISPR-Cas9 gene editing. The ds-DNA donor vector for homology-directed repair was composed of left homologous arm (1098bp), T2A(Diao et al., 2016), LexA.GADfl (Pfeiffer et al., 2010), and the right homologous arm (799bp); the fragments were amplified with PCR and then assembled in pHD-DsRed (addgene #51434) with NEBuilder (New England BioLabs). The gRNAs were generated from the vector pCFD4-U6:1_U6:3tandemgRNAs (Port, Chen, Lee, & Bullock, 2014) containing target sequence GAAACTTAGGTCTAGAATTAG and GGACGCCGTCGAACTGGCAC. The ds-DNA donor vectors and gRNA vectors were co-injected into yw;nos-Cas9 (Kondo & Ueda, 2013) flies by BestGene. The selection marker 3xP3-DsRed was then removed in transgenic flies by hs-Cre (FBti0012692).

Lineages were identified in the EM volume by finding neurons with morphologies that matched the clonal morphology, and then identifying their neuropil entry point. We then examined every neuron which entered the neuropil in the same fascicle. In most cases, every neuron in the fascicle had a morphology that matched the clonal morphology. In a small number of cases, the fascicles diverged slightly before the neuropil entry point. We verified the number of neurons by looking at fasciculating cell populations from at least two hemisegments (A1L and A1R). In some cases, we were able to identify a stereotyped number of cells across as many as four hemisegments, suggesting that fasciculation is stereotyped and reliable.

## Morphological analysis of lineages

Morphological analysis was done using NBLAST and the NAT package (Costa et al., 2016), and analysis and figure generation was done using R. Neurons were preprocessed by pruning the most distal twigs (Strahler order 4), converting neurons to dot-props, and running an all-by-all NBLAST. For individual lineages, clusters were set using a cutoff of 3.0. In the case of NB2-1, where nearly every neuron shares a very similar morphology, we first confirmed the presence of a hemilineage using anti-Hey staining. After confirmation of a hemilineage, we next removed A02o and A02l since we could not find any clones that contained either an anterior projection (A02o) or a second contralateral projection (A02l). We reasoned that the hemilineages would represent the next largest morphological division.

## Synaptic distributions and density analysis

Synapse distribution plots and density contours were generated using MATLAB. Neuron synaptic and skeleton information was imported to MATLAB using pymaid (Schlegel et al., 2016). Cross sectional synapse distribution plots were made by taking all synapse positions between the T3 and A2 segments as positional information becomes lost due to changes in brain shape beyond these bounds. Synapse distribution plots are 1D kernel density estimates. Sensory and motor density maps were made by taking the synapse positions of all sensory neurons entering the A1 nerve, and all motor neurons exiting the A1 nerve as well as all neurons with at least 3 synapses connected to one of these neurons. For sensory and motor maps as well as individual hemilineages, density plots are 2D kernel density estimates of all synapse positions across the neuropil. A cutoff of 60% was used to set the outermost contour. For lineage maps (Figure 4F/G) , we used 80% as a cutoff. Polyadic synapses were counted as many times as they have targets. For synapse distribution plots, polyadic synapses are scaled by their number of targets.

## Temporal Cohort assignment

Cortex neurite length was calculated by converting the skeletonized neuronal arbor into a directed graph away from the soma, and performing a depth-first-search of all vertices. The neuropil borders were defined by a previously created neuropil volume object (10). The neuropil entry point was defined as the first vertex within the neuropil volume object. Cortex neurite length was then the path length between the soma and the neuropil entry point. Neurons were binned into 5 groups with 6μm edges to define temporal cohorts.

## Synapse similarity clustering

Synapse similarity was calculated as described previously (Schlegel et al., 2016):

$$f(is, jk) = e^{\frac{-d_{sk}^2}{2\sigma^2}} e^{\frac{|n_{is} - n_{jk}|}{n_{is} + n_{jk}}}$$

where $f(is,jk)$ is the mean synapse similarity between all synapses of neuron $i$ and neuron $j$. $d_{sk}$ is the Euclidean distance between synapses $s$ and $k$ such that synapse $k$ is the closest synapse of neuron $j$ to synapse s of neuron $i$. σ is a bandwidth term that determines what is considered close. $n_{is}$ and $n_{jk}$ are the fraction of synapses for neuron $i$ and neuron $j$ that are within ω of synapse $s$ and synapse $k$ respectively. We used parameters ω= σ = 4000nm. Clusters for dendrograms were created based on the mean distance between elements of each cluster using the average linkage clustering method.

## Electron microscopy and CATMAID

We reconstructed neurons in CATMAID as previously described (Carreira-Rosario et al., 2018; Heckscher et al., 2015; Ohyama et al., 2015).

## Figures

Figures were generated using Matlab, R, CATMAID, and FIJI, and edited in either Adobe Illustrator or Photoshop.

## Statistical analysis

Statistical significance is denoted by asterisks: ****p<0.0001; ***p<0.001; **p<0.01; *p<0.05; n.s., not significant. All statistical analysis was done in MATLAB. When comparing two groups of quantitative data, an unpaired t-test was performed if data was normally distributed (determined using a one-sample Kolmogorov-Smirnov test) and Wilcoxon rank sum test if the data was not normally distributed. Linear models were generated in MATLAB using lmfit.

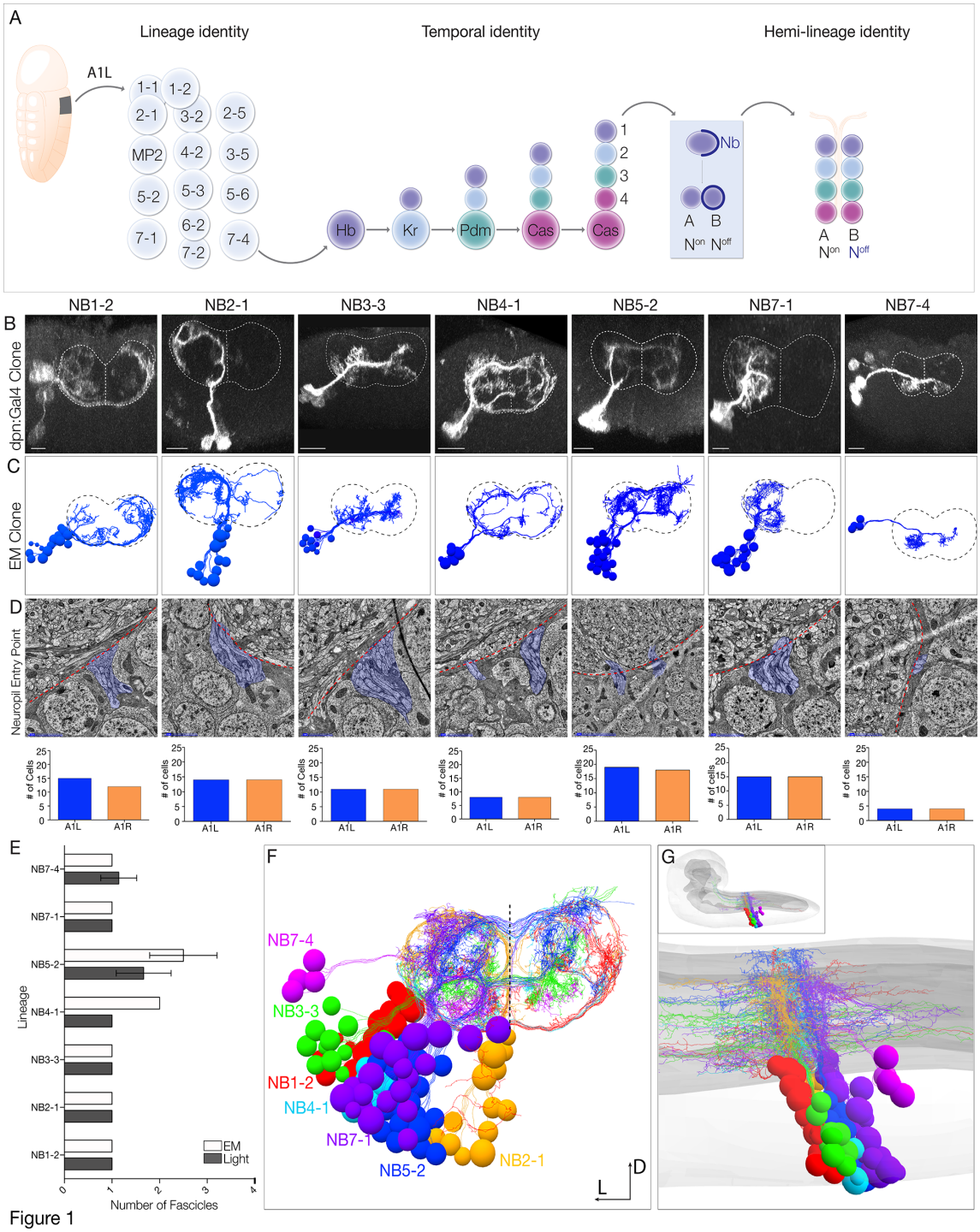


Figure 1

***Figure 1***

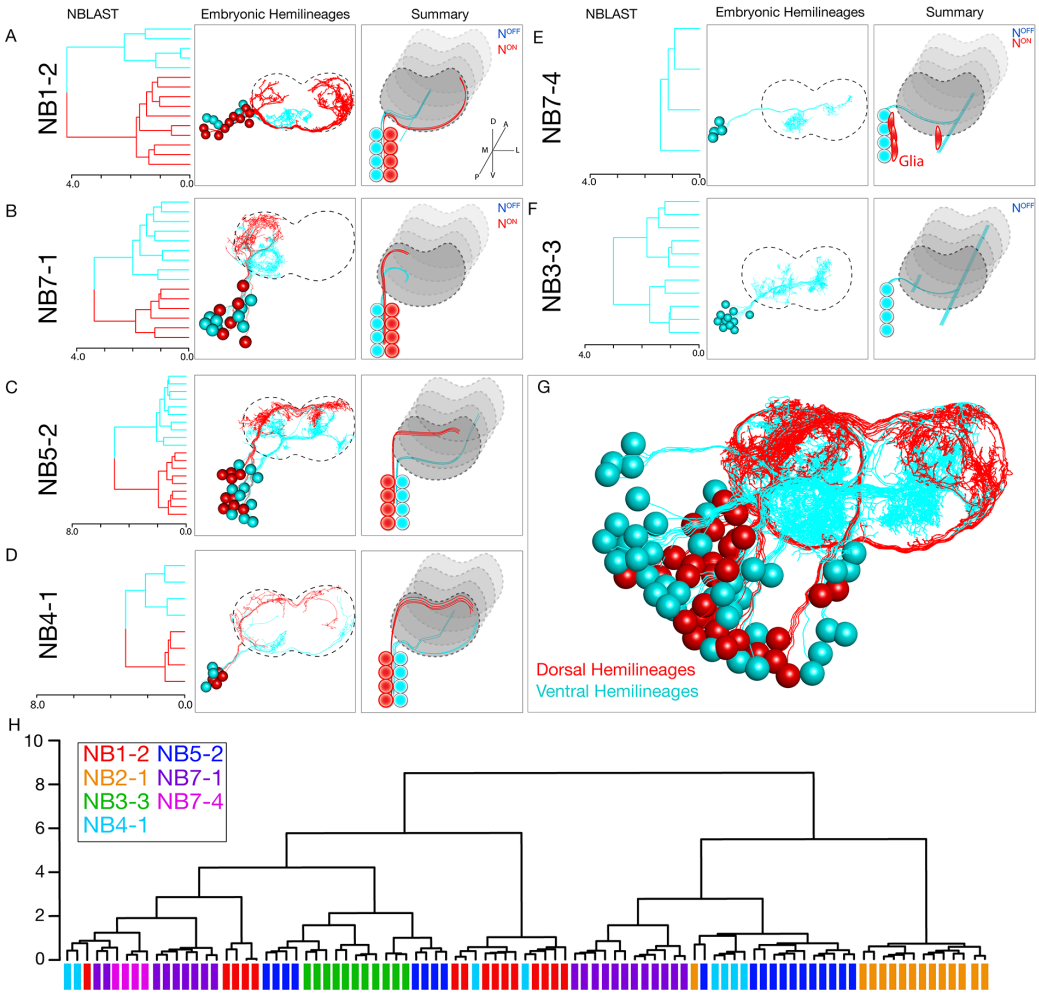


Figure 2

*Figure 2*

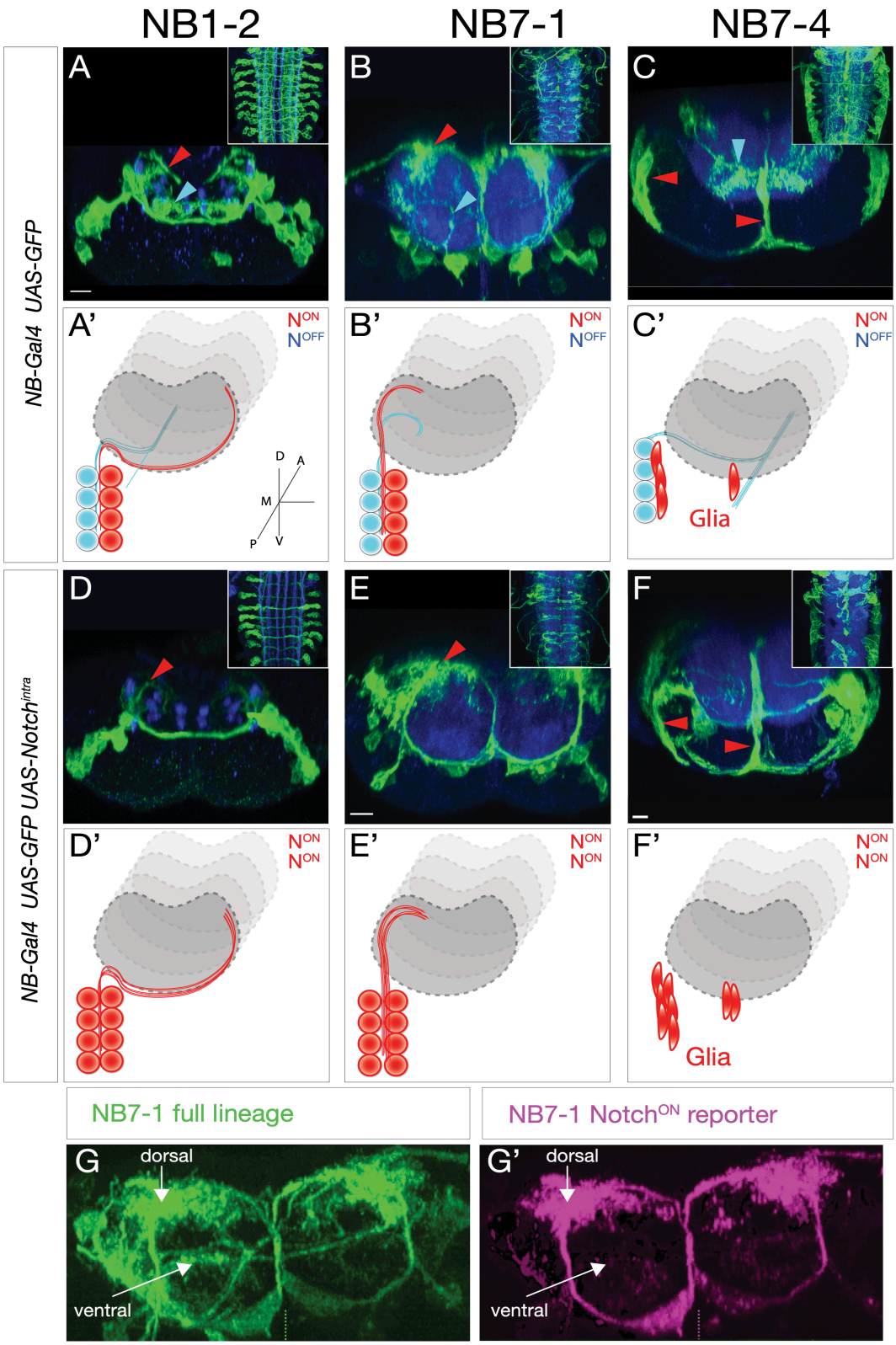


Figure 3

*Figure 3*

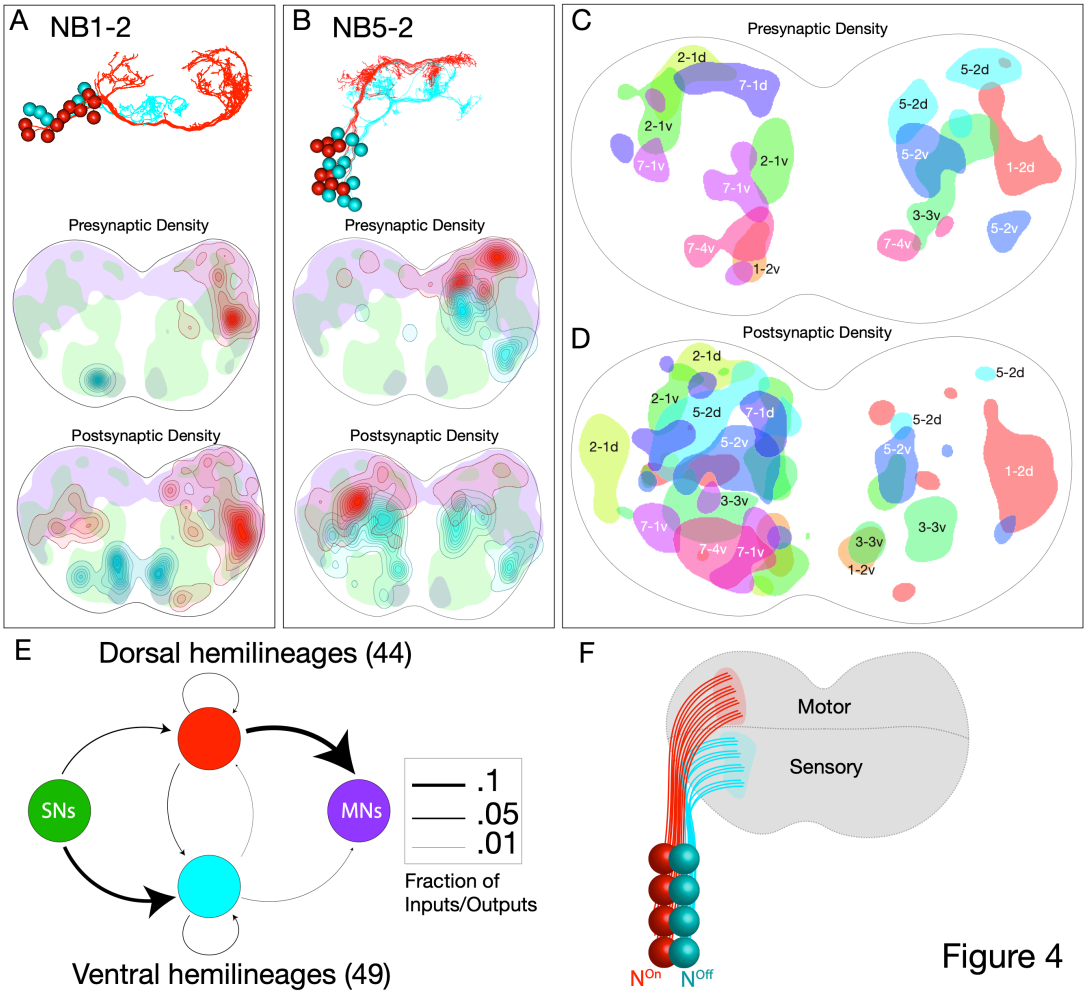


Figure 4

*Figure 4*

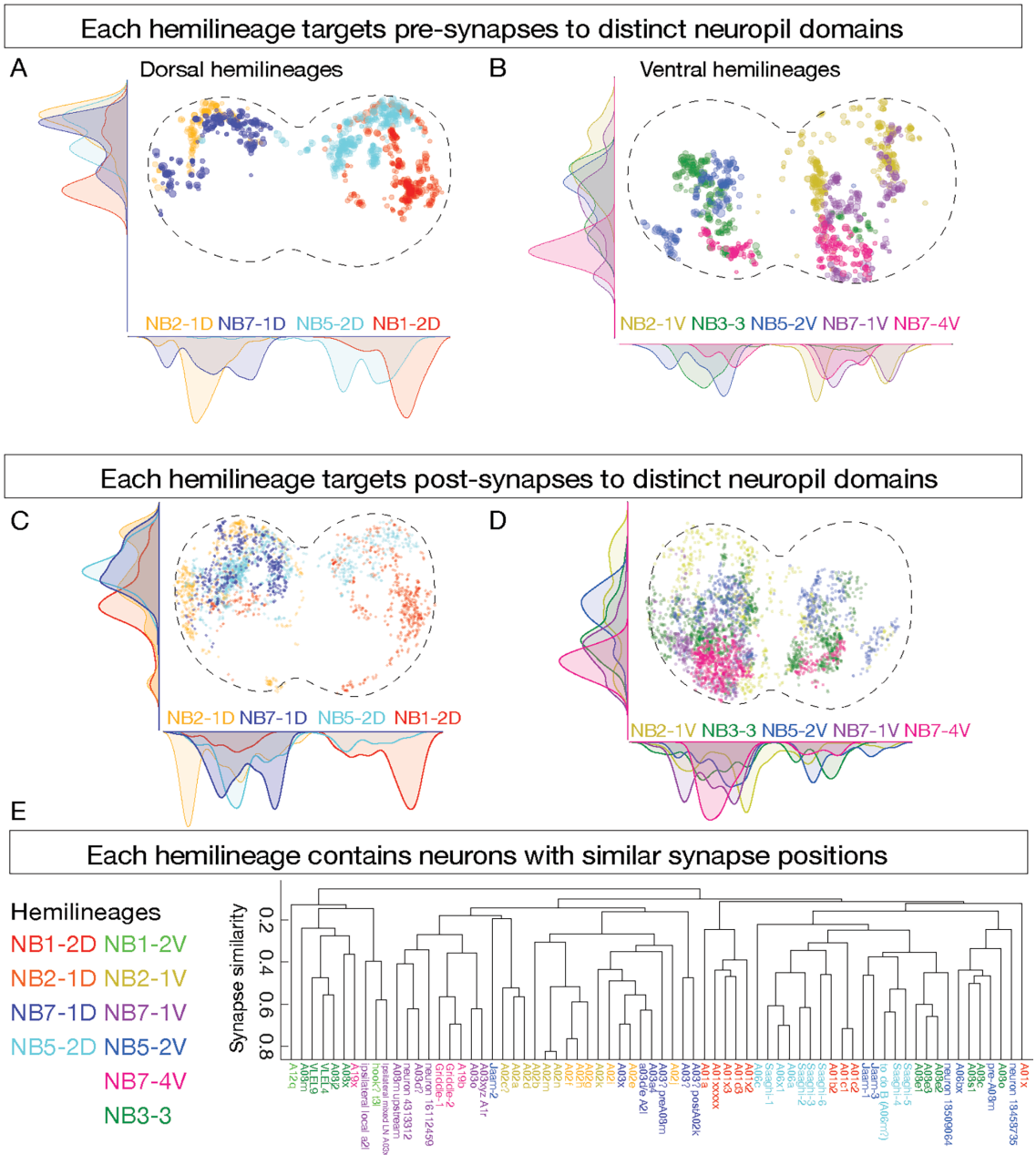


Figure 5

*Figure 5*

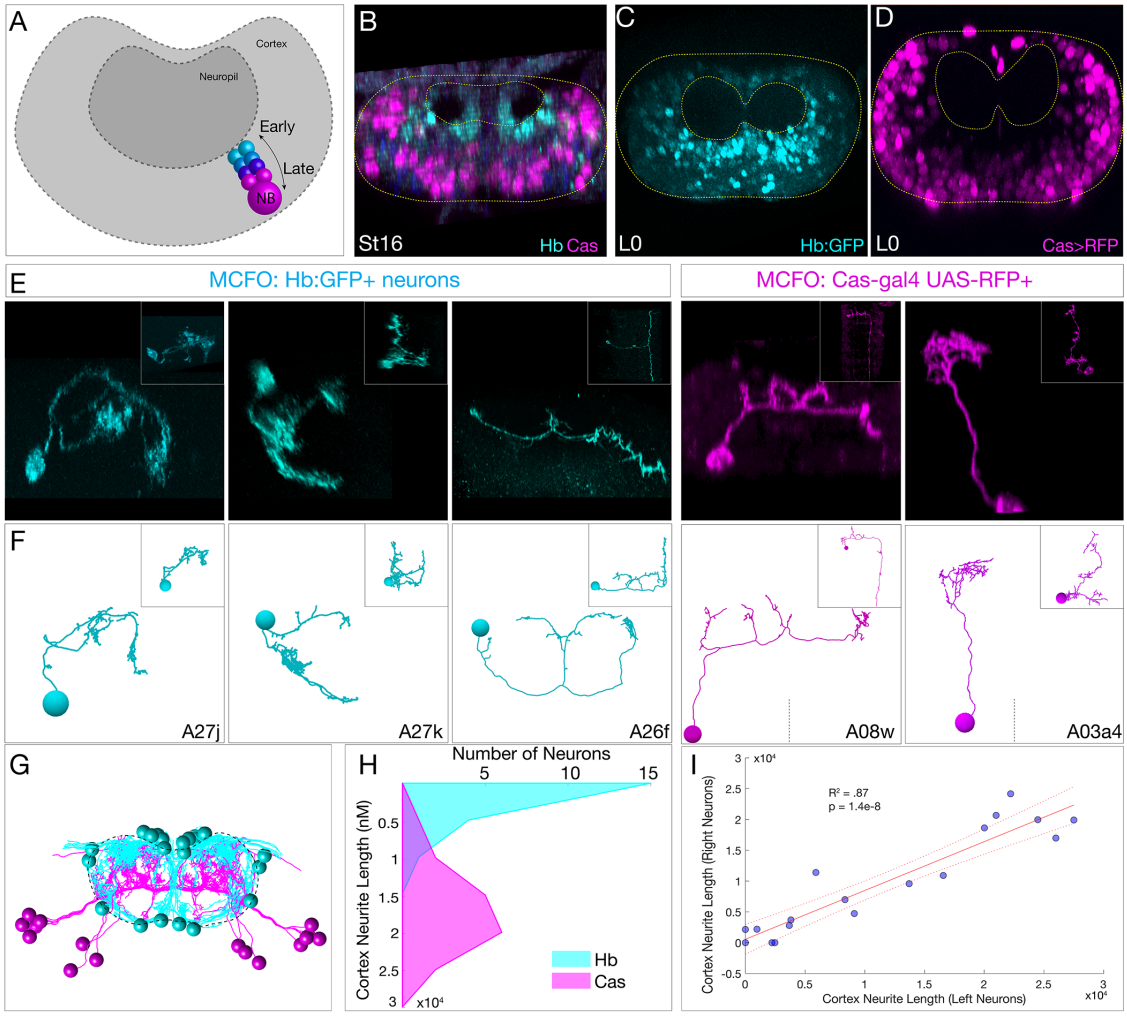


Figure 6

*Figure 6*

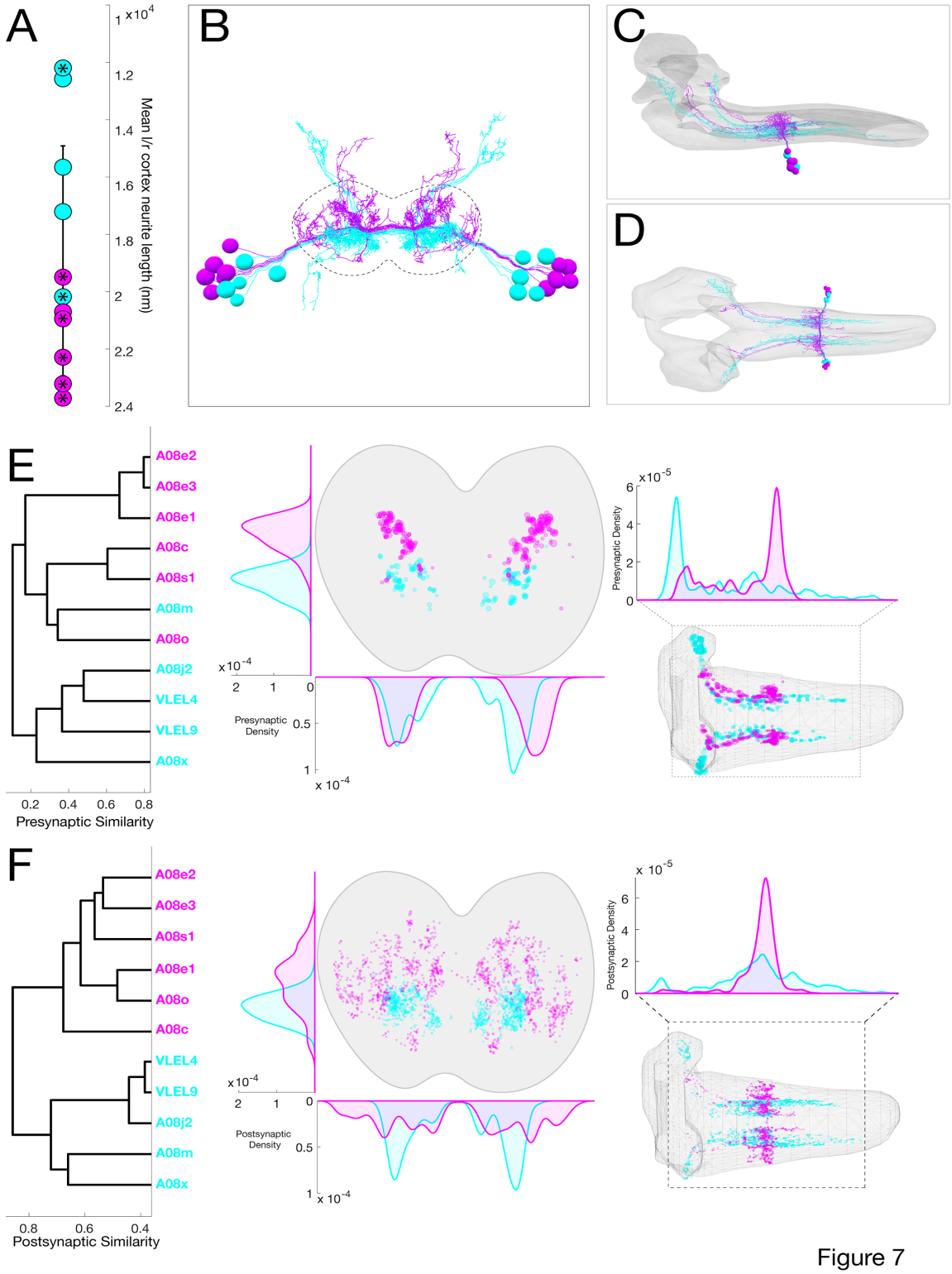


Figure 7

*Figure 7*

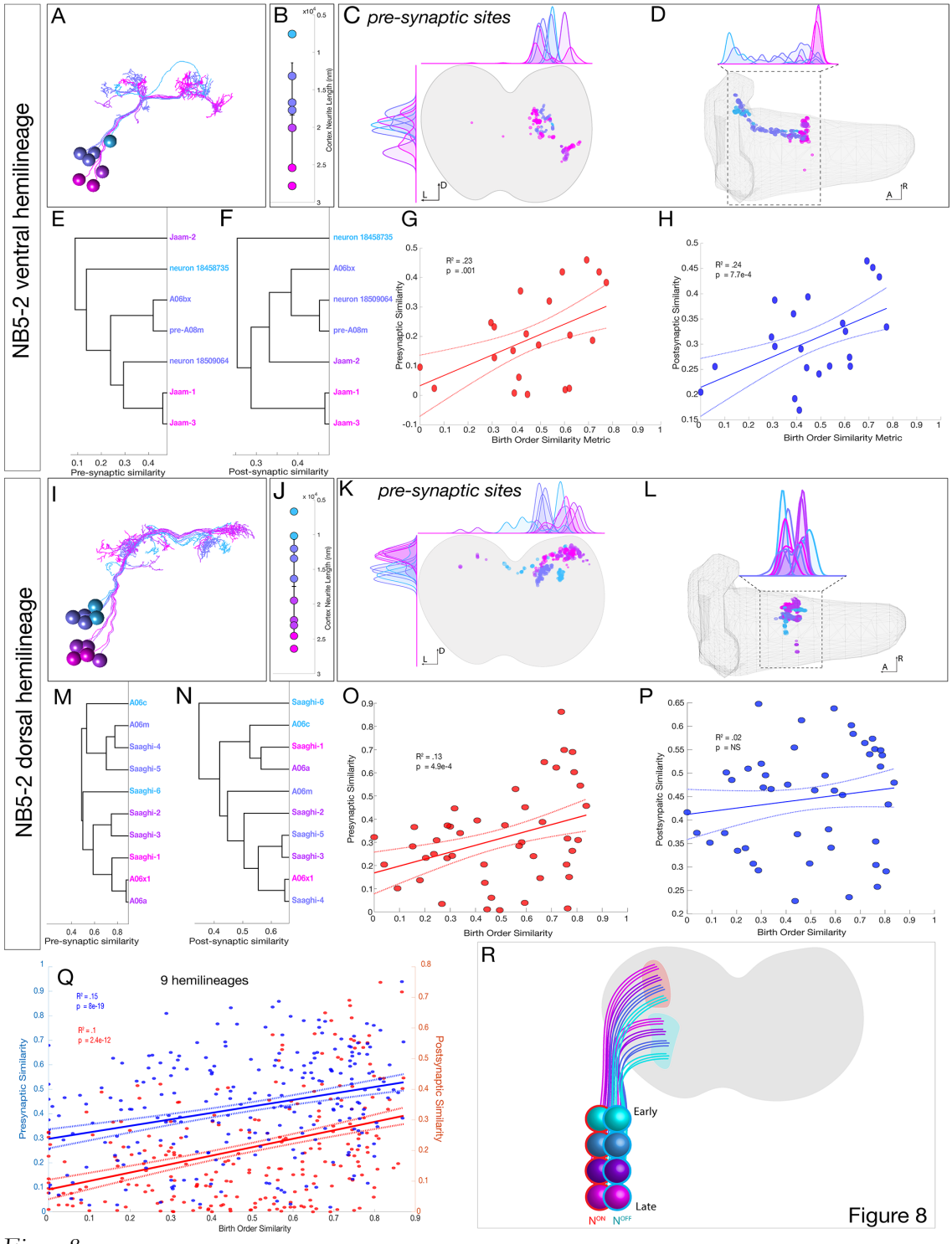
NB5-2 ventral hemilineage
NB5-2 dorsal hemilineage
pre-synaptic sites
Jaam-2
neuron 18458735
A06bx
pre-A08m
neuron 18509064
Jaam-1
Jaam-3
Pre-synaptic similarity
Post-synaptic similarity
Presynaptic Similarity
Postsynaptic Similarity
Birth Order Similarity Metric
R² = .23
p = .001
R² = .24
p = 7.7e-4
A06c
A06m
Saaghi-4
Saaghi-5
Saaghi-6
Saaghi-2
Saaghi-3
Saaghi-1
A06x1
A06a
R² = .13
p = 4.9e-4
R² = .02
p = NS
Birth Order Similarity
9 hemilineages
R² = .15
p = 8e-19
R² = .1
p = 2.4e-12
Early
Late
Figure 8

*Figure 8*

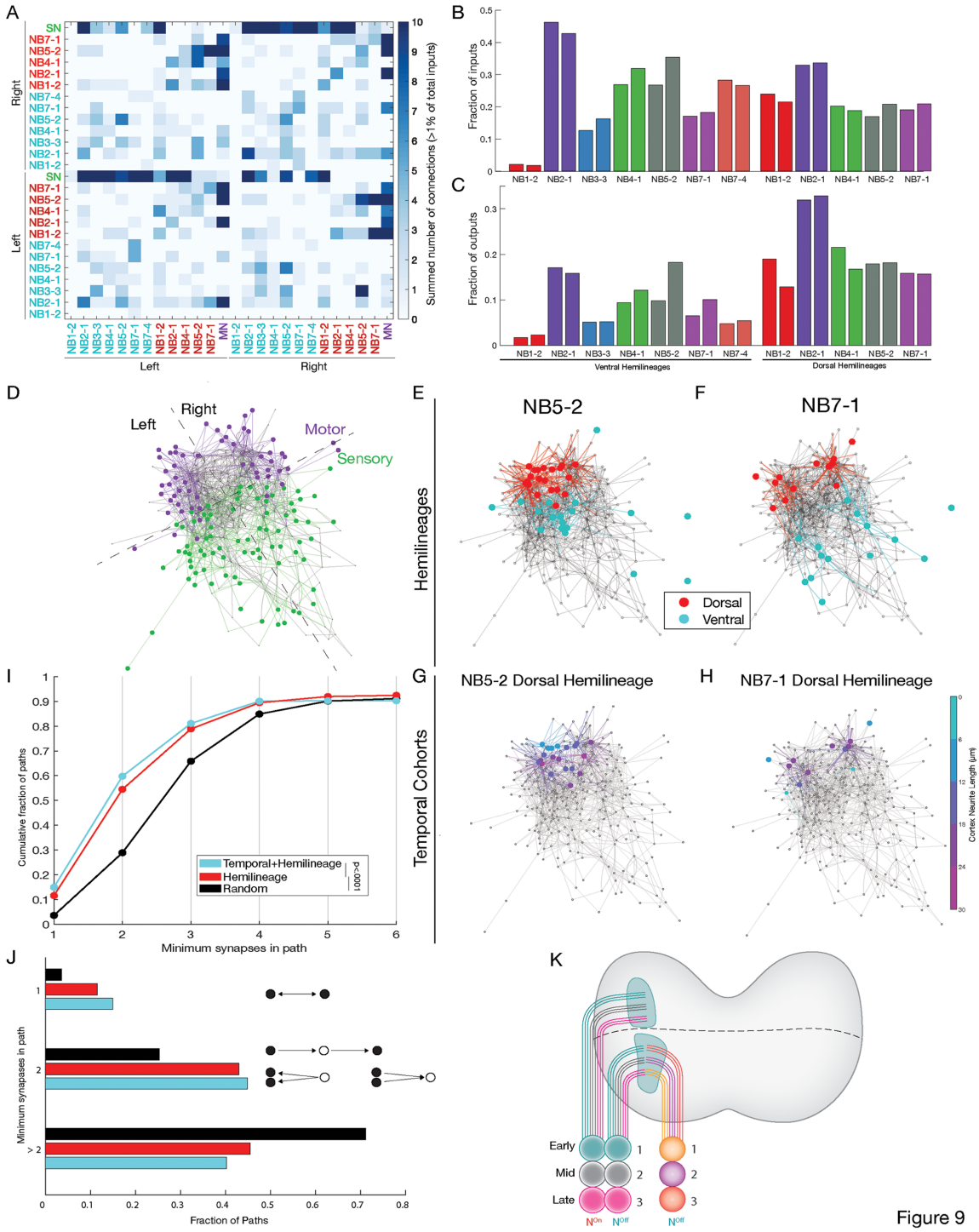


Figure 9

*Figure 9*

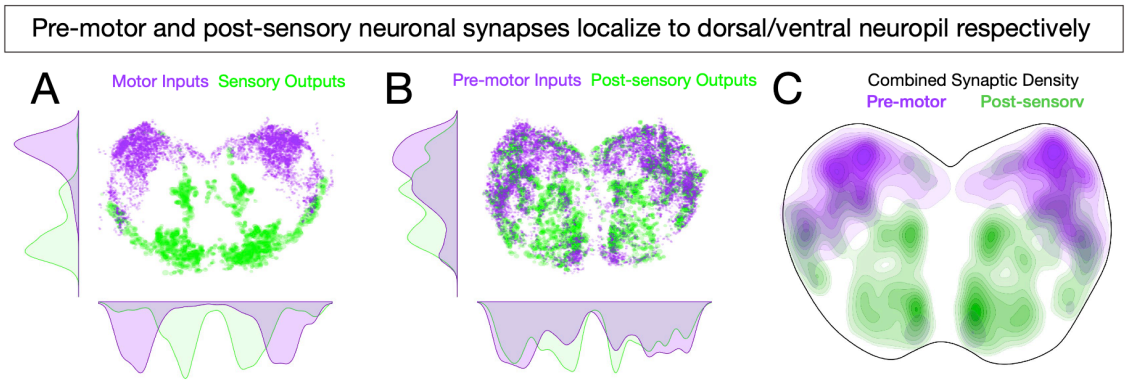


Supplemental Figure 1

*Supplemental Figure 1*

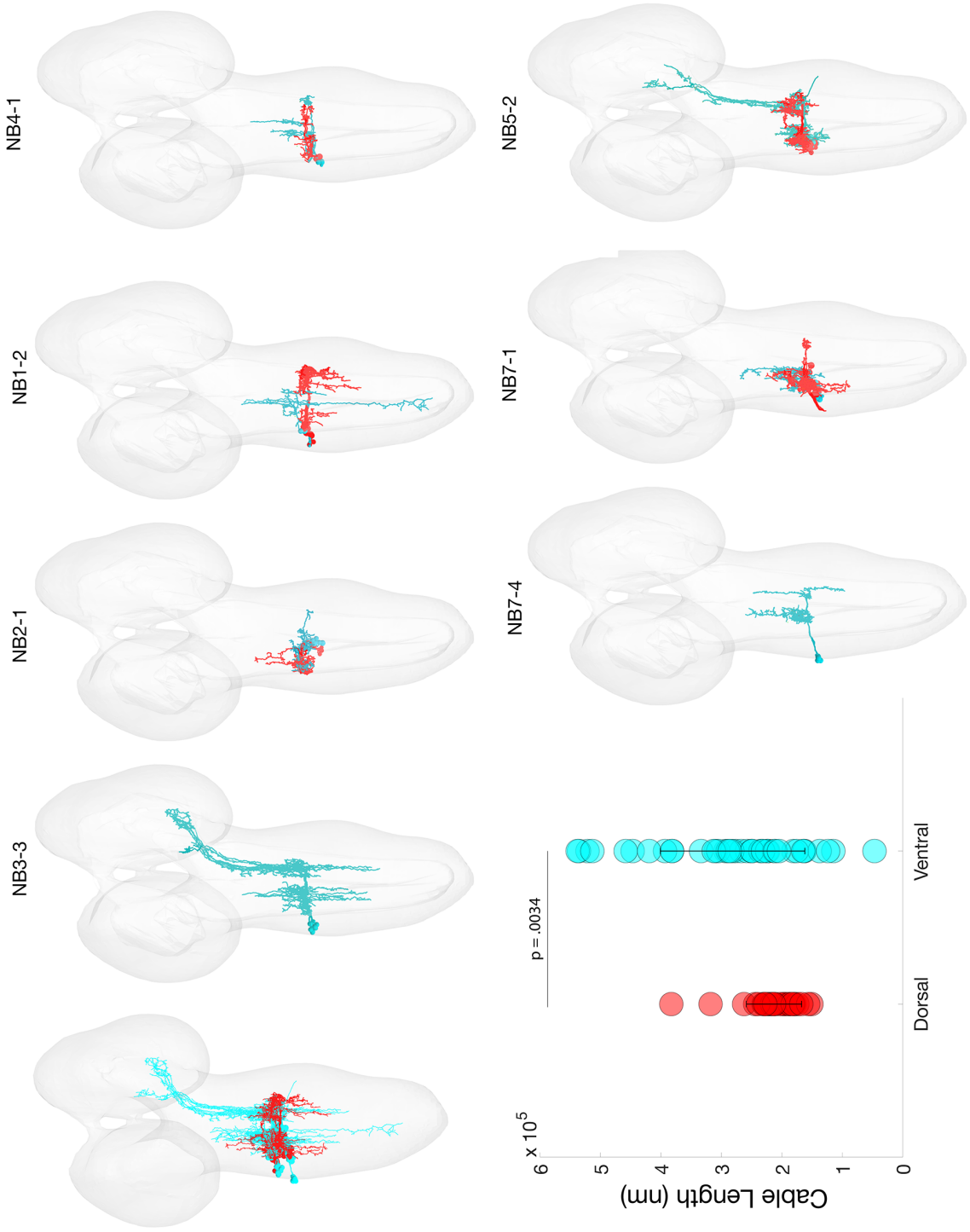


Supplemental Figure 2

*Supplemental Figure 2*

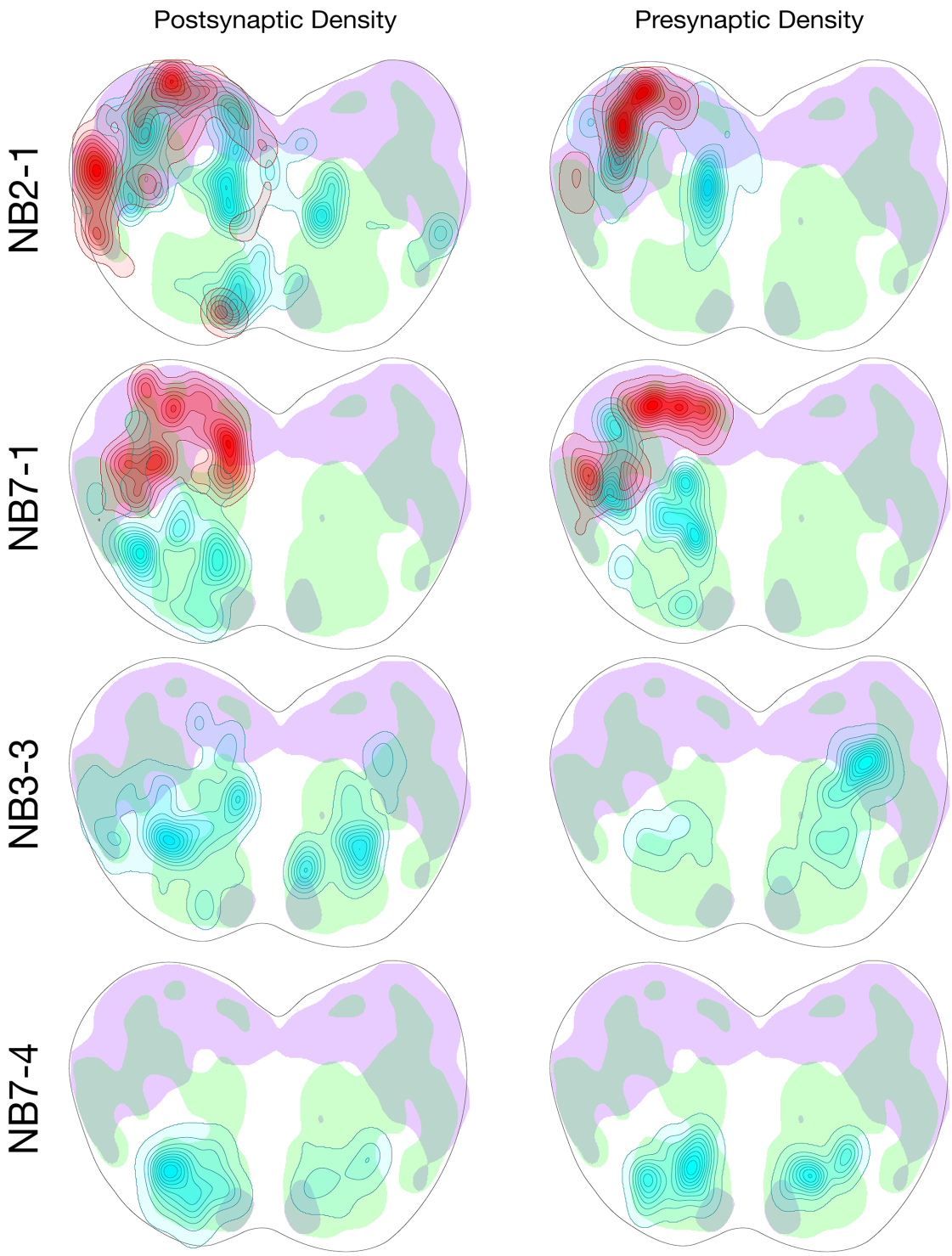


Supplemental Figure 3

*Supplemental Figure 3*

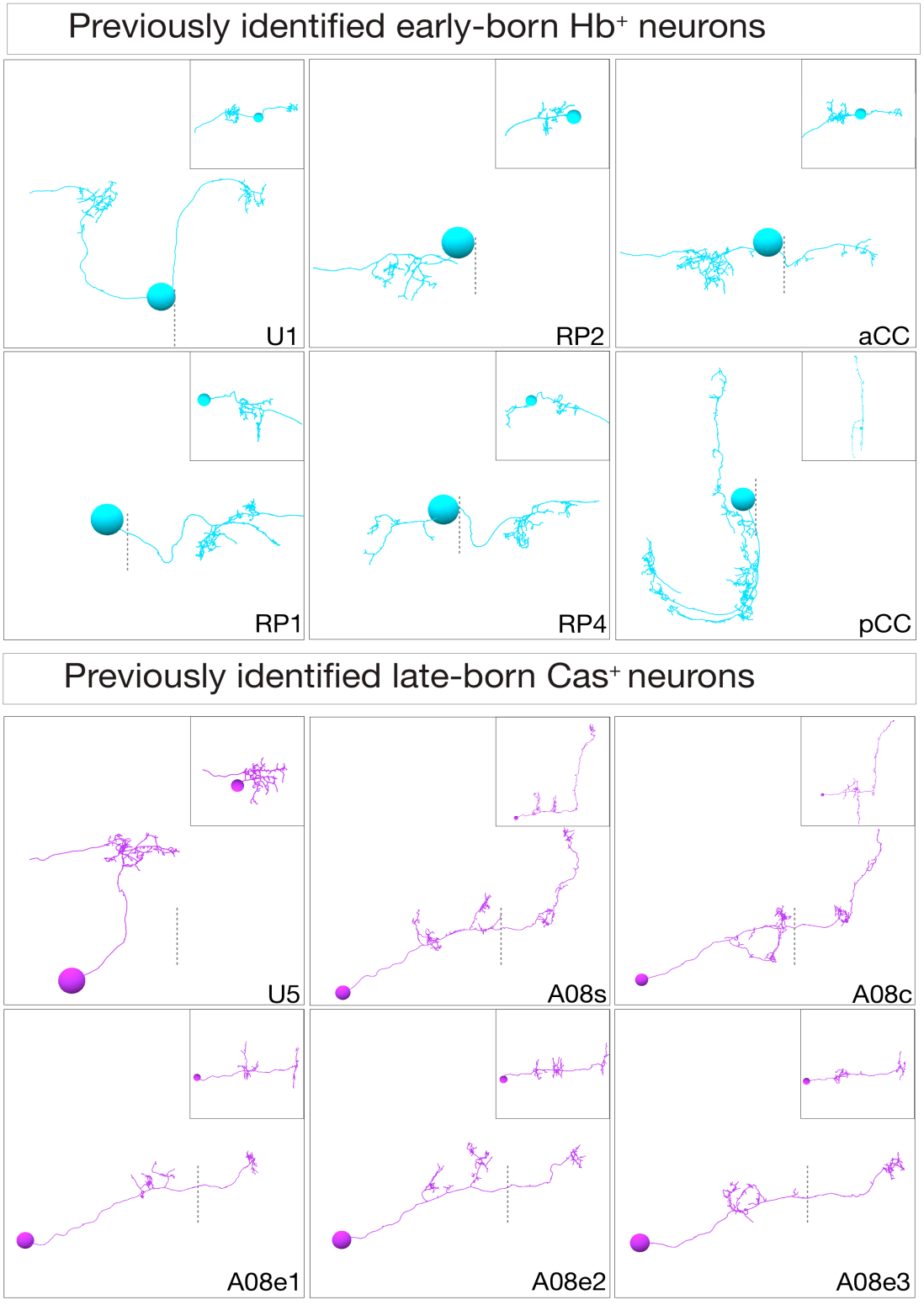


# Supplemental Figure 4

*Supplemental Figure 4*

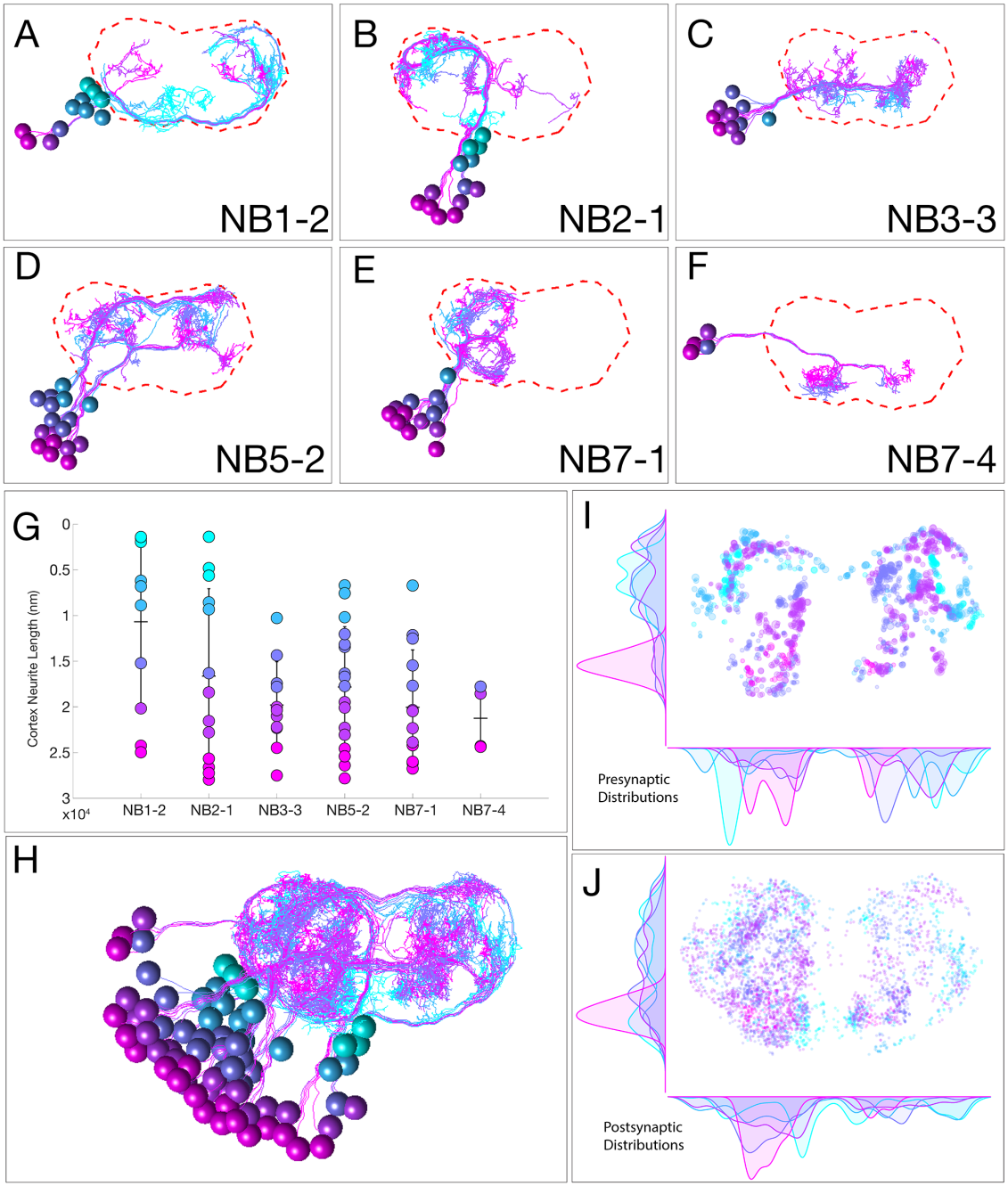


Supplemental Figure 5

***Supplemental Figure 5***

| Lineage | Hemilineage | Neuron Name | Temporal Cohort | Cortex Neurite Length (µm) | Totale Cable Length (µm) |
|---|---|---|---|---|---|
| NB1-2 | Dorsal | A01x3_a1l | 1 | 1.40 | 223.73 |
| NB1-2 | Dorsal | A01x2_a1l (A01d4) | 1 | 1.52 | 257.28 |
| NB1-2 | Dorsal | A01d3_a1l | 2 | 6.19 | 276.80 |
| NB1-2 | Dorsal | A01xxxxx_a1l | 2 | 6.80 | 243.36 |
| NB1-2 | Dorsal | A01c2_ipsi_dendrite_a1l | 2 | 8.88 | 219.72 |
| NB1-2 | Dorsal | A01c1_a1l | 3 | 15.21 | 221.60 |
| NB1-2 | Dorsal | A01b2_a1l | 4 | 20.16 | 249.96 |
| NB1-2 | Dorsal | A01a_a1l | 5 | 24.24 | 246.89 |
| NB1-2 | Dorsal | A01x_l | 5 | 24.96 | 286.82 |
| NB1-2 | Ventral | A12q_a1l | 1 | 1.95 | 584.41 |
| NB1-2 | Ventral | hook? t3l | 2 | 6.20 | 122.69 |
| NB2-1 | Dorsal | A02j_a1l | 2 | 8.55 | 243.45 |
| NB2-1 | Dorsal | A02i_a1l | 2 | 9.33 | 222.13 |
| NB2-1 | Dorsal | A02g_a1l | 4 | 21.54 | 267.47 |
| NB2-1 | Dorsal | A02f_a1l | 5 | 25.65 | 206.66 |
| NB2-1 | Dorsal | A02h_a1l | 5 | 26.61 | 174.49 |
| NB2-1 | Dorsal | A02e_a1l | 5 | 27.24 | 368.74 |
| NB2-1 | Ventral | A02m_a1l Pseudolooper-3 | 1 | 1.39 | 163.74 |
| NB2-1 | Ventral | A02n_a1l Pseudolooper-4 | 1 | 4.81 | 188.41 |
| NB2-1 | Ventral | A02k Pseudolooper-1_a1l | 1 | 5.64 | 313.19 |
| NB2-1 | Ventral | A02c?_a1l | 3 | 16.31 | 203.56 |
| NB2-1 | Ventral | A02a-looper-1_a1l_JMpair1 | 4 | 18.41 | 235.06 |
| NB2-1 | Ventral | A02d_a1l | 4 | 22.79 | 327.23 |
| NB2-1 | Ventral | A02b_a1l | 5 | 27.96 | 292.57 |
| NB3-3 | Ventral | A08x_a1l | 2 | 10.28 | 616.72 |

| | | | | | |
|---|---|---|---|---|---|
| NB3-3 | Ventral | VLEL4_a1l | 3 | 14.35 | 514.16 |
| NB3-3 | Ventral | VLEL9_a1l | 3 | 17.43 | 594.25 |
| NB3-3 | Ventral | A08o_a1l | 3 | 17.81 | 431.79 |
| NB3-3 | Ventral | A08c_a1l | 4 | 20.01 | 464.45 |
| NB3-3 | Ventral | A08j2_a1l | 4 | 20.36 | 617.51 |
| NB3-3 | Ventral | A08e2_a1l | 4 | 20.99 | 285.30 |
| NB3-3 | Ventral | A08e3_a1l | 4 | 22.21 | 273.51 |
| NB3-3 | Ventral | A08m_a1l | 4 | 22.30 | 435.20 |
| NB3-3 | Ventral | A08s1_a1l | 5 | 24.48 | 508.55 |
| NB3-3 | Ventral | A08e1_a1l | 5 | 27.50 | 267.28 |
| NB4-1 | Dorsal | A14a_a1l | 3 | 15.66 | 169.24 |
| NB4-1 | Dorsal | A14a2/c?_a1l | 3 | 17.63 | 192.51 |
| NB4-1 | Dorsal | A14b a1l | 4 | 20.53 | 250.20 |
| NB4-1 | Dorsal | A14a1_a1l | 4 | 21.80 | 165.16 |
| NB4-1 | Ventral | A05q_a1l | 4 | 18.56 | 409.75 |
| NB4-1 | Ventral | A27k_up_a1l | 4 | 20.92 | 234.53 |
| NB4-1 | Ventral | A01x_a1l | 5 | 26.36 | 170.07 |
| NB4-1 | Ventral | A01bx_a1l | 5 | 26.86 | 153.65 |
| NB5-2 | Dorsal | Saaghi-6_a1l (AAZ6 (A06b)) | 2 | 6.69 | 202.04 |
| NB5-2 | Dorsal | A06c_a1l | 2 | 10.19 | 209.18 |
| NB5-2 | Dorsal | to do B (A06m?)_a1l | 3 | 12.03 | 175.85 |
| NB5-2 | Dorsal | Saaghi-5_a1l (AAZ5 (A06g2)) | 3 | 13.43 | 198.21 |
| NB5-2 | Dorsal | Saaghi-4_a1l (AAZ4 (A06g)) | 3 | 16.34 | 281.40 |
| NB5-2 | Dorsal | Saaghi-3_a1l (AAZ3 (A06e)) | 4 | 19.47 | 253.67 |
| NB5-2 | Dorsal | A06a_a1l | 4 | 22.29 | 251.33 |

| | | | | | |
|---|---|---|---|---|---|
| NB5-2 | Dorsal | Saaghi-2_a1l (AAZ2 (A06f)) | 4 | 23.05 | 260.00 |
| NB5-2 | Dorsal | Saaghi-1_a1l (AAZ1 (A06l)) | 5 | 24.56 | 438.86 |
| NB5-2 | Dorsal | A06x1_a1l | 5 | 26.41 | 210.94 |
| NB5-2 | Ventral | A06k_a1l | 2 | 7.56 | 315.80 |
| NB5-2 | Ventral | pre-A08m_a1l _to be completed | 3 | 13.16 | 452.51 |
| NB5-2 | Ventral | neuron 18509064 with a soma | 3 | 16.70 | 236.26 |
| NB5-2 | Ventral | A06bx_a1l | 3 | 17.72 | 278.32 |
| NB5-2 | Ventral | Jaam-2_a1l (HMD2 (A12g)) | 4 | 20.08 | 258.55 |
| NB5-2 | Ventral | Jaam-1_a1l (HMD1 (A12p)) | 5 | 25.40 | 361.20 |
| NB5-2 | Ventral | Jaam-3_a1l (HMD3 (A12 c3)) | 5 | 27.82 | 328.10 |
| NB7-1 | Dorsal | A03?_a1l | 2 | 6.72 | 254.44 |
| NB7-1 | Dorsal | A03?_post _A02k_a1l | 3 | 12.14 | 192.79 |
| NB7-1 | Dorsal | a03d/e?_a 2l | 3 | 17.68 | 199.23 |
| NB7-1 | Dorsal | A03x_a2l (EGHBAL ) | 4 | 20.34 | 211.44 |
| NB7-1 | Dorsal | A03a4_a2l | 5 | 25.99 | 236.01 |
| NB7-1 | Dorsal | A03?_pre A08m_a1l | 5 | 26.16 | 220.59 |
| NB7-1 | Ventral | Ipsilateral mixed LN a1l A03xxx | 3 | 12.52 | 192.89 |
| NB7-1 | Ventral | neuron 16112459 | 3 | 15.46 | 136.16 |
| NB7-1 | Ventral | ipsilateral local a2l | 4 | 20.46 | 262.44 |

| | | | | | |
|---|---|---|---|---|---|
| NB7-1 | Ventral | A03o_a1l | 4 | 22.33 | 329.90 |
| NB7-1 | Ventral | A08m upstream 1? left | 4 | 23.86 | 243.75 |
| NB7-1 | Ventral | A03d?_a1l | 5 | 24.20 | 257.18 |
| NB7-1 | Ventral | A03xyz_a1r | 5 | 26.01 | 251.80 |
| NB7-1 | Ventral | neuron 4313312 (ad) | 5 | 26.75 | 179.72 |
| NB7-4 | Ventral | A19b a1l | 3 | 17.77 | 277.67 |
| NB7-4 | Ventral | A19x a1l | 4 | 18.54 | 375.71 |
| NB7-4 | Ventral | Griddle-2 a1l | 5 | 24.29 | 349.34 |
| NB7-4 | Ventral | Griddle-1 a1l | 5 | 24.37 | 290.78 |

***Supplementary table 1***

# CHAPTER IV

# A MULTILAYER CIRCUIT ARCHITECTURE FOR THE GENERATION OF DISTINCT LOCOMOTOR BEHAVIORS IN *DROSOPHILA*

Aref Arzan Zarin1,4#*, Brandon Mark1#, Albert Cardona2, Ashok Litwin-Kumar3, and Chris Q. Doe1*

1Institute of Neuroscience, Institute of Molecular Biology, Howard Hughes Medical Institute, University of Oregon, Eugene, OR 97403

2Janelia Research Campus, Howard Hughes Medical Institute, Ashburn, VA 20147

3Mortimer B. Zuckerman Mind Brain Behavior Institute, Department of Neuroscience, Columbia University, 3227 Broadway, New York, New York 10027 ORCID 0000-0003-2422-6576

4 Current address: Department of Biology, Texas A&M University, College Station, TX 77840

# Authors contributed equally

* Authors for correspondence at cdoe@uoregon.edu (CQD) and azarin@bio.tamu.edu (AAZ)

Author Contributions : A.A Zarin and B. Mark contributed to conceptualization, formal analysis, investigation, visualization, methodology, writing—original draft, writing—review and editing. A. Cardona. A. Litwin-Kumar and C.Q. Doe contributed to conceptualization, formal analysis, investigation, methodology, writing—original draft.

## Introduction

Locomotion is a rhythmic and flexible motor behavior that enables animals to explore and interact with their environment. Birds and insects fly, fish swim, limbed animals walk and run, and soft-body

invertebrates crawl. In all cases, locomotion results from coordinated activity of muscles with different biomechanical output. This precisely regulated task is mediated by neural circuits composed of motor neurons (MNs), premotor interneurons (PMNs), proprioceptors, and descending command-like neurons (Arber, 2017; Arber & Costa, 2018; Marder & Bucher, 2001). A partial map of neurons and circuits regulating rhythmic locomotion have been made in mouse (Bikoff et al., 2016; Crone et al., 2008; Dougherty et al., 2013; Goetz, Pivetta, & Arber, 2015; Grillner & Jessell, 2009; Zagoraiou et al., 2009), cat (Kiehn, 2006; Nishimaru & Kakizaki, 2009), fish (Kimura et al., 2013; Song, Ampatzis, Bjornfors, & El Manira, 2016), tadpole (A. Roberts, Li, & Soffe, 2010; A. Roberts, Li, Soffe, & Wolf, 2008), lamprey (Grillner, 2003; Mullins, Hackett, Buchanan, & Friesen, 2011), leech (Brodfuehrer & Thorogood, 2001; Kristan, Calabrese, & Friesen, 2005; Marin-Burgin, Kristan, & French, 2008; Mullins et al., 2011), crayfish (Mulloney & Smarandache-Wellmann, 2012; Mulloney, Smarandache-Wellmann, Weller, Hall, & DiCaprio, 2014), and worm (Haspel, Donovan, & Hart, 2010; Kawano et al., 2011; Piggott, Liu, Feng, Wescott, & Xu, 2011; W. M. Roberts et al., 2016; Tsalik & Hobert, 2003; Wakabayashi, Kitagawa, & Shingai, 2004; Quan Wen et al., 2012; Zhen & Samuel, 2015). These pioneering studies have provided a wealth of information on motor circuits, but with the exception of *C. elegans* (White, Southgate, Thomson, & Brenner, 1986), there has been no system where all MNs and PMNs have been identified and characterized. Thus, we are missing a comprehensive picture of how an ensemble of interconnected neurons generate diverse locomotor behaviors.

We are interested in understanding how the *Drosophila* larva executes multiple behaviors, in particular forward versus backward locomotion (Carreira-Rosario et al., 2018). Are there different MNs used in each behavior? Are the same MNs used but with distinct patterns of activity determined by premotor input? A rigorous answer to these questions requires both comprehensive anatomical information – i.e. a PMN/MN connectome – and the ability to measure rhythmic neuronal activity and perform functional experiments. All of these tools are currently available in *Drosophila*, and here we use them to characterize the neuronal circuitry used to generate forward and backward locomotion.

The *Drosophila* larva is composed of 3 thoracic (T1-T3) and 9 abdominal segments (A1-A9; Figure 1A), with sensory neurons extending from the periphery into the CNS, and motor neurons extending out of the CNS to innervate body wall muscles. Most segments contain 30 bilateral body wall muscles that form "spatial muscle groups" based on common location and orientation: dorsal longitudinal (DL; includes previously described DA and some DO muscles), dorsal oblique (DO), ventral longitudinal (VL), ventral oblique (VO), ventral acute (VA) and lateral transverse (LT)(Figure

1B)(Bate, 1990; Crossley, 1978; Hooper, 1986). Using these muscles, the larval nervous system can generate both forward and backward locomotion (reviewed in Clark, Zarin, Carreira-Rosario, & Doe, 2018; Kohsaka, Guertin, & Nose, 2017). Forward crawling behavior in larvae involves a peristaltic contraction wave from posterior to anterior segments; backward crawling entails a posterior propagation of the contraction wave (Berni, Pulver, Griffith, & Bate, 2012; Crisp, Evers, Fiala, & Bate, 2008; Dixit, Vijayraghavan, & Bate, 2008; Gjorgjieva, Berni, Evers, & Eglen, 2013; Heckscher et al., 2015; Kohsaka et al., 2019; Loveless, Lagogiannis, & Webb, 2018; Pulver et al., 2015) (Figure 1A).

There are ~30 bilateral pair of MNs in each segment: 26 pair of type Ib MNs with big boutons that typically innervate one muscle; two pair of type Is MNs with small boutons that innervate large groups of dorsal or ventral muscles; one or two type III insulinergic MNs innervating muscle 12; and three type II ventral unpaired median MNs that provide octopaminergic innervation to most muscles (Table 1) (Choi, Park, & Griffith, 2004; Gorczyca, Augart, & Budnik, 1993; Hoang & Chiba, 2001; Koon et al., 2011; Koon & Budnik, 2012; Landgraf, Bossing, Technau, & Bate, 1997; Landgraf, Jeffrey, Fujioka, Jaynes, & Bate, 2003; Mauss et al., 2009; Zarin & Labrador, 2017). Elegant pioneering work showed that type Ib MNs innervating muscles in the same spatial muscle group typically projected dendrites to the same region of the dorsal neuropil, creating a myotopic map (Landgraf et al., 1997; Mauss et al., 2009). Several MNs have been shown to be rhythmically active during larval locomotion (Heckscher, Lockery, & Doe, 2012; Zwart et al., 2016), but only a few of their premotor inputs have been described (Carreira-Rosario et al., 2018; Fushiki et al., 2016; Hasegawa, Truman, & Nose, 2016; Heckscher et al., 2015; Kohsaka, Takasu, Morimoto, & Nose, 2014; Kohsaka et al., 2019; Takagi et al., 2017; Zwart et al., 2016). Some excitatory PMNs are involved in initiating activity in their target MNs (Carreira-Rosario et al., 2018; Fushiki et al., 2016; Hasegawa et al., 2016; Takagi et al., 2017; Zwart et al., 2016), while some inhibitory PMNs limit the duration of MN activity (Kohsaka et al., 2014; MacNamee et al., 2016; Schneider-Mizell et al., 2016) or produce intrasegmental activity offsets (Zwart et al., 2016). Interestingly, some PMNs are active specifically during forward locomotion or backward locomotion (Carreira-Rosario et al., 2018; Fushiki et al., 2016; Hasegawa et al., 2016; Heckscher et al., 2015; Kohsaka et al., 2014; Kohsaka et al., 2019; Takagi et al., 2017). Yet a comprehensive map of the activity and connectivity of the PMN-MN-muscle network, which is essential for a full understanding of how locomotor behavior is generated, remains unknown.

Here we address the question of how the same MNs and muscles generate two distinct behaviors: forward and backward locomotion. There are multiple mechanisms that could generate

different forward and backward locomotor behaviors. (1) Different muscles could be used in each behavior. (2) One or more spatial muscle group may show a different time of recruitment in each behavior. (3) One or more single MNs may show a different time of recruitment in each behavior. (4) PMNs and/or MNs could have asymmetric morphology along the anteroposterior body axis (e.g. post-synapses in one segment, pre-synapses a different segment), resulting in a different time of recruitment in each behavior. (5) One or more PMNs could be active only in forward or backward locomotion, changing the phase relationship of their target MNs. Here we use pan-muscle activity imaging, comprehensive TEM reconstruction of all MNs and well-connected PMNs, functional optogenetics, and development of a recurrent network model to sequentially test each of these hypotheses. We identify four mechanisms that act together to generate distinct forward and backward locomotor behaviors.

## Results

### All body wall muscles are activated during forward and backward locomotion

Forward and backward locomotor behaviors could be generated by recruiting different muscles for each behavior, or by changing the timing of muscle recruitment for each behavior. To distinguish between these mechanisms, we performed ratiometric calcium imaging to map the activation onset of each body wall muscle during forward and backward locomotion. To date only muscle contraction data have been reported, not muscle activity data, and only for five of the 30 body wall muscles (Heckscher et al., 2012; Zwart et al., 2016). Muscle contraction could occur passively due to biomechanical linkage between adjacent muscles, so it may not be a perfect substitute for directly measuring muscle activity.

We used GCaMP6f/mCherry live imaging to measure the activation time of all 30 individual body wall muscles in the abdominal segments. We expressed GCaMP6f and mCherry using the muscle line *R44H10-LexA*, which has variable expression in sparse to dense patterns of muscles. For this experiment we analyzed larvae with dense muscle expression. We imaged both forward and backward locomotion in 2nd instar larvae (a representative animal shown in Figure 2A, D). We found that an increased GCaMP6f signal correlated with muscle contraction during both forward and backward locomotion (representative examples of muscle 6 shown in Figure 2B, E). Most importantly, all imaged muscles (30 for forward and 29 for backward) showed a significant rise in

GCaMP6f fluorescence during forward and backward locomotion (Figure 2C, F; Movies 1, 2). In addition, because each type Ib MN typically innervates a single muscle, we can use muscle depolarization as a proxy for the activity of its innervating MN. We conclude that all MNs and their target muscles are activated during forward and backward locomotion.

## Hierarchical clustering identifies different MN/muscle recruitment patterns during forward and backward locomotion

All muscles are recruited in both forward and backward locomotion, leading to the hypothesis that forward and backward locomotion show different muscle recruitment times. To test this hypothesis, we embedded the multidimensional crawl cycle data in two-dimensional space using principal component analysis (PCA)(Lemon et al., 2015). We aligned crawl trials by finding peaks in this 2D space which corresponded to the highest contraction amplitude of the most muscles in a given crawl (Figure 3 – figure supplement 1; see Methods). Although muscle activity appeared as a continuum with the sequential recruitment of individual muscles, hierarchical clustering of the mean activity of each muscle during forward and backward crawling revealed four groups of co-active muscles for both behaviors (Figure 3B-E; summarized in Figure 3F,G; Table 2). We call these co-activated muscle groups F1-F4 for forward and B1-B4 for backward crawling. Overall, we analyzed 27 muscles during forward locomotion and 25 muscles during backward locomotion (missing muscles were too tightly packed to extract clear activity profiles) (Table 2). Analysis of forward locomotion showed that each co-activated muscle group had a characteristic pattern of activation: e.g. F1 muscles had a more variable time of onset, whereas F4 muscles had a highly coherent onset (Figure 3B,C). Furthermore, the activation time of each co-activated muscle group was more coherent than the time of their inactivation (Figure 3B-C). Notably, these co-activated muscle groups do not fully match previously identified spatial muscle groups (compare Figure 1 and 3).

We found that the largest change in recruitment time between forward and backward locomotion was in six muscles: the three muscles in the VO spatial muscle group, and muscles 2, 11, and 18 (each in a different spatial muscle group) (Figure 3F,G; Figure 3 – figure supplement 2). The VO spatial muscle group switched from late activity during forward locomotion (F3) to early activity during backward locomotion (B1), whereas the three other neurons switched from early activity during forward locomotion (F1/2) to late activity during backward locomotion (B3/4) (Figure 3A,F,G). These changes led to a complete inversion in the timing of the VO muscles and muscle 18 (Figure 3H). Other spatial muscle groups typically did not change their timing of activation; e.g.

longitudinal muscles tended to be active early and transverse muscles activated late in both behaviors (Figure 3A,F,G), consistent with prior reports tracking single muscles within each group (Heckscher et al., 2012; Zwart et al., 2016). We conclude that forward and backward locomotor behaviors arise from a relatively small number of MN/muscles that show differential recruitment during each behavior. Our results raise two new questions. (1) What mechanisms produce co-active muscle groups? (2) What mechanism produce the differential timing of the VO and 2/11/18 muscles in forward and backward locomotion? Answering these questions will help determine how the same MNs and muscles can generate two different locomotor behaviors.

## TEM reconstruction of all segmental motor neurons shows that co-active motor neurons have dispersed post-synaptic sites within the dorsal neuropil

There are two hypotheses for how co-active muscle groups are established. Each pool of co-active MNs could target their dendritic post-synaptic sites to a distinct neuropil locations, where they can be innervated by different PMNs. Alternatively, each pool of co-active MNs could have overlapping post-synaptic sites, which can be selectively targeted by distinct PMNs ("labeled line" synaptic specificity) or targeted by different combinations of PMNs (combinatorial code). To distinguish between these hypotheses, we identified all MNs with single synapse resolution in a comprehensive TEM connectome (Figure 4) and mapped the neuropil location of their post-synaptic sites (Figure 5). To date, only a small fraction of MNs have been reconstructed (Carreira-Rosario et al., 2018; Fushiki et al., 2016; Heckscher et al., 2015; Zwart et al., 2016). Here, we identify and reconstruct all differentiated MNs in segment A1, which can be used as a proxy for other abdominal segments. We identified all 25 pair of type Ib MNs, both pair of type Is MNs that target large muscle groups (RP2, RP5), one pair of type III MNs that target muscle 12, and the three unpaired midline octopaminergic MNs (VUMs) (Figure 4; Table 1). The presence of yet another type Is MN has been suggested (Hoang & Chiba, 2001), but we did not find it in the TEM volume; it may be late-differentiating or absent in A1. We linked all bilateral MNs in the TEM volume to their muscle target by matching the dendritic morphology in the EM reconstruction to the dendritic morphology determined experimentally (Landgraf et al., 1997; Landgraf, Jeffrey, et al., 2003; Mauss et al., 2009) (Figure 4; Figure 4 – figure supplements 1, 2; Table 1). A dataset of all MNs that can be opened in CATMAID (Saalfeld, Cardona, Hartenstein, & Tomancak, 2009) is provided as Supplemental File 1. Note that the transverse nerve MN (MN25-1b) is only present in the A2-A7 segments (Hessinger, Technau, & Rogulja-Ortmann, 2017), so we traced it in A2. Note that in subsequent analyses we did not include the neuromodulatory VUMs MNs due to relatively undifferentiated state (few post-

synapses). We found that all MNs had a dense array of post-synapses on their dendritic projections, but unlike *C. elegans* (Quan Wen et al., 2012), we observed no pre-synaptic contacts to other MNs or interneurons (Figure 4 – figure supplements 1, 2). In conclusion, we have successfully identified and reconstructed, at single synapse-level resolution, all differentiated MNs in segment A1 of the newly hatched larval CNS. This is a pre-requisite for mapping the location of post-synaptic sites, as well as for mapping PMN-MN connectivity (below).

Previous work has shown that motor neurons innervating a single spatial muscle group target their dendrites to a similar region of the neuropil, creating a myotopic map that provides the first layer of functional organization of the motor neuropil (Landgraf, Jeffrey, et al., 2003; Mauss et al., 2009). Given our observation that co-active muscle groups do not precisely match previously reported spatial muscle groups, we first sought to confirm the existence of a myotopic organization using every motor neuron. First, we compared MNs in the left and right A1 hemisegments and observed highly similar post-synapse clustering within the neuropil volume (Pearson correlation coefficient, $r = 0.97$), which we averaged for subsequent analysis. This validated the quality and reproducibility of the MN dendritic reconstructions and highlighted the stereotypy of MN post-synaptic locations in the neuropil. To confirm and extend previous findings, we mapped post-synaptic site location in the neuropil for MNs innervating each spatial muscle group (Figure 5A). We show that MNs innervating spatial muscle groups DL, VL, VO, VA, and LT have significantly different spatial distributions in all three axes (two sample Kolmogorov-Smirnov test; $p<.05$) with the exception of the DL/VL muscle groups which showed significance only in the mediolateral and anteroposterior axes (Figure 5A). Additionally, we observe a highly ordered hierarchical relationship between the target regions of spatial muscle groups. The largest distinction between MN input fields are those of the SN and ISN nerves. Within the MNs of the ISN, there is first a dorsal/ventral segregation followed by a longitudinal/oblique segregation (Figure 5B). Thus, we confirm and extend previous reports of MN myotopic maps, but now at the level of resolution of individual synapses.

To determine if MNs innervating each co-active muscle group also have distinct post-synaptic sites in the neuropil, we mapped post-synaptic site localization for MNs targeting each co-active muscle group. We found that post-synaptic sites of MNs innervating different forward co-active muscle groups had unique neuropil localization along all axes (Figure 5C). A similar result was observed for MNs innervating backward co-active muscle groups (data not shown). Thus, MNs targeting both spatial and co-active muscle groups show segregation of post-synaptic sites within the neuropil, although not to the extent observed for MNs targeting spatial muscle groups (Figure 5B, bottom right). Our results raise the possibility of dedicated PMNs targeting neuropil domains that

contain MN post-synapses linked to different co-active muscle groups, which could be a mechanism for generating different recruitment of MNs in each co-active muscle group (see below).

To examine the relationship between differential recruitment of MNs and post-synapse localization, we analyzed three MNs that have strikingly different recruitment times between forward and backward locomotion. MN2 is active in F1 and B3 groups, MN11 is active in F1 and B4 groups, and MN18 is active in F2 and B4 groups. Do these MNs have different post-synapse localization compared to the remainder of their spatial muscle group? If so, this could explain why they have such different recruitment times, compared to the other MNs in the same spatial muscle group. Interestingly, MN18 targeted it post-synapses to a neuropil domain distinct from the other MNs in the LT spatial muscle group (Figure 5D). In contrast, MNs 2 and 11 had post-synapse localization fully embedded within the neuropil domain containing post-synapses from the DL and DO spatial muscle groups, respectively (Figure 5E, and data not shown). We conclude that differential distributions of post-synaptic inputs can explain some but not all of the observed differences between spatial muscle groups and co-active muscle groups.

## TEM reconstruction of 118 premotor neurons reveals premotor neuron pools targeting each group of co-active motor neurons

Some co-active muscle groups are innervated by MNs that target their post-synaptic sites to a common region of the dorsal neuropil, whereas other co-active muscle groups are innervated by MNs with widely distributed post-synaptic sites. In either case, the co-active MNs could be targeted by PMNs dedicated to each pool of co-active MNs, similar to the case in the mammalian spinal cord (reviewed in Arber, 2017; Arber & Costa, 2018). To determine whether there are "labeled lines" of PMNs innervating co-active MNs – or combinatorial coding of PMN-MN connectivity – requires a comprehensive identification of all PMNs and their MN partners. Hence, we identified and reconstructed all PMNs with dense monosynaptic contacts to MNs in segment A1. This included local premotor neurons with somata in A1 as well as neurons from adjacent segments with dense connectivity to A1 MN dendrites. We identified 118 bilateral PMNs (236 total) with connectivity to A1 MNs (Supplementary Table 1; see Methods for selection criteria). PMN cell bodies were distributed throughout the segment (Figure 6A), and as expected, their pre-synaptic (output) sites were strongly enriched in the dorsal neuropil (Figure 6B; Figure 6 – supplement 1) similar to partner MN post-synaptic sites (Landgraf et al., 1997; Mauss et al., 2009). In contrast, PMN post-synaptic (input) sites were distributed throughout the neuropil (Figure 6B,C).

We observed widespread connectivity of PMNs to multiple MNs. Each PMN synapsed with an average of 7.99 MNs (Figure 6D), and each MN had an average of 32.5 input PMNs (Figure 6E). All PMNs targeted both MNs and interneurons; there were no PMNs exclusively innervating MNs (Figure 6F). The 118 bilateral PMNs make 7495 synapses on A1 MNs which account for 12.7% of PMN output and 76% of the A1 MN input (excluding A2 MN-25) (Figure 6G). In addition, most PMNs projected contralaterally, had local arbors, and had post-synaptic inputs on their more proximal processes (Figure 6H-J). The few PMNs with pre- and post-synapses co-clustered distally (Figure 6 – supplement 1, boxed) are good candidates for non-spiking interneurons that perform local computations (reviewed in Marder & Bucher, 2001; K. G. Pearson, 1976). Neurotransmitter expression is known for a fraction of the PMNs (Burgos et al., 2018; Carreira-Rosario et al., 2018; Fushiki et al., 2016; Hasegawa et al., 2016; Heckscher et al., 2015; Kohsaka et al., 2014; Kohsaka et al., 2019; MacNamee et al., 2016; Takagi et al., 2017; Yoshino, Morikawa, Hasegawa, & Emoto, 2017; Zwart et al., 2016). To increase coverage, we screened for Gal4 lines with sparse expression patterns, performed MultiColorFlpOut (Nern et al., 2015) to match their morphology to individual PMNs, and mapped neurotransmitter expression. We found 46 GABAergic (presumptive inhibitory), 22 glutamatergic (presumptive inhibitory), 100 cholinergic (presumptive excitatory), and 6 corozonergic (neuromodulatory) neurons; 62 PMNs could not be characterized due to lack of Gal4 lines (Figure 6K, Supplemental Table 1), and we did not identify any neurons co-expressing two fast neurotransmitters. A file that can be opened in CATMAID showing all 118 bilateral PMNs is provided as Supplemental File 2. Thus, we have identified a large majority of the PMN inputs to the MN population in segment A1.

Next we asked whether there are PMNs dedicated to innervating individual spatial or co-active muscle groups. We identified PMN pools that primarily target MNs innervating single spatial muscle groups, although many PMNs target multiple spatial muscle groups (Figure 7A). Similarly, we identified PMN pools that primarily target MNs innervating single forward co-active muscle groups, although many PMNs target multiple co-active muscle groups (Figure 7B). For example, PMNs in orange text preferred MNs innervating co-activated muscle group F2, whereas PMNs in green and dark blue text were targeted MNs in co-activated muscle group F3 and F4 respectively. More specifically, the A27h PMN (arrow in Figure 7B) has strong connections to the F3 MNs, and sparser connections to other co-activated groups. We used functional optogenetics to show that A27h activity onset followed the onset of F1/F2 pool of MNs (Figure 7C), consistent with preferential connectivity of A27h to F3 MNs (Figure 7B). Not surprisingly, we also identified PMN pools that primarily target MNs innervating single backward co-active muscle groups, although many PMNs target multiple co-active muscle groups (Figure 7D). We conclude that there are PMNs preferentially

targeting individual co-activated muscle groups (consistent with a "labeled line" model), although there are many PMNs that innervate multiple co-activated muscle groups (consistent with a "combinatorial code" model).

## Neuronal asymmetry linked to different muscle recruitment times during forward and backward locomotion

Neurons that are asymmetric along the anteroposterior axis are excellent candidates for differential recruitment during forward and backward locomotion. We found two MNs that are highly asymmetric: MN18 and MN25 (Figure 8A,B). In both cases, the asymmetric distribution of pre- and post-synaptic sites should lead to earlier activation during forward locomotion (for MN18) or during backward locomotion (for MN25). This is confirmed by the differential recruitment of their target muscles. Similar anterior/posterior asymmetry was observed in multiple PMNs: A02i and A03a4 have axons extending 1-2 segments anterior of the cell body and dendrites, and A01j and A03a5 have axons projecting 1-2 segments posterior to the cell body and dendrites (Figure 8C-F; Figure 3 – supplement 1). Due to the opposite direction of wave propagation in backward and forward locomotion, these PMNs are likely to contribute to the differential MN/muscle recruitment in forward and backward locomotion.

## A recurrent network model that generates the observed forward and backward pattern of muscle activity

Recurrent interactions among PMNs have been shown to control the timing of the muscle outputs of central pattern generator circuits in a variety of organisms (Grillner, 2003; Marder & Bucher, 2001). We hypothesized that these types of interactions are responsible for the timing of muscle activation during *Drosophila* larval forward and backward crawling. To assess whether the reconstructed PMN connectome is capable of producing the observed timing of MN/muscle activation, we developed a recurrent network model of two adjacent segments. Previous models have focused on wave propagation during forward and backward crawling by modeling the average activity of excitatory and inhibitory subpopulations in each segment (Gjorgjieva et al., 2013; Pehlevan, Paoletti, & Mahadevan, 2016). Access to the detailed connectivity of PMNs and MNs (Supplemental Table 2 and Supplemental Table 3), as well as knowledge of the activation patterns of different co-

activated muscle groups, allowed us to develop a substantially more detailed model whose circuitry was constrained to match the TEM reconstruction. For PMNs whose neurotransmitter identity we could determine, we also constrained the signs (excitatory or inhibitory) of connection strengths in the model. The firing rates of PMNs and MNs were modeled as simple threshold-linear functions of their synaptic inputs, and model parameters were adjusted to produce target MN patterns of activity that matched the sequences identified during forward and backward crawling. These patterns were assumed to be evoked by external command signals, representing descending input to the PMNs, that differed for forward and backward crawling but did not themselves contain information about the timing of individual muscle groups. We also constrained the activity of two PMNs, A18b and A27h, that are known to be specifically active during backward and forward locomotion, respectively (Carreira-Rosario et al., 2018; Fushiki et al., 2016). We found that, although the connectivity among PMNs within a segment is sparse (roughly 7% of all possible pairwise connections), the observed connections are nonetheless sufficient to generate appropriately timed MN activity for the two distinct behaviors (Figure 9A,B; Figure 9 – Figure supplement 1; see Methods). As has been described previously in other pattern-generating systems (Prinz, Bucher, & Marder, 2004), there is a space of models that is capable of producing the observed activity. We therefore analyzed the activity of neurons in an ensemble of models. In the models, distinct sequences of PMN activity for forward and backward locomotion tile the period of time over which MNs are active (Figure 9C; Figure 9 – Figure supplement 1). These sequences give rise to the distinct timing of MN activation during each behavior. With the exception of *C. elegans* models (Izquierdo & Beer, 2013; Izquierdo, Williams, & Beer, 2015; Karbowski, Schindelman, Cronin, Seah, & Sternberg, 2008; Kunert, Maia, & Kutz, 2017; Macosko et al., 2009; Rakowski & Karbowski, 2017; Q. Wen et al., 2012), the networks constructed here represent the first models of the neural circuitry underlying a timed motor behavior whose connectivity has been constrained by a synaptic wiring diagram.

Next we asked if the sequences of PMN activity predicted by the model are consistent with prior experimentally determined activity patterns. In our model, the PMN A14a is active at F1 and is inactive at F4 (Figure 9C). Similarly, experimental data show that A14a is inhibitory and is active during co-activated muscle group F1; and blocking A14a activity removes the contraction delay between muscles in co-activated muscle group F1 and F4 (Zwart et al., 2016), thereby validating our model. In our model, the PMNs A18b3 and A18a are both active during forward locomotion, but only A18a is active during backward locomotion (Figure 9C). Experimental data show that A18a and A18b3 are active precisely as proposed in our model (Hasegawa et al., 2016). Furthermore, our model predicts the cholinergic A18j and A01c PMNs are active at F4, which is supported by experimental data on these neurons (where they were called eIN1,2; Zwart et al. 2016).

To provide new, additional experimental tests of our model, we performed dual color calcium imaging on previously uncharacterized GABAergic PMNs A31k and A06l. Our model predicted that both A31k and A06l neurons show peak activity later than the early-activated MNs during both forward and backward locomotion (Figure 9C; Figure 9 – Figure supplement 1). To determine experimentally the phase-relationship between A31k and MNs, we expressed GCaMP6m in a subset of MNs and jRCaMP1b in A31k. Dual color calcium imaging data revealed that the A31k activity peak coincides with a decline of activity in MNs innervating early co-activated muscle groups during both forward and backward locomotion (Figure 10A,B), further validating our model. Second, our model predicts that both A31k and A06l PMNs show concurrent, rhythmic activity during forward and backward locomotion (Figure 9 – Figure supplement 1). We expressed GCaMP6m in both neurons, which we could distinguish based on their different axon projections, and found that they showed concurrent, rhythmic activity (Figure 10C,D), and thus both neurons show a delayed activation relative to MNs. Our third experimental test focused on the GABAergic A23a PMN (Schneider-Mizell et al., 2016). Our model predicted that A23a was active earlier during backward locomotion than forward locomotion (Figure 9C). We expressed GCaMP6m in a subset of MNs and jRCaMP1b in A23a, and validated the prediction of our model (Figure 10E,F). We conclude that our model accurately predicts many, but not all (see Discussion), of the experimentally determined PMN-MN phase relationships.

## Circuit motifs specific for forward or backward locomotion

PMNs, in addition to connecting to MNs, make pre-synapses onto other neurons (Supplemental Table 3), generating circuit motifs that may play important roles during larval locomotion (Fushiki et al., 2016; Kohsaka et al., 2019). Interestingly, some of these PMNs are active only during forward or backward locomotion (Carreira-Rosario et al., 2018; Fushiki et al., 2016; Kohsaka et al., 2019), indicating they may change the dynamics of motor circuits during forward versus backward locomotion, resulting in different muscle activity patterns during forward or backward crawling. Here we used connectome and neurotransmitter data to examine circuit motifs that include these direction-specific PMNs and asked how they can contribute to the generation of different coactive muscle groups during forward and backward locomotion.

The previously described forward-specific excitatory PMN A27h (Carreira-Rosario et al., 2018; Fushiki et al., 2016), with F3 onset, connects to the excitatory PMNs A18b2 and A18b3 innervating F1-F4 MNs. Thus, when A27h activates F3, it also maintains activity of A18b2 and

A18b3 to ensure continued excitation of F1/F2 MNs (Figure 11A). These motifs provide testable hypotheses for how specific phase relationships between co-activated muscle groups are generated by PMNs. Furthermore, A27h is a component of feedforward excitatory and inhibitory motifs that could explain how different co-activated muscle groups in the adjacent segments are coordinated. A27h innervates the excitatory PMN A18b3 in the next anterior segment, which could advance the forward contraction wave, while A18b3 excites the inhibitory PMNs A06c/A14a to prevent premature activation of F3/4 MNs in the next adjacent segment (Figure 11B). Another forward-specific PMN A01d3 (also known as ifb-FWD) (Kohsaka et al., 2019), is also a component of feedforward excitation and feedforward inhibition motifs involved in temporally segregating F1-F3 from F4 coactive-muscle groups (Figure 11C).

Next, we examined circuit motifs composed of a backward-specific PMN, A27k (also known as ifb-BWD) locomotion (Kohsaka et al., 2019). We identified both feedforward excitation and feedforward inhibition motifs that could explain the sequential activation of a specific co-activated muscle group in adjacent segments during backward motor waves. A27k (innervating B4) is involved in a feedforward inhibitory circuit in which it excites the inhibitory local PMNs A02e and A02g (innervating B1/B2). This motif could coordinate excitation of B3/B4 MNs and termination of B1/B2 MN activity as the contraction wave moves posteriorly (Figure 11D). A27k also synapses in the next anterior segment with the excitatory neurons A01c1, A01c2, and A18j (innervating B4), as well as with the inhibitory PMN A02e innervating B1/B2. This could coordinately terminate B1/B2 MN activity and activate B4 MN activity (Figure 11E). We conclude that circuit motifs composed of forward or backward specific PMNs are likely to be an additional mechanism for generating distinct forward or backward coactivated muscle groups. Functional examination of these motifs is beyond the scope of the current study.

## Discussion

It is a major goal of neuroscience to comprehensively reconstruct neuronal circuits that generate specific behaviors, but to date this has been done only in *C. elegans* (Izquierdo & Beer, 2013; Izquierdo et al., 2015; Karbowski et al., 2008; Kunert et al., 2017; Macosko et al., 2009; Rakowski & Karbowski, 2017). Recent studies in mice and zebrafish have shed light on the overall distribution of PMNs and their connections to several well-defined MN pools (Bagnall & McLean, 2014; Eklof-Ljunggren et al., 2012; Kimura et al., 2013; Ljunggren, Haupt, Ausborn, Ampatzis, & El Manira, 2014). However, in mouse and zebrafish it remains unknown if there are additional PMNs that have

yet to be characterized, and the connectivity between PMNs is not well described, which would be important for understanding the network properties that produce coordinated motor output. In the locomotor central pattern generator circuitry of leech, lamprey, and crayfish, the synaptic connectivity between PMNs or between PMNs and other interneurons are known to play critical roles in regulating the swimming behavior (Brodfuehrer & Thorogood, 2001; Grillner, 2003; Kristan et al., 2005; Mullins et al., 2011; Mulloney & Smarandache-Wellmann, 2012; Mulloney et al., 2014). However, it is difficult to be certain that all the neural components and connections of these circuits have been identified. The comprehensive anatomical circuitry reconstructed in our study provides an anatomical constraint on the functional connectivity used to drive larval locomotion; all synaptically-connected neurons may not be relevant, but at least no highly connected local PMNs are absent from our analysis.

Our results confirm and extend previous studies of *Drosophila* larval locomotion. For example, a recent study (Zwart et al., 2016) has shown that the GABAergic A14a inhibitory PMN (also called iIN1) selectively inhibits MNs innervating muscle 22/LT2 (co-activated muscle group F4), thereby delaying muscle contraction relative to muscle 5/LO1 (co-activated muscle group F2). We extend this study by showing that A14a also disinhibits MNs in early co-activated muscle groups F1/2 via the inhibitory PMN A02e. Thus, A14a both inhibits late co-activated muscle groups and disinhibits early co-activated muscle groups. In addition, previous work has suggested that all MNs receive simultaneous excitatory inputs from different cholinergic PMNs (Zwart et al., 2016). However, our dual calcium imaging data of the A27h excitatory PMN shows that it is active during co-activated muscle group F3 and not earlier. Therefore, MNs may receive temporally distinct excitatory inputs, in addition to the previously reported temporally distinct inhibitory inputs. We have identified dozens of new PMNs that are candidates for regulating motor rhythms; functional analysis of all of these PMNs is beyond the scope of this paper, particularly due to the additional work required to screen and identify Gal4/LexA lines selectively targeting these PMNs, but our predictions are clear and testable when reagents become available.

We show that MNs innervating a single spatial muscle group can belong to more than one co-activated muscle group, therefore spatial muscle groups do not invariably match co-activated muscle groups. This could be due to several reasons: (i) MNs in each spatial muscle groups receive inputs from overlapping but not identical array of PMNs (Supplementary Table 1). (ii) Different MNs in the same spatial muscle group receive a different number of synapses from the same PMN (Supplementary Table 1). (iii) MNs in the same spatial muscle group vary in overall dendritic size and

total number of post-synapses (Supplementary Table 1), thereby resulting in MNs of the same spatial muscle group falling into different co-activated muscle groups.

We demonstrate that during both forward and backward locomotion, most of longitudinal and transverse muscles of a given segment contract as early and late groups, respectively. In contrast, muscles with oblique or acute orientation often show different phase relationships during forward and backward crawling. Future studies will be needed to provide a biomechanical explanation for why oblique muscles – but not longitudinal or transverse muscles – need to be recruited differentially during forward or backward crawling. Also, it will be interesting to determine whether the VO or VL MNs are responsible for elevating cuticular denticles during propagation of the peristaltic wave; if the VOs, it would mean that lifting the denticles occurs at different phases of the crawl cycle in forward and backward locomotion.

Our recurrent network model accurately predicts the order of activation of specific PMNs, yet many of its parameters remain unconstrained, and some PMNs may have biological activity inconsistent with activity predicted by our model. Sources of uncertainty in the model include incomplete reconstruction of inter-segmental connectivity and descending command inputs, the potential role of gap junctions (which are not resolved in the TEM reconstruction), as well as incomplete characterization of PMN and MN biophysical properties. Recent studies have suggested that models constrained by TEM reconstructions of neuronal connectivity are capable of predicting features of neuronal activity and function in the *Drosophila* olfactory (Eichler et al., 2017) and visual (Takemura et al., 2013; Tschopp, Reiser, & Turaga, 2018) systems, despite the unavoidable uncertainty in some model parameters and the likely presence of multiple distinct models that produce activity consistent with recordings (Bargmann & Marder, 2013; Brenner, 2010; Prinz et al., 2004). For the locomotor circuit described here, we anticipate that the addition of model constraints from future experiments will lead to progressively more accurate models of PMN and MN dynamics. Despite its limitations, the ability of the PMN network to generate appropriate muscle timing for two distinct behaviors in the absence of third-layer or command-like interneurons suggests that a single layer of recurrent circuitry is sufficient to generate multiple behavioral outputs. It is also notable that a model lacking complex single-neuron dynamics such as post-inhibitory rebound or spike-frequency adaptation, which are critical for modeling other central pattern generator circuits (Marder & Bucher, 2001), is sufficient to produce the observed motor pattern. Thus, although there are likely complex intrinsic neuronal dynamics that our model fails to capture, recurrent excitatory and inhibitory interactions may play a large role in establishing appropriate motor timing in the larva.

Previous work in other animal models have identified multifunctional muscles involved in more than one motor behavior: swimming and crawling in *C. elegans* (Butler et al., 2015; Pierce-Shimomura et al., 2008; Vidal-Gadea et al., 2011) and leech (Briggman & Kristan, 2006); walking and flight in locust (Ramirez & Pearson, 1988); respiratory and non-respiratory functions of mammalian diaphragm muscle (Fogarty, Mantilla, & Sieck, 2018; Lieske, Thoby-Brisson, Telgkamp, & Ramirez, 2000) unifunctional muscles which are only active in one specific behavior in the lobster *Homarus americanus* (Mulloney et al., 2014); swimming in the marine mollusk *Tritonia diomedea* (Popescu & Frost, 2002); and muscles in different regions of crab and lobster stomach (Briggman & Kristan, 2008; Bucher, Taylor, & Marder, 2006). Our single-muscle calcium imaging data indicates that all imaged larval body wall muscles are bifunctional and are activated during both forward and backward locomotion. It will be interesting to determine if all imaged muscles are also involved in other larval behaviors, such as escape rolling, self-righting, turning, or digging. It is likely that there are different co-activated muscle groups for each behavior, as we have seen for forward and backward locomotion, raising the question of how different co-activated muscle groups are generated for each distinct behavior.

## Methods

### Electron microscopy and CATMAID reconstructions

Neurons were reconstructed in CATMAID using a Google Chrome browser as previously described (Ohyama et al., 2015). Candidate PMNs were discarded if their maximum MN connectivity was ≤5 synapses (summed across the left and right hemispheres), where the neuron could not be traced due to gaps in the TEM volume, and a few neurons with massive arbors which were beyond our ability to trace. Figures were generated using CATMAID graph or 3D widgets combined with Adobe Illustrator (Adobe, San Jose, CA).

### Synapse spatial distributions and clustering

Synapse spatial distributions were generated using custom MATLAB scripts. Spatial distributions were determined using kernel density estimates with a 1 μm bandwidth. For cross-sectional spatial distributions, points were rotated -12 degrees around the Z-axis (A/P axis) in order to account for the slight offset of the EM-volume. For pre-synaptic sites, polyadic synapses were weighted by their

number of post-synaptic targets. Synapse similarity was calculated as described previously (Schlegel et al., 2016):

$$f(is, jk) = e^{\frac{-d_{sk}^2}{2\sigma^2}} e^{\frac{|n_{is}-n_{jk}|}{n_{is}+n_{jk}}}$$

where *f(is,jk)* is the mean synapse similarity between all synapses of neuron *i* and neuron *j*. $d_{sk}$ is the Euclidean distance between synapses *s* and *k* such that synapse *k* is the closest synapse of neuron *j* to synapse s of neuron *i*. σ is a bandwidth term that determines what is considered close. $n_{is}$ and $n_{jk}$ are the fraction of synapses for neuron *i* and neuron *j* that are within ω of synapse *s* and synapse *k* respectively. For MN inputs, σ = ω = 2 µm. Clustering was performed by using the average synapse similarity scores for the left and right hemisegments as a distance metric, and linkage was calculated using the average synapse similarity. For comparing the distributions across individual axes, a two sample Kolmogorov-Smirnov test was used to determine significance.

## Clustering analysis of PMN-MN connectivity

Weighted PMNs to MNs connectivity matrix was acquired from CATMAID TEM volume as percentage of total number of post-synaptic links to these target MNs. We then calculated the average of left and right pairs of PMNs and MNs. Next, we averaged the mean connections from PMNs to all MNs innervating muscle groups defined in Figure 7A, B, and D. Hierarchical clustering was performed on these averaged connectivity matrixes using Python's seaborn.clustermap ( standard_scale=0, metric= correlation, method= single, https://seaborn.pydata.org/generated/seaborn.clustermap.html).

## Muscle GCaMP6f imaging, length measurement, and quantification

2% melted agarose was used to make pads with similar size: 25mm (W) X 50mm (L) X 2mm (H). Using tungsten wire, a shallow ditch was made on agarose pads to accommodate the larva. To do muscle ratiometric calcium imaging in intact animals, a first or second instar larvae expressing

GCaMP6f and mCherry in body wall muscles were washed with distilled water, then moved into a 2% agarose pad on the slide. A 22 mm × 40 mm cover glass was put on the larva and pressed gently to gently constrain larval locomotion. The larva was mounted dorsolaterally or ventrolaterally to image a different set of muscles (dorsolateral mount excludes the most ventral muscles (15,16,17) whereas the ventrolateral mount excludes the dorsal-most muscles (1,2,9,10); imaging was done with a 10x objective on an upright Zeiss LSM800 microscope. We recorded a total of 38 waves (24 forward and 14 backward) from four different animals, and examined muscle calcium activity in two subsequent hemi-segments for each wave. Muscle length measurement was done using custom MATLAB scripts where muscle length was measured on a frame by frame basis. Calcium imaging data was also analyzed using custom MATLAB scripts. Due to movement artifacts, ROIs were updated on a frame by frame basis to track the muscle movement. ROIs that crossed other muscles during contraction were discarded. In no single preparation was it possible to obtain calcium traces for all 30 muscles. Instead, we used only preparations in which at least 40% of the muscles could be recorded. In order to align crawl cycles that were of variable time and muscle composition, we first produced a 2 dimensional representation of each crawl cycle using PCA. Crawl cycles were represented as circular trajectories away from, and back towards the origin (Figure 3 – figure supplement 1E,F) similar to what has been shown previously (Lemon et al., 2015). The amplitude, or linear distance from the origin, to a point on this trajectory correlated well with both the coherence of the calcium signals as well as the amplitude of the population. Thus, peaks in this 2D amplitude correspond with the time in which most muscles are maximally active, which we defined as the midpoint of a crawl cycle. It should be noted that the muscles used to generate two dimensional representations of crawl cycles were different for each crawl. While this means that each PCA trajectory is slightly different for each crawl cycle, we reasoned that because each experiment contained muscles from every co-activated muscle group, the peak amplitude in PCA space should still correspond to a good approximation of the midpoint of the crawl cycle. We defined the width of a crawl cycle as the width of this 2D peak at half-height (Figure 3 – figure supplement 1G). We aligned all crawl cycles to the crawl onset and offset (which we call 25% and 75% of the crawl cycle respectively) as defined by this width at half-height (Figure 3 – figure supplement 1H,I).

### Calcium imaging in neurons

For dual-color and single-color calcium imaging in fictive preps, freshly dissected brains were mounted on 12mm round Poly-D-Lysine Coverslips (Corning® BioCoat™) in HL3.1 saline (de Castro, Titlow, Majeed, & Cooper, 2014), which were then were placed on 25 mm × 75 mm glass

slides to be imaged with a 40× objective on an upright Zeiss LSM-800 confocal microscopy. To simultaneously image two different neurons expressing GCaMP6m we imaged neuron-specific regions of interest (ROI). In addition, we imaged two neurons differentially expressing GCaMP6m and jRCaMP1b. Image data were imported into Fiji (https://imagej.net/fiji) and GCaMP6m and jRCaMP1b channels were separated. The $\Delta F/F_0$ of each ROI was calculated as $(F-F_0)/F_0$, where $F_0$ was averaged over ~1s immediately before the start of the forward or backward waves in each ROI.

## Antibody staining and imaging

Standard confocal microscopy, immunocytochemistry and MCFO methods were performed as previously described for larvae (Carreira-Rosario et al., 2018). Primary antibodies used: GFP or Venus (rabbit, 1:500, ThermoFisher, Waltham, MA; chicken 1:1000, Abcam13970, Eugene, OR), GFP or Citrine (Camelid sdAB direct labeled with AbberiorStar635P, 1:1000, NanoTab Biotech., Gottingen, Germany), GABA (rabbit, 1:1000, Sigma, St. Louis, MO), mCherry (rabbit, 1:1000, Novus, Littleton, CO), HA (mouse, 1:200, Cell Signaling, Danvers, MA), or V5 (rabbit, 1:400, Rockland, Atlanta, GA), Flag (rabbit, 1:200, Rockland, Atlanta, GA). Secondary antibodies were from Jackson Immunoresearch (West Grove, PA) and used according to manufacturer's instructions. Confocal image stacks were acquired on Zeiss 710 or 800 microscopes. Images were processed in Fiji (https://imagej.net/Fiji), Photoshop, and Illustrator (Adobe, San Jose, CA). Brightness and contrast adjustments were applied to the entire image uniformly; mosaic images were assembled in Photoshop (Adobe, San Jose, CA).

## Recurrent network model

### Model dynamics

We constructed a recurrent network representing the activity of PMNs, which we denote by the vector $\mathbf{p}$, and of MNs, which we denote by the vector $\mathbf{m}$. The firing rate of PMN or MN $i$ is a rectified-linear function of its input: $p_i(t) = [u_i^p(t)]_+$ or $m_i(t) = [u_i^m(t)]_+$, where $[\cdot]_+$ denotes rectification. The PMN input $\mathbf{u}^p$ follows the differential equation:

$$\boldsymbol{\tau}^p \odot \frac{d\mathbf{u}^p}{dt} = -\mathbf{u}^p(t) + \mathbf{g}^p \odot (\mathbf{J}^p\mathbf{p}(t) + \mathbf{b}^p + \mathbf{I}(t)),$$

where $\tau_i^p$ is the time constant of PMN $i$, $b_i^p$ its baseline excitability, $I_i(t)$ its descending input from other regions, $\odot$ denotes element-wise multiplication, and $\mathbf{J}^p$ is the connectivity matrix among PMNs. We also include a neuron-specific gain term $g_i^p$ which determines how sensitive a PMN is to its inputs (this is required because we fix the scale of $\mathbf{J}$ based on the TEM reconstruction). The descending input to the PMNs $\mathbf{I}(t)$ is represented as a pulse of activity: $\mathbf{I}(t) = \mathbf{I}^{FWD}$ during FWD crawling, $\mathbf{I}(t) = \mathbf{I}^{BWD}$ during BWD crawling, and $\mathbf{I}(t) = 0$ otherwise.

MNs follow similar dynamics:

$$\boldsymbol{\tau}^m \odot \frac{d\mathbf{u}^m}{dt} = -\mathbf{u}^m(t) + \mathbf{g}^m \odot (\mathbf{J}^m \mathbf{p}(t) + \mathbf{b}^m),$$

where $\mathbf{J}^m$ is the connectivity matrix from PMNs to MNs.

To generate PMNs and MNs corresponding to the A2 segment, we duplicated the A1 MNs and the PMNs we reconstructed for which no corresponding neuron in the next anterior segment was reconstructed. This produces a connectivity matrix with an approximate block structure:

$$\mathbf{J}^p = \begin{pmatrix} \mathbf{J}_{11}^p & \mathbf{J}_{12}^p \\ \mathbf{J}_{21}^p & \mathbf{J}_{22}^p \end{pmatrix}, \ \mathbf{J}^m = \begin{pmatrix} \mathbf{J}_{11}^m & \mathbf{J}_{12}^m \\ \mathbf{J}_{21}^m & \mathbf{J}_{22}^m \end{pmatrix},$$

where $\mathbf{J}_{rs}^{p/m}$ represents connections from segment $r$ to segment $s$.

*Target activity*

The model parameters ($\mathbf{J}$, $\mathbf{g}$, $\mathbf{b}$, $\boldsymbol{\tau}$, $\mathbf{I}$) are adjusted using gradient descent so that the MN activity $\mathbf{m}$ reproduces target patterns of activity during FWD and BWD crawling. These targets are defined for 6 s trials that contain one sequence of CMUG activation in each of the two segments. Time is discretized into 50 ms bins. At the beginning of each trial, $\mathbf{u}^p$ is initialized with random values from a truncated Gaussian distribution with standard deviation 0.1, and $\mathbf{u}^m$ is initialized to 0. A trial consists of sequential activity in each segment with a 1 s inter-segmental delay (Figure 9). Trials begin and end with 1 and 1.5 s of quiescence, respectively. Each MN's target activity is given by a rectified cosine pulse of activity whose start and end times depend on the CMUG to which it belongs. The first CMUG is active for 2 s, and subsequent CMUGs activate with a delay of 0.25 s between each group and end with a delay of 0.125 s between groups. The participation of MNs in CMUGs and the order

in which the segments are active during FWD and BWD crawling are inferred from the data (Figure 3).

**Parameter constraints and optimization**

Constraints are placed on the model parameters based on knowledge of the circuit. The nonzero elements of $\mathbf{J}^p$ and $\mathbf{J}^m$ are determined from the TEM reconstruction (normalized based on the percent input received by the post-synaptic target), and signs are constrained using neurotransmitter identity when available. If the neurotransmitter identity of a neuron is not known, we initialize the connection to be inhibitory but do not constrain its sign during optimization. Time constants $\boldsymbol{\tau}$ are constrained to be between 50 ms and 1 s (these represent combined membrane and synaptic time constants), and gains $\mathbf{g}$ are constrained to be positive.

At the beginning of optimization, the biases $\mathbf{b}^p$ and $\mathbf{b}^m$ are initialized equal to 0.1 and 0, respectively. Time constants $\boldsymbol{\tau}$ are initialized to 200 ms and gains $\mathbf{g}$ to 1. $\mathbf{I}^{FWD}$ and $\mathbf{I}^{BWD}$ are initialized uniformly between 0.05 and 0.15 for each neuron. To initialize $\mathbf{J}^p$ and $\mathbf{J}^m$, initial connection strengths are taken in proportion to synapse counts from the TEM reconstruction with a scaling factor of $\pm 0.005$ for excitatory/inhibitory connections. Connections within a model segment are taken from the TEM reconstruction of A1, while connections from A1 to A2 or A2 to A1 are taken from the corresponding cross-segmental reconstructions (and are thus likely less complete than the within-segmental connectivity).

The cost function that is optimized consists of a term $C_{targ}$ that penalizes deviations of the MN activities from their targets and three regularization terms to promote realistic solutions. The target term is given by $C_{targ} = \sum_{t,i} w_i \, ||m_i(t) - m_i^*(t)||^2$, where $m_i^*(t)$ is the target activity for MN $i$ and $w_i$ is a weighting term, proportional to $1/\sqrt{N_{CMUG,i}}$ where $N_{CMUG,i}$ is the number of neurons in the CMUG of neuron $i$ (this scaling ensures the target patterns of CMUGs with few MNs are still reproduced accurately).

The first regularization term is given by $C_{A18b,A27h} = 0.05 \cdot (\sum_{t \in FWD} |p_{A18}(t)| + \sum_{t \in BWD} |p_{A27}(t)|)$, which suppresses the activity of the A18b and A27h neurons for behaviors during which they are known to be quiescent. The second regularization term $C_{seg}$ constrains PMN activity to reflect the timing of segmental activation. It is given by

$$C_{seg} = \alpha_n \sum_{t \in active1} ||\mathbf{p}_1(t) - \mathbf{p}_2(t - t_{delay})||^2 ,$$

where active1 represents the times when segment 1 is active, $\mathbf{p}_1$ and $\mathbf{p}_2$ represent vectors of PMN activities corresponding to pairs of homologous neurons in adjacent segments, and $t_{delay}$ is the time delay between segment 1 and 2 activations (equal to -1 s for forward and +1 s for backward crawling). This term ensures that PMN activity in the A1 and the A2 segments is similar but offset in time. The scaling term $\alpha_n$ increases quadratically from 0 to 0.1 over the 1000 training epochs. The final term $C_J = \alpha_n\left(||\mathbf{J}^p - \mathbf{J}_0^p||^2 + ||\mathbf{J}^m - \mathbf{J}_0^m||^2\right)$ penalizes deviations of model weights from the initial weights given by the TEM reconstruction.

The total cost, equal to $C_{targ} + C_{A18b,A27h} + C_{seg} + C_J$, is optimized using the RMSProp optimizer for 1000 epochs. During each epoch, the costs corresponding to one FWD and one BWD trial are averaged. The learning rate decreases from $10^{-2}$ to $10^{-3}$ logarithmically over the course of optimization.

## Acknowledgements

We thank Luis Sullivan, Emily Sales, and Hiroshi Kohsaka for comments. B.M. was supported by an NIH training grant T32HD007348. A.C. was supported by HHMI. A.L.-K. was supported by the Burroughs Wellcome Foundation, the Gatsby Charitable Foundation, the Simons Collaboration on the Global Brain, and NSF award DBI-1707398. C.Q.D. and A.A.Z were supported by HHMI and NIH HD27056.

**Table 1. Motor neurons present in the CATMAID reconstruction.**

All MNs were identified in the first abdominal segment on both left and right sides, with the exception of MN25 which is not present in A1 and thus annotated in A2. See text for abbreviations.

| Spatial Muscle Group | Nerve | Motor neurons (synonyms) | Target Muscles (synonyms) | Synapse Type |
|---|---|---|---|---|
| DL | $ISN^{DM}$ | MN1 (aCC) | 1 (DA1) | Ib |
| | $ISN^{DM}$ | MN2 (U3) | 2 (DA2) | Ib |
| | $ISN^{DM}$ | MN3 (U4) | 3 (DA3) | Ib |
| | $ISN^{DM}$ | MN4 (U5) | 4 (LL1) | Ib |
| | $ISN^{DM}$ | MN9 (U1) | 9 (DO1) | Ib |
| | $ISN^{DM}$ | MN10 (U2) | 10 (DO2) | Ib |
| DO | $ISN^{L}$ | MN11 | 11 (DO3) | Ib |
| | $ISN^{L}$ | MN19 | 19 (DO4) | Ib |
| | $ISN^{L}$ | MN20 | 20 (DO5) | Ib |
| | SNa | MN5 (LO1) | 5 (LO1) | Ib |
| VL | ISNb | MN6/7 (RP3) | 6/7 (VL3/VL4) | Ib |
| | ISNb | MN12 (V-MN) | 12 (VL1) | III |
| | ISNb | MN13 (MN-VL2) | 13 (VL2) | Ib |
| | ISNb | MN14 (RP1) | 14 (VO2) | Ib |
| | ISNb | MN30 (RP4) | 30 (VO1) | Ib |
| VA | SNc | MN26 | 26 (VA1) | Ib |
| | SNc | MN27 | 27 (VA2) | Ib |
| | SNc | MN29 | 29 (VA3) | Ib |
| VO | ISNd | MN15/16 (MN-VO4/5) | 15/16 (VO4/VO5) | Ib |
| | ISNd | MN15/16/17 (MN-VO4-6) | 15/16/17 (VO4/VO5/VO6) | Ib |
| | ISNb | MN28 | 28 (VO3) | Ib |
| T | SNa | MN8 (SBM) | 8 (SBM) | Ib |
| | SNa | MN21/22 (LT1/LT2) | 21/22 (LT1/LT2) | Ib |
| | SNa | MN22/23 (LT2/LT3) | 22/23 (LT2/LT3) | Ib |
| | SNa | MN23/24 (LT3/LT4) | 23/24 (LT3/LT4) | Ib |
| | $ISN^{L}$ | MN18 | 18 (DT1) | Ib |
| | TN | MN25 (VT1) | 25 (VT1) | Ib |
| Broad | $ISN^{DM}$ | MNISN (RP2) | 1/2/3/4/9/10/11/[18]/19/20 (DA/DO) | Is |
| | ISNb | MNISNb/d (RP5) | 6/7/12/13/14/15/16/30 (VL/VO) | Is |
| | SNa | MNSNa-II (VUM) | 21/22/[23/24/25] (LT) | II |
| | $ISN^{DM}$ | MNISN-II (VUM) | 1/2/3/4/9/10/11/18/19/20 (DA/DO) | II |
| | ISNb | MNISNb/d-II (VUM) | 12/13/14/15/16/17/30 (VL/VO) | II |

**Table 2. Co-activated muscle groups during forward or backward locomotion.**

There are four co-activated muscle groups during backward and forward locomotion, but the muscles in each group differ in forward versus backward locomotion. Note that backward locomotion is not simple a reverse of the pattern seen in forward locomotion. This represents the most common activation sequences, although there is some variation, particularly during the fastest locomotor velocities.

| Forward | Co-activated muscles |
|---|---|
| F1 | 2,6,10,11,14,30 |
| F2 | 3,4,5,9,12,13,18,19,25,26,29 |
| F3 | 1,8,15,16,17,20,28 |
| F4 | 21,22,23 |

| Backward | Co-activated muscles |
|---|---|
| B1 | 10,15,16,17 |
| B2 | 1,3,4,6,9,12,13,28 |
| B3 | 2,5,8,19,20,26,29 |
| B4 | 11,18,21,22,23,24 |

## Table 3. Premotor neurons innervating type Ib MNs

Left column, spatial muscle groups named as in Figure 1. Middle column, type Ib MNs innervating 1-3 muscles in each muscle group (synonym, parentheses); the immature neuromodulatory VUMs are not shown. Right column, premotor interneurons innervating the indicated MNs (green, presumed excitatory; red, presumed inhibitory; grey, corozonergic; black, unknown. Premotor connectivity uncertain, parentheses.

| Muscle position | Motor Neurons | Pre-Motor Neurons |
|---|---|---|
| DL | MN1-Ib (aCC) | A27h, A18a, A18b, A03g, A31k, A31b, A06e, A23a, A02h, A10e, A03a1, A03a3, A05k, A07f2, DLN2, TJPMN, Thoracic descending pre-longitudinals, T27Y, |
| | MN2-Ib (U3) | dsnPMN2, DLN1, A18neo |
| | MN3-Ib (U4) | A01x2, A18a, A03a5, A31k, A31b, A23a, A02h, A03a3, A03a1, A10e, A10a , T27Y, dsnPMN2, |
| | MN4-Ib (U5) | A18a, A03a5 A03g, A31k, A31b, A06e, A02h, A02e, A02f, A03a3, A03a6, A03d/e, A03x-eghb, A07f2, A10a, DLN2, A18neo |
| | MN9-Ib (U1) | A03a5, A03g, A31k, A27l, A06l, A06m, A06g2, A02e, A02f, A03a6, A03a1, A03x-eghb, SePN02b, DLN2, Descending pre RP3, A18neo |
| | MN10-Ib (U2) | A01x2, A18a, A31k, A31b, A06x1, A27l, A23a, A02m, A02n, A02h, A03a1, A03a3, A03x-eghb, A03xyz, A05k, DLN2, TJPMN, Tipsi, T27Y, dsnPMN2, DLN1, A18neo, |
| | | A01x2, A18b, A08e1, A31k, A27j, A23a, A06a, A06x1, A02h, A02e, A02g, A10e, |
| DO | MN11-Ib | A03a1, A03a3, A03x, A03a4, A03d/e, A03x-eghb, VLELX4, Tipsi, dsnPMN2, |
| | MN19-Ib | DLN2, DLN1, A18neo, A18c |
| | MN20-Ib | |
| | MN5-Ib (LO1) | A31k, A06x1, A23a, A06a, A27l, T03g2, A03a1, A03a3, A03x-eghb |
| | | A27k, A18j, A18b, A18b3, T01d2, A31k, A27j, A23a, A06a, A06l, A06x1, A02f, A03a1, A03a3, T27Y, dsnPMN2, A27neo |
| VL | MN6/7-Ib (RP3) | A27h, A18j, A01c1, T01d2, T01d4, A19l, A06e, A03d/e, A27neo, a14neo, A03xyz, |
| | MN12-III (V-MN) | A26f |
| | MN13-Ib (MN-VL2) | A18b3, A18b2, A23a, A03a1, A03a3, A03a4, VLELX4, T27Y |
| | MN14-Ib (RP1) | |
| | MN30-Ib (RP4) | A18b3, A03a5, A27l, A06l, A06e, A02g, A02e, A03a4, T)6WW, T06PP, Descending pre RP3, |
| | | A27h, A03a5, A03g, A02g, A02e A27l, A06l,, A06e A03a6, A03a4, A03d/e, DLN1, Descending pre RP3, |
| VA | MN26-Ib | A27k, A03a5, A03g, A01d3, T01d4, A06l, A06a, A06e, A02g, A02e, A27l, A03a6, A03a4, A03x-eghb, A03d/e |
| | | A27h, A18b2, A18b3, A27l, A06l, A02i, A03a4, A03a1, DLN1 |
| | MN27-Ib | |
| | | A18b3, A03a5, A01x2, A01d3,A01d4, A06e , A27l, A06l, A02g, A02e, A03a4, |
| | MN29-Ib | A03a6, A03x-eghb, A03d/e, A03SNC, A10a, A27Uniq, DLN1, A03xyz, SePN02b |
| VO | MN15/16-Ib | A27h, A01x3, A18f, A02j, A06e, A06l, A27l, T03g2, A03x-eghb, Descending |
| | MN15/16/17-Ib | neuron_SEZ, A03SNC, A03xKT, , A03d/e, T11v, T27Y, |
| | MN28-Ib | |
| | | A27h, A27k, A03g, A18j, A18f, A01x3, A01c1, A01c2, T01d2, T01d4, A06e, A06f, A19l, A14a, A31b, T03g2, A27n, , A27neo, A03xKT, T11v, A26f |
| T | MN8-1b (SBM) | A01x3, A01x2, A01x3, T01d2, T01d4, A27l, A02g, A06e, T03g2, A27e2, A03a6, |
| | MN18-Ib | A03d/e, A10a, A27neo, T11v, A03SNC |
| | MN21/22-Ib (LT1/LT2) | A27h, A27k, A18b2, A06c, A06l, A06e, A02g, A02i, A03a6, DLN1 |
| | | A27h, A03g, A06c, A06e, A27l, A02g, A02i, A01j, A27Uniq, |
| | MN22/23-1b (LT2/LT3) | A01x2, A27h, A18b2, A06c, A06l, A06e, A02g, A02i, A03a6 |
| | MN23/24-1b (LT3/LT4) | A01c1, A01c2, A01d3, A27k, A03g, T01d1, A18j, A19l, A14a, A27n, A27e2, A27neo, A26f |

| | | |
|---|---|---|
| | MN25-Ib (MN-VT1) | A01c1, A01c2, A01d3, A03g, A03o, A18j, A06a, A23a, A19l, A14a, A06x1, A02i, A01j, A27n, A10a, A10b, A27neo, T27Y, A26f |
| DL/DO | MNISN (RP2) | A01c1, A01c2, A27k, A03g, A18j, A18b2, T01d1, T01d2, A19l, A14a, A02i,A02f, A03xKT, T27Y, TGun, A27n, A27neo, A26f |
| VL/VO | MSNISNb/d(RP5) | A01x, A01c1, A01c2, A27k, A03g, A09l, A18j, T01d1, T01d2, A01d3, A19l, A14a, A02f, A27n, A27neo, A27e2, T27Y, A26f<br><br>A27k, A18j, A03g, A01c1, A01c2, T01d1, T01d2, A01d3, A19l, A27n, A27neo, A26f<br><br>A01c1, A18a, A18b2, A18j, A18f, A27l, A14a, A19l, A02i, A31d, A03xKT, A05a<br><br>A01x2, A18b, A03g, A31k, A27j, A27l, A02m, A02n, A02b, A06a, A23a, A03a1, A03a3, A03d/e, A03x-eghb, A05k, A10a, DLN2, DLN1, A18neo, dsnPMN2, SePN02b, T27Y, TJPMN, Projection neuron, A18c,<br><br>A27h, A03a5, A06l, A06c, A06f, A02g, A02e, A02b, A03a4, A03a6, A03x-eghb, A03d/e, A19d, A27Uniq, DLN1, SePN02b |

**Figure 1. Schematic depiction of the larval neuromuscular system.**

(A) *Drosophila* larva contain three thoracic and nine abdominal segments, the muscles of which are innervated by MNs located in the corresponding thoracic and abdominal segments of the CNS.

(B) Schematic of the 30 muscles of abdominal segments (A2-A6) from internal and external view. Segment A1 is similar to A2-A6, with the exception that it lacks muscle 25 and MN-25.

**Figure 2. All body wall muscles are utilized during forward and backward locomotion.**

(A,D) Sequential images of muscle GCaMP6f ΔF/F signal during forward (A) or backward (D) locomotion. GCaMP6f levels were normalized to mCherry. Anterior to left, dorsal up; time in seconds. Genotype: *GMR44H10-LexA lexAOP-GCaMP6f; -LexA lexAOP--mCherry*. Arrowheads mark the same segment at each timepoint.

(B,E) Mean calcium transient (blue) vs mean muscle length (red) measurements for muscle 6 during forward (B) or backward (E) locomotion. N = 3 segments. $T_0$ was set as the point of maximum contraction as determined by muscle length for each crawl. Shaded bars represent standard deviation.

(C,F) All observed muscles show calcium transients greater than 100% ΔF/F during forward (C) or backward (F) locomotion. Each dot represents the maximum GCaMP ΔF/F signal in the indicated muscle during a single crawl, normalized to mCherry. Error bars represent standard deviation. Muscle names as in Figure 1.

**Figure 3. Larval body wall muscles form four co-activated muscle groups during forward and backward locomotion**

(A) Hierarchical clustering of mean activity for all observed muscles yields four co-activated muscle groups during forward locomotion (F1-F4) and a different group of four during backward locomotion (B1-B4). Heatmaps represent the mean range-normalized calcium activity of each muscle (n > 3 forward crawl bouts for each muscle, with a total of 337 individual muscles analyzed across 23 crawls for forward and 188 individual muscles analyzed across 14 crawls for backward locomotion). Muscles 6/7 are grouped because they are both innervated by the same MN. Clustering was

performed only on the first half of the crawl cycle to determine the onset time for each co-activated muscle group. Cluster number was determined by visual inspection of the dendrogram as well as the gap-criterion optimal cluster number.

(B) Plots of average muscle activity for muscles in each forward co-activated muscle group. Error bars represent the standard deviation of individual muscles.

(C) Plots of average forward co-activated muscle group activity timing. Error bars represent the standard deviation of the average muscle activity of each muscle in a given co-activated muscle group. Dotted lines represent the average muscle activity for each muscle in a given co-activated muscle group. Red line along the x-axis represents the fraction of the crawl cycle that was used for clustering.

(D) Plots of average muscle activity for muscles in each backward co-activated muscle group. Error bars represent the standard deviation of individual muscles.

(E) Plots of average backward co-activated muscle group activity timing. Error bars represent the standard deviation of the average muscle activity of each muscle in a given co-activated muscle group. Dotted lines represent the average muscle activity for each muscle in a given co-activated muscle group. Red line along the x-axis represents the fraction of the crawl cycle that was used for clustering.

(F) Schematic representation of the co-activated muscle group for forward locomotion.

(G) Schematic representation of the co-activated muscle group for backward locomotion.

(H) During forward locomotion, muscle 11 is activated before muscle 15-17, while their order is flipped during backward crawling.

## **Figure 3 – supplement 1. PCA-based alignment of crawl cycles.**

(A-D) Plots of four representative forward crawls show a high degree of variability in the crawl structure.

(E-F) 2D projection of forward and backward crawl cycles. Crawl cycles are represented as rotations away from and back towards the origin. Color changes (from blue to red) represent time. Directionality is not uniform given that the group of analyzed muscles in each crawl cycle is different in each case (all crawls used had at least 40% of the muscles analyzed in the segment).

(G)Amplitude of a representative forward crawl in the same 2D space. The peak of this activity was defined as the center of a crawl cycle, and the peak width at half the height of the peak was used to find crawl-start and crawl-end times.

(H) All analyzed forward muscles aligned. Grey lines represent individual muscles, black line represents the average activity of all muscles with error bars representing standard deviation. Red dotted line represents the crawl-start alignment point, and the blue line represents the crawl-end alignment point.

(I) Average activity of forward (black) and backward (red) crawls across all experiments.

(J) Single segment crawl length determined for each crawl (n = 24 forward / 14 backward). Crawl length is determined by calculating the width of the 2D representation of the crawl cycle.

**Figure 3 - supplement 2. Muscles recruited at similar and different phases of the forward and backward crawl cycle.**

Red dotted lines represents the activity onset (see Methods for details). Red solid line represents the average activity of the muscles during backward locomotion with error bars (light red ribbon) representing the standard deviation. Black line represents the average activity of the muscles during forward locomotion with error bars (gray ribbon) representing the standard deviation. Muscles show differential (top) or similar (bottom) phase of onset during forward and backward locomotion.

**Figure 4. Identification of all differentiated motor neurons in segment A1 of the TEM volume.**

(A) Dorsal view of the TEM reconstruction of the L1 CNS (gray shading) showing all bilateral MNs reconstructed at single synapse level. The one intersegmental dendrite is from RP3 in A1; it is not observed in other abdominal segments.

(B) Dorsal view of centered on the A1 segment; midline, arrowhead. MNs are color-coded as in Figure 1B.

(C) Posterior (cross-section) view of the neuropil (outlined) and cortex in A1. Note the MN dendrites target the dorsal neuropil.

(D) Representative images showing the morphological similarity between MNs identified in vivo by backfills (Mauss et al., 2009) versus the most similar MN reconstruction from the TEM volume. The top section in each panel shows the morphology of the MN dendrites based on in vivo backfills; used with permission); six distinct Fas2 fascicles (three per hemisegment) are shown in white; midline, arrowhead. The bottom section shows MN dendrite morphology reconstructed from the TEM volume in A1.

**Figure 4 – Supplement 1a,b. Reconstruction and Identification of A1 MNs using ssTEM.**

MN names are shown in bottom left for each reconstruction. The morphology of each MN is shown in cross-sectional (left) and dorsal view (right). In the cross-sectional views, neuropil boundary is shown in gray. In the dorsal views, L, M, R stand for Left neuropil border, Midline, Right neuropil border, respectively. Cyan dot depicts the post-synaptic sites on MNs.

**Figure 5. Motor neurons innervating spatial muscle groups or co-activated muscle groups have post-synapses in distinct regions of neuropil.**

(A) Spatial distributions of post-synaptic sites for MN pools innervating distinct spatial muscle groups (labeled in box). Plots are 1D kernel density estimates for the mediolateral (ML), dorsoventral

(DV) and anteroposterior (AP) axes. Arrowheads represent peaks of significantly different distributions (two sample Kolmogorov-Smirnov test; $p<.05$).

(B) Hierarchical clustering of MNs by their synapse similarity score reveals MN myotopic organization. To generate a similarity matrix, pairwise synapse similarity scores were generated separately for MNs exiting the left A1 nerve and right A1 nerve. The pairwise similarities for the left and right pools of MNs were highly correlated; $R = .95$. Clustering was performed on the average of the left and right similarity matrices.

(C) Density estimates of the post-synaptic sites for MN pool innervating forward co-active muscle groups (labeled in box). Arrowheads represent peaks of significantly different distributions (two sample Kolmogorov-Smirnov test; $p<.05$)

(D) Spatial distribution of post-synapse locations for MN18 (red) vs remaining transverse muscles (black) shows MN18 has more posterior distribution of post-synapses compared to the remaining neurons in the same spatial muscle group. (E) Spatial distribution of post-synapse locations for MN2 (red) versus remaining dorsal longitudinal muscles (black) shows no difference in spatial distribution compared to the remaining neurons in the same spatial muscle group.

**Figure 6. Identification of 118 premotor neurons at synapse-level in the EM reconstruction.**

(A) Dorsal view centered on the A1 segment showing all 118 pair of PMNs reconstructed in this study.

(B) Posterior (cross-section) view of the PMN pre-synapse location (red) and post-synapse location (cyan) within the A1 neuropil. Density plots shown for the dorsoventral axis (left) and mediolateral axis (bottom). Dorsal, up.

(C) Dorsal view of entire larval neuropil to show anteroposterior distribution of pre-synapse (red) and post-synapse (cyan) location. Density plots shown for the anteroposterior axis (bottom).

(D-G) Quantification of PMN-MN connectivity. All A1 MNs, A2 MN-25, and 118 pair of PMNs were used to generate these histograms. (D) PMNs innervate an average of 8 MNs. X-axis shows binned number of MNs receiving inputs from PMNs. Y-axis shows number of PMNs in each bin (D') Swarm-violin plot representation of the same dataset used in D. (E) MNs receive inputs from an average of 32.5 PMNs from this population of PMNs. X-axis shows binned number of PMNs providing output to MNs. Y-axis shows number of MNs in each bin. (E') Swarm-violin plot representation of the same dataset used in E. (F) Histogram showing binned fraction of PMN output to MNs. Y-axis shows number of PMNs in each bin. (F') Swarm-violin plot representation of the same dataset used in F. (G) Histogram showing binned fraction of MN inputs from PMNs. Y-axis shows number of MNs in each bin. 76% of total MN post-synapses receive input from the 118 PMNs. (G') Swarm-violin plot representation of the same dataset used in G.

(H-J) Quantification of PMN morphology.

**Figure 6 – supplement 1. All premotor neurons traced in the TEM volume.**

Dorsal view (top) and posterior view (bottom) of all 118 premotor neurons. In all panels, neuron names are at the top; red and cyan dots indicate pre-synaptic and post-synaptic sites respectively. Neurons with all pre- and post-synaptic sites intermixed are boxed.

**Figure 7. PMN pools preferentially connected to individual spatial muscle groups and co-activated muscle groups.**

(A,B,D) Hierarchical clustering of PMNs based on their connectivity to MNs of the same spatial muscle group (A), forward co-activated muscle group (B), or backward co-activated muscle group (D). The data were standardized within the rows, with maximum assigned 1.0 and other row values relative to that maximum value. Heat maps represent the mean of normalized weighted-synaptic output of a given left/right pair of PMNs onto left/right pair of MNs grouped in each panel. (A) Pools of PMNs show enriched connectivity to spatial muscle groups (dark blue). (B) Pools of PMNs show enriched connectivity to F1-F4 co-activated muscle groups (dark blue); arrow, A27h. (D) Pools of PMNs show enriched connectivity to B1-B4 co-activated muscle groups (dark blue).

(C) Dual color calcium imaging of jRCaMP1b in A27h (red) and GCaMP6m in U1-U5 MNs (black).

Consistent with predictions from the connectome, U1-U5 MNs (co-activated muscle group F1/2) are activated before A27h (co-activated muscle group F3) during forward locomotion. Red and dark error bars (ribbons) represent the standard deviation of the average neuronal activity. Genotype: *CQ-lexA/+; lexAop-GCaMP6m/R36G02-Gal4 UAS-jRCaMP1b.*

**Figure 8. Neuronal asymmetry along the anterior-posterior axis may contribute to differences seen between forward and backward co-activated muscle groups.** (A) MN18 has asymmetric posterior dendrites that could be activated earlier during forward locomotion than during backward locomotion. (B) MN25 has asymmetric anterior dendrites that could be activated earlier during backward locomotion than during forward locomotion. (C) PMN A02i has an asymmetric anterior axon that could inhibit target MNs earlier during forward locomotion than during backward locomotion. (D) PMN A03a4 has an asymmetric anterior axon that could excite target MNs earlier during forward locomotion than during backward locomotion.

(E, F) Both PMN A03a5and A01j have asymmetric posterior axon that could induce target MNs earlier during backward locomotion than during forward locomotion.

**Figure 9. Recurrent network model generating sequential MN activity.**

(A) The PMN and MN network of the A1 and A2 segments was modeled using connectivity taken from the EM reconstruction. Connections within each segment (light gray circles) are identical. The network was optimized using gradient descent to produce a sequential pattern of activity in the MNs (MNs) when a tonic external command input for forward (forward, black) or backward (backward, red) locomotion was applied.

(B) The network in A was optimized to produce an appropriate sequential activity pattern of co-activated muscle groups during forward and backward crawling. The direction of propagation from the posterior (A2) to anterior (A1) segment or vice versa differs for forward and backward crawling. To compare PMN activity relative to MN activation, time is measured in units normalized to the onset and offset of MN activity in a segment (bottom right).

(C) Y-Axis is the normalized activity of a subset of PMNs in the model during forward and backward crawling. Thick lines denote averages over the ensemble of models generated. X-axis (time) is measured relative to A1 MN onset and offset as in B. Arrowheads denote the peak activation onset time for the MNs innervating different co-activated muscle groups (color key as in panel B); exc, excitatory; inh, inhibitory.

**Figure 9 – Supplement 1A, B. Recurrent network model of PMNs activity aligned to onset and offset of A1 MNs during locomotion.** Y-Axis is the normalized activity of PMNs in the model during forward (black traces) and backward (red traces) crawling. Thick lines denote averages over the ensemble of models generated. X-axis (time) is measured relative to A1 MN onset and offset as in Figure 10B. e, excitatory;(e), presumed excitatory based on lineage; i, inhibitory; (i), presumed inhibitory based on lineage.

## Figure 10. Calcium imaging of A31k/A06l/A23a PMNs and their target MNs validates the activity pattern predicted by recurrent modeling.

(A-B) Dual color calcium imaging of jRCaMP1b in A31k (red) and GCaMP6m in MNs (black).

Consistent with the recurrent model predictions, A31k fires with a delay after its post-synaptic MNs in both forward (A) and backward (B) waves. Red and dark error bars (ribbons) represent the standard deviation of the average neuronal activity. Genotype: *CQ-lexA/+; lexAop-GCaMP6m/R87H09-Gal4 UAS-jRCaMP1b.*

(C-D) Single color calcium imaging of jRCaMP1b in A31k (red) and A06l (black). Consistent with the recurrent model predictions, A31k and A06l show synchronous activity patterns during forward (C) and backward waves (D). Red and dark error bars (ribbons) represent the standard deviation of the average neuronal activity. Genotype: *R87H09-Gal4 UAS-jRCaMP1b.*

(E) A23a fires later during forward locomotion than during backward locomotion. Dual color calcium imaging of jRCaMP1b in A23a (red) and GCaMP6m in MNs (black). Red and dark error bars (ribbons) represent the standard deviation of the average neuronal activity. Genotype: *CQ-lexA/+; lexAop-GCaMP6m/R78F07-Gal4 UAS-jRCaMP1b.*

**Figure 11. Neural circuit motifs specific for forward or backward locomotion.**

Circuit motifs composed of forward-specific PMNs (A-C) and backward specific PMNs (D-E). See text for details. Arrow/green, excitatory connection; T-bar/red, inhibitory connection; F1-F4, forward co-active group; B1-B4, backward co-active group.

**Supplemental File 1**. CATMAID .json file of all reconstructed MNs in segment A1 as of 17 February 2019.

**Supplemental File 2**. CATMAID .json file of all reconstructed PMNs in segment A1 as of 21 August 2019.

**Supplemental Table 1**. Excel file of PMN neurotransmitter identity as of 31 August 2019.

**Supplemental Table 2**. Excel file of PMN to MN connectivity as of 31 August 2019.

**Supplemental Table 3**. Excel file of PMN to PMN connectivity as of 31 August 2019.

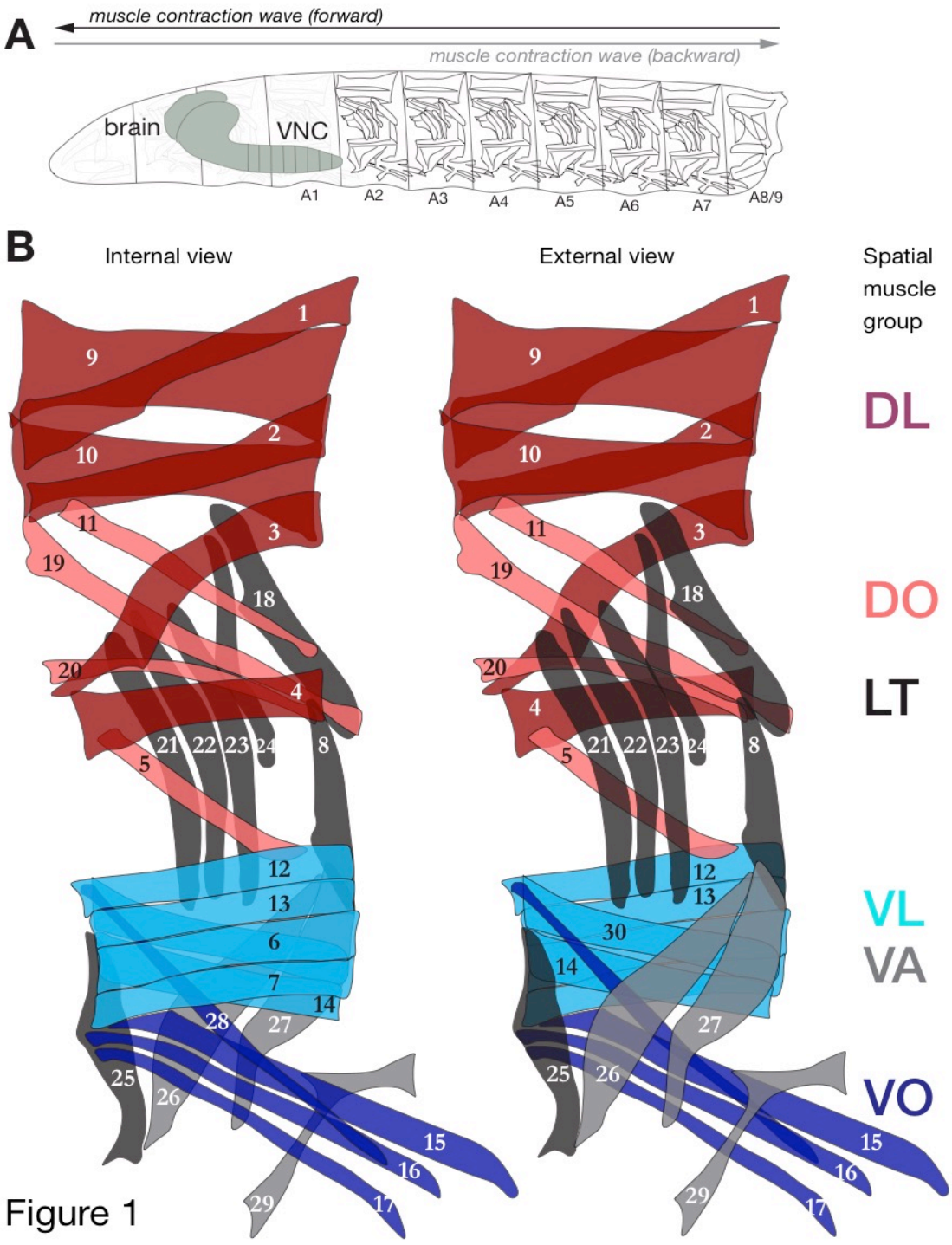


Figure 1

***Figure 1***

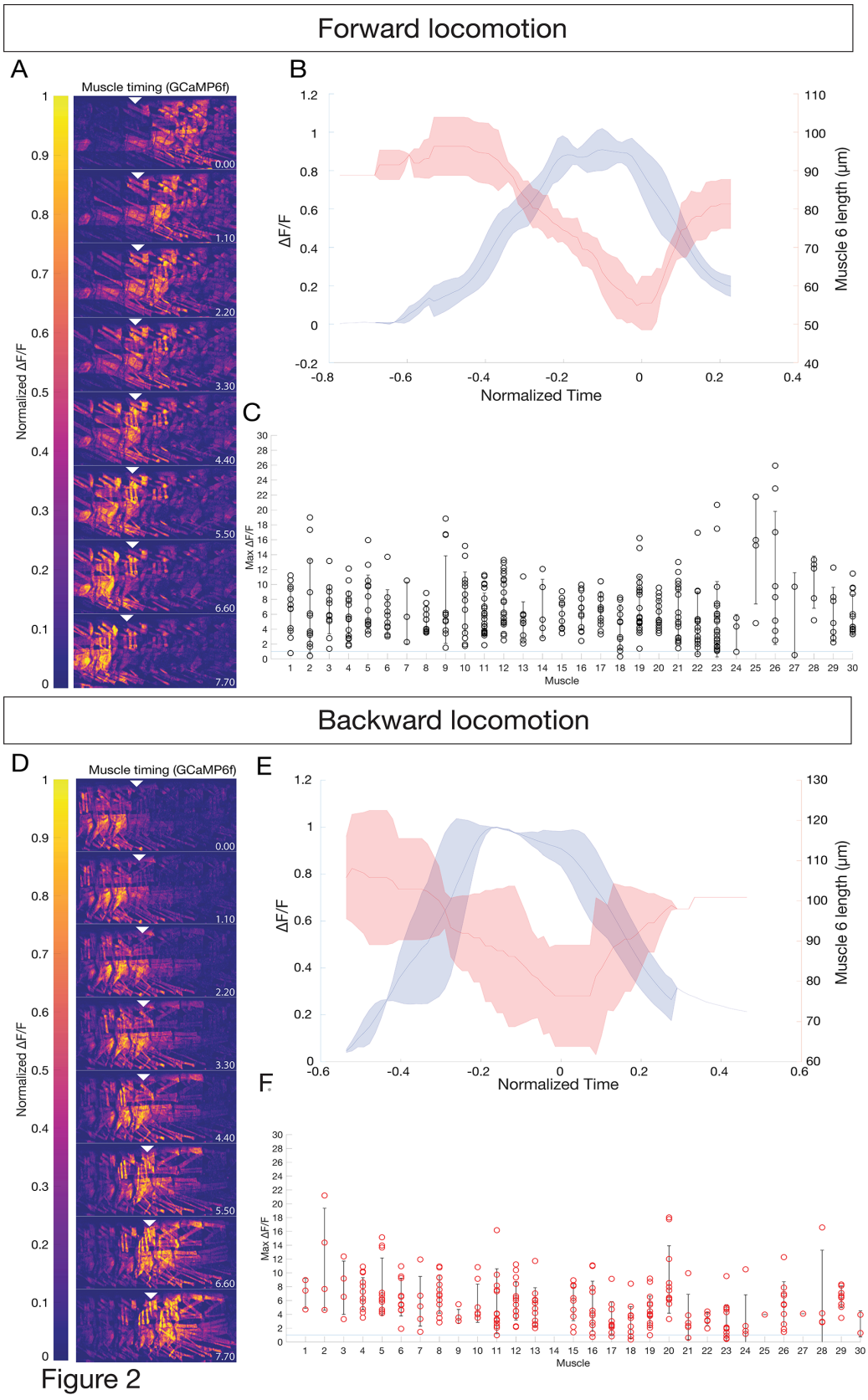


Figure 2

***Figure 2***

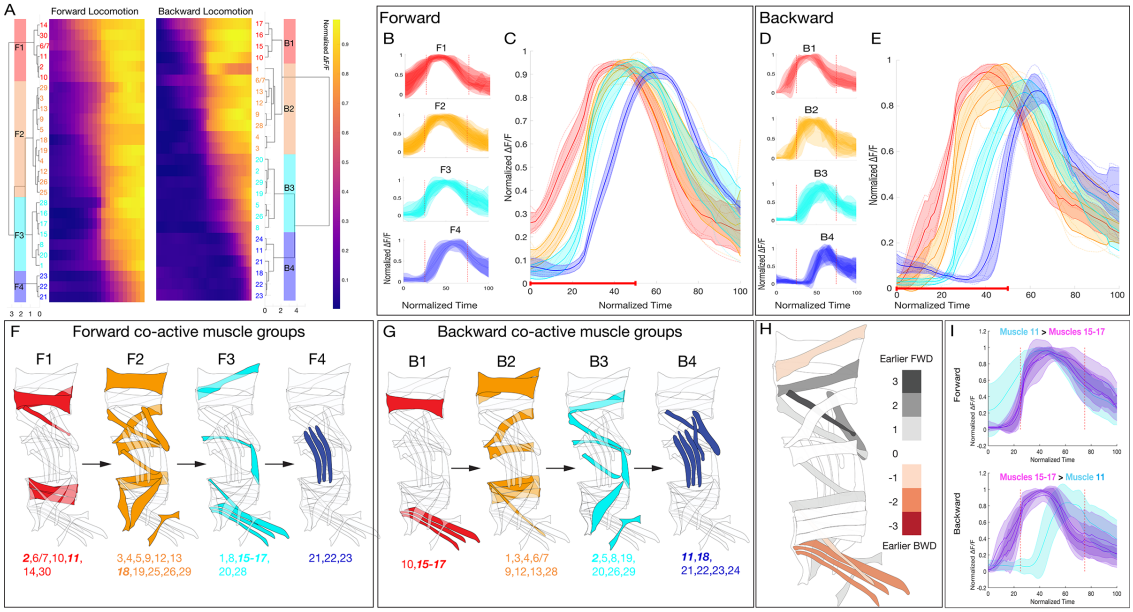


Figure 3

***Figure 3***

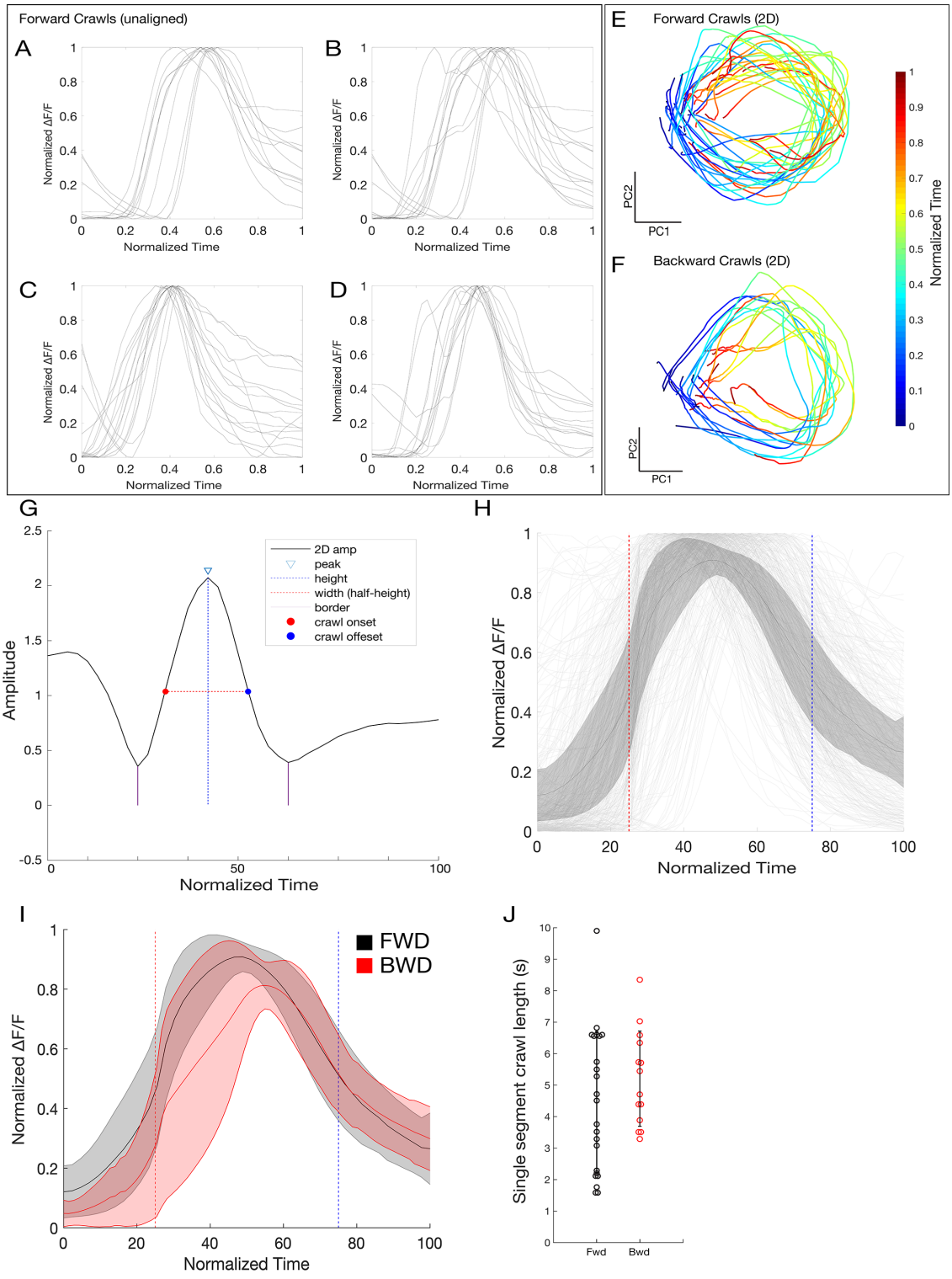


Figure 3 -- supp1

***Figure 3 – Supplement 1***

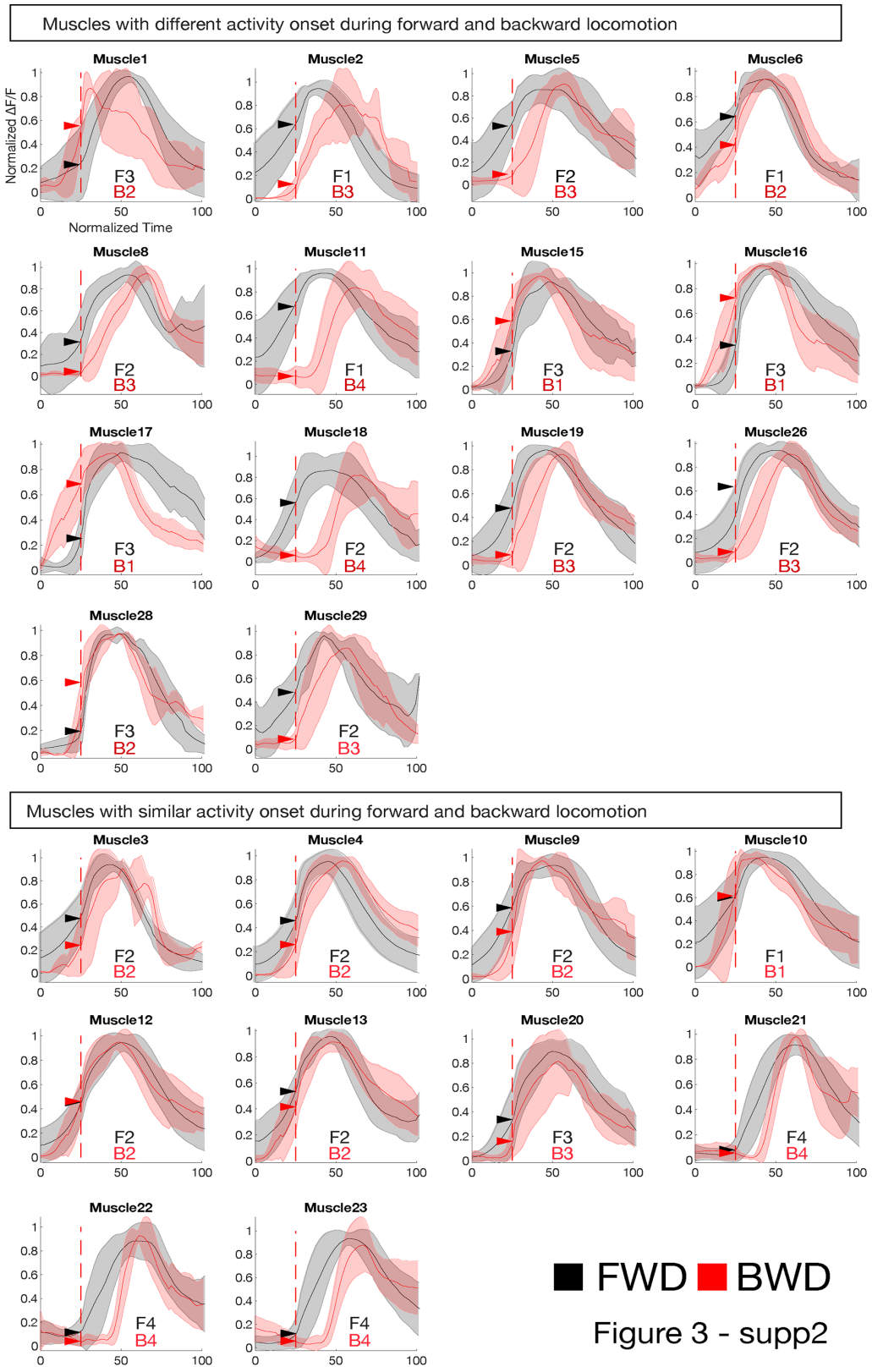


***Figure 3 – Supplement 2***

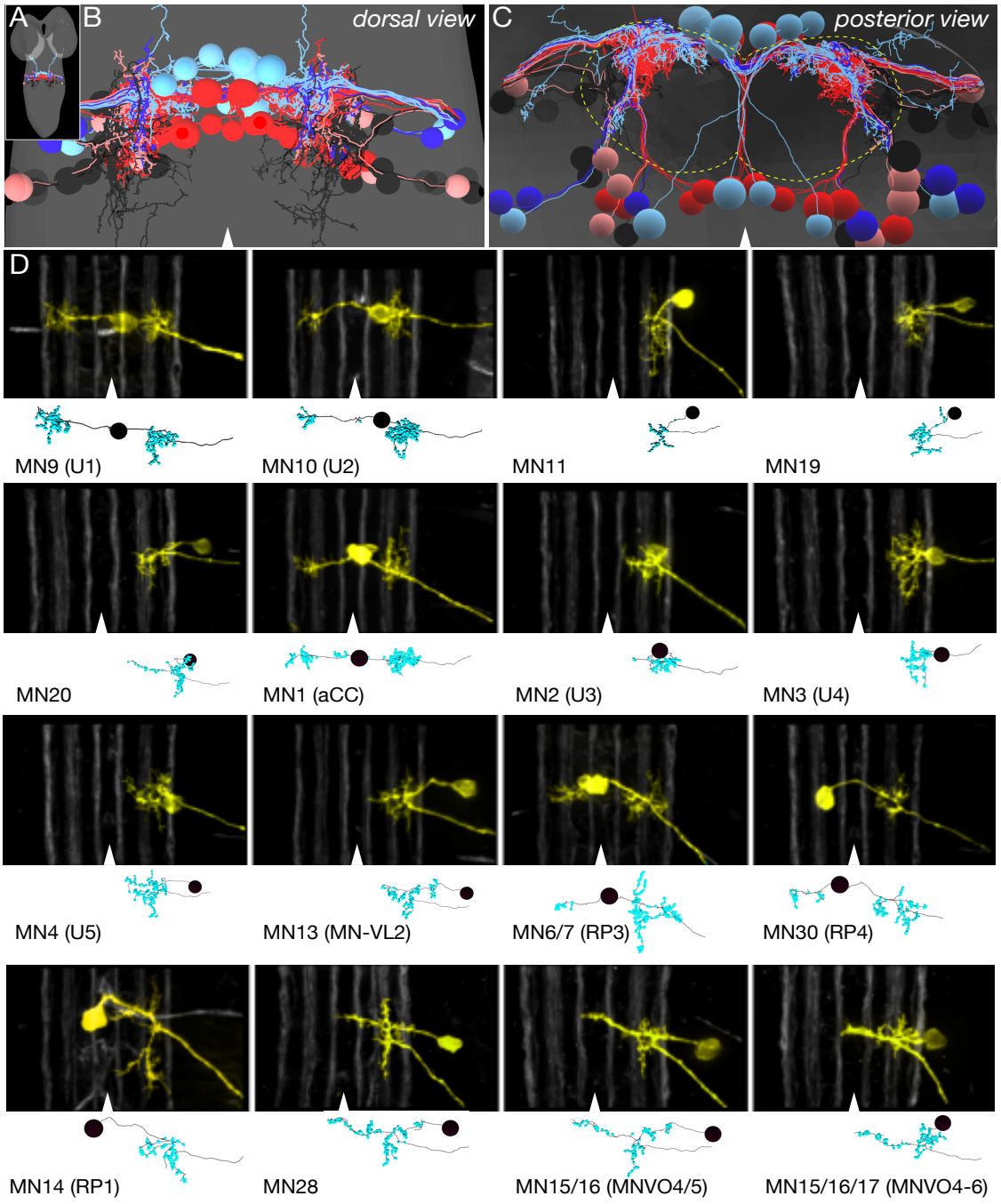


Figure 4

***Figure 4***

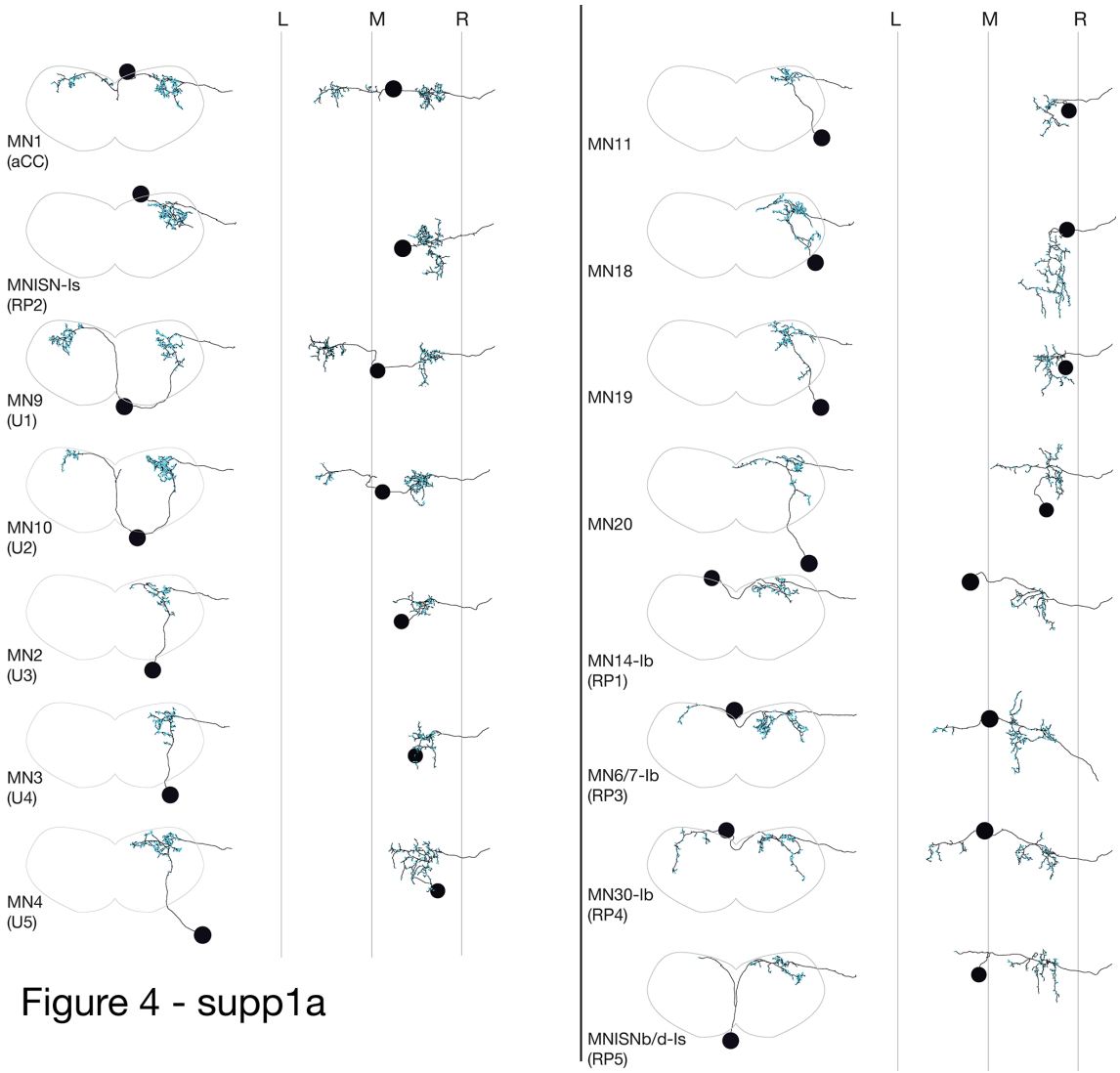


Figure 4 - supp1a

***Figure 4 – Supplement 1a***

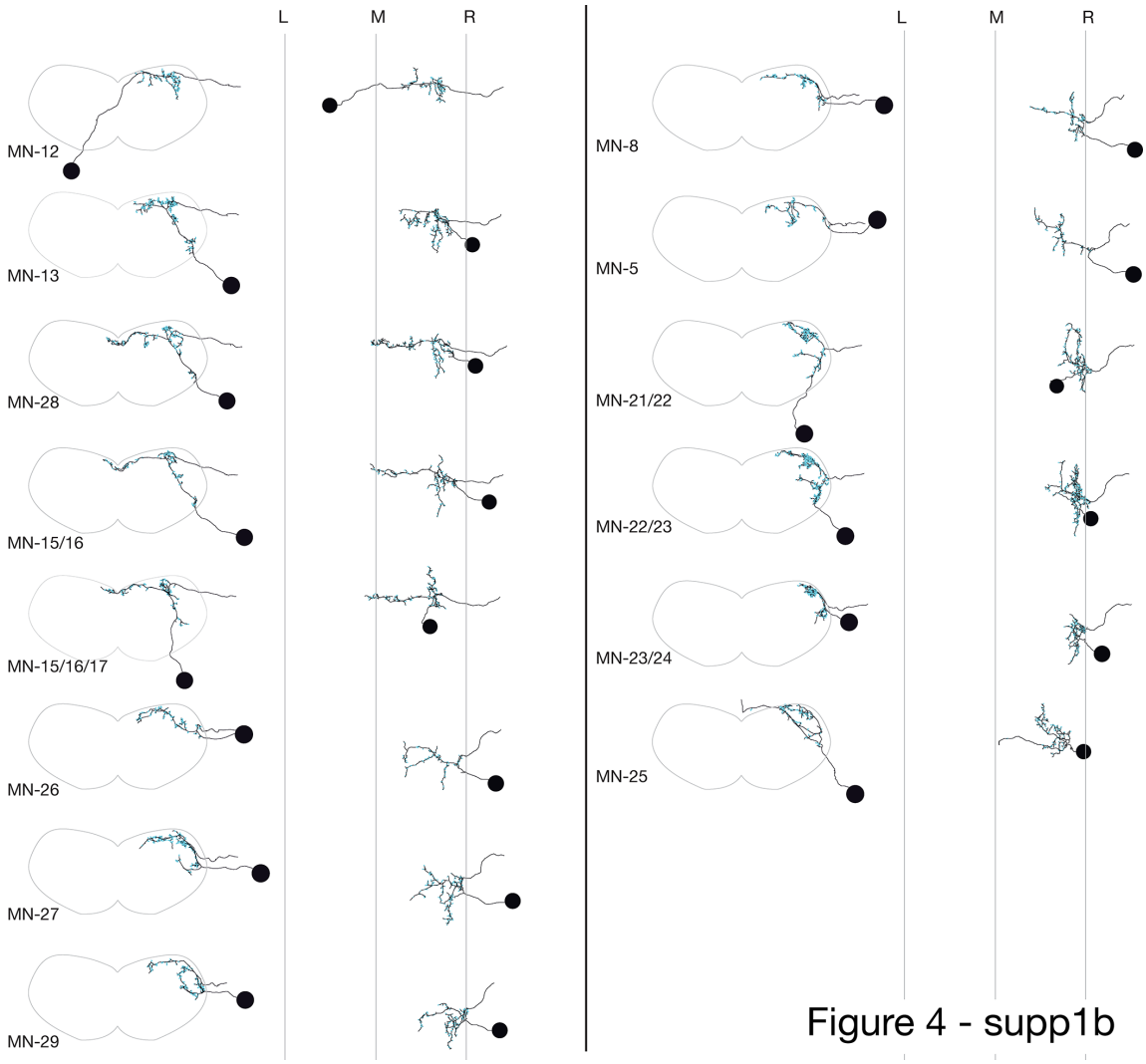


***Figure 4 – Supplement 1b***

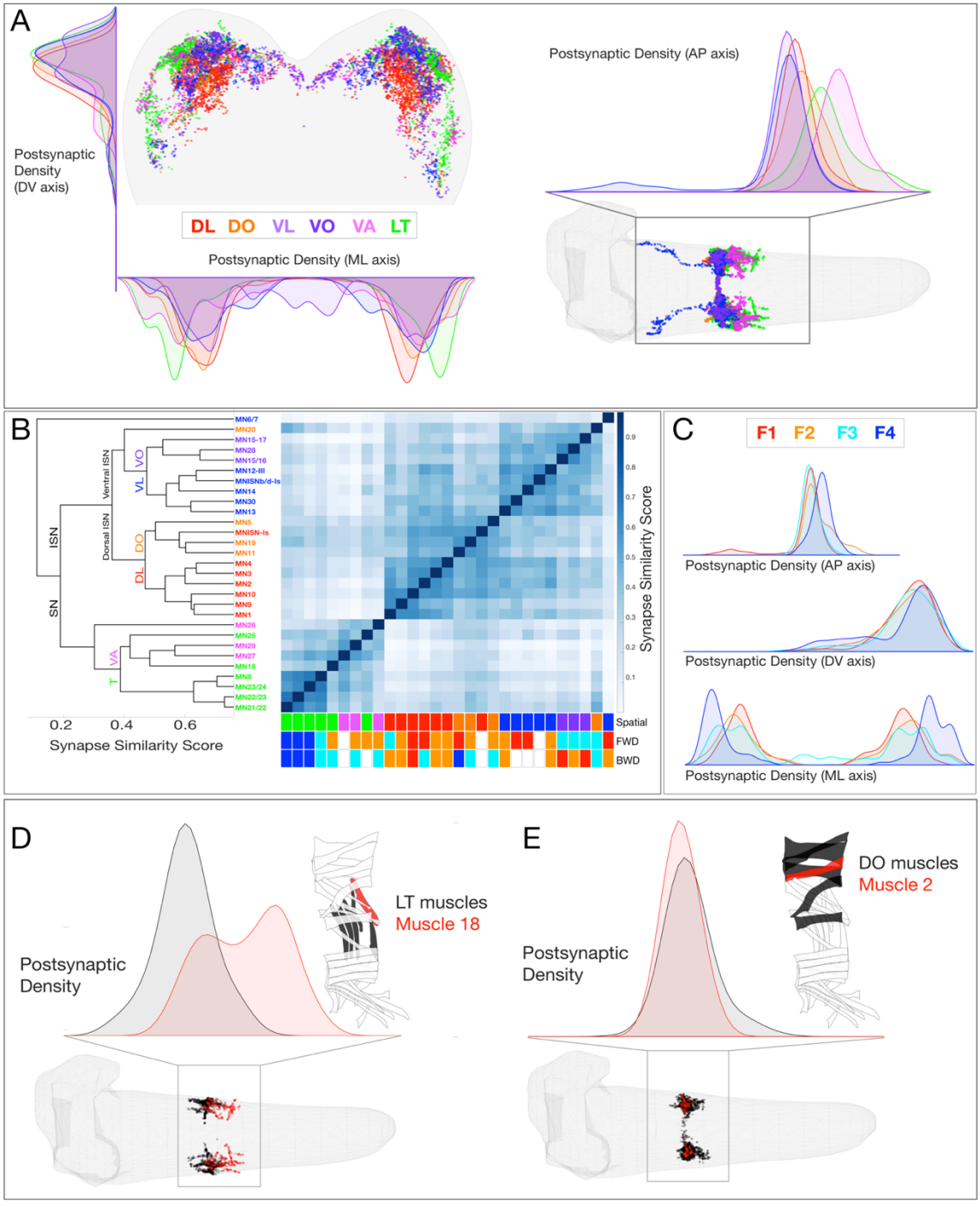


Figure 5

Figure 5

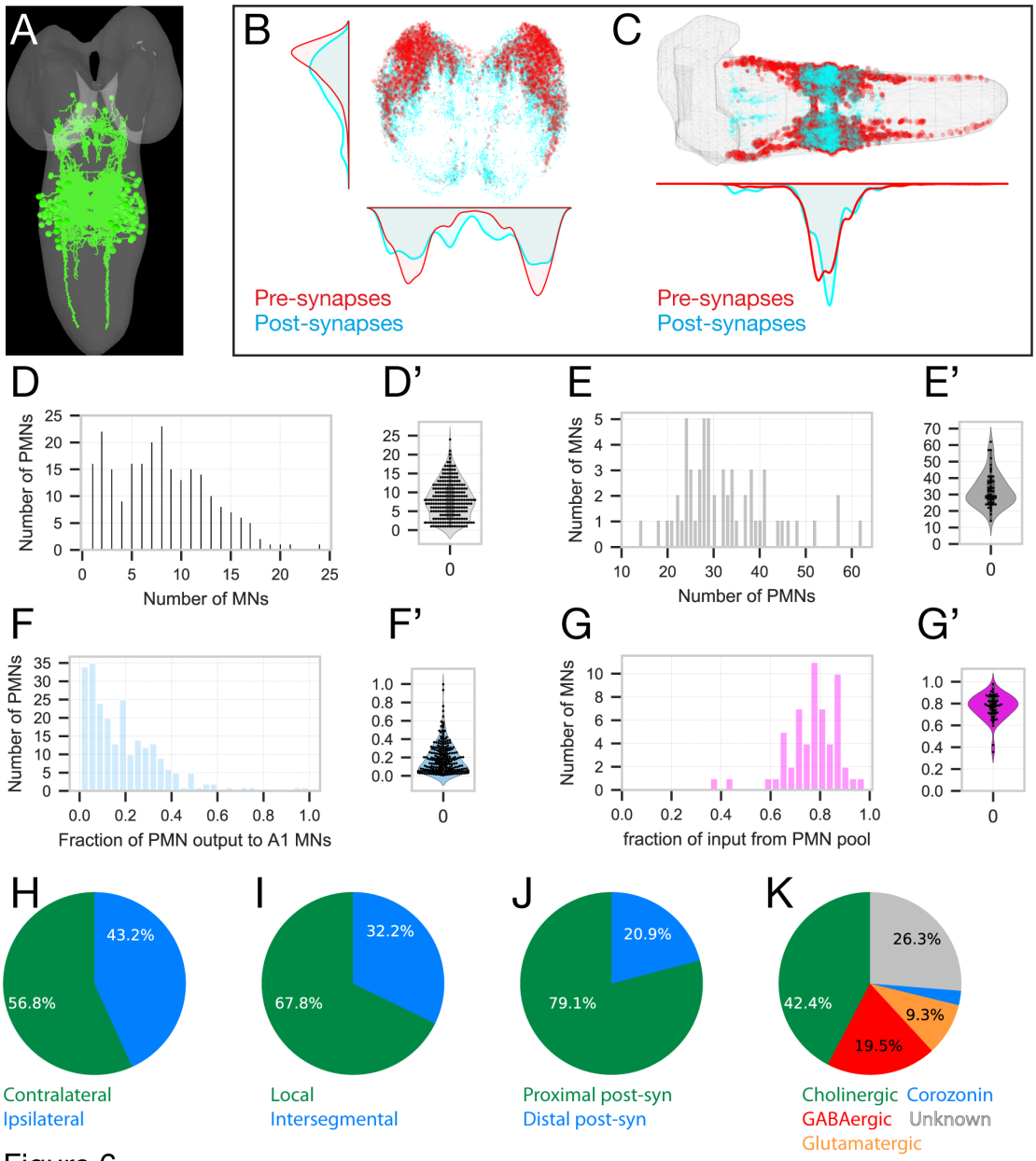


Figure 6

*Figure 6*


Figure 6
supplement 1

***Figure 6 – Supplement 1***

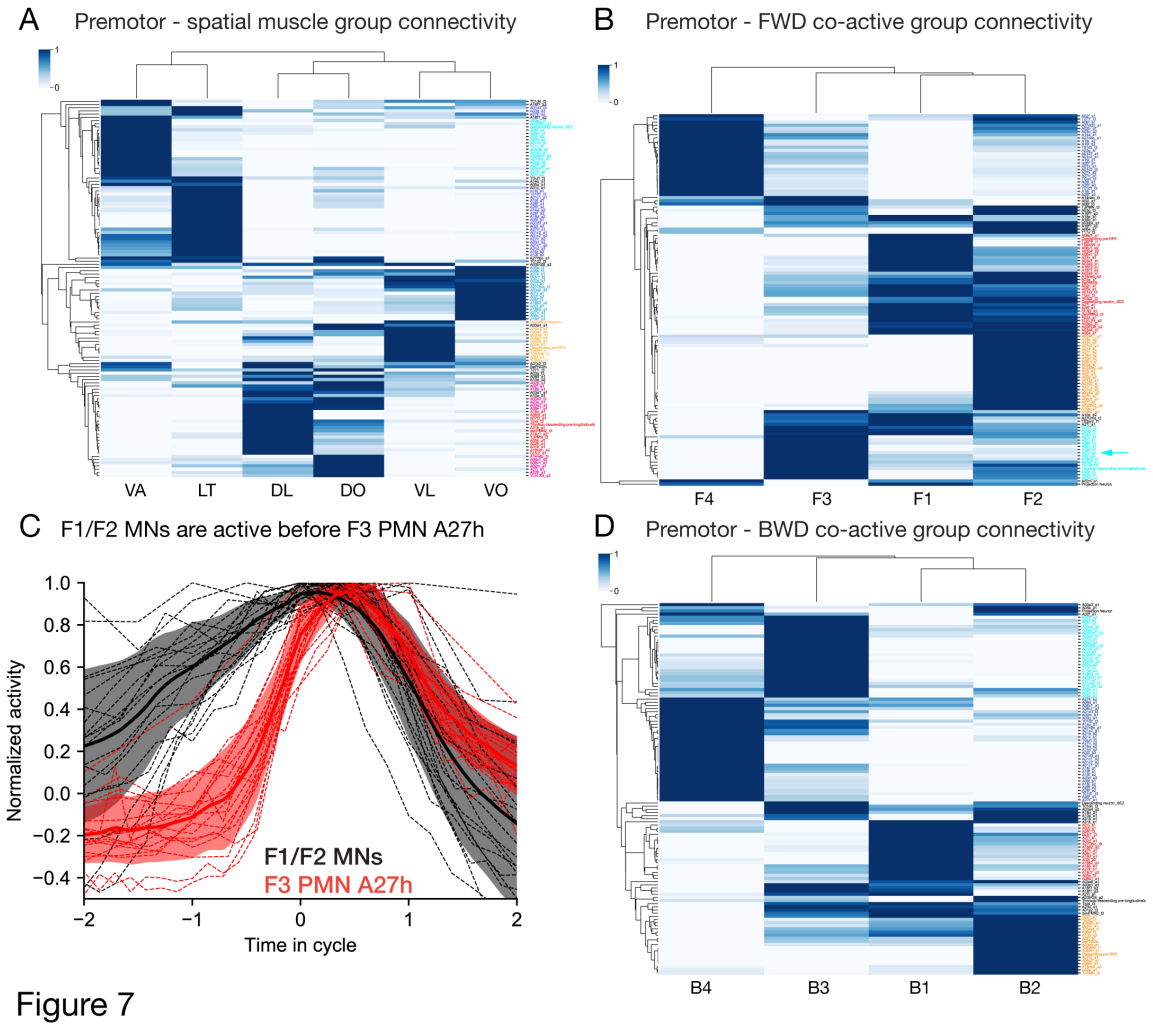


Figure 7

*Figure 7*

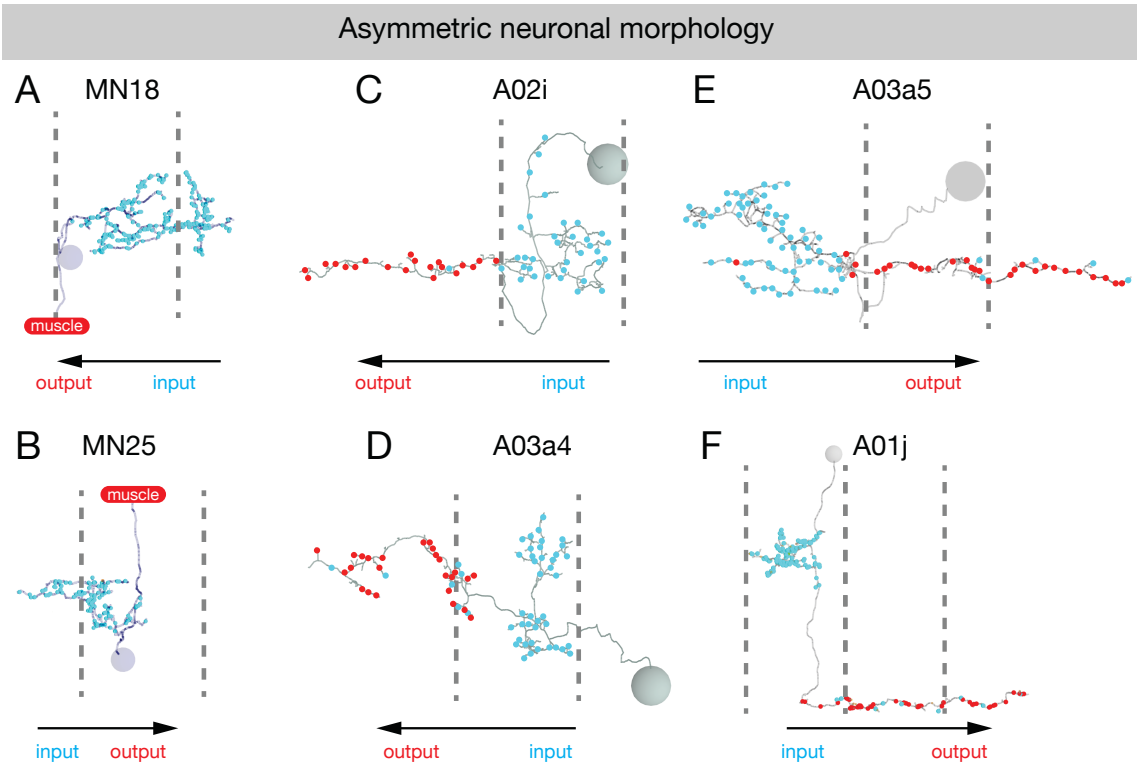


Figure 8

*Figure 8*

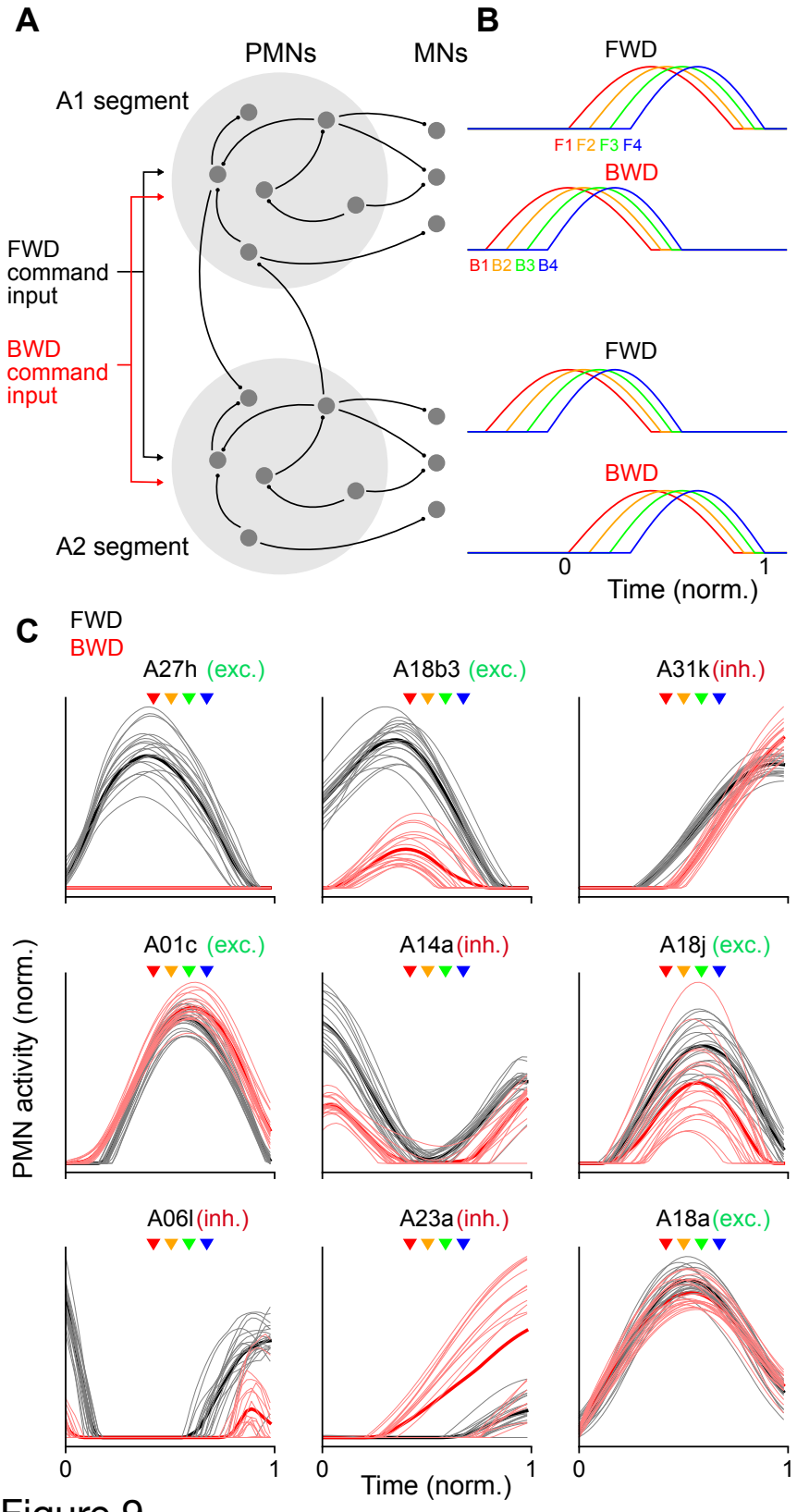


Figure 9

*Figure 9*

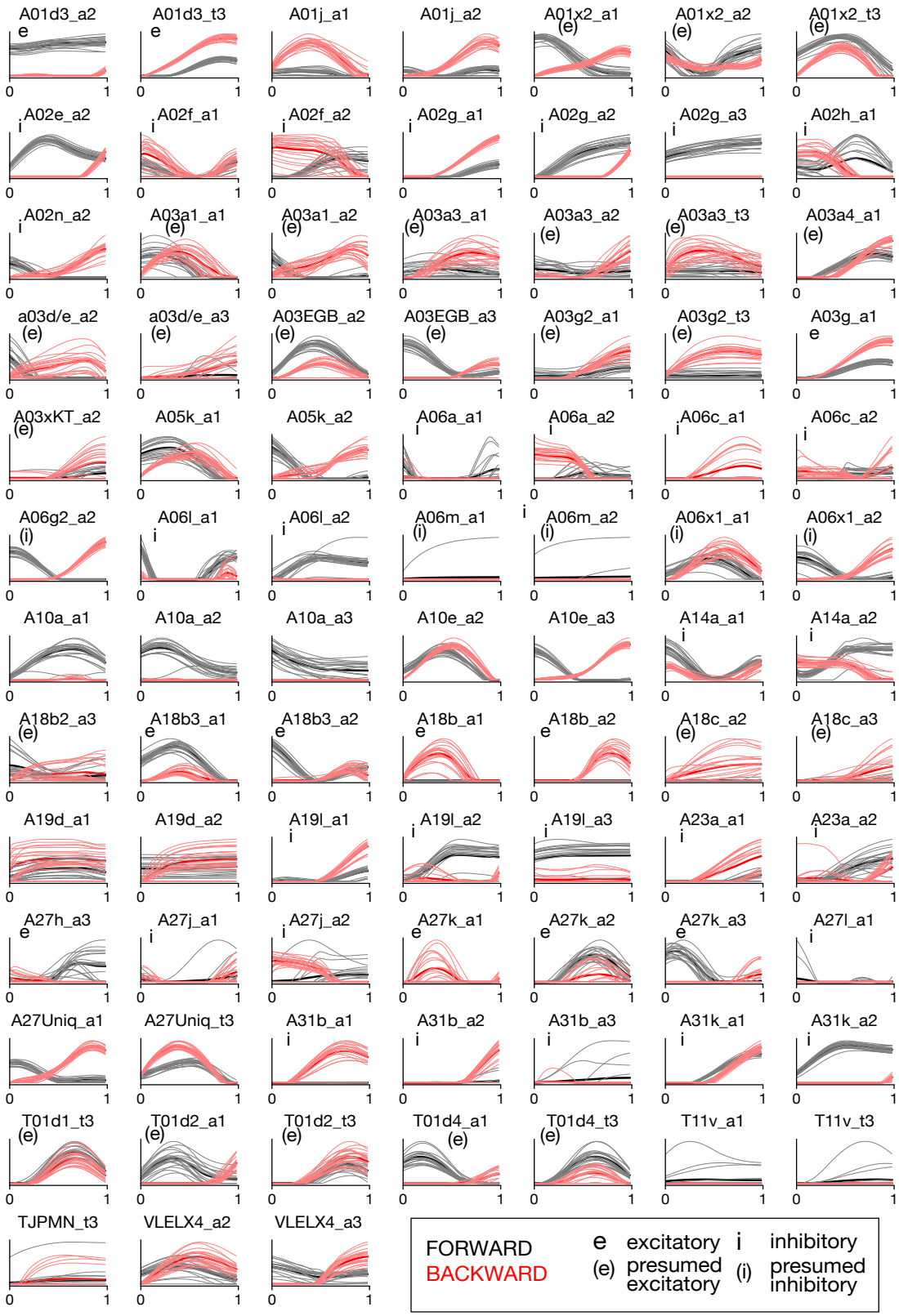


Figure 9 supp1A

***Figure 9 – Supplement 1a***

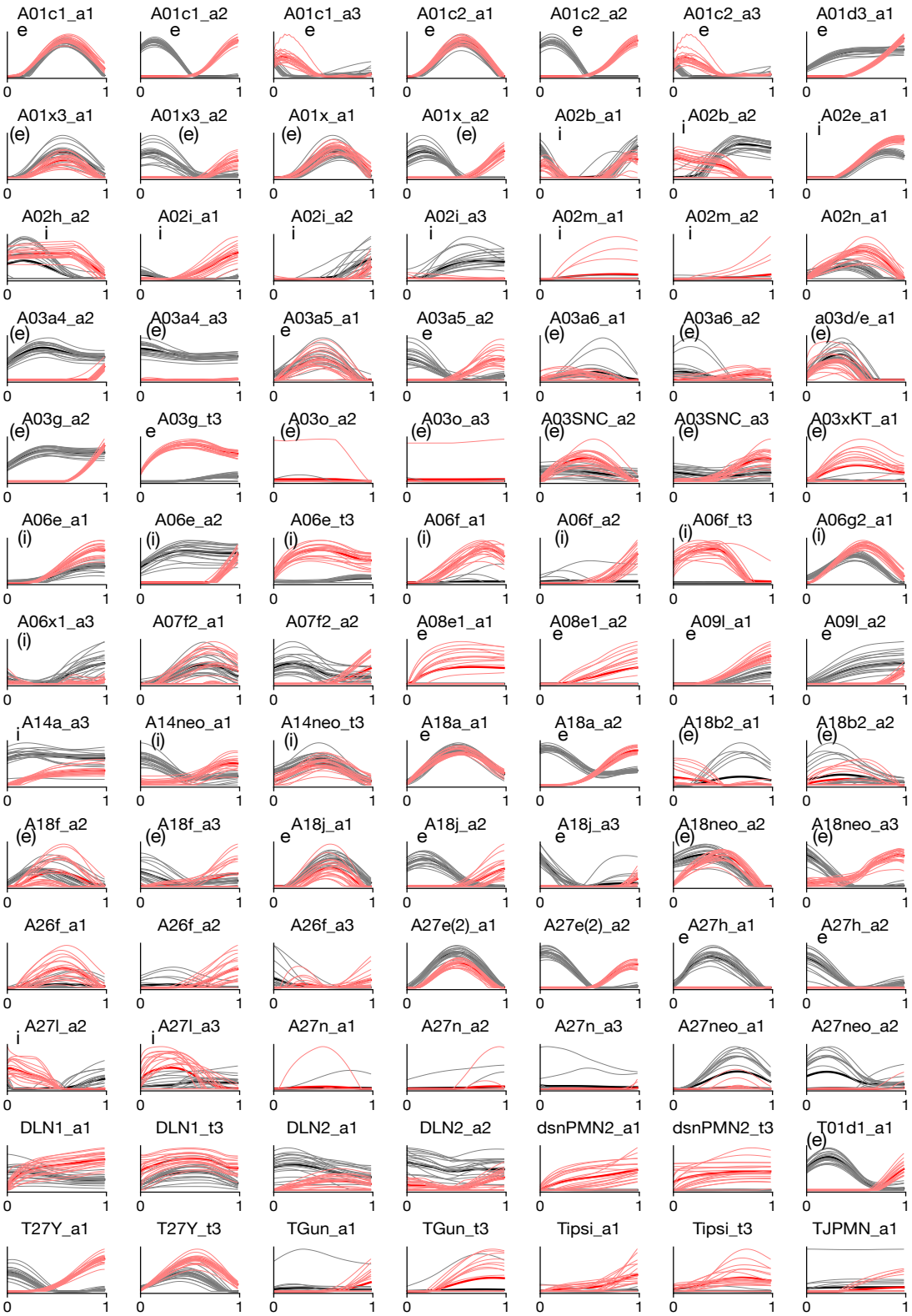


Figure 9 supp1B

***Figure 9 – Supplement 1b***

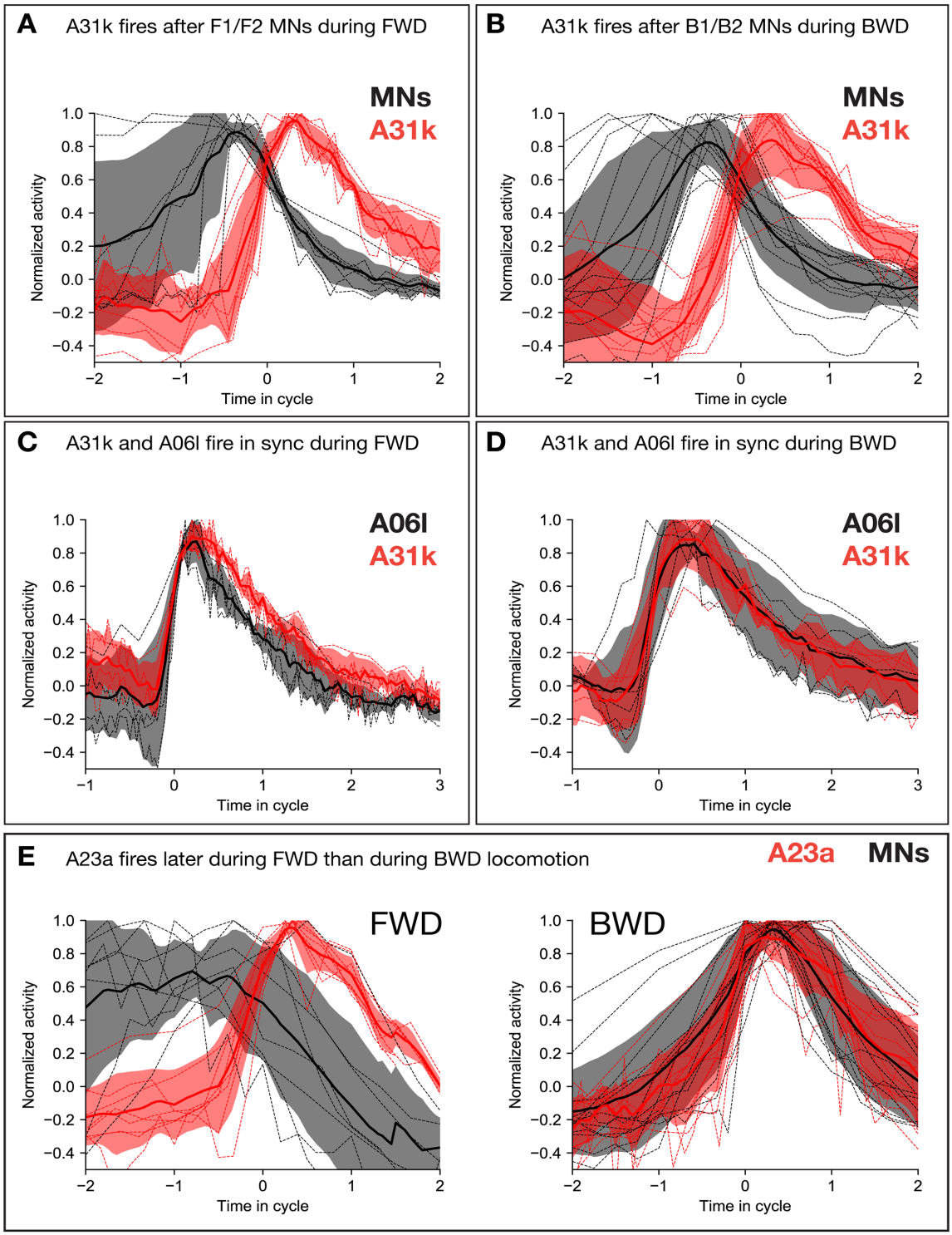


Figure 10

*Figure 10*

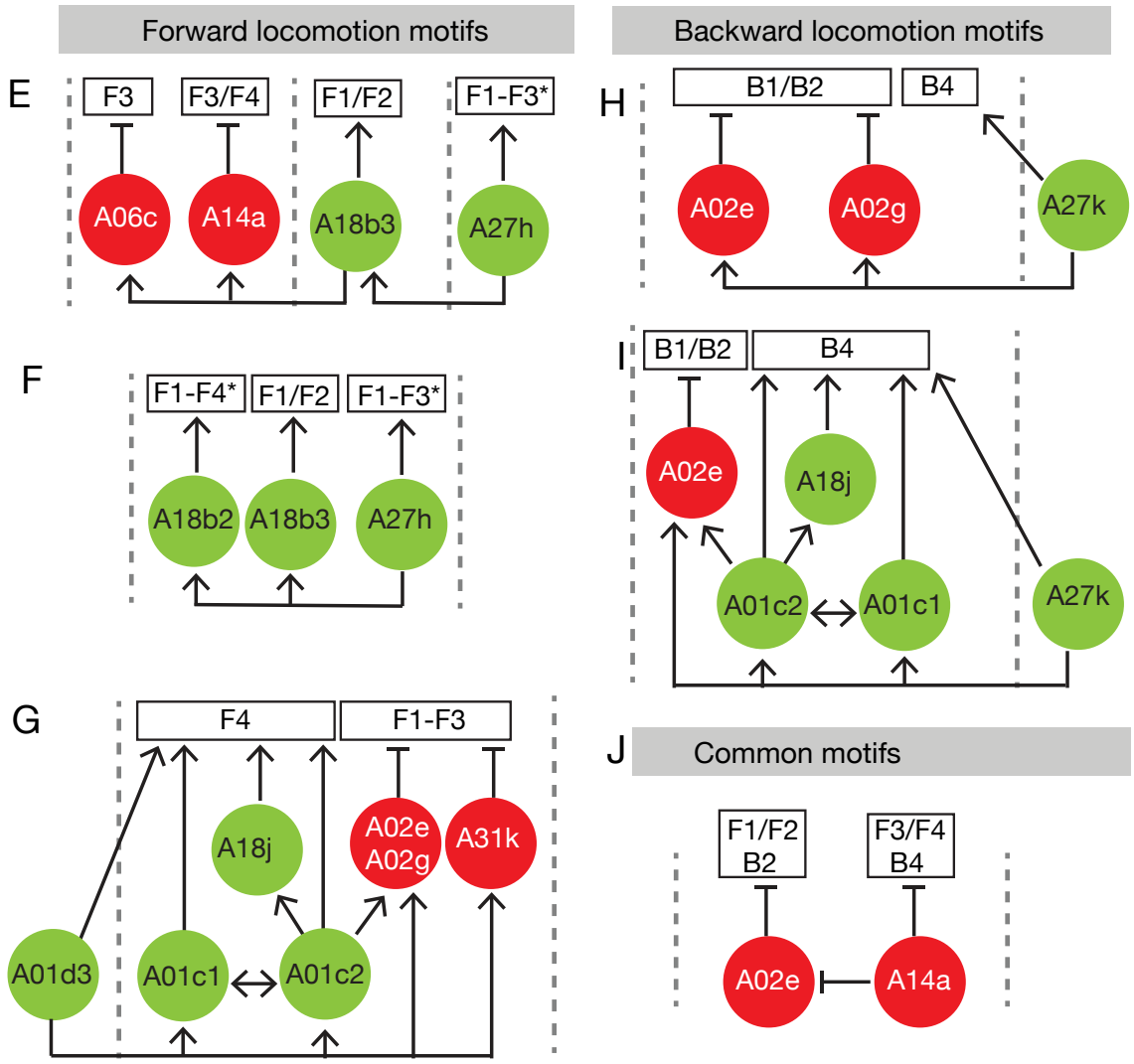


Figure 11

*Figure 11*

# REFERENCES CITED


Agathocleous, M., & Harris, W. A. (2009). From progenitors to differentiated cells in the vertebrate retina. *Annu Rev Cell Dev Biol, 25*, 45-69. doi:10.1146/annurev.cellbio.042308.113259

Arber, S. (2017). Organization and function of neuronal circuits controlling movement. *EMBO Mol Med, 9*(3), 281-284. doi:10.15252/emmm.201607226

Arber, S., & Costa, R. M. (2018). Connecting neuronal circuits for movement. *Science, 360*(6396), 1403-1404. doi:10.1126/science.aat5994

Awasaki, T., & Lee, T. (2011). Orphan nuclear receptors control neuronal remodeling during fly metamorphosis. *Nature neuroscience, 14*(1), 6-7. doi:10.1038/nn0111-6

Baehrecke, E. H. (1996). Ecdysone signaling cascade and regulation of *Drosophila* metamorphosis. *Arch Insect Biochem Physiol, 33*(3-4), 231-244. doi:10.1002/(sici)1520-6327(1996)33:3/4<231::aid-arch5>3.0.co;2-v

Bagnall, M. W., & McLean, D. L. (2014). Modular organization of axial microcircuits in zebrafish. *Science, 343*(6167), 197-200. doi:10.1126/science.1245629

Bandler, R. C., Mayer, C., & Fishell, G. (2017). Cortical interneuron specification: the juncture of genes, time and geometry. *Current Opinion in Neurobiology, 42*, 17-24. doi:https://doi.org/10.1016/j.conb.2016.10.003

Bargmann, C. I., & Marder, E. (2013). From the connectome to brain function. *Nat Methods, 10*(6), 483-490.

Barnabe-Heider, F., Wasylnka, J. A., Fernandes, K. J., Porsche, C., Sendtner, M., Kaplan, D. R., & Miller, F. D. (2005). Evidence that embryonic neurons regulate the onset of cortical gliogenesis via cardiotrophin-1. *Neuron, 48*(2), 253-265. doi:10.1016/j.neuron.2005.08.037

Bate, M. (1990). The embryonic development of larval muscles in *Drosophila*. *Development, 110*(3), 791-804.

Baumgardt, M., Karlsson, D., Salmani, B. Y., Bivik, C., MacDonald, R. B., Gunnar, E., & Thor, S. (2014). Global programmed switch in neural daughter cell proliferation mode triggered by a temporal gene cascade. *Dev Cell, 30*(2), 192-208. doi:10.1016/j.devcel.2014.06.021

Baumgardt, M., Karlsson, D., Terriente, J., Diaz-Benjumea, F. J., & Thor, S. (2009). Neuronal subtype specification within a lineage by opposing temporal feed-forward loops. *Cell, 139*(5), 969-982. doi:S0092-8674(09)01358-0 [pii]

10.1016/j.cell.2009.10.032

Bayraktar, O. A., & Doe, C. Q. (2013). Combinatorial temporal patterning in progenitors expands neural diversity. *Nature, 498*, 445-455. doi:10.1038/nature12266

Bello, B. C., Izergina, N., Caussinus, E., & Reichert, H. (2008). Amplification of neural stem cell proliferation by intermediate progenitor cells in *Drosophila* brain development. *Neural Dev, 3*, 5. doi:1749-8104-3-5 [pii] 10.1186/1749-8104-3-5

Benito-Sipos, J., Ulvklo, C., Gabilondo, H., Baumgardt, M., Angel, A., Torroja, L., & Thor, S. (2011). Seven up acts as a temporal factor during two different stages of neuroblast 5-6 development. *Development, 138*(24), 5311-5320. doi:10.1242/dev.070946

Berni, J., Pulver, S. R., Griffith, L. C., & Bate, M. (2012). Autonomous circuitry for substrate exploration in freely moving *Drosophila* larvae. *Curr Biol, 22*(20), 1861-1870. doi:10.1016/j.cub.2012.07.048

Bertet, C., Li, X., Erclik, T., Cavey, M., Wells, B., & Desplan, C. (2014). Temporal patterning of neuroblasts controls Notch-mediated cell survival through regulation of Hid or Reaper. *Cell, 158*(5), 1173-1186. doi:10.1016/j.cell.2014.07.045

Bielen, H., Pal, S., Tole, S., & Houart, C. (2017). Temporal variations in early developmental decisions: an engine of forebrain evolution. *Current Opinion in Neurobiology, 42*, 152-159. doi:https://doi.org/10.1016/j.conb.2016.12.008

Bikoff, J. B., Gabitto, M. I., Rivard, A. F., Drobac, E., Machado, T. A., Miri, A., . . . Jessell, T. M. (2016). Spinal Inhibitory Interneuron Diversity Delineates Variant Motor Microcircuits. *Cell, 165*(1), 207-219. doi:10.1016/j.cell.2016.01.027

Birkholz, O., Rickert, C., Nowak, J., Coban, I. C., & Technau, G. M. (2015). Bridging the gap between postembryonic cell lineages and identified embryonic neuroblasts in the ventral nerve cord of *Drosophila* melanogaster. *Biol Open, 4*(4), 420-434. doi:10.1242/bio.201411072

Boone, J. Q., & Doe, C. Q. (2008). Identification of *Drosophila* type II neuroblast lineages containing transit amplifying ganglion mother cells. *Dev Neurobiol, 68*(9), 1185-1195. doi:10.1002/dneu.20648

Bossing, T., Udolph, G., Doe, C. Q., & Technau, G. M. (1996). The embryonic central nervous system lineages of *Drosophila* melanogaster. I. Neuroblast lineages derived from the ventral half of the neuroectoderm. *Dev Biol, 179*(1), 41-64. doi:S0012-1606(96)90240-7 [pii] 10.1006/dbio.1996.0240

Boulanger, A., Clouet-Redt, C., Farge, M., Flandre, A., Guignard, T., Fernando, C., . . . Dura, J. M. (2011). ftz-f1 and Hr39 opposing roles on EcR expression during *Drosophila* mushroom body neuron remodeling. *Nature neuroscience, 14*(1), 37-44. doi:10.1038/nn.2700

Bowman, S. K., Rolland, V., Betschinger, J., Kinsey, K. A., Emery, G., & Knoblich, J. A. (2008). The tumor suppressors Brat and Numb regulate transit-amplifying neuroblast lineages in *Drosophila*. *Dev Cell, 14*(4), 535-546. doi:S1534-5807(08)00112-3 [pii] 10.1016/j.devcel.2008.03.004

Brenner, S. (2010). Sequences and consequences. *Philos Trans R Soc Lond B Biol Sci, 365*(1537), 207-212. doi:10.1098/rstb.2009.0221

Briggman, K. L., & Kristan, W. B. (2008). Multifunctional pattern-generating circuits. *Annu Rev Neurosci, 31*, 271-294. doi:10.1146/annurev.neuro.31.060407.125552

Briggman, K. L., & Kristan, W. B., Jr. (2006). Imaging dedicated and multifunctional neural circuits generating distinct behaviors. *J Neurosci, 26*(42), 10925-10933. doi:10.1523/jneurosci.3265-06.2006

Britton, J. S., & Edgar, B. A. (1998). Environmental control of the cell cycle in *Drosophila*: nutrition activates mitotic and endoreplicative cells by distinct mechanisms. *Development, 125*(11), 2149-2158. Retrieved from https://www.ncbi.nlm.nih.gov/pubmed/9570778

Brodfuehrer, P. D., & Thorogood, M. S. (2001). Identified neurons and leech swimming behavior. *Prog Neurobiol, 63*(4), 371-381.

Brody, T., & Odenwald, W. F. (2000). Programmed transformations in neuroblast gene expression during *Drosophila* CNS lineage development. *Dev Biol, 226*(1), 34-44. doi:10.1006/dbio.2000.9829 S0012-1606(00)99829-4 [pii]

Brown, H. L., Cherbas, L., Cherbas, P., & Truman, J. W. (2006). Use of time-lapse imaging and dominant negative receptors to dissect the steroid receptor control of neuronal remodeling in *Drosophila*. *Development, 133*(2), 275-285. doi:10.1242/dev.02191

Brown, K. N., Chen, S., Han, Z., Lu, C. H., Tan, X., Zhang, X. J., . . . Shi, S. H. (2011). Clonal production and organization of inhibitory interneurons in the neocortex. *Science, 334*(6055), 480-486. doi:10.1126/science.1208884

Bucher, D., Taylor, A. L., & Marder, E. (2006). Central pattern generating neurons simultaneously express fast and slow rhythmic activities in the stomatogastric ganglion. *J Neurophysiol, 95*(6), 3617-3632. doi:10.1152/jn.00004.2006

Burgos, A., Honjo, K., Ohyama, T., Qian, C. S., Shin, G. J., Gohl, D. M., . . . Grueber, W. B. (2018). Nociceptive interneurons control modular motor pathways to promote escape behavior in *Drosophila*. *Elife, 7*. doi:10.7554/eLife.26016

Butler, V. J., Branicky, R., Yemini, E., Liewald, J. F., Gottschalk, A., Kerr, R. A., . . . Schafer, W. R. (2015). A consistent muscle activation strategy underlies crawling and swimming in Caenorhabditis elegans. *J R Soc Interface, 12*(102), 20140963. doi:10.1098/rsif.2014.0963

Carreira-Rosario, A., Zarin, A. A., Clark, M. Q., Manning, L., Fetter, R. D., Cardona, A., & Doe, C. Q. (2018). MDN brain descending neurons coordinately activate backward and inhibit forward locomotion. *Elife, 7*. doi:10.7554/eLife.38554

Caussinus, E., & Hirth, F. (2007). Asymmetric stem cell division in development and cancer. *Prog Mol Subcell Biol, 45*, 205-225. Retrieved from http://www.ncbi.nlm.nih.gov/entrez/query.fcgi?cmd=Retrieve&db=PubMed&dopt=Citation&list_uids=17585502

Cepko, C. (2014). Intrinsically different retinal progenitor cells produce specific types of progeny. *Nat Rev Neurosci, 15*(9), 615-627. doi:10.1038/nrn3767

Chai, P. C., Liu, Z., Chia, W., & Cai, Y. (2013). Hedgehog signaling acts with the temporal cascade to promote neuroblast cell cycle exit. *PLoS Biol, 11*(2), e1001494. doi:10.1371/journal.pbio.1001494

Chawla, G., & Sokol, N. S. (2012). Hormonal activation of let-7-C microRNAs via EcR is required for adult *Drosophila* melanogaster morphology and function. *Development, 139*(10), 1788-1797. doi:10.1242/dev.077743

Chell, J. M., & Brand, A. H. (2010). Nutrition-responsive glia control exit of neural stem cells from quiescence. *Cell, 143*(7), 1161-1173. doi:10.1016/j.cell.2010.12.007

Choi, J. C., Park, D., & Griffith, L. C. (2004). Electrophysiological and morphological characterization of identified motor neurons in the *Drosophila* third instar larva central nervous system. *J Neurophysiol, 91*(5), 2353-2365. doi:10.1152/jn.01115.2003

Chu-LaGraff, Q., & Doe, C. Q. (1993). Neuroblast specification and formation regulated by wingless in the *Drosophila* CNS. *Science, 261*(5128), 1594-1597.

Clark, M. Q., McCumsey, S. J., Lopez-Darwin, S., Heckscher, E. S., & Doe, C. Q. (2016). Functional Genetic Screen to Identify Interneurons Governing Behaviorally Distinct Aspects of *Drosophila* Larval Motor Programs. *G3 (Bethesda)*. doi:10.1534/g3.116.028472

Clark, M. Q., Zarin, A. A., Carreira-Rosario, A., & Doe, C. Q. (2018). Neural circuits driving larval locomotion in *Drosophila*. *Neural Dev, 13*(1), 6. doi:10.1186/s13064-018-0103-z

Costa, M., Manton, J. D., Ostrovsky, A. D., Prohaska, S., & Jefferis, G. S. (2016). NBLAST: Rapid, Sensitive Comparison of Neuronal Structure and Construction of Neuron Family Databases. *Neuron, 91*(2), 293-311. doi:10.1016/j.neuron.2016.06.012

Crisp, S., Evers, J. F., Fiala, A., & Bate, M. (2008). The development of motor coordination in *Drosophila* embryos. *Development, 135*(22), 3707-3717. doi:10.1242/dev.026773

Crone, S. A., Quinlan, K. A., Zagoraiou, L., Droho, S., Restrepo, C. E., Lundfald, L., . . . Sharma, K. (2008). Genetic ablation of V2a ipsilateral interneurons disrupts left-right locomotor coordination in mammalian spinal cord. *Neuron, 60*(1), 70-83. doi:10.1016/j.neuron.2008.08.009

Crossley, A. (1978). The morphology and development of the *Drosophila* muscular system. In *The Genetics and Biology of Drosophila* (Vol. 2b, pp. 499-560). London, New York, and San Francisco: Academic Press.

Cui, X., & Doe, C. Q. (1992). ming is expressed in neuroblast sublineages and regulates gene expression in the *Drosophila* central nervous system. *Development, 116*(4), 943-952. Retrieved from http://www.ncbi.nlm.nih.gov/entrez/query.fcgi?cmd=Retrieve&db=PubMed&dopt=Citation&list_uids=1339340

de Castro, C., Titlow, J., Majeed, Z. R., & Cooper, R. L. (2014). Analysis of various physiological salines for heart rate, CNS function, and synaptic transmission at neuromuscular junctions in *Drosophila* melanogaster larvae. *J Comp Physiol A Neuroethol Sens Neural Behav Physiol, 200*(1), 83-92. doi:10.1007/s00359-013-0864-0

Desai, A. R., & McConnell, S. K. (2000). Progressive restriction in fate potential by neural progenitors during cerebral cortical development. *Development, 127*(13), 2863-2872.

Diao, F., Mena, W., Shi, J., Park, D., Diao, F., Taghert, P., . . . White, B. H. (2016). The Splice Isoforms of the *Drosophila* Ecdysis Triggering Hormone Receptor Have Developmentally Distinct Roles. *Genetics, 202*(1), 175-189. doi:10.1534/genetics.115.182121

Dias, J. M., Alekseenko, Z., Applequist, J. M., & Ericson, J. (2014). Tgfbeta signaling regulates temporal neurogenesis and potency of neural stem cells in the CNS. *Neuron, 84*(5), 927-939. doi:10.1016/j.neuron.2014.10.033

Ding, R., Weynans, K., Bossing, T., Barros, C. S., & Berger, C. (2016). The Hippo signalling pathway maintains quiescence in *Drosophila* neural stem cells. *Nat Commun, 7*, 10510. doi:10.1038/ncomms10510

Dixit, R., Vijayraghavan, K., & Bate, M. (2008). Hox genes and the regulation of movement in *Drosophila*. *Dev Neurobiol, 68*(3), 309-316. doi:10.1002/dneu.20589

Doe, C. Q. (2008). Neural stem cells: balancing self-renewal with differentiation. *Development, 135*(9), 1575-1587. doi:dev.014977 [pii] 10.1242/dev.014977

Doe, C. Q. (2017). Temporal Patterning in the *Drosophila* CNS. *Annu. Rev. Cell Dev. Biol. , 33*, in press.

Doe, C. Q., & Goodman, C. S. (1985). Early events in insect neurogenesis. I. Development and segmental differences in the pattern of neuronal precursor cells. *Dev Biol, 111*(1), 193-205.

Dougherty, K. J., Zagoraiou, L., Satoh, D., Rozani, I., Doobar, S., Arber, S., . . . Kiehn, O. (2013). Locomotor rhythm generation linked to the output of spinal shox2 excitatory interneurons. *Neuron, 80*(4), 920-933. doi:10.1016/j.neuron.2013.08.015

Dumstrei, K., Wang, F., & Hartenstein, V. (2003). Role of DE-cadherin in neuroblast proliferation, neural morphogenesis, and axon tract formation in *Drosophila* larval brain development. *J Neurosci, 23*(8), 3325-3335. Retrieved from http://www.ncbi.nlm.nih.gov/entrez/query.fcgi?cmd=Retrieve&db=PubMed&dopt=Citation&list_uids=12716940

Ebens, A. J., Garren, H., Cheyette, B. N., & Zipursky, S. L. (1993). The *Drosophila* anachronism locus: a glycoprotein secreted by glia inhibits neuroblast proliferation. *Cell, 74*(1), 15-27. Retrieved from http://www.ncbi.nlm.nih.gov/entrez/query.fcgi?cmd=Retrieve&db=PubMed&dopt=Citation&list_uids=7916657

Eichler, K., Li, F., Litwin-Kumar, A., Park, Y., Andrade, I., Schneider-Mizell, C. M., . . . Cardona, A. (2017). The complete connectome of a learning and memory centre in an insect brain. *Nature, 548*(7666), 175-182. doi:10.1038/nature23455

Eklof-Ljunggren, E., Haupt, S., Ausborn, J., Dehnisch, I., Uhlen, P., Higashijima, S., & El Manira, A. (2012). Origin of excitation underlying locomotion in the spinal circuit of zebrafish. *Proc Natl Acad Sci U S A, 109*(14), 5511-5516. doi:10.1073/pnas.1115377109

Elliott, J., Jolicoeur, C., Ramamurthy, V., & Cayouette, M. (2008). Ikaros confers early temporal competence to mouse retinal progenitor cells. *Neuron, 60*(1), 26-39. doi:S0896-6273(08)00676-4 [pii] 10.1016/j.neuron.2008.08.008

Enriquez, J., Venkatasubramanian, L., Baek, M., Peterson, M., Aghayeva, U., & Mann, R. S. (2015). Specification of individual adult motor neuron morphologies by combinatorial transcription factor codes. *Neuron, 86*(4), 955-970. doi:10.1016/j.neuron.2015.04.011

Faunes, F., & Larrain, J. (2016). Conservation in the involvement of heterochronic genes and hormones during developmental transitions. *Dev Biol, 416*(1), 3-17. doi:10.1016/j.ydbio.2016.06.013

Fekete, D. M., Perez-Miguelsanz, J., Ryder, E. F., & Cepko, C. L. (1994). Clonal analysis in the chicken retina reveals tangential dispersion of clonally related cells. *Developmental biology, 166*(2), 666-682. doi:10.1006/dbio.1994.1346

Fogarty, M. J., Mantilla, C. B., & Sieck, G. C. (2018). Breathing: Motor Control of Diaphragm Muscle. *Physiology (Bethesda), 33*(2), 113-126. doi:10.1152/physiol.00002.2018

Franco, S. J., & Muller, U. (2013). Shaping our minds: stem and progenitor cell diversity in the mammalian neocortex. *Neuron, 77*(1), 19-34. doi:10.1016/j.neuron.2012.12.022

Fushiki, A., Zwart, M. F., Kohsaka, H., Fetter, R. D., Cardona, A., & Nose, A. (2016). A circuit mechanism for the propagation of waves of muscle contraction in *Drosophila*. *Elife, 5*. doi:10.7554/eLife.13253

Gao, P., Postiglione, M. P., Krieger, T. G., Hernandez, L., Wang, C., Han, Z., . . . Shi, S. H. (2014). Deterministic progenitor behavior and unitary production of neurons in the neocortex. *Cell, 159*(4), 775-788. doi:10.1016/j.cell.2014.10.027

Garen, A., Kauvar, L., & Lepesant, J. A. (1977). Roles of ecdysone in *Drosophila* development. *Proceedings of the National Academy of Sciences of the United States of America, 74*(11), 5099-5103.

Gay, L., Karfilis, K. V., Miller, M. R., Doe, C. Q., & Stankunas, K. (2014). Applying thiouracil tagging to mouse transcriptome analysis. *Nat Protoc, 9*(2), 410-420. doi:10.1038/nprot.2014.023

Gay, L., Miller, M. R., Ventura, P. B., Devasthali, V., Vue, Z., Thompson, H. L., . . . Doe, C. Q. (2013). Mouse TU tagging: a chemical/genetic intersectional method for purifying cell type-specific nascent RNA. *Genes Dev, 27*(1), 98-115. doi:10.1101/gad.205278.112

Gissendanner, C. R., Crossgrove, K., Kraus, K. A., Maina, C. V., & Sluder, A. E. (2004). Expression and function of conserved nuclear receptor genes in Caenorhabditis elegans. *Dev Biol, 266*(2), 399-416.

Gjorgjieva, J., Berni, J., Evers, J. F., & Eglen, S. J. (2013). Neural circuits for peristaltic wave propagation in crawling *Drosophila* larvae: analysis and modeling. *Front Comput Neurosci, 7*, 24. doi:10.3389/fncom.2013.00024

Goetz, C., Pivetta, C., & Arber, S. (2015). Distinct limb and trunk premotor circuits establish laterality in the spinal cord. *Neuron, 85*(1), 131-144. doi:10.1016/j.neuron.2014.11.024

Gorczyca, M., Augart, C., & Budnik, V. (1993). Insulin-like receptor and insulin-like peptide are localized at neuromuscular junctions in *Drosophila*. *J Neurosci, 13*(9), 3692-3704.

Grillner, S. (2003). The motor infrastructure: from ion channels to neuronal networks. *Nat Rev Neurosci, 4*(7), 573-586. doi:10.1038/nrn1137

Grillner, S., & Jessell, T. M. (2009). Measured motion: searching for simplicity in spinal locomotor networks. *Curr Opin Neurobiol, 19*(6), 572-586. doi:10.1016/j.conb.2009.10.011

Grosskortenhaus, R., Pearson, B. J., Marusich, A., & Doe, C. Q. (2005). Regulation of temporal identity transitions in *Drosophila* neuroblasts. *Dev Cell, 8*(2), 193-202. doi:S1534-5807(04)00456-3 [pii] 10.1016/j.devcel.2004.11.019

Grosskortenhaus, R., Robinson, K. J., & Doe, C. Q. (2006). Pdm and Castor specify late-born motor neuron identity in the NB7-1 lineage. *Genes Dev, 20*(18), 2618-2627. doi:20/18/2618 [pii] 10.1101/gad.1445306

Gunnar, E., Bivik, C., Starkenberg, A., & Thor, S. (2016). sequoia controls the type I>0 daughter proliferation switch in the developing *Drosophila* nervous system. *Development, 143*(20), 3774-3784. doi:10.1242/dev.139998

Harris, R. M., Pfeiffer, B. D., Rubin, G. M., & Truman, J. W. (2015). Neuron hemilineages provide the functional ground plan for the *Drosophila* ventral nervous system. *Elife, 4*. doi:10.7554/eLife.04493

Hasegawa, E., Kitada, Y., Kaido, M., Takayama, R., Awasaki, T., Tabata, T., & Sato, M. (2011). Concentric zones, cell migration and neuronal circuits in the *Drosophila* visual center. *Development, 138*(5), 983-993. doi:10.1242/dev.058370

Hasegawa, E., Truman, J. W., & Nose, A. (2016). Identification of excitatory premotor interneurons which regulate local muscle contraction during *Drosophila* larval locomotion. *Sci Rep, 6*, 30806. doi:10.1038/srep30806

Haspel, G., Donovan, M. J., & Hart, A. C. (2010). Motoneurons Dedicated to Either Forward or Backward Locomotion in the Nematode <em>Caenorhabditis elegans</em&gt. *The Journal of Neuroscience, 30*(33), 11151. doi:10.1523/JNEUROSCI.2244-10.2010

Heckscher, E. S., Lockery, S. R., & Doe, C. Q. (2012). Characterization of *Drosophila* larval crawling at the level of organism, segment, and somatic body wall musculature. *J Neurosci, 32*(36), 12460-12471. doi:10.1523/jneurosci.0222-12.2012

Heckscher, E. S., Long, F., Layden, M. J., Chuang, C. H., Manning, L., Richart, J., . . . Doe, C. Q. (2014). Atlas-builder software and the eNeuro atlas: resources for developmental biology and neuroscience. *Development, 141*(12), 2524-2532. doi:10.1242/dev.108720

Heckscher, E. S., Zarin, A. A., Faumont, S., Clark, M. Q., Manning, L., Fushiki, A., . . . Doe, C. Q. (2015). Even-Skipped(+) Interneurons Are Core Components of a Sensorimotor Circuit that Maintains Left-Right Symmetric Muscle Contraction Amplitude. *Neuron, 88*(2), 314-329. doi:10.1016/j.neuron.2015.09.009

Hessinger, C., Technau, G. M., & Rogulja-Ortmann, A. (2017). The *Drosophila* Hox gene Ultrabithorax acts in both muscles and motoneurons to orchestrate formation of specific neuromuscular connections. *Development, 144*(1), 139-150. doi:10.1242/dev.143875

Hoang, B., & Chiba, A. (2001). Single-cell analysis of *Drosophila* larval neuromuscular synapses. *Dev Biol, 229*(1), 55-70. doi:10.1006/dbio.2000.9983

Homem, C. C., Reichardt, I., Berger, C., Lendl, T., & Knoblich, J. A. (2013). Long-term live cell imaging and automated 4D analysis of *Drosophila* neuroblast lineages. *PLoS One, 8*(11), e79588. doi:10.1371/journal.pone.0079588

Homem, C. C., Repic, M., & Knoblich, J. A. (2015). Proliferation control in neural stem and progenitor cells. *Nat Rev Neurosci, 16*(11), 647-659. doi:10.1038/nrn4021

Homem, C. C., Steinmann, V., Burkard, T. R., Jais, A., Esterbauer, H., & Knoblich, J. A. (2014). Ecdysone and mediator change energy metabolism to terminate proliferation in *Drosophila* neural stem cells. *Cell, 158*(4), 874-888. doi:10.1016/j.cell.2014.06.024

Hooper, J. E. (1986). Homeotic gene function in the muscles of *Drosophila* larvae. *EMBO J, 5*(9), 2321-2329.

Isshiki, T., Pearson, B., Holbrook, S., & Doe, C. Q. (2001). *Drosophila* neuroblasts sequentially express transcription factors which specify the temporal identity of their neuronal progeny. *Cell, 106*(4), 511-521. doi:S0092-8674(01)00465-2 [pii]

Isshiki, T., Takeichi, M., & Nose, A. (1997). The role of the msh homeobox gene during *Drosophila* neurogenesis: implication for the dorsoventral specification of the neuroectoderm. *Development, 124*(16), 3099-3109. Retrieved from http://www.ncbi.nlm.nih.gov/entrez/query.fcgi?cmd=Retrieve&db=PubMed&dopt=Citation&list_uids=9272951

Ito, K., Awano, W., Suzuki, K., Hiromi, Y., & Yamamoto, D. (1997). The *Drosophila* mushroom body is a quadruple structure of clonal units each of which contains a virtually identical set of neurones and glial cells. *Development, 124*(4), 761-771.

Ito, K., & Awasaki, T. (2008). Clonal unit architecture of the adult fly brain. *Advances in experimental medicine and biology, 628*, 137-158. doi:10.1007/978-0-387-78261-4_9

Ito, M., Masuda, N., Shinomiya, K., Endo, K., & Ito, K. (2013). Systematic analysis of neural projections reveals clonal composition of the *Drosophila* brain. *Curr Biol, 23*(8), 644-655. doi:10.1016/j.cub.2013.03.015

Izquierdo, E. J., & Beer, R. D. (2013). Connecting a connectome to behavior: an ensemble of neuroanatomical models of C. elegans klinotaxis. *PLoS Comput Biol, 9*(2), e1002890. doi:10.1371/journal.pcbi.1002890

Izquierdo, E. J., Williams, P. L., & Beer, R. D. (2015). Information Flow through a Model of the C. elegans Klinotaxis Circuit. *PLoS One, 10*(10), e0140397. doi:10.1371/journal.pone.0140397

Jessell, T. M. (2000). Neuronal specification in the spinal cord: inductive signals and transcriptional codes. *Nature reviews. Genetics, 1*(1), 20-29. doi:10.1038/35049541

Jiang, Y., & Reichert, H. (2014). *Drosophila* neural stem cells in brain development and tumor formation. *J Neurogenet, 28*(3-4), 181-189. doi:10.3109/01677063.2014.898639

Kambadur, R., Koizumi, K., Stivers, C., Nagle, J., Poole, S. J., & Odenwald, W. F. (1998). Regulation of POU genes by castor and hunchback establishes layered compartments in the *Drosophila* CNS. *Genes Dev, 12*(2), 246-260. Retrieved from http://www.ncbi.nlm.nih.gov/entrez/query.fcgi?cmd=Retrieve&db=PubMed&dopt=Citation&list_uids=9436984

Kanai, M. I., Okabe, M., & Hiromi, Y. (2005). seven-up Controls switching of transcription factors that specify temporal identities of *Drosophila* neuroblasts. *Developmental cell, 8*(2), 203-213. doi:10.1016/j.devcel.2004.12.014

Kao, C. F., Yu, H. H., He, Y., Kao, J. C., & Lee, T. (2012). Hierarchical deployment of factors regulating temporal fate in a diverse neuronal lineage of the *Drosophila* central brain. *Neuron, 73*(4), 677-684. doi:10.1016/j.neuron.2011.12.018

Karbowski, J., Schindelman, G., Cronin, C. J., Seah, A., & Sternberg, P. W. (2008). Systems level circuit model of C. elegans undulatory locomotion: mathematical modeling and molecular genetics. *J Comput Neurosci, 24*(3), 253-276. doi:10.1007/s10827-007-0054-6

Kawano, T., Po, Michelle D., Gao, S., Leung, G., Ryu, William S., & Zhen, M. (2011). An Imbalancing Act: Gap Junctions Reduce the Backward Motor Circuit Activity to Bias C. elegans for Forward Locomotion. *Neuron, 72*(4), 572-586. doi:https://doi.org/10.1016/j.neuron.2011.09.005

Kessaris, N., Pringle, N., & Richardson, W. D. (2001). Ventral neurogenesis and the neuron-glial switch. *Neuron, 31*(5), 677-680.

Kiehn, O. (2006). Locomotor circuits in the mammalian spinal cord. *Annu Rev Neurosci, 29*, 279-306. doi:10.1146/annurev.neuro.29.051605.112910

Kimura, Y., Satou, C., Fujioka, S., Shoji, W., Umeda, K., Ishizuka, T., . . . Higashijima, S. (2013). Hindbrain V2a neurons in the excitation of spinal locomotor circuits during zebrafish swimming. *Curr Biol, 23*(10), 843-849. doi:10.1016/j.cub.2013.03.066

King-Jones, K., & Thummel, C. S. (2005). Developmental biology. Less steroids make bigger flies. *Science, 310*(5748), 630-631. doi:10.1126/science.1120410

Kiss, I., Bencze, G., Fekete, E., Fodor, A., Gausz, J., Maroy, P., . . . Szidonya, J. (1976). Isolation and characterization of X-linked lethal mutants affecting differentiation of the imaginal discs in *Drosophila* melanogaster. *Theor Appl Genet, 48*(5), 217-226. doi:10.1007/bf00281284

Kohsaka, H., Guertin, P. A., & Nose, A. (2017). Neural Circuits Underlying Fly Larval Locomotion. *Curr Pharm Des, 23*(12), 1722-1733. doi:10.2174/1381612822666161208120835

Kohsaka, H., Takasu, E., Morimoto, T., & Nose, A. (2014). A group of segmental premotor interneurons regulates the speed of axial locomotion in *Drosophila* larvae. *Curr Biol, 24*(22), 2632-2642. doi:10.1016/j.cub.2014.09.026

Kohsaka, H., Zwart, M. F., Fushiki, A., Fetter, R. D., Truman, J. W., Cardona, A., & Nose, A. (2019). Regulation of forward and backward locomotion through intersegmental feedback circuits in *Drosophila* larvae. *Nat Commun, 10*(1), 2654. doi:10.1038/s41467-019-10695-y

Kohwi, M., & Doe, C. Q. (2013). Temporal fate specification and neural progenitor competence during development. *Nat Rev Neurosci, 14*(12), 823-838. Retrieved from http://www.ncbi.nlm.nih.gov/pubmed/24400340

Kohwi, M., Lupton, J. R., Lai, S. L., Miller, M. R., & Doe, C. Q. (2013). Developmentally regulated subnuclear genome reorganization restricts neural progenitor competence in *Drosophila*. *Cell, 152*(1-2), 97-108. doi:10.1016/j.cell.2012.11.049

Kolodkin, A. L., & Tessier-Lavigne, M. (2011). Mechanisms and molecules of neuronal wiring: a primer. *Cold Spring Harb Perspect Biol, 3*(6). doi:10.1101/cshperspect.a001727

Kondo, S., & Ueda, R. (2013). Highly improved gene targeting by germline-specific Cas9 expression in *Drosophila*. *Genetics, 195*(3), 715-721. doi:10.1534/genetics.113.156737

Koon, A. C., Ashley, J., Barria, R., DasGupta, S., Brain, R., Waddell, S., . . . Budnik, V. (2011). Autoregulatory and paracrine control of synaptic and behavioral plasticity by octopaminergic signaling. *Nature neuroscience, 14*(2), 190-199. doi:10.1038/nn.2716

Koon, A. C., & Budnik, V. (2012). Inhibitory control of synaptic and behavioral plasticity by octopaminergic signaling. *J Neurosci, 32*(18), 6312-6322. doi:10.1523/jneurosci.6517-11.2012

Koyama, T., & Mirth, C. K. (2016). Growth-Blocking Peptides As Nutrition-Sensitive Signals for Insulin Secretion and Body Size Regulation. *PLoS Biol, 14*(2), e1002392. doi:10.1371/journal.pbio.1002392

Kozlova, T., & Thummel, C. S. (2000). Steroid Regulation of Postembryonic Development and Reproduction in *Drosophila*. *Trends in Endocrinology & Metabolism, 11*(7), 276-280. doi:10.1016/S1043-2760(00)00282-4

Kristan, W. B., Jr., Calabrese, R. L., & Friesen, W. O. (2005). Neuronal control of leech behavior. *Prog Neurobiol, 76*(5), 279-327. doi:10.1016/j.pneurobio.2005.09.004

Kucherenko, M. M., Barth, J., Fiala, A., & Shcherbata, H. R. (2012). Steroid-induced microRNA let-7 acts as a spatio-temporal code for neuronal cell fate in the developing *Drosophila* brain. *EMBO J, 31*(24), 4511-4523. doi:10.1038/emboj.2012.298

Kucherenko, M. M., & Shcherbata, H. R. (2013). Steroids as external temporal codes act via microRNAs and cooperate with cytokines in differential neurogenesis. *Fly (Austin), 7*(3), 173-183. doi:10.4161/fly.25241

Kulkarni, A., Ertekin, D., Lee, C. H., & Hummel, T. (2016). Birth order dependent growth cone segregation determines synaptic layer identity in the *Drosophila* visual system. *Elife, 5*, e13715. doi:10.7554/eLife.13715

Kunert, J. M., Maia, P. D., & Kutz, J. N. (2017). Functionality and Robustness of Injured Connectomic Dynamics in C. elegans: Linking Behavioral Deficits to Neural Circuit Damage. *PLoS Comput Biol, 13*(1), e1005261. doi:10.1371/journal.pcbi.1005261

Lacin, H., & Truman, J. W. (2016a). Lineage mapping identifies molecular and architectural similarities between the larval and adult *Drosophila* central nervous system. *Elife, 5*, e13399. doi:10.7554/eLife.13399

Lacin, H., & Truman, J. W. (2016b). Lineage mapping identifies molecular and architectural similarities between the larval and adult *Drosophila* central nervous system. *Elife, 5*, eLife.13399. doi:10.7554/eLife.13399

Lai, S. L., Awasaki, T., Ito, K., & Lee, T. (2008). Clonal analysis of *Drosophila* antennal lobe neurons: diverse neuronal architectures in the lateral neuroblast lineage. *Development, 135*(17), 2883-2893. doi:dev.024380 [pii] 10.1242/dev.024380

Lai, S. L., & Doe, C. Q. (2014). Transient nuclear Prospero induces neural progenitor quiescence. *Elife, 3*. doi:10.7554/eLife.03363

Lam, G., Hall, B. L., Bender, M., & Thummel, C. S. (1999). DHR3 is required for the prepupal-pupal transition and differentiation of adult structures during *Drosophila* metamorphosis. *Dev Biol, 212*(1), 204-216. doi:10.1006/dbio.1999.9343

Landgraf, M., Bossing, T., Technau, G. M., & Bate, M. (1997). The origin, location, and projections of the embryonic abdominal motorneurons of *Drosophila*. *J Neurosci, 17*(24), 9642-9655.

Landgraf, M., Jeffrey, V., Fujioka, M., Jaynes, J. B., & Bate, M. (2003). Embryonic origins of a motor system: motor dendrites form a myotopic map in *Drosophila*. *PLoS Biol, 1*(2), E41. doi:10.1371/journal.pbio.0000041

Landgraf, M., Sanchez-Soriano, N., Technau, G. M., Urban, J., & Prokop, A. (2003). Charting the *Drosophila* neuropile: a strategy for the standardised characterisation of genetically amenable neurites. *Dev Biol, 260*(1), 207-225. Retrieved from http://www.ncbi.nlm.nih.gov/pubmed/12885565

Lee, C. Y., Andersen, R. O., Cabernard, C., Manning, L., Tran, K. D., Lanskey, M. J., . . . Doe, C. Q. (2006). *Drosophila* Aurora-A kinase inhibits neuroblast self-renewal by regulating aPKC/Numb cortical polarity and spindle orientation. *Genes Dev, 20*(24), 3464-3474. doi:20/24/3464 [pii] 10.1101/gad.1489406

Lee, T., Lee, A., & Luo, L. (1999). Development of the *Drosophila* mushroom bodies: sequential generation of three distinct types of neurons from a neuroblast. *Development, 126*(18), 4065-4076.

Lee, T., Marticke, S., Sung, C., Robinow, S., & Luo, L. (2000). Cell-autonomous requirement of the USP/EcR-B ecdysone receptor for mushroom body neuronal remodeling in *Drosophila*. *Neuron, 28*(3), 807-818.

Lemon, W. C., Pulver, S. R., Hockendorf, B., McDole, K., Branson, K., Freeman, J., & Keller, P. J. (2015). Whole-central nervous system functional imaging in larval *Drosophila*. *Nat Commun, 6*, 7924. doi:10.1038/ncomms8924

Li, X., Erclik, T., Bertet, C., Chen, Z., Voutev, R., Venkatesh, S., . . . Desplan, C. (2013a). Temporal patterning of *Drosophila* medulla neuroblasts controls neural fates. *Nature, 498*(7455), 456-462. doi:10.1038/nature12319

Li, X., Erclik, T., Bertet, C., Chen, Z., Voutev, R., Venkatesh, S., . . . Desplan, C. (2013b). Temporal patterning of *Drosophila* medulla neuroblasts controls neural fates. *Nature*. doi:10.1038/nature12319

Lieske, S. P., Thoby-Brisson, M., Telgkamp, P., & Ramirez, J. M. (2000). Reconfiguration of the neural network controlling multiple breathing patterns: eupnea, sighs and gasps [see comment]. *Nature neuroscience, 3*(6), 600-607. doi:10.1038/75776

Lin, S., Marin, E. C., Yang, C. P., Kao, C. F., Apenteng, B. A., Huang, Y., . . . Lee, T. (2013). Extremes of lineage plasticity in the *Drosophila* brain. *Curr Biol, 23*(19), 1908-1913. doi:10.1016/j.cub.2013.07.074

Liu, Z., Yang, C. P., Sugino, K., Fu, C. C., Liu, L. Y., Yao, X., . . . Lee, T. (2015). Opposing intrinsic temporal gradients guide neural stem cell production of varied neuronal fates. *Science, 350*(6258), 317-320. doi:10.1126/science.aad1886

Ljunggren, E. E., Haupt, S., Ausborn, J., Ampatzis, K., & El Manira, A. (2014). Optogenetic activation of excitatory premotor interneurons is sufficient to generate coordinated locomotor activity in larval zebrafish. *J Neurosci, 34*(1), 134-139. doi:10.1523/jneurosci.4087-13.2014

Llorens-Bobadilla, E., & Martin-Villalba, A. (2017). Adult NSC diversity and plasticity: the role of the niche. *Current Opinion in Neurobiology, 42*, 68-74. doi:https://doi.org/10.1016/j.conb.2016.11.008

Lodato, S., & Arlotta, P. (2015). Generating neuronal diversity in the mammalian cerebral cortex. *Annu Rev Cell Dev Biol, 31*, 699-720. doi:10.1146/annurev-cellbio-100814-125353

Love, M. I., Huber, W., & Anders, S. (2014). Moderated estimation of fold change and dispersion for RNA-seq data with DESeq2. *Genome Biol, 15*(12), 550. doi:10.1186/s13059-014-0550-8

Loveless, J., Lagogiannis, K., & Webb, B. (2018). Mechanics of exploration in *Drosophila* melanogaster. *bioRxiv*, 354795. doi:10.1101/354795

MacNamee, S. E., Liu, K. E., Gerhard, S., Tran, C. T., Fetter, R. D., Cardona, A., . . . Oland, L. A. (2016). Astrocytic glutamate transport regulates a *Drosophila* CNS synapse that lacks astrocyte ensheathment. *J Comp Neurol, 524*(10), 1979-1998. doi:10.1002/cne.24016

Macosko, E. Z., Pokala, N., Feinberg, E. H., Chalasani, S. H., Butcher, R. A., Clardy, J., & Bargmann, C. I. (2009). A hub-and-spoke circuit drives pheromone attraction and social behaviour in C. elegans. *Nature, 458*(7242), 1171-1175. doi:10.1038/nature07886

Marder, E., & Bucher, D. (2001). Central pattern generators and the control of rhythmic movements. *Curr Biol, 11*(23), R986-996.

Marin-Burgin, A., Kristan, W. B., Jr., & French, K. A. (2008). From synapses to behavior: development of a sensory-motor circuit in the leech. *Dev Neurobiol, 68*(6), 779-787. doi:10.1002/dneu.20551

Mattar, P., Ericson, J., Blackshaw, S., & Cayouette, M. (2015). A conserved regulatory logic controls temporal identity in mouse neural progenitors. *Neuron, 85*(3), 497-504. doi:10.1016/j.neuron.2014.12.052

Maurange, C., Cheng, L., & Gould, A. P. (2008). Temporal transcription factors and their targets schedule the end of neural proliferation in *Drosophila*. *Cell, 133*(5), 891-902. doi:S0092-8674(08)00499-6 [pii] 10.1016/j.cell.2008.03.034

Maurange, C., & Gould, A. P. (2005). Brainy but not too brainy: starting and stopping neuroblast divisions in *Drosophila*. *Trends Neurosci, 28*(1), 30-36. doi:S0166-2236(04)00337-6 [pii]

10.1016/j.tins.2004.10.009

Mauss, A., Tripodi, M., Evers, J. F., & Landgraf, M. (2009). Midline signalling systems direct the formation of a neural map by dendritic targeting in the *Drosophila* motor system. *PLoS Biol, 7*(9), e1000200. doi:10.1371/journal.pbio.1000200

McConnell, S. K., & Kaznowski, C. E. (1991). Cell cycle dependence of laminar determination in developing neocortex. *Science, 254*(5029), 282-285.

McDonald, J. A., & Doe, C. Q. (1997). Establishing neuroblast-specific gene expression in the *Drosophila* CNS: huckebein is activated by Wingless and Hedgehog and repressed by Engrailed and Gooseberry. *Development, 124*(5), 1079-1087. Retrieved from http://www.ncbi.nlm.nih.gov/entrez/query.fcgi?cmd=Retrieve&db=PubMed&dopt=Citation&list_uids=9056782

McDonald, J. A., Holbrook, S., Isshiki, T., Weiss, J., Doe, C. Q., & Mellerick, D. M. (1998). Dorsoventral patterning in the *Drosophila* central nervous system: the vnd homeobox gene specifies ventral column identity. *Genes Dev, 12*(22), 3603-3612. Retrieved from http://www.ncbi.nlm.nih.gov/entrez/query.fcgi?cmd=Retrieve&db=PubMed&dopt=Citation&list_uids=9832511

Mettler, U., Vogler, G., & Urban, J. (2006). Timing of identity: spatiotemporal regulation of hunchback in neuroblast lineages of *Drosophila* by Seven-up and Prospero. *Development, 133*(3), 429-437. doi:dev.02229 [pii] 10.1242/dev.02229

Mihalas, A. B., & Hevner, R. F. (2018). Clonal analysis reveals laminar fate multipotency and daughter cell apoptosis of mouse cortical intermediate progenitors. *Development, 145*(17). doi:10.1242/dev.164335

Miller, M. R., Robinson, K. J., Cleary, M. D., & Doe, C. Q. (2009). TU-tagging: cell type-specific RNA isolation from intact complex tissues. *Nat Methods, 6*(6), 439-441. doi:nmeth.1329 [pii] 10.1038/nmeth.1329

Mlodzik, M., Hiromi, Y., Weber, U., Goodman, C. S., & Rubin, G. M. (1990). The *Drosophila* seven-up gene, a member of the steroid receptor gene superfamily, controls photoreceptor cell fates. *Cell, 60*(2), 211-224.

Moris-Sanz, M., Estacio-Gomez, A., Alvarez-Rivero, J., & Diaz-Benjumea, F. J. (2014). Specification of neuronal subtypes by different levels of Hunchback. *Development, 141*(22), 4366-4374. doi:10.1242/dev.113381

Mullins, O. J., Hackett, J. T., Buchanan, J. T., & Friesen, W. O. (2011). Neuronal control of swimming behavior: comparison of vertebrate and invertebrate model systems. *Prog Neurobiol, 93*(2), 244-269. doi:10.1016/j.pneurobio.2010.11.001

Mulloney, B., & Smarandache-Wellmann, C. (2012). Neurobiology of the crustacean swimmeret system. *Prog Neurobiol, 96*(2), 242-267. doi:10.1016/j.pneurobio.2012.01.002

Mulloney, B., Smarandache-Wellmann, C., Weller, C., Hall, W. M., & DiCaprio, R. A. (2014). Proprioceptive feedback modulates coordinating information in a system of segmentally distributed microcircuits. *J Neurophysiol, 112*(11), 2799-2809. doi:10.1152/jn.00321.2014

Naka, H., Nakamura, S., Shimazaki, T., & Okano, H. (2008). Requirement for COUP-TFI and II in the temporal specification of neural stem cells in CNS development. *Nature neuroscience, 11*(9), 1014-1023. doi:10.1038/nn.2168

Narbonne-Reveau, K., Lanet, E., Dillard, C., Foppolo, S., Chen, C. H., Parrinello, H., . . . Maurange, C. (2016). Neural stem cell-encoded temporal patterning delineates an early window of malignant susceptibility in *Drosophila*. *Elife, 5*. doi:10.7554/eLife.13463

Nern, A., Pfeiffer, B. D., & Rubin, G. M. (2015). Optimized tools for multicolor stochastic labeling reveal diverse stereotyped cell arrangements in the fly visual system. *Proc Natl Acad Sci U S A, 112*(22), E2967-2976. doi:10.1073/pnas.1506763112

Nishimaru, H., & Kakizaki, M. (2009). The role of inhibitory neurotransmission in locomotor circuits of the developing mammalian spinal cord. *Acta Physiol (Oxf), 197*(2), 83-97. doi:10.1111/j.1748-1716.2009.02020.x

Novotny, T., Eiselt, R., & Urban, J. (2002). Hunchback is required for the specification of the early sublineage of neuroblast 7-3 in the *Drosophila* central nervous system. *Development, 129*(4), 1027-1036. Retrieved from http://www.ncbi.nlm.nih.gov/pubmed/11861485

Ohyama, T., Schneider-Mizell, C. M., Fetter, R. D., Aleman, J. V., Franconville, R., Rivera-Alba, M., . . . Zlatic, M. (2015). A multilevel multimodal circuit enhances action selection in *Drosophila*. *Nature, 520*(7549), 633-639. doi:10.1038/nature14297

Okano, H., & Temple, S. (2009). Cell types to order: temporal specification of CNS stem cells. *Curr Opin Neurobiol, 19*(2), 112-119. doi:S0959-4388(09)00022-1 [pii] 10.1016/j.conb.2009.04.003

Otsuki, L., & Brand, A. H. (2017). The vasculature as a neural stem cell niche. *Neurobiol Dis*. doi:10.1016/j.nbd.2017.01.010

Pearson, B. J., & Doe, C. Q. (2003). Regulation of neuroblast competence in *Drosophila*. *Nature, 425*(6958), 624-628. doi:10.1038/nature01910 nature01910 [pii]

Pearson, K. G. (1976). Nerve cells without action potentials. In J. C. Fentress (Ed.), *Comparative neurobiology: modes of communcation in the nervous system* (pp. 99-110). Sunderland, MA: Sinauer.

Pehlevan, C., Paoletti, P., & Mahadevan, L. (2016). Integrative neuromechanics of crawling in D. melanogaster larvae. *Elife, 5*, e11031. doi:10.7554/eLife.11031

Petrovic, M., & Hummel, T. (2008). Temporal identity in axonal target layer recognition. *Nature, 456*(7223), 800-803. doi:10.1038/nature07407

Pfeiffer, B. D., Jenett, A., Hammonds, A. S., Ngo, T. T., Misra, S., Murphy, C., . . . Rubin, G. M. (2008). Tools for neuroanatomy and neurogenetics in *Drosophila*. *Proc Natl Acad Sci U S A, 105*(28), 9715-9720. doi:0803697105 [pii] 10.1073/pnas.0803697105

Pfeiffer, B. D., Ngo, T. T., Hibbard, K. L., Murphy, C., Jenett, A., Truman, J. W., & Rubin, G. M. (2010). Refinement of tools for targeted gene expression in *Drosophila*. *Genetics, 186*(2), 735-755. doi:10.1534/genetics.110.119917

Pierce-Shimomura, J. T., Chen, B. L., Mun, J. J., Ho, R., Sarkis, R., & McIntire, S. L. (2008). Genetic analysis of crawling and swimming locomotory patterns in C. elegans. *Proc Natl Acad Sci U S A, 105*(52), 20982-20987. doi:10.1073/pnas.0810359105

Piggott, Beverly J., Liu, J., Feng, Z., Wescott, Seth A., & Xu, X. Z. S. (2011). The Neural Circuits and Synaptic Mechanisms Underlying Motor Initiation in C. elegans. *Cell, 147*(4), 922-933. doi:https://doi.org/10.1016/j.cell.2011.08.053

Poon, C. L., Mitchell, K. A., Kondo, S., Cheng, L. Y., & Harvey, K. F. (2016). The Hippo Pathway Regulates Neuroblasts and Brain Size in *Drosophila* melanogaster. *Curr Biol, 26*(8), 1034-1042. doi:10.1016/j.cub.2016.02.009

Popescu, I. R., & Frost, W. N. (2002). Highly dissimilar behaviors mediated by a multifunctional network in the marine mollusk Tritonia diomedea. *J Neurosci, 22*(5), 1985-1993.

Port, F., Chen, H. M., Lee, T., & Bullock, S. L. (2014). Optimized CRISPR/Cas tools for efficient germline and somatic genome engineering in *Drosophila*. *Proc Natl Acad Sci U S A, 111*(29), E2967-2976. doi:10.1073/pnas.1405500111

Powsner, L. (1935). The Effects of Temperature on the Durations of the Developmental Stages of *Drosophila* melanogaster. *Physiological Zoology, 8*(4), 474-520. doi:10.1086/physzool.8.4.30151263

Prinz, A. A., Bucher, D., & Marder, E. (2004). Similar network activity from disparate circuit parameters. *Nat Neurosci, 7*(12), 1345-1352. doi:10.1038/nn1352

Pulver, S. R., Bayley, T. G., Taylor, A. L., Berni, J., Bate, M., & Hedwig, B. (2015). Imaging fictive locomotor patterns in larval *Drosophila*. *J Neurophysiol, 114*(5), 2564-2577. doi:10.1152/jn.00731.2015

Rakowski, F., & Karbowski, J. (2017). Optimal synaptic signaling connectome for locomotory behavior in Caenorhabditis elegans: Design minimizing energy cost. *PLoS Comput Biol, 13*(11), e1005834. doi:10.1371/journal.pcbi.1005834

Ramirez, J. M., & Pearson, K. G. (1988). Generation of motor patterns for walking and flight in motoneurons supplying bifunctional muscles in the locust. *J Neurobiol, 19*(3), 257-282. doi:10.1002/neu.480190307

Ren, Q., Yan, C.-P., Liu, Z., Sugino, K., Mok, K., He, Y., & Lee, T. (2017). Stem cell intrinsic, Seven-up-triggered temporal factor gradients diversify intermediate neural progenitors. *Current Biology, in press*.

Richardson, H. E., & Portela, M. (2017). Tissue growth and tumorigenesis in *Drosophila*: cell polarity and the Hippo pathway. *Curr Opin Cell Biol, 48*, 1-9. doi:10.1016/j.ceb.2017.03.006

Roberts, A., Li, W. C., & Soffe, S. R. (2010). How neurons generate behavior in a hatchling amphibian tadpole: an outline. *Front Behav Neurosci, 4*, 16. doi:10.3389/fnbeh.2010.00016

Roberts, A., Li, W. C., Soffe, S. R., & Wolf, E. (2008). Origin of excitatory drive to a spinal locomotor network. *Brain Res Rev, 57*(1), 22-28. doi:10.1016/j.brainresrev.2007.06.015

Roberts, W. M., Augustine, S. B., Lawton, K. J., Lindsay, T. H., Thiele, T. R., Izquierdo, E. J., . . . Lockery, S. R. (2016). A stochastic neuronal model predicts random search behaviors at multiple spatial scales in C. elegans. *Elife, 5*. doi:10.7554/eLife.12572

Rossi, A. M., Fernandes, V. M., & Desplan, C. (2016). Timing temporal transitions during brain development. *Curr Opin Neurobiol, 42*, 84-92. doi:10.1016/j.conb.2016.11.010

Saalfeld, S., Cardona, A., Hartenstein, V., & Tomancak, P. (2009). CATMAID: collaborative annotation toolkit for massive amounts of image data. *Bioinformatics, 25*(15), 1984-1986. doi:10.1093/bioinformatics/btp266

Schlegel, P., Texada, M. J., Miroschnikow, A., Schoofs, A., Huckesfeld, S., Peters, M., . . . Pankratz, M. J. (2016). Synaptic transmission parallels neuromodulation in a central food-intake circuit. *Elife, 5*. doi:10.7554/eLife.16799

Schmid, A., Chiba, A., & Doe, C. Q. (1999). Clonal analysis of *Drosophila* embryonic neuroblasts: neural cell types, axon projections and muscle targets. *Development, 126*(21), 4653-4689. Retrieved from http://www.ncbi.nlm.nih.gov/entrez/query.fcgi?cmd=Retrieve&db=PubMed&dopt=Citation&list_uids=10518486

Schmidt, H., Rickert, C., Bossing, T., Vef, O., Urban, J., & Technau, G. M. (1997). The embryonic central nervous system lineages of *Drosophila* melanogaster. II. Neuroblast lineages derived from the dorsal part of the neuroectoderm. *Dev Biol, 189*(2), 186-204. doi:S0012160697986607 [pii]

Schneider-Mizell, C. M., Gerhard, S., Longair, M., Kazimiers, T., Li, F., Zwart, M. F., . . . Cardona, A. (2016). Quantitative neuroanatomy for connectomics in *Drosophila*. *Elife, 5*. doi:10.7554/eLife.12059

Schubiger, M., Wade, A. A., Carney, G. E., Truman, J. W., & Bender, M. (1998). *Drosophila* EcR-B ecdysone receptor isoforms are required for larval molting and for neuron remodeling during metamorphosis. *Development, 125*(11), 2053-2062.

Seroka, A. Q., & Doe, C. Q. (2019). The Hunchback temporal transcription factor determines motor neuron axon and dendrite targeting in *Drosophila*. *Development*. doi:10.1242/dev.175570

Seto, Y., Nakatani, T., Masuyama, N., Taya, S., Kumai, M., Minaki, Y., . . . Hoshino, M. (2014). Temporal identity transition from Purkinje cell progenitors to GABAergic interneuron progenitors in the cerebellum. *Nat Commun, 5*, 3337. doi:10.1038/ncomms4337

Shen, Q., Wang, Y., Dimos, J. T., Fasano, C. A., Phoenix, T. N., Lemischka, I. R., . . . Temple, S. (2006). The timing of cortical neurogenesis is encoded within lineages of individual progenitor cells. *Nature neuroscience, 9*(6), 743-751. doi:10.1038/nn1694

Skeath, J. B., & Doe, C. Q. (1998). Sanpodo and Notch act in opposition to Numb to distinguish sibling neuron fates in the *Drosophila* CNS. *Development, 125*(10), 1857-1865. Retrieved from http://www.ncbi.nlm.nih.gov/entrez/query.fcgi?cmd=Retrieve&db=PubMed&dopt=Citation&list_uids=9550718

Skeath, J. B., & Thor, S. (2003). Genetic control of *Drosophila* nerve cord development. *Curr Opin Neurobiol, 13*(1), 8-15. doi:S0959438803000072 [pii]

Skeath, J. B., Zhang, Y., Holmgren, R., Carroll, S. B., & Doe, C. Q. (1995). Specification of neuroblast identity in the *Drosophila* embryonic central nervous system by gooseberry-distal. *Nature, 376*(6539), 427-430. doi:10.1038/376427a0

Song, J., Ampatzis, K., Bjornfors, E. R., & El Manira, A. (2016). Motor neurons control locomotor circuit function retrogradely via gap junctions. *Nature, 529*(7586), 399-402. doi:10.1038/nature16497

Sousa-Nunes, R., Yee, L. L., & Gould, A. P. (2011). Fat cells reactivate quiescent neuroblasts via TOR and glial insulin relays in *Drosophila*. *Nature, 471*(7339), 508-512. doi:10.1038/nature09867

Speder, P., & Brand, A. H. (2014). Gap junction proteins in the blood-brain barrier control nutrient-dependent reactivation of *Drosophila* neural stem cells. *Dev Cell, 30*(3), 309-321. doi:10.1016/j.devcel.2014.05.021

Stratmann, J., Gabilondo, H., Benito-Sipos, J., & Thor, S. (2016). Neuronal cell fate diversification controlled by sub-temporal action of Kruppel. *Elife, 5*, e19311. doi:10.7554/eLife.19311.001

Suzuki, T., Kaido, M., Takayama, R., & Sato, M. (2013). A temporal mechanism that produces neuronal diversity in the *Drosophila* visual center. *Dev Biol, 380*(1), 12-24. doi:10.1016/j.ydbio.2013.05.002

Syed, M. H., Mark, B., & Doe, C. Q. (2017). Steroid hormone induction of temporal gene expression in *Drosophila* brain neuroblasts generates neuronal and glial diversity. *Elife, 6*. doi:10.7554/eLife.26287

Takagi, S., Cocanougher, B. T., Niki, S., Miyamoto, D., Kohsaka, H., Kazama, H., . . . Nose, A. (2017). Divergent Connectivity of Homologous Command-like Neurons Mediates Segment-Specific Touch Responses in *Drosophila*. *Neuron, 96*(6), 1373-1387.e1376. doi:10.1016/j.neuron.2017.10.030

Takemura, S. Y., Bharioke, A., Lu, Z., Nern, A., Vitaladevuni, S., Rivlin, P. K., . . . Chklovskii, D. B. (2013). A visual motion detection circuit suggested by *Drosophila* connectomics. *Nature, 500*(7461), 175-181. doi:10.1038/nature12450

Thummel, C. S. (2001). Molecular mechanisms of developmental timing in C. elegans and *Drosophila*. *Dev Cell, 1*(4), 453-465.

Toma, K., Kumamoto, T., & Hanashima, C. (2014). The timing of upper-layer neurogenesis is conferred by sequential derepression and negative feedback from deep-layer neurons. *J Neurosci, 34*(39), 13259-13276. doi:10.1523/jneurosci.2334-14.2014

Tran, K. D., & Doe, C. Q. (2008). Pdm and Castor close successive temporal identity windows in the NB3-1 lineage. *Development, 135*(21), 3491-3499. doi:dev.024349 [pii] 10.1242/dev.024349

Truman, J. W., & Bate, M. (1988). Spatial and temporal patterns of neurogenesis in the central nervous system of *Drosophila* melanogaster. *Dev Biol, 125*(1), 145-157.

Truman, J. W., Moats, W., Altman, J., Marin, E. C., & Williams, D. W. (2010). Role of Notch signaling in establishing the hemilineages of secondary neurons in *Drosophila* melanogaster. *Development, 137*(1), 53-61. doi:10.1242/dev.041749

Tsalik, E. L., & Hobert, O. (2003). Functional mapping of neurons that control locomotory behavior in Caenorhabditis elegans. *Journal of Neurobiology, 56*(2), 178-197. doi:10.1002/neu.10245

Tschopp, F., Reiser, M., & Turaga, S. (2018). A Connectome Based Hexagonal Lattice Convolutional Network Model of the *Drosophila* Visual System. *https://arxiv.org/abs/1806.04793v2*.

Tsuji, T., Hasegawa, E., & Isshiki, T. (2008). Neuroblast entry into quiescence is regulated intrinsically by the combined action of spatial Hox proteins and temporal identity factors. *Development, 135*(23), 3859-3869. doi:10.1242/dev.025189

Turrero García, M., Mazzola, E., & Harwell, Corey C. (2016). Lineage Relationships Do Not Drive MGE/PoA-Derived Interneuron Clustering in the Brain. *Neuron, 92*(1), 52-58. doi:https://doi.org/10.1016/j.neuron.2016.09.034

Vidal-Gadea, A., Topper, S., Young, L., Crisp, A., Kressin, L., Elbel, E., . . . Pierce-Shimomura, J. T. (2011). Caenorhabditis elegans selects distinct crawling and swimming gaits via dopamine and serotonin. *Proc Natl Acad Sci U S A, 108*(42), 17504-17509. doi:10.1073/pnas.1108673108

Wakabayashi, T., Kitagawa, I., & Shingai, R. (2004). Neurons regulating the duration of forward locomotion in Caenorhabditis elegans. *Neuroscience Research, 50*(1), 103-111. doi:https://doi.org/10.1016/j.neures.2004.06.005

Wang, W., Jossin, Y., Chai, G., Lien, W. H., Tissir, F., & Goffinet, A. M. (2016). Feedback regulation of apical progenitor fate by immature neurons through Wnt7-Celsr3-Fzd3 signalling. *Nat Commun, 7*, 10936. doi:10.1038/ncomms10936

Wang, Y. C., Yang, J. S., Johnston, R., Ren, Q., Lee, Y. J., Luan, H., . . . Lee, T. (2014). *Drosophila* intermediate neural progenitors produce lineage-dependent related series of diverse neurons. *Development, 141*(2), 253-258. doi:10.1242/dev.103069

Weiss, J. B., Von Ohlen, T., Mellerick, D. M., Dressler, G., Doe, C. Q., & Scott, M. P. (1998). Dorsoventral patterning in the *Drosophila* central nervous system: the intermediate neuroblasts defective homeobox gene specifies intermediate column identity. *Genes Dev, 12*(22), 3591-3602. Retrieved from http://www.ncbi.nlm.nih.gov/entrez/query.fcgi?cmd=Retrieve&db=PubMed&dopt=Citation&list_uids=9832510

Wen, Q., Po, M. D., Hulme, E., Chen, S., Liu, X., Kwok, S. W., . . . Samuel, A. D. (2012). Proprioceptive coupling within motor neurons drives C. elegans forward locomotion. *Neuron, 76*(4), 750-761. doi:10.1016/j.neuron.2012.08.039

Wen, Q., Po, M. D., Hulme, E., Chen, S., Liu, X., Kwok, Sen W., . . . Samuel, Aravinthan D. T. (2012). Proprioceptive Coupling within Motor Neurons Drives C. elegans Forward Locomotion. *Neuron, 76*(4), 750-761. doi:https://doi.org/10.1016/j.neuron.2012.08.039

White, J. G., Southgate, E., Thomson, J. N., & Brenner, S. (1986). The structure of the nervous system of the nematode Caenorhabditis elegans. *Philos Trans R Soc Lond B Biol Sci, 314*(1165), 1-340.

Wong, L. L., & Rapaport, D. H. (2009). Defining retinal progenitor cell competence in Xenopus laevis by clonal analysis. *Development, 136*(10), 1707-1715. doi:136/10/1707 [pii] 10.1242/dev.027607

Wreden, C. C., Meng, J. L., Feng, W., Chi, W., Marshall, Z. D., & Heckscher, E. S. (2017). Temporal Cohorts of Lineage-Related Neurons Perform Analogous Functions in Distinct Sensorimotor Circuits. *Curr Biol, 27*(10), 1521-1528.e1524. doi:10.1016/j.cub.2017.04.024

Wu, T. D., & Nacu, S. (2010). Fast and SNP-tolerant detection of complex variants and splicing in short reads. *Bioinformatics, 26*(7), 873-881. doi:10.1093/bioinformatics/btq057

Wu, Y. C., Chen, C. H., Mercer, A., & Sokol, N. S. (2012). Let-7-complex microRNAs regulate the temporal identity of *Drosophila* mushroom body neurons via chinmo. *Dev Cell, 23*(1), 202-209. doi:10.1016/j.devcel.2012.05.013

Xu, H. T., Han, Z., Gao, P., He, S., Li, Z., Shi, W., . . . Shi, S. H. (2014). Distinct lineage-dependent structural and functional organization of the hippocampus. *Cell, 157*(7), 1552-1564. doi:10.1016/j.cell.2014.03.067

Yamanaka, N., Rewitz, K. F., & O'Connor, M. B. (2013). Ecdysone control of developmental transitions: lessons from *Drosophila* research. *Annu Rev Entomol, 58*, 497-516. doi:10.1146/annurev-ento-120811-153608

Yang, C.-P., Samuels, T. J., Huang, Y., Yang, L., Ish-Horowicz, D., Davis, I., & Lee, T. (2017). Imp/Syp Temporal Gradients Govern Decommissioning Of *Drosophila* Neural Stem Cells. *bioRxiv*. doi:10.1101/136655

Yang, L., Samuels, T. J., Arava, Y., Robertson, F., Järvelin, A. I., Yang, C.-P., . . . Davis, I. (2017). Regulating prospero mRNA Stability Determines When Neural Stem Cells Stop Dividing. *bioRxiv*. doi:10.1101/135848

Yoon, K. J., Ming, G. L., & Song, H. (2018). Coupling Neurogenesis to Circuit Formation. *Cell, 173*(2), 288-290. doi:10.1016/j.cell.2018.03.046

Yoshikawa, S., McKinnon, R. D., Kokel, M., & Thomas, J. B. (2003). Wnt-mediated axon guidance via the *Drosophila* Derailed receptor. *Nature, 422*(6932), 583-588. doi:10.1038/nature01522

Yoshino, J., Morikawa, R. K., Hasegawa, E., & Emoto, K. (2017). Neural Circuitry that Evokes Escape Behavior upon Activation of Nociceptive Sensory Neurons in *Drosophila* Larvae. *Curr Biol, 27*(16), 2499-2504.e2493. doi:10.1016/j.cub.2017.06.068

Yu, F., & Schuldiner, O. (2014). Axon and dendrite pruning in *Drosophila*. *Curr Opin Neurobiol, 27*, 192-198. doi:10.1016/j.conb.2014.04.005

Yu, H. H., Awasaki, T., Schroeder, M. D., Long, F., Yang, J. S., He, Y., . . . Lee, T. (2013). Clonal development and organization of the adult *Drosophila* central brain. *Curr Biol, 23*(8), 633-643. doi:10.1016/j.cub.2013.02.057

Yu, H. H., Chen, C. H., Shi, L., Huang, Y., & Lee, T. (2009). Twin-spot MARCM to reveal the developmental origin and identity of neurons. *Nature neuroscience, 12*(7), 947-953. doi:10.1038/nn.2345

Yu, H. H., Kao, C. F., He, Y., Ding, P., Kao, J. C., & Lee, T. (2010). A complete developmental sequence of a *Drosophila* neuronal lineage as revealed by twin-spot MARCM. *PLoS Biol, 8*(8). doi:10.1371/journal.pbio.1000461

Yu, H. H., & Lee, T. (2007). Neuronal temporal identity in post-embryonic *Drosophila* brain. *Trends Neurosci, 30*(10), 520-526. doi:S0166-2236(07)00184-1 [pii] 10.1016/j.tins.2007.07.003

Yu, Y. C., Bultje, R. S., Wang, X., & Shi, S. H. (2009). Specific synapses develop preferentially among sister excitatory neurons in the neocortex. *Nature, 458*(7237), 501-504. doi:10.1038/nature07722

Zagoraiou, L., Akay, T., Martin, J. F., Brownstone, R. M., Jessell, T. M., & Miles, G. B. (2009). A cluster of cholinergic premotor interneurons modulates mouse locomotor activity. *Neuron, 64*(5), 645-662. doi:10.1016/j.neuron.2009.10.017

Zarin, A. A., & Labrador, J. P. (2017). Motor axon guidance in *Drosophila*. *Semin Cell Dev Biol*. doi:10.1016/j.semcdb.2017.11.013

Zelhof, A. C., Yao, T. P., Chen, J. D., Evans, R. M., & McKeown, M. (1995). Seven-up inhibits ultraspiracle-based signaling pathways in vitro and in vivo. *Molecular and cellular biology, 15*(12), 6736-6745. Retrieved from http://www.ncbi.nlm.nih.gov/pubmed/8524239

Zhang, X. J., Li, Z., Han, Z., Sultan, K. T., Huang, K., & Shi, S. H. (2017). Precise inhibitory microcircuit assembly of developmentally related neocortical interneurons in clusters. *Nat Commun, 8*, 16091. doi:10.1038/ncomms16091

Zhang, Y., Ungar, A., Fresquez, C., & Holmgren, R. (1994). Ectopic expression of either the *Drosophila* gooseberry-distal or proximal gene causes alterations of cell fate in the epidermis and central nervous system. *Development, 120*(5), 1151-1161. Retrieved from http://www.ncbi.nlm.nih.gov/pubmed/8026326

Zhen, M., & Samuel, A. D. T. (2015). C. elegans locomotion: small circuits, complex functions. *Current Opinion in Neurobiology, 33*, 117-126. doi:https://doi.org/10.1016/j.conb.2015.03.009

Zhou, B., Williams, D. W., Altman, J., Riddiford, L. M., & Truman, J. W. (2009). Temporal patterns of broad isoform expression during the development of neuronal lineages in *Drosophila*. *Neural Dev, 4*, 39. doi:10.1186/1749-8104-4-39

Zhu, S., Lin, S., Kao, C. F., Awasaki, T., Chiang, A. S., & Lee, T. (2006). Gradients of the *Drosophila* Chinmo BTB-zinc finger protein govern neuronal temporal identity. *Cell, 127*(2), 409-422. doi:S0092-8674(06)01230-X [pii] 10.1016/j.cell.2006.08.045

Zipursky, S. L., & Grueber, W. B. (2013). The molecular basis of self-avoidance. *Annu Rev Neurosci, 36*, 547-568. doi:10.1146/annurev-neuro-062111-150414

Zlatic, M., Landgraf, M., & Bate, M. (2003). Genetic specification of axonal arbors: atonal regulates robo3 to position terminal branches in the *Drosophila* nervous system. *Neuron, 37*(1), 41-51.

Zlatic, M., Li, F., Strigini, M., Grueber, W., & Bate, M. (2009). Positional cues in the *Drosophila* nerve cord: semaphorins pattern the dorso-ventral axis. *PLoS Biol, 7*(6), e1000135. doi:10.1371/journal.pbio.1000135

Zwart, M. F., Pulver, S. R., Truman, J. W., Fushiki, A., Fetter, R. D., Cardona, A., & Landgraf, M. (2016). Selective Inhibition Mediates the Sequential Recruitment of Motor Pools. *Neuron, 91*(3), 615-628. doi:10.1016/j.neuron.2016.06.031